Measurement of the vector boson production cross sections at $\sqrt{s} = 13.6$ TeV with the ATLAS detector

Mihaela Marinescu

Thesis submitted for the degree of
Doctor of Philosophy

Particle Physics Group,
School of Physics and Astronomy,
University of Birmingham.

September 2024

Abstract

The measurement of the inclusive $W^{\pm}$ and Z boson production cross sections, and their ratios, are presented using 29 fb^{-1} of pp collision data at a centre of mass energy of $\sqrt{s}$ = 13.6 TeV, collected by the ATLAS detector at the Large Hadron Collider (LHC). The measured fiducial cross sections for $W^{+} \rightarrow \ell^{+}\nu$, $W^{-} \rightarrow \ell^{-}\bar{\nu}$ and $Z \rightarrow \ell^{+}\ell^{-}$ boson production are 4250 ± 150 pb, 3310 ± 120 pb, and 744 ± 20 pb, respectively, where the total uncertainties on the fiducial cross sections are reported. The ratios of top-antitop quark pair to W boson fiducial cross sections are also presented. These measurements are compared to Standard Model predictions calculated at next-to-next-to-leading order in the strong coupling, next-to-next-to-logarithmic accuracy and next-to-leading-order electroweak accuracy, where good agreement is found between the measurements and predictions. The large cross sections of the $W^{\pm}$ and Z bosons, coupled with the clean final states from their leptonic decays, allow excellent experimental precision to be achieved in their measurements.

The upgrade of the ATLAS detector, undertaken in preparation for the third LHC data-taking period currently underway, has led to the improvement of various sub-components of the detector, including the Level-1 Calorimeter Trigger, which now has access to higher granularity information from the electromagnetic calorimeter. A novel set of energy corrections applied to the Level-1 Calorimeter Trigger as a result of this upgrade are also presented in this thesis, which contribute to the increased efficiency of single electron triggers for the ATLAS detector during the third LHC data-taking period.

Declaration

While this thesis is the result of my own work, most of the results presented here are the outcome of collaboration with other members of the ATLAS experiment, and would not have been possible in isolation.

The first two Chapters present a review of the theoretical background and experimental aspects related to the measurements presented later in the thesis. Thus, these do not include original work and the scientific publications and textbooks used to write these Chapters are referenced therein.

Chapter 3 presents a new energy correction applied on the upgraded L1 Calorimeter (L1Calo) trigger for improving trigger efficiencies during Run 3 at the LHC. Section 3.1 presents a review of the L1Calo system and of the e/γ identification algorithm on the new eFEX, while Section 3.3 presents trigger efficiencies for single EM object L1 triggers, which is not original work and is referenced accordingly. The dead material corrections presented in Section 3.2 are the result of my own work, under the supervision of members of the L1Calo group, and with the help of software developed by other members of this group. In addition to the work presented in this Chapter, I also contributed to ATLAS Run 3 operations by performing ATLAS control room shifts for the Run Control and Trigger roles, and L1Calo on-call shifts.

Chapters 4, 5 and 6 present the Run 3 $W^{\pm}$ and Z boson cross section measurement, for which I was one of the main analysers, working as part of an analysis team with other members of the ATLAS collaboration. The results presented in these Chapters are published in Ref. [1], for which I was also an editor.

Chapter 4 presents an overview of this analysis, including the cross section methodology, data and simulation samples, event selection performed, background estimation, theory predictions, systematic uncertainties and kinematic distributions and event yields for the W and Z channels. I have contributed to several aspects of this analysis, including early validation studies for the W and Z boson channels, where I have produced earlier versions of the control plots presented in Section 4.7 and upgrading software for compatibility with the Run 3 data format and combined performance tools. My major role in this analysis, however, was on the data-driven background measurement for the W boson channels, presented in Chapter 5, where most of the results presented in this Chapter are of my own work. Section 5.1 is an introduction to the methodology, based on previous ATLAS W boson cross section measurements, referenced accordingly. The nominal method for the data-driven background measurement presented in Section 5.2 is the result of my own work, under close collaboration with the other members of the analysis team, who offered guidance throughout the development of this measurement. Section 5.3 presents alternative measurements for the multijet background. The method denoted "method 2" is also the result of my own work, developed before the nominal method used in the published result, while "method 1" was developed by another member of the analysis team and the results for this are provided in this Section for reference. Chapter 6 present the results for the cross-section measurements. While I did not perform the cross-section fits for the results presented in this Chapter, I have contributed to discussions related to these, and produced the majority of the plots presented in this Chapter.

Acknowledgements

Firstly, I would like to thank my supervisor Kostas Nikolopoulos for his invaluable advice, continuous support and guidance throughout my PhD. This PhD would not have been possible without you, and I am eternally grateful for everything I have learned under your supervision.

I would like to thank Juraj Bracinik for his patience in supervising me during my qualification task within the Birmingham L1Calo group, and for always having a kind word. I would also like to thank the other members of the Birmingham L1Calo group, particularly Steve Hillier and Alan Watson for their guidance, and Paul Thompson for all the help and support while I was at CERN.

The *W* and *Z* cross section analysis, which is central to this thesis, was the result of an analysis team, which I am grateful to have been part of. I would like to especially thank Zhiqing Zhang and Ulla Blumenschein for their guidance and support throughout this analysis.

I am grateful to the members of the Birmingham ATLAS group for helping me become a better researcher, particularly Andy Chisholm for always making the time to discuss my questions and provide solid advice, and Aleksandra Dimitrievska for her support during the daunting final months of the PhD.

I would also like to thank my PhD colleagues and friends, especially Júlia Silva, Adrien Auriol and Dan Thompson, with whom I have shared many happy memories these past 4 years.

Finally, I would like to thank my family for their continuous love and support: to my parents, for supporting me through all my years of education, and for believing in me; to my sister, for sharing my love of science and always being interested in what I am working on. To Edi, thank you for staying by my side all these years, and for encouraging me to continue on this path. I couldn't have done it without you.

Contents

Chapter 1.

Introduction

The development of the Standard Model describing elementary particles and their interactions is considered one of the greatest achievements of the particle physics community in the 20th century. It has been thoroughly tested through experimental measurements, proving it to be the most accurate representation of the elementary constituents of the Universe and the fundamental forces by which they interact. Predictions of the Standard Model continue to be tested at high energy particle colliders such as the Large Hadron Collider (LHC). This thesis presents the measurement of the inclusive $W^{\pm}$ and Z boson production cross sections, performed using proton-proton (pp) collision data collected by the ATLAS detector at the highest energy achieved by the LHC so far, $\sqrt{s} = 13.6$ TeV [1].

This Chapter provides the theoretical background for this thesis, including an overview of the Standard Model and proton collision physics at the LHC, with a focus on W and Z boson physics. The LHC and the ATLAS detector, are described in Chapter 2, followed by a description of the techniques used for reconstructing particles in the ATLAS detector. Conducting measurements on LHC data relies foremost on the ability of detectors such as ATLAS to collect data efficiently, reducing the immense amount of data generated by proton-proton collisions in the LHC to manageable rates, achieved by triggering on interesting signatures. Chapter 3 describes the first level of data filtering performed by the ATLAS Level-1 Calorimeter trigger using information on energy deposits in the calorimeter, and a new type of energy correction applied in the trigger for a more efficient identification of electron candidates. An overview of the W and Z boson cross section measurement at $\sqrt{s} = 13.6$ TeV is provided in Chapter 4. Chapter 5 describes the data-driven measurement of the multijet background for the

W cross section measurement, and cross section results are shown in Chapter 6. Finally, the conclusion for this thesis is found in Chapter 7.

1.1. The Standard Model

The Standard Model (SM) is a theory which describes elementary particles and their interactions. Particles are classified according to their spin into two categories (summarised in Figure 1.1): half-integer spin particles called *fermions* and integer-spin particles called *bosons*.

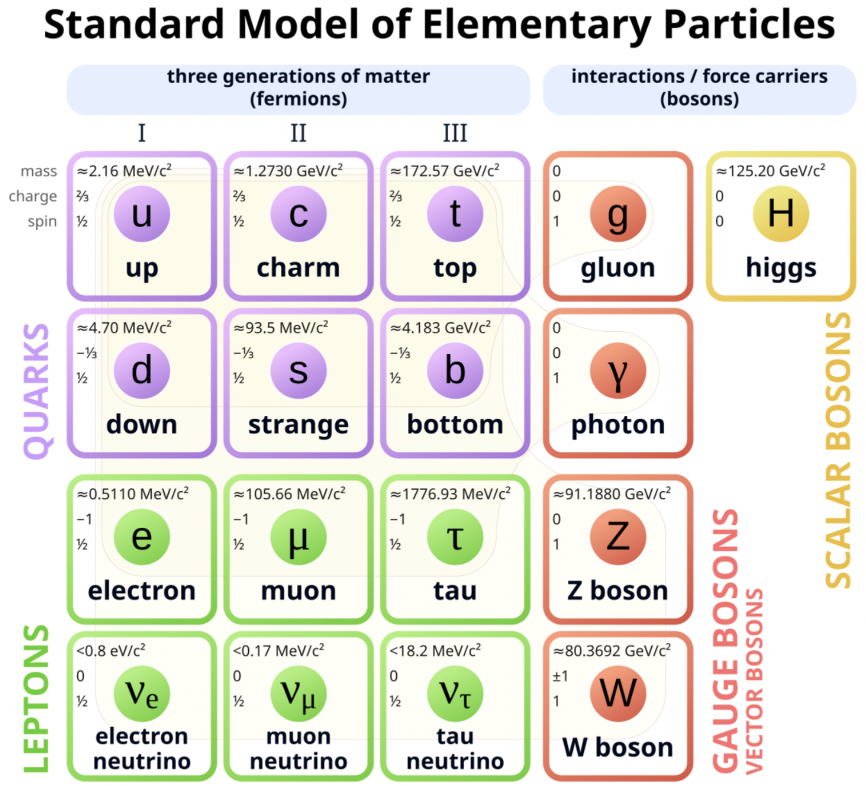

Figure 1.1.: The elementary particles of the Standard Model, classified into fermions and bosons [2].

Fermions are further divided into three generations of *leptons* and *quarks*, where each generation has progressively larger masses. Leptons include the electron (e), muon (μ) and tau (τ), which carry negative electromagnetic charge, and are associated with a neutrino partner (ν_e, ν_μ and ν_τ) with no electromagnetic charge. Quarks carry fractional electromagnetic charge: up-type quarks (u, c and t) carry $+2/3$ charge while down-type quarks (d, s and b) carry -1/3 charge. Besides electromagnetic charge, quarks also carry another type of charge called *colour*, which can take three values: red, green and blue (r, b, g). Vector bosons, which are spin-1 bosons, are force mediating particles. Gluons (g) are massless and carry colour charge as well. They mediate the strong force, and couple to other particles that carry color charge, which are quarks and gluons themselves. Photons (γ) are also massless and mediate the electromagnetic force, coupling to particles that carry electromagnetic charge. As photons are electromagnetically neutral, they do not couple with themselves. The weak force is mediated by the exchange of $W^{\pm}$ and Z bosons, which have mass. The $W^{\pm}$ and Z bosons couple to particles that carry *weak isospin* or *hypercharge*, explained further in Section 1.1.1. Quarks can interact through all three forces. Charged leptons interact through both weak and electromagnetic forces, and neutrinos only interact through the weak force. All fermions have a corresponding anti-particle with the same mass and opposite charge. Finally, the only scalar spin-0 boson predicted by the SM is the Higgs boson, which couples to all massive particles. It arises as a result of spontaneous electroweak symmetry breaking, which is the mechanism responsible for providing mass to all other particles [3].

The SM is formulated as a *quantum field theory*, where the elementary particles arise from excitations of quantum fields. Interactions in the SM are formulated in terms of local gauge symmetries described by the $\mathrm{SU}(3)_c \times \mathrm{SU}(2)_L \times \mathrm{U}(1)_Y$ gauge group. The strong interaction is described by Quantum Chromodynamics, based on local gauge invariance under the $\mathrm{SU}(3)_c$ gauge group. Electromagnetic and weak interactions are described jointly by electroweak theory, based on local gauge invariance under the $\mathrm{SU}(2)_L \times \mathrm{U}(1)_Y$ gauge group, which predicts massless gauge bosons, contrary to experimental evidence of the massive $W^{\pm}$ and Z bosons. Mass terms for the weak vector bosons are instead generated as local gauge invariance under $\mathrm{SU}(2)_L \times \mathrm{U}(1)_Y$ is spontaneously broken through the Brout-Englert-Higgs (BEH) mechanism [4, 5], which also allows the introduction of fermion mass terms. This mechanism also predicted the existence of the scalar Higgs boson, which was discovered by the ATLAS and CMS experiments at the Large Hadron Collider in 2012, almost 50 years after it was first theorised [6, 7].

1.1.1. Electroweak theory

Electroweak theory, developed by Glashow, Weinberg and Salam in the 1960s, combines the theory of electromagnetic interaction, quantum electrodynamics (QED), with the theory of weak interactions into a common framework [8–10]. The unified electroweak interaction is described by the $\mathrm{SU}(2)_L \times \mathrm{U}(1)_Y$ gauge group, where four gauge fields are introduced in order to preserve local gauge invariance.

The electromagnetic interaction, represented by the $\mathrm{U}(1)_Y$ gauge group, introduces the field B_μ, which couples to the hypercharge Y. The hypercharge is the conserved quantity arising from $\mathrm{U}(1)_Y$ gauge invariance. The weak interaction, modelled by the $\mathrm{SU}(2)_L$ symmetry, introduces three additional gauge boson fields $W^i_\mu = (W^1_\mu, W^2_\mu, W^3_\mu)$, which only couple to left-handed fermions and right-handed anti-fermions. The conserved quantity arising from $\mathrm{SU}(2)_L$ gauge invariance is the weak isospin. Hypercharge, Y, unites the fundamental properties of electromagnetic charge, Q, and weak isospin through the relation $Q = I_3 + Y/2$, where I_3 is the third component of the weak isospin. Fermions in the SM are chiral, such that mass eigenstates ψ can be represented by their left- and right-handed chiral components: $\psi = \psi_L + \psi_R$. The left- and right-handed chiral states $\psi_{L,R}$ are eigenstates of the projecion operators $\hat{P}_{L,R} = \frac{1\mp\gamma_5}{2}$: $\psi_{L,R} = \hat{P}_{L,R}\psi$. Left-handed fermion fields form weak isospin doublets, with the third component of the isospin I_3 = +1/2 for up-type quarks and neutrinos, and I_3 = -1/2 for down-type quarks and charged leptons:

$$\psi_L^{quarks} = \begin{pmatrix} u \\ d' \end{pmatrix}, \begin{pmatrix} c \\ s' \end{pmatrix}, \begin{pmatrix} t \\ b' \end{pmatrix} \qquad \psi_L^{leptons} = \begin{pmatrix} \nu_e \\ e \end{pmatrix}, \begin{pmatrix} \nu_\mu \\ \mu \end{pmatrix}, \begin{pmatrix} \nu_\tau \\ \tau \end{pmatrix}.$$

Right-handed fermion fields form singlets, with I_3 = 0. The weak interaction eigenstates (d', s' and b') are related to mass eigenstates (d, s and b) through the Cabibbo-Kobayashi-Maskawa (CKM) matrix [11, 12], which is a unitary 3 × 3 matrix describing quark mixing through the weak charged current interaction. Transitions between quarks of the same generations are favoured, while transitions across generations are suppressed.

The B_μ and three W_μ^i gauge fields mix to form the the physical mediators of the weak and electromagnetic interaction ($W^\pm$, Z and γ) after spontaneous electroweak symmetry breaking, described in Section 1.1.2.

1.1.2. Electroweak symmetry breaking

Local gauge invariance under the $\mathrm{SU}(2)_L \times \mathrm{U}(1)_Y$ gauge group explicitly forbids mass terms for the gauge bosons, despite experimental evidence of the massive $W^\pm$ and Z bosons mediating the weak force. In order to generate mass terms for the weak bosons while maintainting the gauge invariance of the electroweak theory under $\mathrm{SU}(2)_L \times \mathrm{U}(1)_Y$, this symmetry is spontaneously broken to $\mathrm{U}(1)_{EM}$ via the Brout-Englert-Higgs (BEH) mechanism [4, 5].

The BEH mechanism introduces the scalar complex Higgs field ϕ, placed in a weak isospin doublet of the form

$$\Phi = \begin{pmatrix} \phi^+ \\ \phi^0 \end{pmatrix} = \frac{1}{\sqrt{2}} \begin{pmatrix} \phi_1 + i\phi_2 \\ \phi_3 + i\phi_4 \end{pmatrix}, \tag{1.1}$$

where the potential associated with the Higgs field has the form

$$V(\Phi) = \mu^2 \Phi^\dagger \Phi + \lambda (\Phi^\dagger \Phi)^2, \tag{1.2}$$

with $\lambda > 0$ and μ^2 as free parameters of the potential.

For $\mu^2 > 0$, the potential has a single minimum at the origin, while for $\mu^2 < 0$, the potential has an infinite set of minima satisfying

$$\Phi^\dagger \Phi = \frac{1}{2}(\phi_1^2 + \phi_2^2 + \phi_3^2 + \phi_4^2) = \frac{v^2}{2} = \frac{|\mu|^2}{2\lambda}, \tag{1.3}$$

where $v = \frac{\mu}{\sqrt{\lambda}}$ is the vacuum expectation value (VEV).

The choice of a particular value for the physical vacuum v among the infinite set of minima will spontaneously break the symmetry of the system. In order for the photon to remain massless after symmetry breaking, a vacuum state is chosen such that $\phi_1 = \phi_2 = \phi_4 = 0$ and $\phi_3 = v$, where only the neutral scalar field ϕ^0 has a non-zero VEV v [3]:

$$\phi^0 = \frac{1}{\sqrt{2}} \begin{pmatrix} 0 \\ v \end{pmatrix}. \tag{1.4}$$

Expanding the system about this minimum then results in

$$\Phi = \frac{1}{\sqrt{2}} \begin{pmatrix} \phi_1 + i\phi_2 \\ v + \eta(x) + i\phi_4 \end{pmatrix}, \tag{1.5}$$

where ϕ_1, ϕ_2 and ϕ_4 are the Goldstone fields, associated with three unphysical Goldstone bosons [13], which can be removed by re-writing Eq 1.5 in terms of a unitarity gauge. The Higgs potential can then be written as

$$\Phi = \frac{1}{\sqrt{2}} \begin{pmatrix} 0 \\ v + h(x) \end{pmatrix}, \tag{1.6}$$

where $h(x)$ is the Higgs scalar field, which gives rise to the scalar Higgs boson observed experimentally. The remaining degrees of freedom associated with the three Goldstone bosons are absorbed into the longitudinal components of the $W^{\pm}$ and Z bosons [14].

Substituting Eq. 1.6 into the Lagrangian of the Higgs sector, given by

$$\mathcal{L}_{\text{Higgs}} = (D_\mu \Phi)^\dagger (D^\mu \Phi) - V(\Phi), \tag{1.7}$$

allows the B_μ and three W^i_μ gauge fields to mix by coupling with the Higgs field through the covariant derivative, D_μ. Thus, the fields for the physical $W^\pm$, Z and γ mediators are given by:

$$W^\pm_\mu = \frac{1}{\sqrt{2}}(W^1_\mu \pm iW^2_\mu), \tag{1.8}$$

$$Z_\mu = \frac{g_W W^3_\mu - g' B_\mu}{\sqrt{g^2_W - g'^2}}, \tag{1.9}$$

$$A_\mu = \frac{g_W W^3_\mu + g' B_\mu}{\sqrt{g^2_W - g'^2}}, \tag{1.10}$$

where A_μ represents the photon field, and g_W and g' are the coupling constants for the $\mathrm{SU(2)}_L$ and $\mathrm{U(1)}_Y$ gauge interactions, respectively, which are related to the electroweak mixing angle θ_W as

$$\frac{g'}{g_W} = \tan\theta_W. \tag{1.11}$$

Finally, the masses of the $W^\pm$ and Z bosons can be defined in terms of v as

$$m_W = \frac{1}{2} v g_W, \tag{1.12}$$

$$m_Z = \frac{1}{2} v \sqrt{g^2_W + g'^2}, \tag{1.13}$$

and the photon remains massless.

Fermions acquire mass through their interactions with the Higgs field. The Lagrangian of the Higgs sector from Eq. 1.7 can be expanded by adding interaction terms between the fermion and Higgs field, such that after electroweak symmetry breaking, mass terms of the form $m_f = \frac{y_f v}{\sqrt{2}}$ arise, where different Yukawa couplings y_f represent the strength of the interaction between the Higgs field and fermions.

1.1.3. Quantum Chromodynamics

Quantum chromodynamics (QCD) is the theory describing strong interactions, based on the SU(3)$_c$ gauge group, where the conserved quantity is the colour charge c. There are three possible colours (r, b, g) and anti-colours ($\bar{r}$, $\bar{b}$, $\bar{g}$). Quarks carry a single colour charge and anti-quarks carry a single anti-colour charge, while gluons carry simultaneously both colour and anti-colour charges, resulting in eight different gluons which can also self-interact.

The strength of the strong interaction is expressed in terms of the strong coupling constant α_s, which is dependent on an energy scale Q^2, increasing with increasing distance or decreasing energy scale.

Given a known value for α_s at an energy scale μ^2, the evolution or the *running* of α_s for an energy scale Q^2 to first order accuracy is given by [15]:

$$\alpha_s(Q^2) = \frac{\alpha_s(\mu^2)}{[1 - \frac{\alpha_s(\mu^2)}{12\pi}(33 - 2n_f)\ln\frac{\mu^2}{Q^2}]}, \tag{1.14}$$

where n_f is the number of quark flavours kinematically allowed to contribute to loop corrections, with quark masses $m_f < |Q|$. Eq. 1.14 arises as a result of *renormalisation*, where corrections corresponding to an infinite number of quark and gluon loops, which are needed to calculate physical observables such as cross sections, are absorbed in the definition of α_s.

This running coupling phenomenon can be interpreted physically as the response of the vacuum to the presence of a strongly interacting particle, analogous to the effect of vacuum polarisation in QED. In quantum field theory, vacuum is composed of quantum fluctuations leading to the creation and annihilation of fermion-anti-fermion pairs on very short time scales. Thus in QED, an electron in vacuum would be surounded by charged fermion anti-fermion pairs which would orient themselves such that the positively charged fermions are closer to the electron, effectively screening the charge of the electron and inducing an energy scale dependence on the interaction strength between a photon propagator and the electron, given by the momentum transfer between the two. Similarly, virtual quark anti-quark pairs spontaneously created surrounding a quark induce a similar screening effect due to the colour charge.

However, in the case of QCD, gluons also carry colour charge, resulting in them contributing to an anti-screening effect due to gluon self-interaction [15].

Eq. 1.14 can be rearranged in terms of a QCD energy scale Λ_{QCD}, such that

$$\alpha_s(Q^2) = \frac{12\pi}{(33 - 2n_f)\ln\frac{Q^2}{\Lambda^2_{QCD}}}. \tag{1.15}$$

The QCD energy scale $\Lambda_{QCD} \approx 1$ GeV sets the energy regime for which perturbation theory can be applied in QCD. For large Q^2 values, or over short distances, α_s is small, allowing it to be expressed perturbatively as a power series. This is known as the *asymptotic freedom* regime, where quarks are free. For small Q^2 values close to Λ_{QCD}, or over long distances, α_s values diverge due to the logarithmic term in Eq. 1.15, and perturbation theory can no longer be used. In this energy regime, quarks are confined to colour-neutral states called *hadrons*. Considering an example where a quark anti-quark ($q\bar{q}$) pair is pulled apart, the colour field between these, arising from gluon self-interaction, becomes larger until it is energetically favourable to produce a new $q\bar{q}$ pair. The process continues until the energy is sufficiently small for quarks to combine, producing *jets* of hadrons [3].

1.2. Proton collisions at the LHC

High energy particle colliders such as the Large Hadron Collider (LHC), which primarily collides protons in pp collisions, are used to test the Standard Model experimentally. Most commonly, tests are performed by comparing measurements of cross sections, which describe the probability of a process occuring in a pp collision, with predictions of the SM based on fixed-order calculations. Figure 1.2 shows the comparison between theory predictions and cross section measurements for a large number processes predicted by the SM, performed by the ATLAS experiment using pp collision data collected at different centre-of-mass energies $\sqrt{s}$. In this thesis, pp collision data collected at $\sqrt{s}$ = 13.6 TeV by the ATLAS experiment are used to measure the inclusive production cross sections of the W and Z bosons. This Section provides an overview of proton collision physics, with a focus on W and Z boson physics at the LHC.

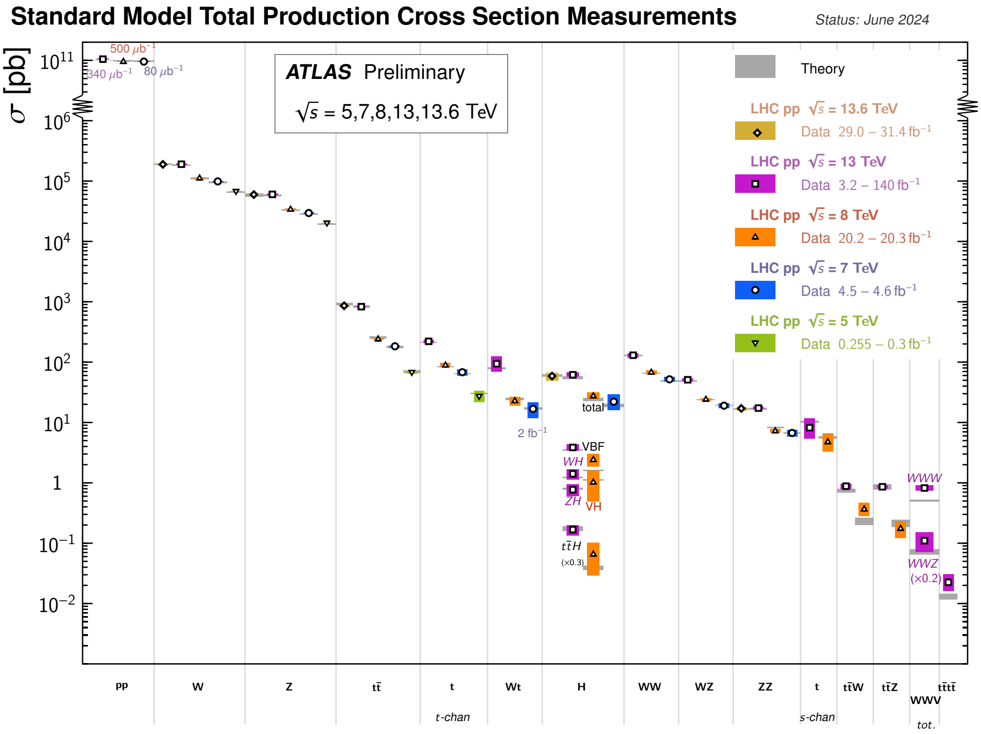

Figure 1.2.: Summary of cross section measurements of several processes predicted by the Standard Model, measured by the ATLAS experiment at different centre-of-mass energies of the LHC. All cross sections are compared to their corresponding theoretical predictions [16].

Protons are composite particles, composed of a bound state of three valence quarks, two u quarks and a d quark, and a sea of quarks, anti-quarks and gluons produced by quantum fluctuations and interactions between the valence quarks. These proton constituents are collectively known as *partons*. When high-energy protons collide in the LHC, some interactions occur with an exchange of high transverse momentum, known as the *hard scatter* interaction, where the energy scale is sufficiently high for perturbative QCD calculations to be applicable. Thus, for a hard scatter interaction $qq' \to X$, where the final state X is produced from partons q and q', the cross section of this parton-level hard scatter interaction $\sigma_{qq'\to X}$ is calculable as a perturbative series of the strong coupling α_s,

$$\sigma_{qq'\to X}(\mu_R) = \sigma_0 + \alpha_s(\mu_R)\sigma_1 + \alpha_s^2(\mu_R)\sigma_2 + ...,$$

where the cross section is shown up to next-to-next-to-leading order (NNLO) accuracy. At non-perturbative energy scales, divergences occur in the value of α_s, as explained in Section 1.1.3, and so α_s must be defined in terms of a *renormalisation scale* μ_R.

Cross sections involving protons in the initial state are not calculable in perturbative QCD, and in order to calculate these, the cross section is factorised into process-independent parton distribution functions (PDFs) and the cross section of the parton-level hard scatter interaction [15]:

$$\sigma_{pp\to X} = \sum_{q,q'} \int_0^1 dx_q dx_{q'} f_q(x_q, \mu_F, Q^2) f_{q'}(x_{q'}, \mu_F, Q^2) \times \sigma_{qq'\to X}(\mu_F, \mu_R). \tag{1.16}$$

The sum in Eq. 1.16 is over all partons q and q' within the proton which may contribute to the parton-level hard scattering process $qq' \to X$. At the energy scales of pp collisions in the LHC, hard scatter interactions occur on shorter timescales than the quantum fluctuations giving rise to sea gluons and quarks of different flavours. Thus, besides the u and d valence quarks present in protons, these partons can also participate in the $qq' \to X$ hard scatter interaction, although with smaller contributions to the cross sections. The probability of different partons participating in the hard scatter is encoded in PDFs, which generally describe the probability of finding a parton of type q carrying a fraction x_q of the proton momentum, also called *Bjorken-x*, when the proton is probed at an energy scale Q^2. The PDFs $f_q(x_q, \mu_F, Q^2)$ and $f_{q'}(x'_q, \mu_F, Q^2)$ in Eq. 1.16 are defined in terms of a *factorisation scale* μ_F, where this is the energy scale at which the PDFs are evaluated in the cross-section calculation, chosen as a cut-off value below which partons are still considered to be part of the proton. For processes of the type $pp \to X$, the value of μ_R and μ_R is typically chosen to be equal to the energy scale of the process, $\mu_R = \mu_F = m_X$.

PDFs cannot be obtained perturbatively since the length scales inside the proton are large enough that QCD is in the non-perturbative regime. Instead, these are approximated by some parametrisation, and final distributions are obtained through global fits to experimental data from a large set of processes, performed by different PDF groups [17]. The dependence of PDFs on the energy scale Q^2 can be described through a perturbative framework by the DGLAP equations [18–20], such that PDFs obtained from measurements performed at a specific energy scale can be evolved to a different energy scale, μ_F, relevant for calculating cross sections of different processes.

Figure 1.3 shows the MSHT20NNLO PDF set [21], estimated at different energy scales of $Q^2 = 10$ GeV^2 and $Q^2 = 10^4$ GeV^2. PDFs are provided separately for gluons and different quark flavours as a function of Bjorken-x. For large Bjorken-x values, equivalent to large momentum transfer in the hard scatter interaction, valence quark PDFs (u_V and d_V) are seen to dominate, while for intermediate x values, sea quarks and gluons dominate. Finally, gluons dominate at low-x values, where gluon splitting processes become more important.

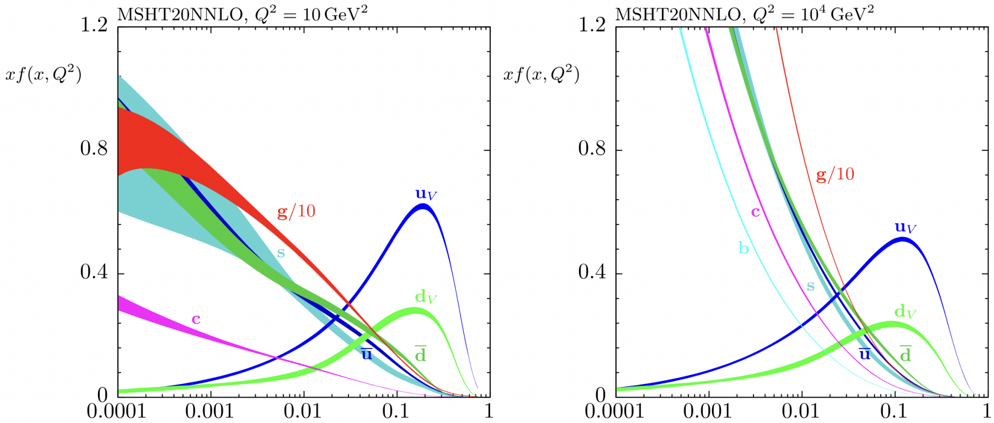

Figure 1.3.: MSHT20NNLO proton parton distribution functions for gluons and different quark flavours, including valence quarks denoted with a V subscript, at energy scale $Q^2 = 10$ GeV^2 (left) and $Q^2 = 10^4$ GeV^2 (right). The x-axis represents Bjorken-x, the fraction of the proton momentum carried by the parton [21].

1.2.1. Event simulation

Cross section calculations at a fixed order of QCD discussed so far are only performed in the perturbative regime of QCD, at the parton level. In order to obtain an accurate comparison between SM predictions and data, non-perturbative effects in proton collisions such as parton shower and hadronisation must also be considered. Monte Carlo (MC) generators are used to simulate proton collision events, where a number of steps are involved, described in this Section [22].

The simulation chain begins with the hard scatter cross section calculation, where the Matrix Element (ME) describing the probability amplitude of the hard scattering process $qq' \rightarrow X$ is generated at a particular order in QCD. Eq. 1.16 becomes

$$\sigma_{pp\to X} = \sum_{q,q'} \int_0^1 dx_q dx_{q'} f_q(x_q, \mu_F, Q^2) f_{q'}(x_{q'}, \mu_F, Q^2) \int d\Phi_X \frac{1}{2\hat{s}} |\mathcal{M}_{qq'\to X}|^2 (\Phi_X, \mu_F, \mu_R), \tag{1.17}$$

where the hard scatter cross section $\sigma_{qq'\to X}$ depends on the momenta given by the final-state phase space Φ_X, and the product between the corresponding matrix element squared $|\mathcal{M}_{qq'\to X}|^2$ and the parton flux $1/2\hat{s} = 1/(2x_q x_{q'} s)$, where s is the centre-of-mass energy squared. Phase space events are randomly sampled, and when the desired number of events is produced, the result is an integration over the generated incoming and outgoing particle momenta. Monte Carlo techniques are used to perform this multi-dimensional intergation.

Additional radiative corrections are applied in the parton shower (PS) stage of the simulation chain, which simulates the propagation of initial and final state partons after the hard scatter interaction. Partons are subject to collinear gluon or $q\bar{q}$ pair emissions, where the probabilities of these collinear emissions are described by splitting functions. Since gluons self interact, gluon emissions give rise to futher gluon emissions, which can split into further $q\bar{q}$ pairs, effectively creating a shower of partons. The shower progresses until eventually the energy scale reaches the non-perturbative regime, and partons can no longer be treated as free particles. The cut-off scale for the PS algorithm is usually at 1 GeV, after which hadronisation must take place, combining partons into colour-neutral hadrons. Since hadronisation cannot be calculated perturbatively, QCD phenomenological models tuned to experimental data are used to simulate this stage. The most common classes of models used to simulate hadronisation are string models, which are based on the assumption of linear confinement idea where a string of colour flux carrying potential energy forms between separating quarks and gluons, and cluster models, which are based on the pre-confinement property of parton showers into colour-singlet clusters of partons. Unstable particles produced after hadronisation are decayed into final state particles.

When considering higher order predictions, the interplay between the ME and PS stage becomes complicated and parton emissions may be double counted. This is resolved by calculating MEs separately for each final state parton multiplicity and by defining a momentum scale below which partons are handled by the PS algorithm rather than the ME calculation.

In addition to the hard scatter interaction, other softer interactions can occur in pp collisions, which must be simulated for an accurate representation of the event. Spectator partons from the colliding protons, which did not contribute to the hard scatter interaction, can interact to produce additional parton showers as part of the *underlying event* (UE).

Since protons are collided in bunches at the LHC, more than one pp interaction may occur per bunch crossing, known as *pile-up*. These effects are simulated by adding soft inelastic pp interactions to the simulated hard-scatter event, based on the pile-up profile in data.

An illustration of a pp collision, including the various stages considered in simulating these events, is shown in Figure 1.4. The event begins with the hard scatter interaction, shown as a red blob. Final state radiation, also shown in red, gives rise to the secondary process, simulated by parton shower algorithms. Initial state radiation, shown in blue, also contibutes to parton showers. Spectator partons from the colliding protons give rise to the underlying event, shown as a purple blob, which produces further parton showers. Hadronisation processes, where emerging partons hadronise to colourless states and eventually decay, are shown in green.

1.2.2. W and Z boson physics

At leading order (LO) in perturbative QCD, W and Z bosons are produced in proton collisions via the Drell-Yan (DY) mechanism [23], depicted in diagrams such as those in Figure 1.5 and 1.6. Higher order processes (NLO, NNLO, etc.) may include additional partons in the final state. Figures 1.7 and 1.8 show representative diagrams for the NLO production of the W^+ and Z boson, respectively, where the final state quark or gluon can manifest as a jet in the detector.

Different parton flavours contribute to the LO processes, as shown in Figure 1.9, which depicts the contribution of different sub-processes to the leading order cross section for $W^\pm$ and Z production as a function of the centre-of-mass energy $\sqrt{s}$ for hadron colliders. Looking at $\sqrt{s}$ values close to that currently achieved at the LHC, $\sqrt{s}$ = 13.6 TeV, the cross section for W^+ production, $\sigma_{LO}(W^+)$, is dominated by the $u\bar{d} \to W^+$ sub-process, while the cross section for W^- production, $\sigma_{LO}(W^-)$, is dominated by the $d\bar{u} \to W^-$ sub-process. The difference between $\sigma_{LO}(W^+)$ and $\sigma_{LO}(W^-)$ arises as a result of protons being composed of two valence u_V quarks and

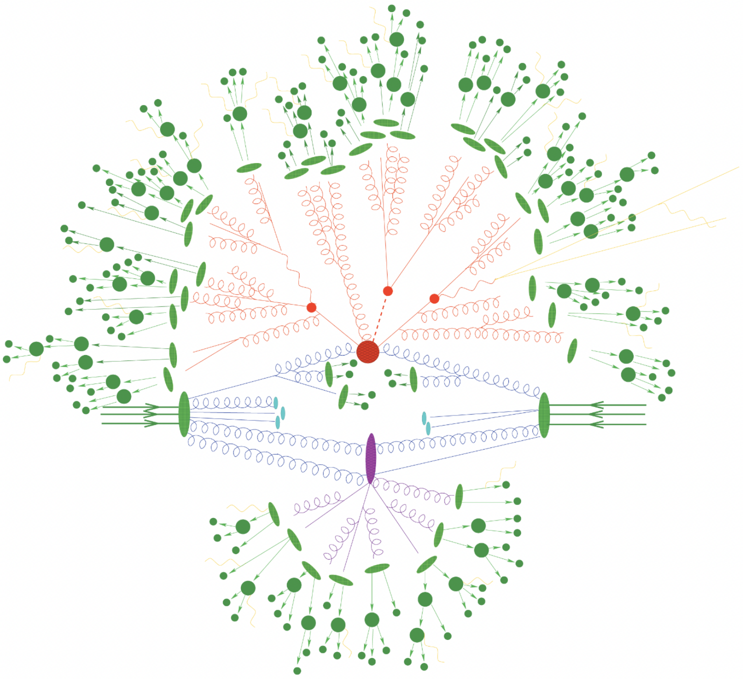

Figure 1.4.: Diagram of a simulated hadron-hadron collision event, such as a pp collision at the LHC. The hard scattersing interaction is shown in red. Initial and final state radiation is shown in blue and red respectively, which gives rise to secondary process. The underlying event produced by spectator partons is shown in purple. Hadronisation processes are shown in green [15].

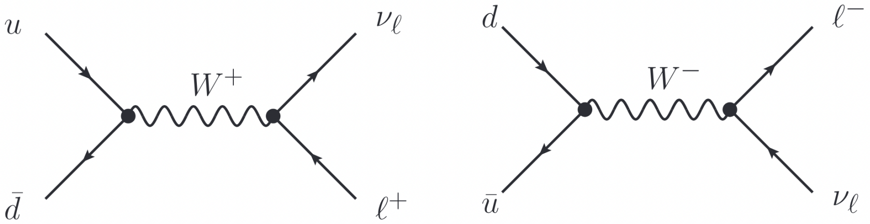

Figure 1.5.: Production of the W^+ and W^- boson at leading perturbative order (LO), via the $u\bar{d} \rightarrow W^+$ and $d\bar{u} \rightarrow W^-$ sub-processes, followed by their leptonic decays [15].

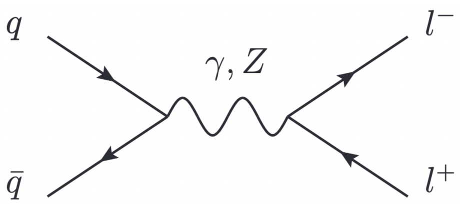

Figure 1.6.: Production of the Z boson at leading perturbative order (LO), and its subsequent leptonic decay [24].

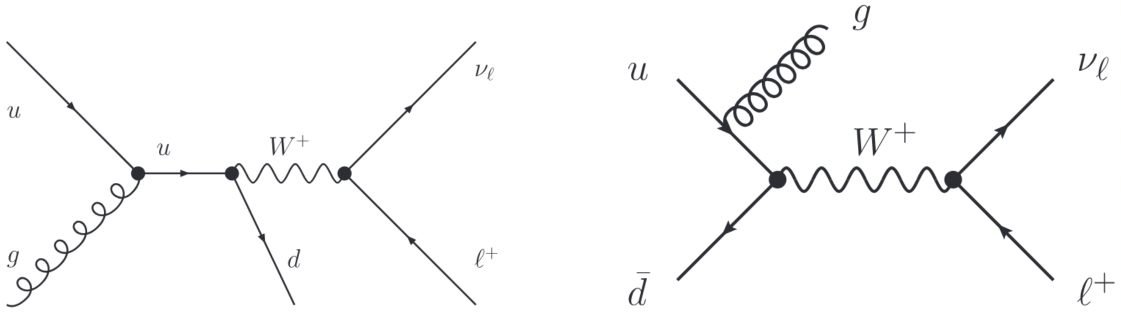

Figure 1.7.: Production of the W^+ boson at next-to-leading perturbative order (NLO), via the $gu \rightarrow W^+ + d$ (left) and $u\bar{d} \rightarrow W^+ + g$ (right) sub-processes, followed by the W^+ boson leptonic decay [15].

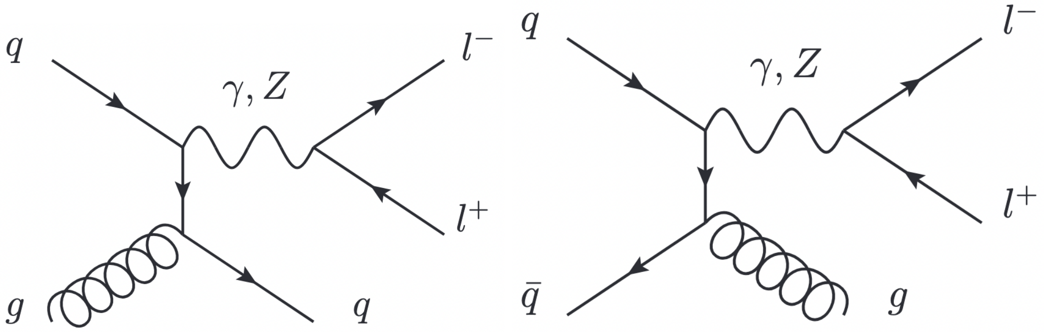

Figure 1.8.: Production of the Z boson at next-to-leading perturbative order (NLO), via the $gq \rightarrow Z + q$ (left) and $q\bar{q} \rightarrow Z + g$ (right) sub-processes, followed by the Z boson leptonic decay [24].

one d_V quark. At Bjorken-x values associated to DY production, $x \sim 0.1$, there is a higher probability of finding u_V quarks compared to d_V quarks, as seen in the PDFs shown in Figure 1.3. Thus, it is more likely for a W^+ to be produced than a W^-in pp collisions. The next largest contributions to $\sigma_{LO}(W^+)$ and $\sigma_{LO}(W^-)$ come from the $c\bar{s} \rightarrow W^+$ and $s\bar{c} \rightarrow W^-$ sub-processes, initiated by sea quarks, followed by contributions from quarks and anti-quarks from different generations, which are suppressed. Z boson production on the other hand is only initiated by quarks and anti-quarks of the same flavour, where the $u\bar{u} \rightarrow Z$ and $d\bar{d} \rightarrow Z$ sub-processes are the leading contributions to $\sigma_{LO}(Z)$ for LHC energies, followed by sub-leading contributions from sea quark anti-quark pairs. Thus, fewer combinations of partons are available to initiate this process, leading to a smaller Z production cross section compared to $W^\pm$ production.

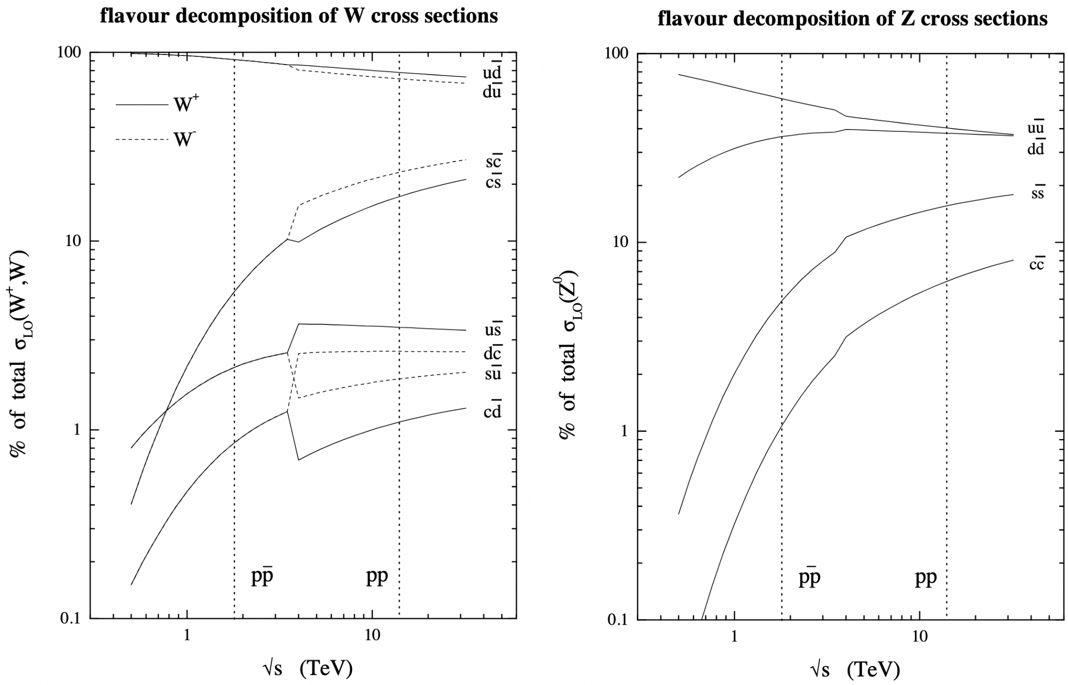

Figure 1.9.: Parton flavour decomposition for production of W^+, W^- and Z bosons at leading perturbative order (LO) as a function of hadron collider centre of mass energy $\sqrt{s}$. Predictions for pp collisions at LHC energies are shown for $\sqrt{s} > 4$ TeV [25].

As shown in Figure 1.2, inclusive W and Z boson production are two of the most common processes measured at the LHC, and are typically measured through their leptonic decay modes, $W^\pm \to \ell^\pm \nu$ and $Z \to \ell^+\ell^-$, where ℓ represents electrons or muons and ν represents their corresponding neutrinos [1]. Despite decays to quark anti-quark pairs having larger branching ratios, leptonic decay modes provide cleaner experimental signatures in detectors such as ATLAS, which have been designed to reconstruct electrons and muons very efficiently and distinguish these signals from the large QCD jet background produced at the LHC, described further in Section 2.3. Thus, W and Z production are an abundant source of electrons and muons, which can also be used for detector calibration and to assess detector performance. Due to their easily identifiable final states, W and Z cross section measurements are often performed at the beginning of a new energy regime at hadron colliders such as the LHC, in order to validate detector performance. Additionally, W and Z cross section measurements achieve excellent experimental precision around the percent level, and

---

[1] W and Z boson decays including τ leptons can also be reconstructed, where the τ is reconstructed from its leptonic or hadronic decay. However, this is often associated with increased systematic uncertainties, which outweighs the contribution to the signal efficiency, and is treated as background instead.

sub-percent level in the case of cross-section ratios, allowing comparisons between these and fixed-order calculations at high precisions.

Figure 1.10 shows a summary of inclusive W and Z production cross section measurements, multiplied by the leptonic decay branching ratios, performed by the CMS experiment using pp collisions at centre-of-mass energies $\sqrt{s}$ ranging from 2.76 TeV to 13 TeV. Additional results using $p\bar{p}$ collisions at lower centre-of-mass energies, between 0.63 TeV and 1.96 TeV, performed by the UA1 and UA2 collaborations at the CERN $Sp\bar{p}S$ collider [26, 27] and by the D0 and CDF collaborations at the Tevatron [28, 29] are also shown. All cross-section measurements were performed using leptonic decays including electrons and muons, and are shown to be in agreement with theory predictions calculated at NNLO precision, based on the NNPDF4.0 PDF set [30].

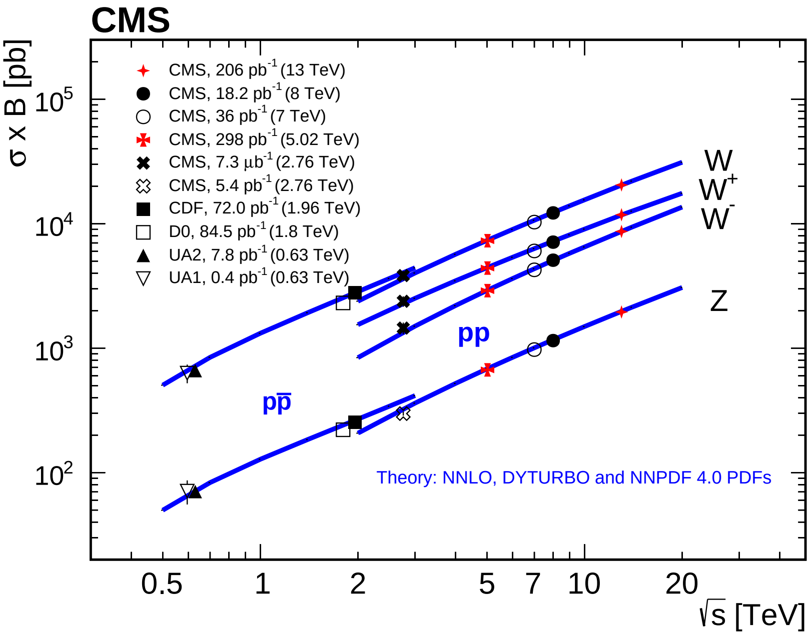

Figure 1.10.: Measurements of the inclusive W and Z production cross section times branching fraction to electron and muon final states performed by the CMS experiment using pp data collected at different centre-of-mass energies $\sqrt{s}$, ranging from 2.76 TeV to 13 TeV. Results obtained from other experiments using lower energy $p\bar{p}$ collisions are also shown. Experimental measurements are compared to theory predictions obtained at NNLO accuracy [31].

The most recent measurements performed by CMS are shown in red, using pp collisions at centre-of-mass energies of 5.02 TeV and 13 TeV [31]. The data sets used correspond to integrated luminosities of 298 $\pm$ 6 pb^{-1} at 5.02 TeV and 206 $\pm$ 5 pb^{-1} at 13 TeV. The data used for these measurements were collected in dedicated runs with reduced instantaneous luminosities [2], resulting in reduced pile-up and associated QCD jet backgrounds. The measured products between the total cross sections and leptonic branching ratios to electron and muon final states are $\sigma(pp \to W + X)\mathcal{B}(W \to \ell\nu)$ = 7300 ± 10 (stat) ± 60 (syst) ± 140 (lumi) pb and $\sigma(pp \to Z + X)\mathcal{B}(Z \to \ell\ell)$ = 669 ± 2 (stat) ± 6 (syst) ± 13 (lumi) pb for the 5.02 TeV data. The X denotes these are the inclusive W and Z cross sections, where additional objects such as jets may be present in the final state, due to higher-order contributions to W and Z boson production such as those shown in Figures 1.7 and 1.8. Statistical, systematic and luminosity uncertianties on the cross sections are shown separately. The corresponding results at 13 TeV are $\sigma(pp \to W + X)\mathcal{B}(W \to \ell\nu)$ = 20480 ± 10 (stat) ± 170 (syst) ± 470 (lumi) pb and $\sigma(pp \to Z + X)\mathcal{B}(Z \to \ell\ell)$ = 1952 ± 4 (stat) ± 18 (syst) ± 45 (lumi) pb.

For the W channels, the fiducial region was defined by the presence of one high-p_T [3], isolated lepton, with additional constraints on the transverse mass of the W boson [4], $m_\mathrm{T} > 40$ GeV, in order to reduce the contribution from QCD backgrounds. For the Z channels, two high-p_T, isolated leptons were required, with di-lepton invariant mass satisfying 60 GeV $< m_{\ell\ell} <$ 120 GeV. All backgrounds were estimated using simulation, with the exception of the QCD jet background, which was estimated using data in a control region obtained by inverting the requirement on the lepton isolation and m_T. The m_T and $m_{\ell\ell}$ distributions, such as those shown in Figure 1.11, were used to extract the W and Z boson fiducial cross sections using maximum likelihood fits. Total cross sections were calculated by extrapolating the fiducial cross sections to the full phase space using a kinematic acceptance factor obtained from simulation.

Figure 1.12 shows the results for the total W and Z boson cross sections, and their ratios, compared to NNLO predictions obtained using different PDF sets. The total uncertainty on each measurement is shown as a gray band, where the largest source of uncertainty is the luminosity, amounting to 1.9% and 2.3% for the 5.02 TeV and 13 TeV results, respectively. The total uncertainties on the cross section ratios are smaller since some uncertainties, such as the luminosity uncertainty, are cancelled. The experimental measurements are compared to theory predictions obtained using various state-of-

---

[2] Hadron collider luminosity is discussed further in Section 2.1.

[3] The transverse momentum p_T and the coordinate system is further described in Section 2.2.

[4] The W transverse mass is defined as $m_\mathrm{T} = \sqrt{2p_\mathrm{T}^{\nu}p_\mathrm{T}^{\ell}(1 - \cos\Delta\phi^{\ell\nu})}$, where p_T^{ℓ} is the transverse momentum of the lepton, p_T^{ν} is the transverse momentum of the neutrino, inferred from the missing transverse momentum in the event, and $\Delta\phi^{\ell\nu}$ is the opening angle between the neutrino and the lepton in the azimuthal plane.

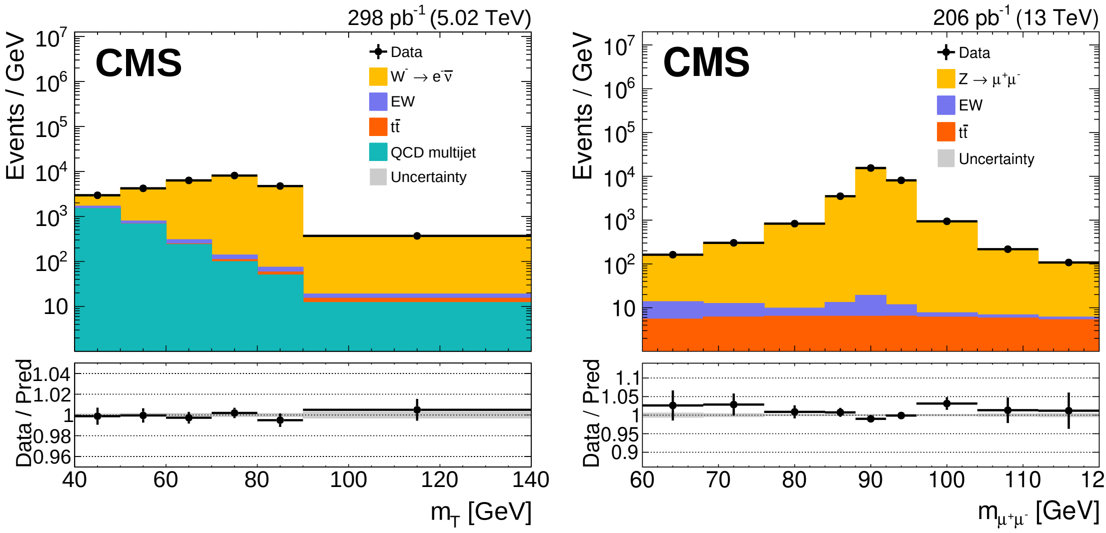

Figure 1.11.: Distributions of the W transverse mass m_T in the $W^- \to e^- \bar{\nu}$ channel for 5.02 TeV data (left), and di-lepton invariant mass $m_{\ell\ell}$ in the $Z \to \mu^+\mu^-$ channel for 13 TeV data (right) used by the CMS experiment to extract W and Z fiducial cross sections [31].

the-art PDF sets, where the 5.02 TeV measurements were found to agree well with the predictions within their uncertainties, while the 13 TeV measured results were generally larger than the predictions. Uncertainties on the theory predictions include the statistical uncertainty, and the PDF, α_S, and renormalization and factorization scale uncertainties.

The W and Z boson inclusive production cross sections have been measured at several centre-of-mass energies by the ATLAS experiment as well. The most recent measurements were performed using pp collisions collected at centre of mass energies of 5.02 TeV and 13 TeV [32], where the W and Z cross sections were measured differentially as a function of their p_T. The data for these measurements were also collected in dedicated low instantaneous luminosity runs, similarly to the CMS measurements presented previously, corresponding to integrated luminosities of 255 $\pm$ 6 pb^{-1} and 338 $\pm$ 3 pb^{-1} at $\sqrt{s}$ = 5.02 TeV and 13 TeV, respectively. The measured products between the total cross sections and leptonic branching ratios are $\sigma(pp \to W + X)\mathcal{B}(W \to \ell\nu) = 7316 \pm 124$ pb and $\sigma(pp \to Z + X)\mathcal{B}(Z \to \ell\ell) = 677 \pm 12$ pb for the 5.02 TeV data, where the total uncertainties are given, including the statistical, systematic and luminosity uncertainties. The corresponding results at 13 TeV are $\sigma(pp \to W + X)\mathcal{B}(W \to \ell\nu) = 20580 \pm 460$ pb and $\sigma(pp \to Z + X)\mathcal{B}(Z \to \ell\ell) = 1986 \pm 59$ pb.

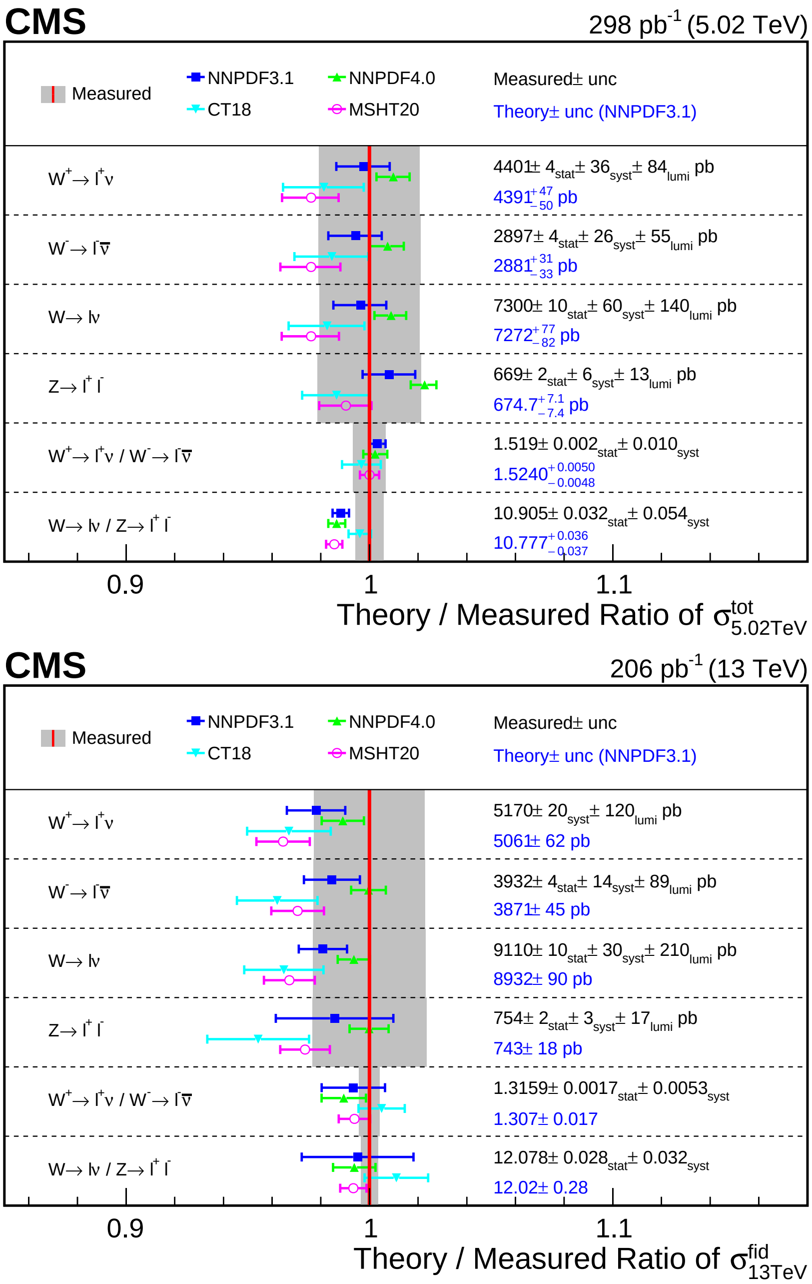

Figure 1.12.: Comparison between $W^{\pm}$ and Z boson total cross sections, and their ratios, using 5.02 TeV (top) and 13 TeV (bottom) pp collision data. Measurements are compared with theory predictions obtained using various PDF sets [31].

The fiducial region for the W boson channels was defined by the presence of one high-p_{T}, isolated lepton, and $m_{\mathrm{T}} > 50$ GeV, with an additional requirement on the missing transverse momentum of the neutrino, inferred using the missing transverse energy in the event, $E_{\mathrm{T}}^{\mathrm{miss}} > 25$ GeV, in order to reduce the QCD background. For the Z boson fiducial region, two high-p_{T}, isolated leptons were required, with di-lepton invariant mass satisfying 66 GeV $< m_{\ell\ell} <$ 116 GeV. Backgrounds were also estimated using simulation, with the exception of the QCD jet background, which was estimated using a data-driven approach based on control regions obtained by inverting the requirement on the lepton isolation and m_{T}. The differential cross sections were obtained by performing profile likelihood fits in the p_{T} distributions of the W and Z boson. In order to reconstruct the W boson p_{T}, the hadronic recoil is used. This is based on the remaining reconstructed particles in the event after the charged lepton from the W decay is selected, and is equal in magnitude and pointing in the opposite direction to the W boson transverse momentum. For the Z boson, the p_{T} can be estimated from both the reconstructed di-lepton p_{T} and the hadronic recoil.

The p_{T} distributions were unfolded to remove detector effects, and compared to predictions based on different Monte Carlo (MC) generators and NNLO predictions performed using the `DYTurbo` program [33] for several PDF sets, as shown in Figures 1.14 and 1.13. The `DYTurbo` predictions are observed to agree best across the p_{T} spectra, while the largest differences occur between the measured differential cross sections and the MC predictions, especially at larger transverse momenta. These measurements, which have an excellent precision at the level of 1-2%, are especially important for measurements of the W boson mass, which rely on a good modelling of the p_{T} spectrum of the W boson [34].

W and Z cross section measurements have also been performed by the LHCb experiment in the forward pseudo-rapidity region, where these complement the measurements performed by the CMS and ATLAS experiments and allow PDFs to be constrained at lower Bjorken-x values, down to 10^{-4} [35]. The W^+, W^- and Z boson cross sections were measured in the muon decay channels, using 2.0 fb^{-1} pp collision data collected at 8 TeV centre-of-mass energy [36], and were found to be $\sigma(W^+ \to \mu^+\nu) = 1093.6 \pm 2.1 \pm 7.2 \pm 10.9 \pm 12.7$ pb, $\sigma(W^- \to \mu^-\nu) = 818.4 \pm 1.9 \pm 5.0 \pm 7.0 \pm 9.5$ pb and $\sigma(Z \to \mu^+\mu^-) = 95.0 \pm 0.3 \pm 0.7 \pm 1.1 \pm 1.1$ pb, where the first uncertainties are statistical, the second are systematic, the third are due to the LHC beam energy and the final are due to the luminosity. The Z boson cross section was also measured in the muon channel using 13 TeV pp collision data, corresponding to an integrated luminosity of 5.1 fb^{-1}, and found to be $\sigma(Z \to \mu^+\mu^-) = 196.4 \pm 0.2 \pm 1.6 \pm 3.9$ pb, where the statistical, systematic and luminosity uncertainties are given. For both 8 TeV and 13 TeV measurements, the fiducial selection is defined by the pseudo-rapidity range $2.0 < \eta < 4.5$, where muons with $p_{\mathrm{T}} >$ 20 GeV were selected, and a di-muon invariant mass range 60 GeV $< m_{\mu\mu} <$ 120 GeV was required

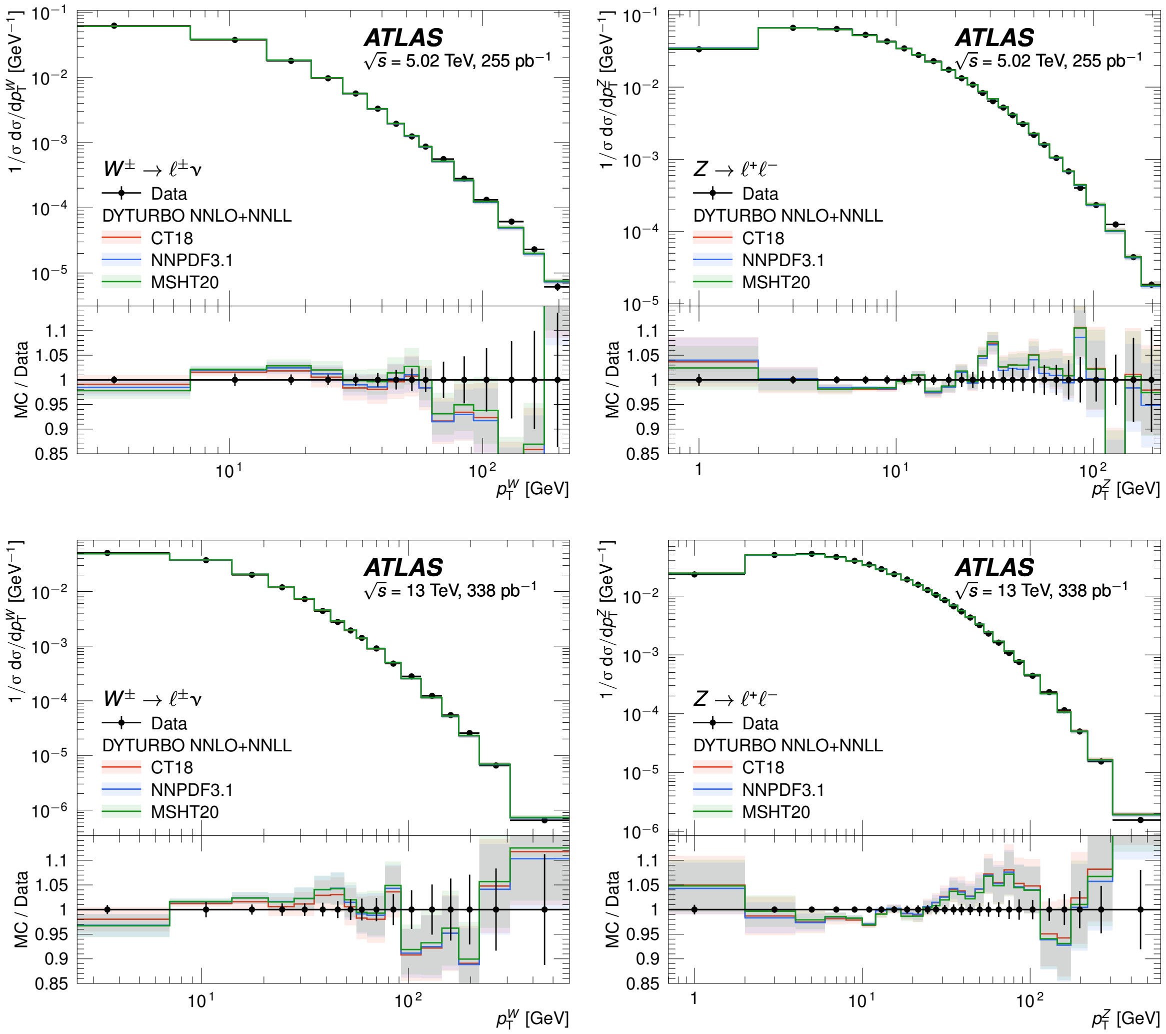

Figure 1.13.: Measurements of normalised differential distributions as a function of W or Z boson p_T for 5.02 TeV and 13 TeV data, compared with DYTurbo predictions with different PDF sets [32].

for the Z boson measurement. The cross sections were also measured differentially, as a function of the muon pseudo-rapidity for the W boson measurements and as a function of the Z boson rapidity. These were compared to theoretical predictions at NNLO accuracy in QCD, calculated using different PDF sets and MC generators, as shown in Figures 1.15 and 1.16, where good agreement was observed between the predictions and measurements.

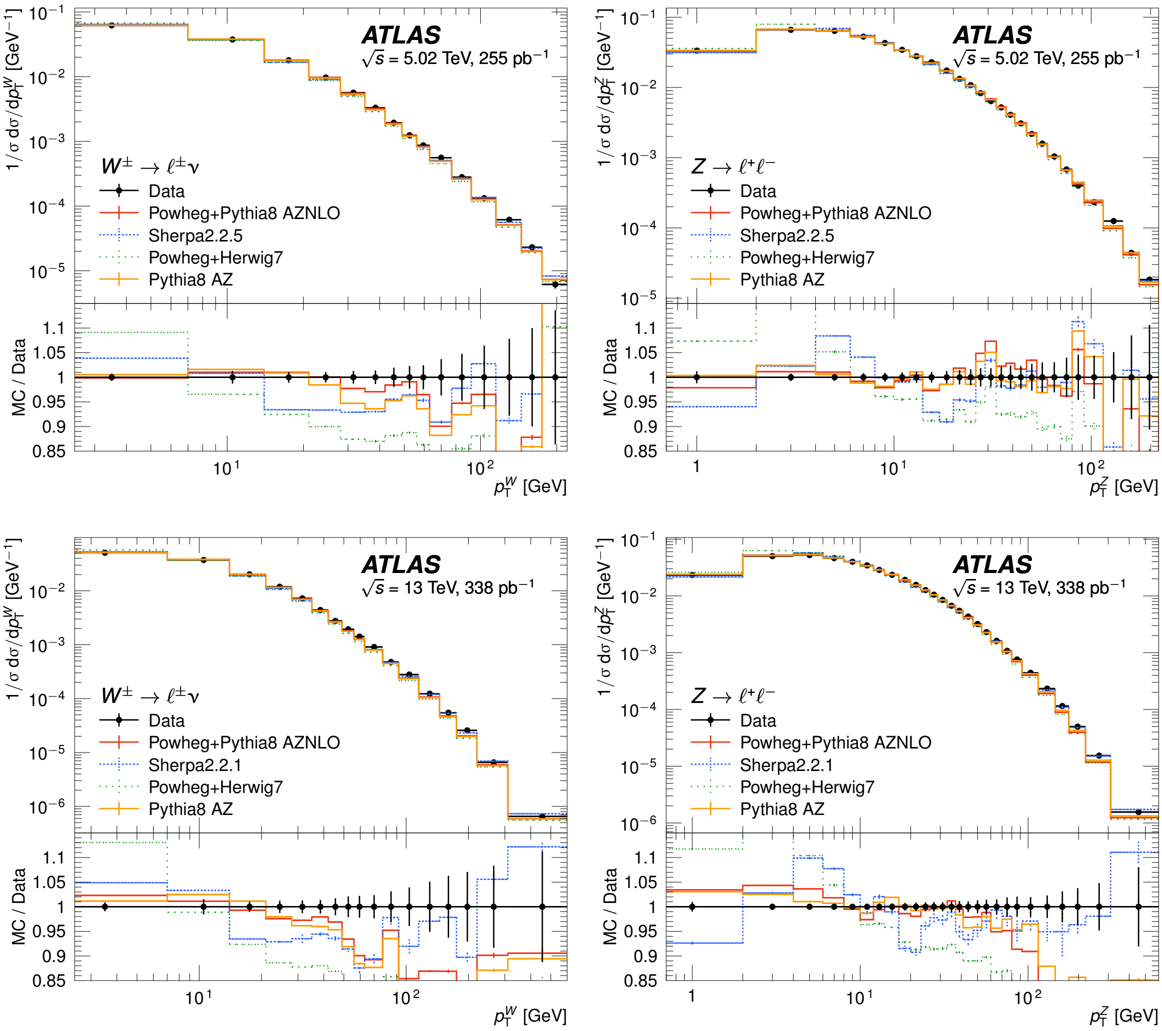

Figure 1.14.: Measurements of normalised differential distributions as a function of W or Z boson p_{T} for 5.02 TeV and 13 TeV data, compared with different MC predictions [32].

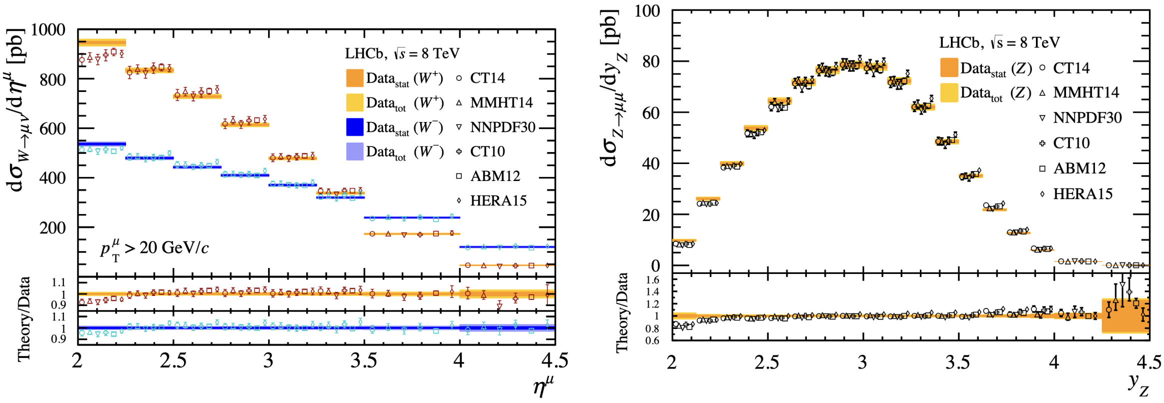

Figure 1.15.: Differential W^+ and W^- boson production cross section as a function of the muon pseudo-rapidity (left) and differential Z boson production cross section as a function of the boson rapidity (right), measured by the LHCb experiment using 8 TeV pp collision data. Measurements are compared to theoretical predictions at NNLO accuracy in QCD, based on different PDF sets [36].

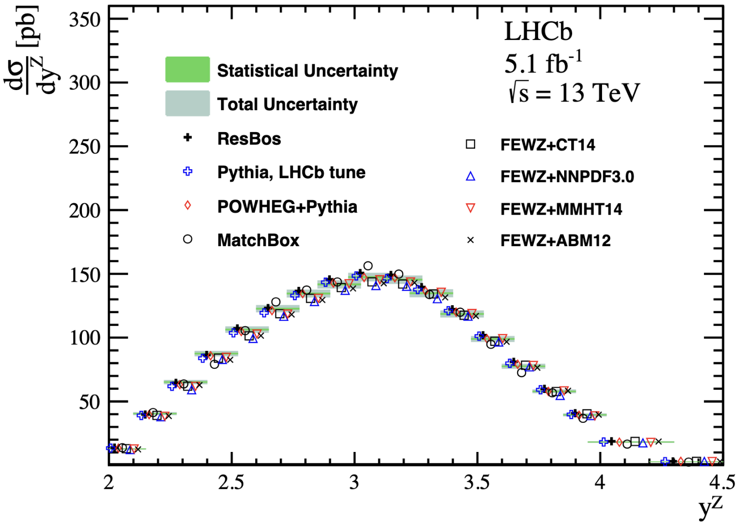

Figure 1.16.: Differential Z boson production cross section as a function of the boson rapidity, measured by the LHCb experiment using 13 TeV pp collision data. Measurements are compared to theoretical predictions at NNLO accuracy in QCD, based on different PDF sets and MC generators. [37].

Chapter 2.

The ATLAS experiment at the LHC

In this chapter, the experimental set-up for the measurement performed in this thesis is described: the Large Hadron Collider in Section 2.1, followed by the ATLAS detector in Section 2.2. Finally, Section 2.3 provides a description of the physics object reconstruction techniques employed by the ATLAS experiment, for objects relevant to the measurement presented in this thesis.

2.1. The Large Hadron Collider

The Large Hadron Collider (LHC) is the world's highest energy particle collider, with a circumference of 27 km [38, 39], operated by the European Organisation for Nuclear Research (CERN). It is located on the border between Switzerland and France, approximately 100 m below ground, in the same tunnel that was used to host the Large Electron Positron (LEP) collider [40]. The LHC is designed to collide protons and heavy ions in pp, pPb and $PbPb$ collisions, with a focus on pp collisions during most of its operation [41]. Currently, centre-of-mass energies up to 13.6 TeV have been achieved in pp collisions. To reach these energies, proton beams are passed through a series of accelerators located in the CERN complex, where each machine increases the energy of the beam of protons. The process starts in LINAC4, where negative hydrogen ions are accelerated to 160 MeV before these are injected in the Proton Synchrotron Booster (PSB) [42]. The hydrogen ions are stripped of their electrons as these are passed through a thin Carbon foil during injection into the PSB, leaving behind protons which are then further accelerated to 2 GeV before injection into the Proton Synchrotron (PS). The acceleration process continues as the proton beam reaches 26 GeV in the PS, before being sent to the Super Proton Synchrotron (SPS), which then injects 450 GeV protons into the LHC ring. The CERN accelerator complex is illustrated in Figure 2.1, where the path of the protons to the LHC is represented by light grey arrows.

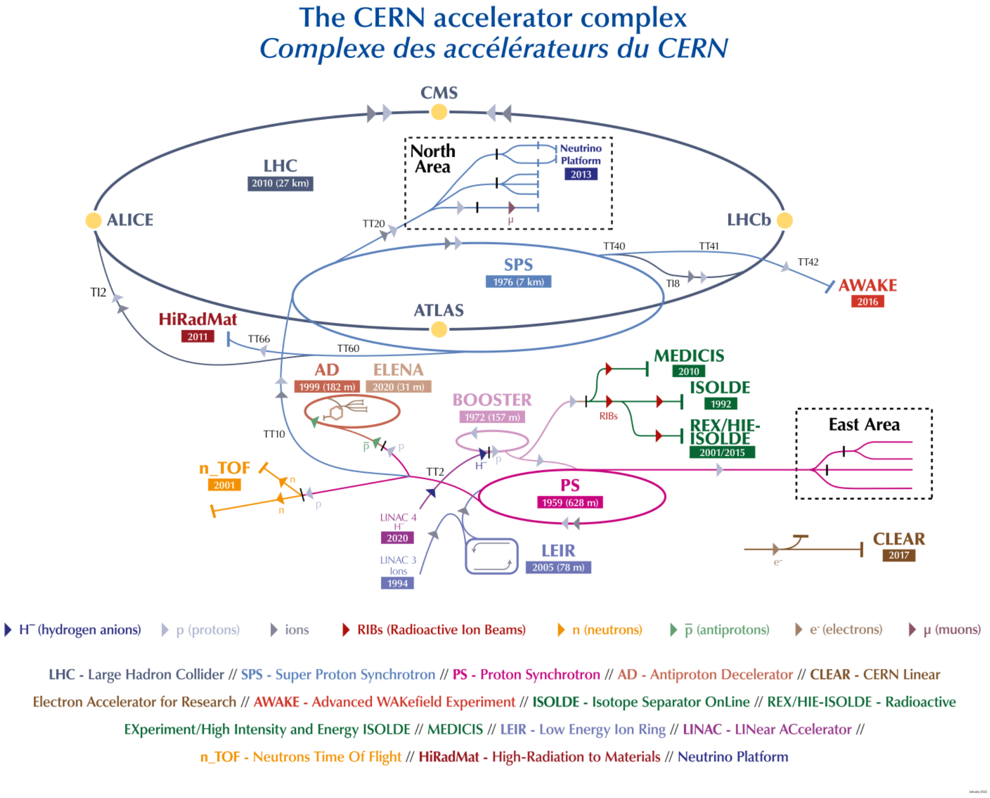

Figure 2.1.: The CERN accelerator complex layout in 2022 [43].

Protons are transferred into the two beam pipes of the LHC, where they circulate in opposite directions, reaching their maximum energy of 6.8 TeV. Radio frequency (RF) cavities are used to accelerate the proton beams in the LHC. These are metallic chambers which contain an electric field, tuned to oscillate at 400 MHz. The proton beams are sorted into segmented bunches, where the bunch structure is first arranged in the PS. The LHC is designed to hold a maximum of 2808 bunches per fill, where each bunch contains around 10^{11} protons. In order to increase the energy of the protons from 450 GeVto 6.8 TeV, the bunches pass through the 16 RF cavities around the LHC more than 10 million times. The RF cavities operate in a superconducting state at 4.5 K for a minimal energy loss. Superconducting magnets, cooled down to 1.9 K, are used for steering and focusing the beams in the LHC. The 1232 main dipole magnets, each 15 m long, provide the strong magnetic fields up to 8.3 T, which bend the beams into their circular trajectories. Quadrupole magnets focus the beams in the transverse plane, ensuring bunches are kept tightly packed together, and additional multipole magnets correct for imperfections in the magnetic field, leading to a total of about 9000 magnets. An ultra-high vacuum is maintained throughout the beampipe in order to avoid collisions between the beam protons and gas molecules.

The beams are collided at four points around the accelerator every 25 ns, corresponding to a collision rate of 40 MHz. Each interaction point corresponds to one of the four main experiments at the LHC. ATLAS [44] and CMS [45] are general-purpose detectors, designed to cover a wide range of physics measurements including precision Standard Model measurements and searches for new physics, while ALICE [46] and LHCb [47] are smaller detectors, built for more specialised measurements. ALICE focuses on the study of quark-gluon plasma, primarily using $PbPb$ and pPb collisions, recreating conditions similar to those in the early Universe, while LHCb is designed to study $\mathcal{CP}$ violation by measuring the properties of b hadrons.

A key parameter for measuring the performance of a particle collider is the *luminosity* [48], where the event rate dN/dt is proportional to the instantaneous luminosity $\mathcal{L}$ and the cross section for a specific physics process σ:

$$\frac{dN}{dt} = \mathcal{L} \cdot \sigma. \tag{2.1}$$

For inelastic collisions with cross section σ_{inel}, the instantaneous luminosity can be defined as:

$$\mathcal{L} = n_b \frac{\langle\mu\rangle f_{rev}}{\sigma_{inel}}, \tag{2.2}$$

where n_b is the number of colliding bunches, f_{rev} is the revolution frequency of the beams and $\langle\mu\rangle$ is the average number of inelastic collisions per bunch crossing, or *pile-up*, averaged over all colliding bunch pairs [49].

The integrated luminosity, L, is the integral of the instantaneous luminosity over time,

$$L = \int \mathcal{L} dt, \tag{2.3}$$

and can be used as a measure of the amount of data collected over a period of time. Considering the finite lifetime of the accelerator, and of the detectors, in order to collect sufficient events to perform measurements on rare physics processes, the collider must operate at high instantaneous luminosities. The design instantaneous luminosity of the LHC is $\mathcal{L} = 10^{34}$ cm^{-2}s^{-1}, although it is currently operating at twice this value. Running at such high luminosities results in a large number of simultaneous collisions during the same bunch crossing, which can deteriorate the performance of reconstruction algorithms as it becomes more challenging to distinguish particles originating from the pp interaction of interest from pile-up particles.

The LHC has operated at several centre-of-mass energies and luminosities since its programme began, where data was collected almost continuously over periods of several years (*Runs*), interspersed with long shutdown periods intended to allow essential upgrades to the accelerator and detectors. Run 1 took place between 2010 and 2012, where 5 fb^{-1} and 21 fb^{-1} of pp collision data were collected at collision energies of 7 TeV and 8 TeV, respectively, after which the first long shutdown (LS1) took place in order to strengthen the accelerator in preparation for higher collision energies. Following this, 140 fb^{-1} of pp collision data were accumulated at $\sqrt{s} = 13$ TeV during Run 2, between 2015 and 2018, after which a second long shutdown (LS2) took place until 2022. Currently, Run 3 of the LHC is ongoing, where data are being collected at a new record energy of $\sqrt{s} = 13.6$ TeV, and is expected to deliver 250 fb^{-1} of pp collision data until the end of 2025. Following Run 3, the LHC is scheduled to undergo a major upgrade in preparation for the high luminosity era (HL-LHC), where the accelerator will operate at five times the designed instantaneous luminosity, and is expected to deliver 3000 fb^{-1} [50].

The work presented in this thesis uses data collected by the ATLAS detector during the first year of Run 3, 2022, which corresponds to an integrated luminosity of approximately 29 fb^{-1}. Figure 2.2 shows the cumulative integrated luminosity per year, collected so far by the ATLAS detector during stable beams for high energy pp collisions at the LHC.

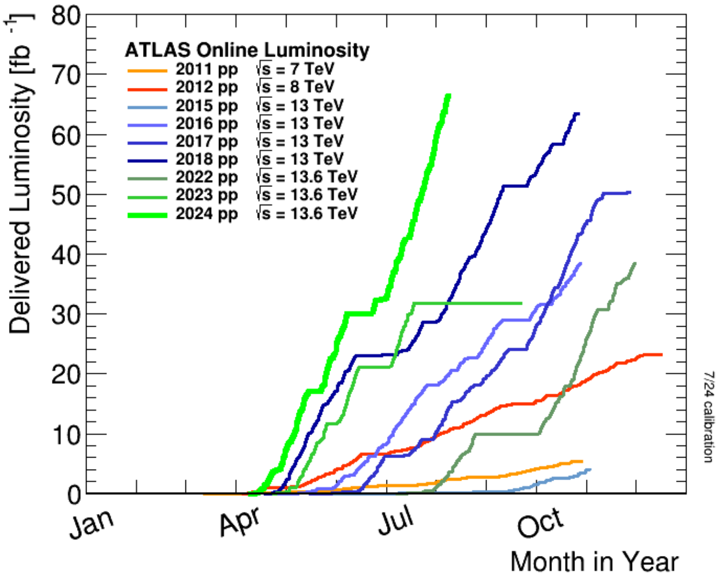

Figure 2.2.: Cumulative integrated luminosity per year collected by ATLAS for high energy pp collisions [51].

2.2. The ATLAS detector

The ATLAS detector [44, 52] is a general-purpose detector designed to be sensitive to as many processes as possible, including precision SM measurements, searches for new phenomena beyond the SM and measurements of the Higgs boson properties. Located 100 m underground, close to the main CERN Meyrin site, it measures 25 m in height and 44 m in length, and weighs approximately 7000 t. It composed of several sub-systems, each purposed for a different type of measurement, arranged around the beam axis in a cylindrical manner. The beams collide at the centre of the detector volume, called the interaction point (IP). The sub-system closest to the IP is the Inner Detector (ID), which provides tracking for charged particles. As particles interact with the detector environment, they produce "hits" in the detector, where a series of hits are used to reconstruct a track. The ID is immersed in a 2 T axial magnetic field provided by a central superconducting solenoid magnet surrounding the ID, bending the trajectory of charged particles, thus allowing their charges and momenta to be measured. Surrounding the ID is the calorimeter system, which provides energy measurements for electromagnetic and hadronic signatures using Liquid Argon (LAr) and Tile scintillator sampling calorimeters. The outermost system is the Muon Spectrometer (MS), whose purpose is to identify muons and measure their trajectories. The MS is also immersed in a magnetic field up to 4 T created by three superconducting toroidal magnets, bending the trajectories of muons and thus allowing their charges and momenta to be measured. A schematic diagram of the ATLAS detector configuration during Run 3 is shown in Figure 2.3, where the different sub-detectors are labelled.

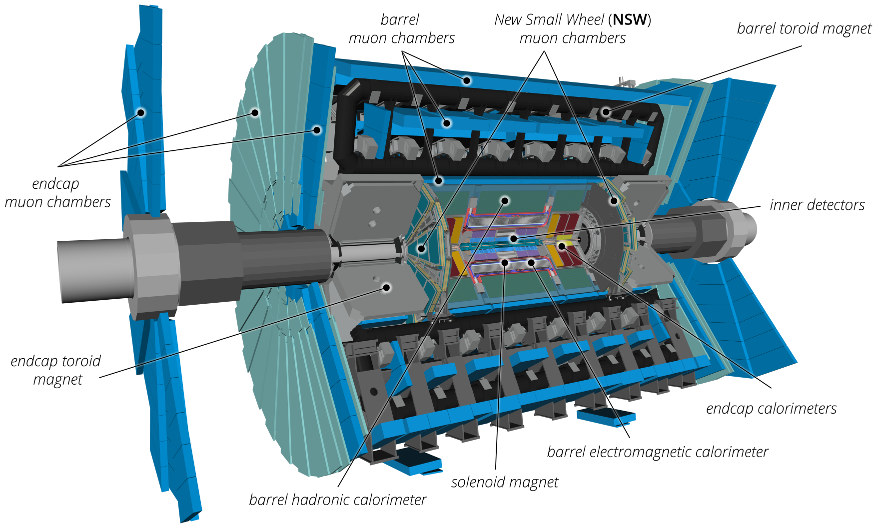

Figure 2.3.: Schematic diagram of the ATLAS detector, where the sub-detector systems including the Inner Detector, calorimeters and muon systems are indicated [52].

Due to the high collision rate of 40 MHz and current limitations in technologies and resources, not all data can be recorded. Instead interesting events, for example those characterised by the presence of large transverse momenta leptons, are selected in real time by the trigger system and recorded to disk for further offline analysis.

Upgrades to the LHC, and the use of luminosity levelling techniques, allow peak instantaneous luminosity conditions ($\mathcal{L} = 2 \times 10^{34}$ cm^{-2}s^{-2}) to be maintained for a larger fraction of the LHC fill, resulting in increased pileup of $\langle\mu\rangle \approx 50$ and beyond during Run 3. In preparation for this, significant upgrades were made to the detector sub-systems and their electronics during LS2 (the “Phase-1 upgrade”) in order to cope with the increased pileup, while maintaining low trigger thresholds without a detrimental increase in the trigger rates [52].

In order to properly describe the ATLAS detector, a coordinate system must be defined. A right-handed coordinate system is used, where the origin is the interaction point at the centre of the detector, and the z-axis is along the beam pipe. The x-axis points towards the centre of the LHC ring, while the y-axis points upwards. Spherical coordinates (r, θ, ϕ) are used, where the polar angle θ is measured from the z-axis, the azimuthal angle ϕ is defined in the $x-y$ plane and $r=\sqrt{x^2+y^2}$. Figure 2.4 shows a diagram of the ATLAS coordinate system with respect to the LHC ring.

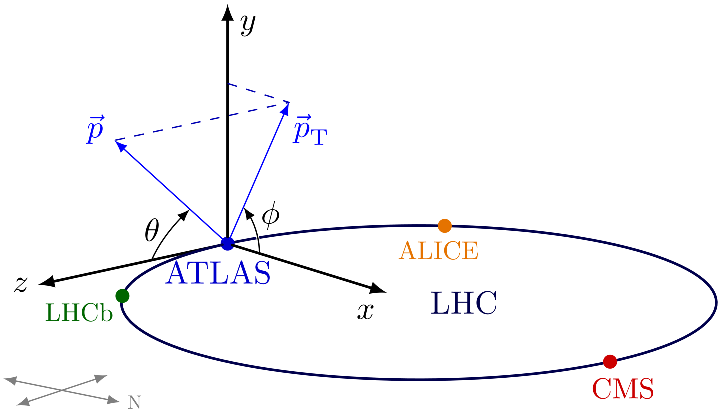

Figure 2.4.: Schematic diagram of the ATLAS coordinate system with respect to the LHC ring [53]. The transverse momentum, $p_{\mathrm{T}}=\sqrt{p_x^2+p_y^2}$, is the momentum projected in the transverse $(x-y)$ plane.

The rapidity y is defined for massive particles in terms of their energy E and longitudinal momentum p_z:

$$y=\frac{1}{2}\ln\left(\frac{\mathrm{E}+p_z}{\mathrm{E}-p_z}\right). \tag{2.4}$$

In the case of ultra-relativistic particles, it is instead more common to use the pseudo-rapidity η, which is defined in terms of the polar angle:

$$\eta=-\ln\tan\left(\frac{\theta}{2}\right). \tag{2.5}$$

The angular distance $\Delta R(i,j)$ between two particles i and j is defined in terms of their difference in pseudo-rapidity and azimuthal angles:

$$\Delta R(i,j)=\sqrt{(\eta_i-\eta_j)^2+(\phi_i-\phi_j)^2}. \tag{2.6}$$

2.2.1. Inner Detector

The ID is the main tracking detector at ATLAS, used for measuring the trajectories of charged particles. It has excellent spatial resolution, allowing the reconstruction of primary and secondary vertices. The momentum resolution of the ID is equal to $\sigma(p_\mathrm{T})/p_\mathrm{T} = 0.05\% \cdot p_\mathrm{T} \oplus 1\%$, where higher transverse momenta particles have worse resolution due smaller track curvatures. The ID is surrounded by a solenoidal magnet, immersing it in a 2 T axial magnetic field, which allows the measurement of charge and momenta of charged particles from the curvature of their trajectory. It consists of three sub-detectors: the pixel detector, followed by the semiconductor tracker (SCT) in the innermost region, and the transition radiation tracker (TRT), in total covering the range $|\eta| < 2.5$. Each sub-detector is composed of a central barrel component, arranged on concentric cylinders around the beam axis, and two end-caps arranged on discs perpendicular to the beam axis. Figure 2.5 shows the ID, including all its sub-detectors.

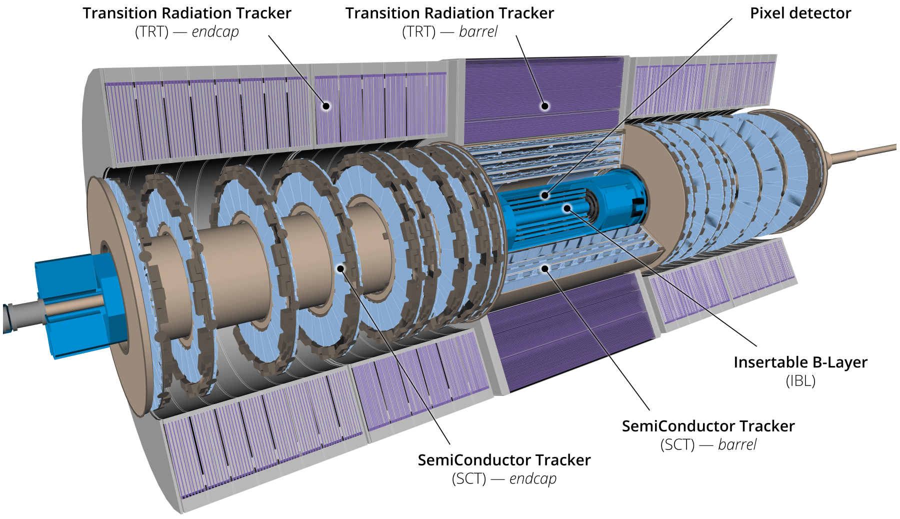

Figure 2.5.: Schematic diagram of the ATLAS Inner Detector [52].

For the pixel and SCT silicon-based sub-detectors, the basic operating principle relies on the creation of electron-hole pairs formed by a traversing charged particle in the silicon active material. An electric field applied across the medium allows the collection of charge to the electrodes, which produce an electrical signal in the detector [54].

The pixel detector [55] is divided into three finely segmented layers of pixel modules in the barrel, covering the pseudo-rapidity range $|\eta| < 1.5$, and three layers in each of the two end-caps, covering the remaining $1.5 < |\eta| < 2.5$. There are a total of 1,744 pixel modules, where each module contains 47,232 pixels with nominal sizes of $50\ \mu\text{m}\ (r - \phi) \times 400\ \mu\text{m}\ (z)$ and intrinsic resolutions of $10\ \mu\text{m}\ (r - \phi) \times 115\ \mu\text{m}\ (z)$. An additional layer, called the Insertable B-Layer (IBL) [56], was added during LS1 in order to improve tracking and vertexing precision through enhanced spatial resolution. There are 26880 pixels in the IBL, where each pixel cell has an area of $50\ \mu\text{m}\ (r - \phi) \times 250\ \mu\text{m}\ (z)$ and intrinsic resolutions of $10\ \mu\text{m}\ (r - \phi) \times 60\ \mu\text{m}\ (z)$ [57]. With the introduction of the IBL, the average distance of the innermost pixel sensors to the beam axis was reduced from 5.05 cm to 3.35 cm, thus increasing the resolution of track parameters and improving vertex reconstruction, as well as recovering reconstruction performance loss due to radiation damage. The pixel detector is designed to provide at least three hits per charged particle track, and an additional hit from the IBL.

The semiconductor tracker (SCT) [58] is a silicon strip detector, composed of 4088 silicon strip modules arranged in four layers in the barrel and nine discs in each of the two end-caps. Each module is composed of two pairs of strip sensors, rotated by 40 mrad with respect to each other. As strip sensors can only perform measurements in a single direction, the information from both pairs of strip modules must be combined. The strip sensors in the barrel have a uniform pitch of 80 μm, while those in the end-cap are arranged in the radial direction with a 161.5 μrad angular pitch. These have an intrinsic spatial resolution of 17 μm in the $(r - \phi)$ direction, and about 580 μm in the r (z) direction for the barrel (end-caps) [57]. The SCT detector typically provides eight strip measurements per track [58].

The Transition Radiation Tracker (TRT) [59] is composed of 298,304 gas-filled drift tubes called *straws*, arranged in 73 layers in the barrel and 40 discs in the end-cap, performing tracking measurements for the range $|\eta| < 2$. The straws are aligned parallel to the beam axis in the barrel region, covering the range $|\eta| < 1$, and perpendicularly to the beam axis, pointing radially outwards, in the two end-caps covering $1 < |\eta| < 2$. The gas mixture used in these straws is composed mainly of Xenon, with a small percentage of O_2 and CO_2, although most have been replaced with an Argon-based mixture since 2015 due to the expense associated with the loss of the Xenon mixture in gas leaks [59]. As charged particles pass through the gas-filled straws, the gas becomes ionised and the charge is collected by the gold-plated tungsten wire anode at the centre. Position information of hits in the TRT are determined by the drift-time measurement in each straw, where the intrinsic spatial resolution per straw in $(r - \phi)$ is 130 μm. A charged particle traversing the TRT will typically provide 30 straw hits.

When a charged particle traverses the boundary between media with different dielectric constants, a small amount of energy is lost from the particle in the form of *transition radiation* (TR), where the intensity of emitted radiation is proportional to the Lorentz factor ($\gamma \equiv E/m$) of the incident particle. As the electron mass is smaller than the mass of pions, the γ factor for an electron of equal momentum to a pion is much larger, resulting in more photons being emitted [54]. This distinction can be used by the TRT to discriminate between electrons and charged hadrons such as pions [1].

2.2.2. Calorimeters

The ATLAS calorimeter system is designed to measure particle energies and positions over a range $|\eta| < 4.9$, and also provide missing transverse energy measurements. It consists of an electromagnetic (ECal) and hadronic calorimeter (HCal), where different technologies are used, depending on the η region. Both calorimeters are sampling calorimeters, consisting of alternating layers of absorber and active materials. The absorber layers are designed to induce electromagnetic or hadronic showers, absorbing some of the shower particles, while the active layers sample part of the total shower energy. The calorimeters are designed to have sufficient depth such that the showering particle is eventually stopped within the calorimeter volume. The ECal only uses liquid argon (LAr) technology [60], while the HCal uses a combination of LAr and tile scintillator technology [61], both covering the range $|\eta| < 3.2$. The forward calorimeter (FCal) also uses LAr technology, and is located in the forward region of the detector ($3.1 < |\eta| < 4.9$). Figure 2.6 shows a detailed layout of the ATLAS calorimeter system, where the different sub-systems with η values are marked for reference.

The LAr ECal consists of accordion-shaped lead absorber plates, interweaved with liquid argon as the active detector medium, and is divided into a barrel section ($|\eta| < 1.475$), and two end-caps ($1.4 < |\eta| < 3.2$). The ECal is designed to provide precision measurements on electrons and photons, especially in the high-granularity region overlapping with the inner detector ($|\eta| < 2.5$). It is also designed to provide information to the Level-1 Calorimeter trigger, further described in Section 3.1.

---

[1] With most of the straws operating with the Argon gas mixture, which has lower TR photon absoption efficiency compared to the Xenon gas mixture, particle identification in the TRT relies on other methods, such as dE/dx.

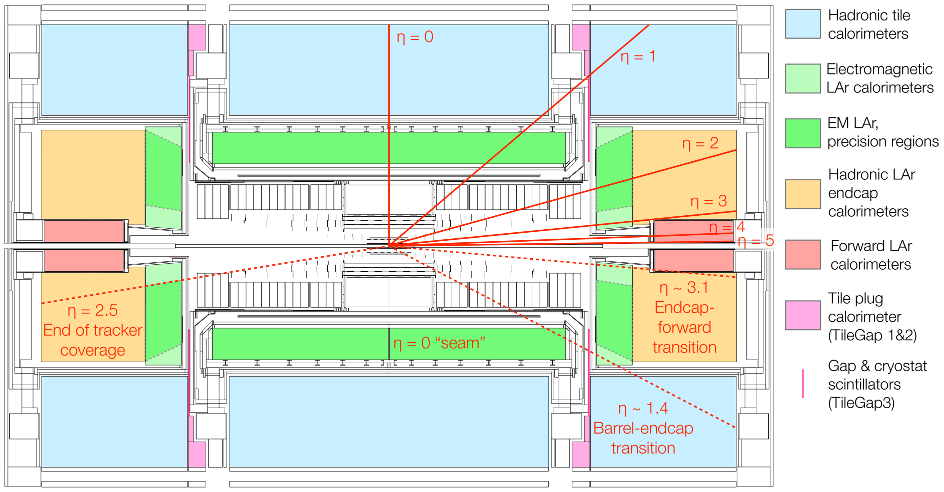

Figure 2.6.: Layout of the ATLAS calorimeters and inner detector system, where η values are also indicated [62].

Electromagnetic (EM) showers are initiated by energetic electrons or photons, with energies over approximately 1 GeV, interacting with the passive lead layers. Electrons decelerate and lose energy via bremsstrahlung photons, while photons create electron-positron pairs, which continue to decelerate and emit photons via bremsstrahlung. This cascade of secondary particles with progressively lower energies continues until the critical energy is reached, where energy losses due to ionisation become equal to energy losses due to radiation processes. Below the critical energy, the EM shower development stops and energy is dissipated through the detector material through ionisation [54, 63]. The free electrons from the ionisation are collected by electrodes, inducing electrical signal to the electrodes as they move, and thus inducing the signal in the detector.

The $|\eta| < 2.5$ region of the ECal is segmented longitudinally into three sampling layers, as shown in Figure 2.7, allowing for the measurement of the energy and direction of the EM shower. The first layer has the highest granularity in η, where the granularity is about 0.003×0.1 in $\Delta\eta \times \Delta\phi$, such that it allows good separation between prompt photons and photons from $\pi^0 \to \gamma\gamma$ decays, and a thickness of 2-5 radiation lengths X_0 [2]. The second layer is where most of the energy of the EM shower is deposited, and has a thickness of 16-20 X_0, and a granularity of about 0.025×0.025

---

[2] The radiation length X_0 represents the average distance which an electron needs to travel through a material to reduce its energy to $1/e$ of its original energy through radiative processes. The average distance travelled by a photon before undergoing pair conversion is $9/7\ X_0$ [63].

in $\Delta\eta \times \Delta\phi$. The third layer is used to correct for leakage of high-energy showers in the material beyond the ECal, and has a coarser granularity of about 0.05×0.025 in $\Delta\eta \times \Delta\phi$, and a thickness of 2-10 X_0. The $2.5 < |\eta| < 3.2$ region of the ECal is segmented into two longitudinal sampling layers. In addition to these layers, there is a thin liquid argon pre-sampler (PS) layer in front of the active material of the ECal in the range $|\eta| < 1.8$, which is used to correct for electron and photon energy losses before traversing the ECal. The PS has a thickness of 11 mm in the barrel and 5 mm in the end-caps, and a granularity of 0.025×0.1 in $\Delta\eta \times \Delta\phi$.

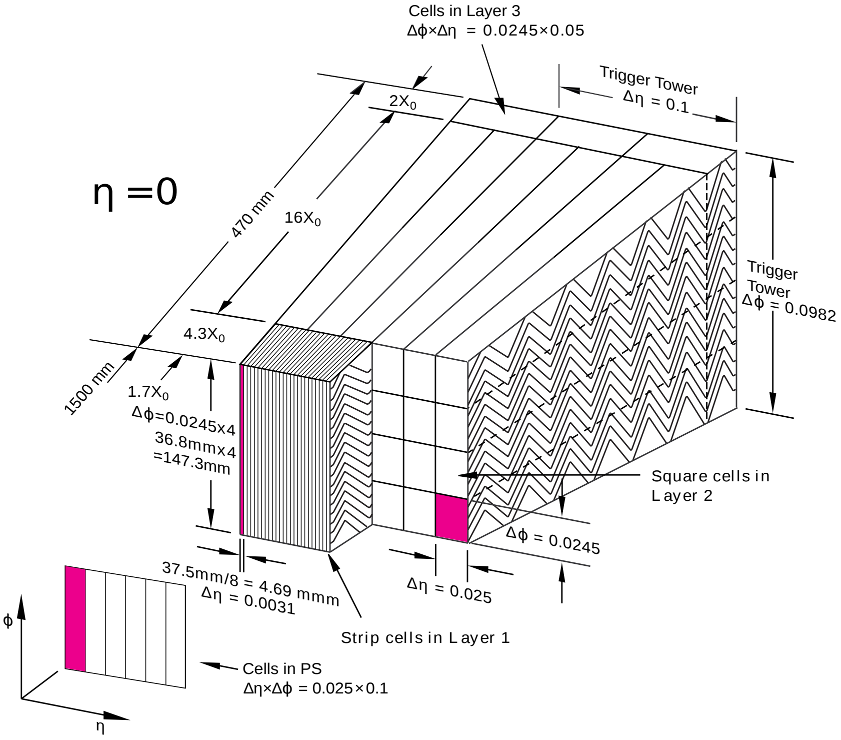

Figure 2.7.: Schematic diagram of a module in the LAr calorimeter barrel, located at $\eta = 0$, where the granularity in η and ϕ of the cells in each of the three layers and the pre-sampler (PS) layer is shown [64].

The barrel-end-cap transition region at $1.37 < |\eta| < 1.52$, commonly known as the *transition region*, provides passage for electronics and service pipes. Several scintillators are placed in this region in order to correct for energy losses in the inactive material. This large amount of upstream material amounts to a thickness of 5-10 X_0, and as a consequence physics objects reconstructed in this region, such as electrons, are typically excluded from analyses. For the region $|\eta| < 0.6$, the amount of upstream material reaches about 2 X_0, while for the region $0.6 < |\eta| < 1.8$ (with the exception of the transition region), the upstream material increases up to a thickness of 3 X_0 [64].

The hadronic calorimeter (HCal) is designed to measure the energies of jets, which are reconstructed from hadronic showers formed where hadrons undergo multiple processes in the calorimeter material, such as nuclear interactions and ionisation. Secondary particles are produced, where these are mostly neutral and charged pions. As neutral pions decay to two photons before they have a chance to re-interact hadronically, these initiate EM sub-cascades to the hadronic shower [54, 63]. The HCal has a thickness of about 11 interaction lengths λ [3] to ensure hadronic shower containment, thus reducing the background in the muon spectrometer from hadronic shower remnants. It is positioned in the outer part of the calorimeter system, and is composed of three Tile calorimeter components in the barrel region, and two LAr hadronic end-cap calorimeters (HEC) and two forward LAr calorimeters (FCal).

Plastic scintillator cells called *tiles*, arranged perpendicularly to the beam axis, act as the active material in the Tile calorimeter, and are interleaved with iron absorber plates which induce showers. Hadronic showers cause light to be emitted by the scintillator tiles, which is collected by wavelength shifting fibres into photomultipliers. The Tile calorimeter covers the range $|\eta| < 1.7$ and consists of a central barrel and two Tile extended barrel sections which are segmented into three layers with a total depth of 9.7 λ. The cells in the first two layers have a granularity of 0.1×0.1 in $\Delta\eta \times \Delta\phi$, while in the third layer the cell sizes are 0.2×0.1 in $\Delta\eta \times \Delta\phi$.

The LAr hadronic end-cap calorimeter is composed of two wheels in each end-cap, which together cover the range $1.5 < |\eta| < 3.2$ and use copper as the absorber material. The LAr forward calorimeters, covering the remaining $3.1 < |\eta| < 4.9$ region, use copper as the absorber material in the electromagnetic layer, and tungsten in the remaining two hadronic layers.

The energy resolution of a calorimeter can be parametrised as

$$\frac{\sigma_E}{E} = \frac{a}{\sqrt{E}} \oplus \frac{b}{E} \oplus c, \tag{2.7}$$

where the first term $\frac{a}{\sqrt{E}}$ is the stochastic term and is a result of intrinsic shower and sampling fluctuations. The second term $\frac{b}{E}$ is the noise term, including electronic and instrumental noise effects in the readout chain, which is typically small and does not

---

[3] The interaction length λ represents the mean free path travelled by a hadron between two inelastic collisions. [63].

play a key role at the high eneries of the LHC. Finally, the constant term c takes into account local non-uniformities in the response of the calorimeter that are not energy-dependent. The ATLAS ECal has a design energy resolution of $\frac{\sigma_E}{E} = \frac{10\%}{\sqrt{E}} \oplus 0.7\%$, while the HCal has a lower resolution of $\frac{\sigma_E}{E} = \frac{50\%}{\sqrt{E}} \oplus 3\%$ due to larger intrinsic fluctuations in hadronic showers [44].

2.2.3. Muon Spectrometer

Muons produced at the LHC, with typical energies of the order 100 MeV to 100 GeV, ionise matter minimally. Due to the fact that they are approximately 200 times heavier than electrons, they do not undergo significant energy loss through radiation. This, combined with their long mean lifetimes, allow them to reach the outermost part of the ATLAS detector. The ATLAS muon spectrometer (MS) [65] is the outermost detector sub-system, designed to measure the trajectories and momenta of muons in the range $|\eta| < 2.7$. The momentum resolution in the MS varies with p_{T}, where this is approximately 10% for $p_{\mathrm{T}} = 1$ TeV particles. The MS also provides information to the Level-1 trigger and High Level Trigger (HLT) for the range $|\eta| < 2.4$, explained further in Section 2.2.4. The MS is immersed in a magnetic field, where over the range $|\eta| < 1.4$ this is provided by a large barrel toroid, while for the range $1.6 < |\eta| < 2.6$ it is provided by two smaller end-cap toroid magnets. Magnetic deflection in the region $1.4 < |\eta| < 1.6$ is provided by a combination of the barrel and toroid end-cap magnetic fields.

The MS is composed of a barrel region, divided into three chambers arranged cylindrically around the beam axis, and two end-caps, consisting of three discs (also called *wheels*), placed perpendicular to the beam axis. The innermost wheels, located at $1.3 < |\eta| < 2.7$ and called the Small Wheels, have been replaced as part of the Phase-1 upgrade to the ATLAS detector with the *New Small Wheels* (NSWs) [66] in order to cope with the increasing background in the forward regions of the detector, and in preparation for the HL-LHC. Precise muon tracking is provided by monitored drift tube (MDT) chambers for $|\eta| < 1.3$, with coverage in the forward region $|\eta| > 1.3$ provided by the NSWs, which use small-strip TGC (sTGC) and Micromegas detectors. Triggering information is provided for the region $|\eta| < 2.4$ by resistive plate chambers (RPCs) in the barrel ($|\eta| < 1.05$) and thin gap chambers (TGCs) in the end-caps ($1.05 < |\eta| < 2.4$), with supplementary coverage in the region $1.3 < |\eta| < 2.7$ provided by the NSWs. A schematic diagram of the MS is provided in Figure 2.8, indicating the location of the MS sub-detectors mentioned so far.

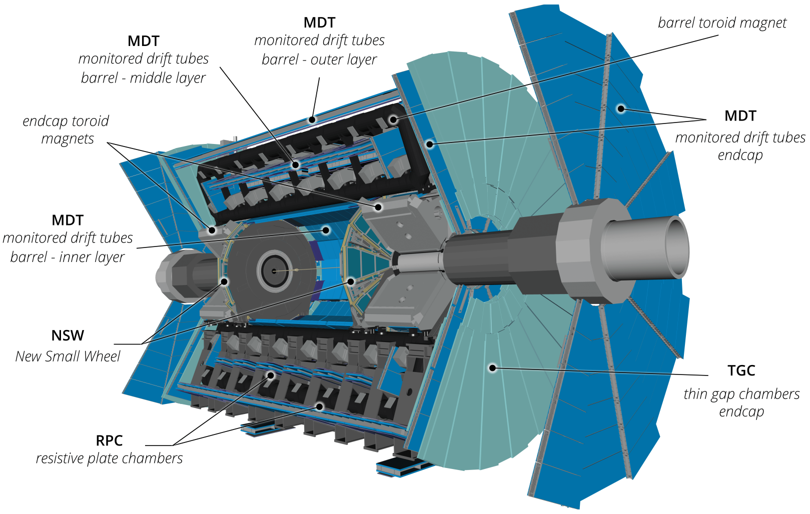

Figure 2.8.: Schematic diagram of the Muon Spectrometer (MS), where different sub-detector technologies are indicated [52].

The MDT sub-detector consists of aluminium pressurised drift tubes, with diameters of 30 mm and filled with an Argon and CO_2 gas mixture. Tungsten-rhenium anode wires at the centre of the tubes, with diameters of 50 μm, collect electrons produced from ionisation as muons traverse the gas mixture. There are approximately 1,200 MDT chambers, with approximately 355,000 individual MDTs, which have hit resolutions of 80 μm per tube layer and 35 μm per chamber.

The precision tracking chambers are complemented by fast triggering chambers, where faster response time outweighs spatial resolution. The RPC is a gaseous parallel electrode-plate detector, composed of three concentric cylindrical layers around the beam axis, also called *trigger stations*. The two resistive plates are kept parallel to each other, and the space between them is filled with a gas mixture, containing mostly tetrafluoroethane. An electric field applied between the plates allows the creation of avalanches along the ionisation track produced by traversing muons. The first two trigger stations provide a low p_{T} threshold trigger, while the last one contributes to the high p_{T} threshold trigger. TGCs, located in the end-caps, are multi-wire proportional chambers, filled with a gas mixture composed of CO_2 and n-pentane. These provide both trigger capabilities, and the determination of the second coordinate in ϕ to complement the measurement provided by the MDTs in the r direction.

The detector technologies used on the NSWs, sTGCs and Micromegas detectors, have both precision tracking and triggering capabilities. The Micromegas detectors consist of a stainless steel micromesh in a gas gap, splitting the gap into two parts: the upper drift gap and the lower amplification gap. Muons interacting with the gas produce ionisation, and the electric field applied to the gap causes the ionisation electrons to drift towards the micromesh. In the amplification gap, which is only 128 μm thick, a voltage is applied, leading to the amplification of ionisation electrons through an avalanche process. Electrons produced in the avalanche drift towards the micromesh quickly, due to the thin amplification gap, resulting in a very fast detector with very little dead time. The sTGCs operate similarly to the TGCs used for triggering, however these have smaller strip pitch of 3.2 mm, resulting in improved resolution. Together, the Micromegas and sTGC detectors achieve excellent spatial resolution of the order of 100 μm [52].

2.2.4. Trigger and Data Acquisition

Protons collide in the LHC at a rate of 40 MHz, producing on average 43 simultaneous collisions per bunch crossing, based on the recorded performance during 2022 [51]. Not all of these collisions give rise to interesting hard scattering interactions, and due to limited computing resources, it is essential to filter out which data to record for further analysis. The ATLAS trigger system [67] is responsible for reducing the 40 MHz collision rate to a manageable read-out rate for the data acquisition system, making decisions in real time based on events with experimental signatures of interest. A two level system is used, composed of a hardware-based Level-1 (L1) system and a software-based High-Trigger Level (HLT) system.

The L1 system uses reduced granularity information from the calorimeters, processed by the L1Calo trigger system [4], and the muon spectrometer, processed by the L1Muon trigger system, to reduce the trigger rate from 40 MHz to 100 kHz, with a latency of 2.5 μs. Regions of interest (RoI) are formed based on the $\eta - \phi$ location of the signals processed by the L1 system, such as large deposits in the calorimeter or high-p_{T} muons in the MS, which are passed on to the HLT. If the signals processed by the L1 system pass pre-defined thresholds, the *L1 accept* decision is passed to the central trigger processor (CTP), which may apply pre-scaling before further processing to reduce the trigger rates of common signatures such as low-p_{T} leptons.

---

[4] The L1Calo system is described in more detail in Section 3.1.

The HLT system exploits full detector granularity to further reduce the average trigger rate from 100 kHz to a few kHz, with a latency of the order of 100 ms. Reconstruction algorithms, similar to those used offline (described in Section 2.3), are used to reconstruct higher level objects such as leptons, $E_{\mathrm{T}}^{\mathrm{miss}}$ and jets based on the RoIs provided by the L1 system. These algorithms are staged in several steps to form *trigger chains*, where many combinations are possible, providing a diverse *trigger menu* used to maximise the types of physics processes recorded.

2.3. Physics object reconstruction

2.3.1. Tracks and primary vertices

Charged particles traversing the ID interact with the material and leave energy deposits, which can be combined and extrapolated to form tracks [68]. Track reconstruction starts with the formation of three-dimensional space points, or *hits*, by combining clusters. One cluster in the pixel is sufficient to define a hit, while in the SCT both clusters from a strip must be combined to yield a hit. Track *seeds* are formed from at least three hits in the pixel or SCT detector, and additional hits which are compatible with the initial trajectory are added to the track using a combinatorial Kalman filter [69]. Multiple track candidates are formed from the same hits, and ambiguities are resolved by placing requirements on the tracks such as the number of Pixel or SCT hits and the number of layers with no hits detected. A χ^2 fit is also performed on track candidates in order to assess the quality of the fit, and preferential treatment is applied to tracks with higher p_{T}, as these are less likely to originate from incorrectly assigned hits. Tracks which survive this ambiguity solving step can then be extrapolated to the TRT. Finally, all tracks must pass additional criteria, including $p_{\mathrm{T}} > 400$ MeV, $|\eta| < 2.5$ and a minimum of 7 hits in the pixel and SCT detectors.

Vertices are spatial points where pp interactions have occured, and from where tracks originate [70]. Multiple interactions per bunch crossing occur as protons collide, mainly from soft QCD processes, which result in multiple interaction vertices reconstructed in the detector, or pile-up. It is essential for every analysis to reconstruct the vertex originating from the hard-scatter interaction, also called the *primary vertex*. Vertices are reconstructed through an iterative process by combining good-quality tracks, and assessing the compatibility at each step, until reconstructed vertices pass specific criteria. Tracks used in the reconstruction of the primary vertex must also satisfy requirements based on their longitudinal (z_0) and transverse (d_0) impact parameters. The d_0 parameter is defined as the shortest distance between the track and primary vertex in the transverse direction, while the z_0 parameter is the distance along the z-axis from the point of closest approach in the $x - y$ plane, as shown in Figure 2.9. The vertex with the largest sum of transverse momenta of associated tracks is then chosen as the primary vertex in the event.

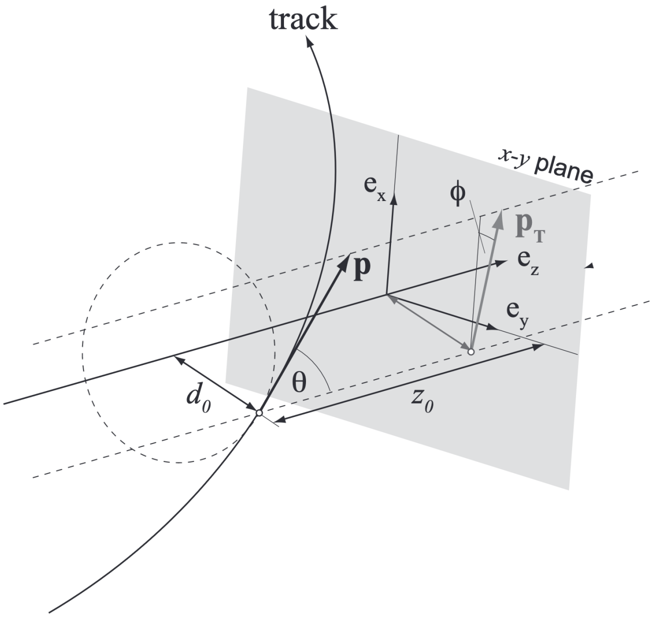

Figure 2.9.: Drawing of a track, where the transverse (d_0) and longitudinal (z_0) impact parameters with respect to the interaction point are shown [71]. The interaction point is located off the figure, to the left.

2.3.2. Electrons

Electrons are reconstructed by matching energy clusters in the calorimeter with tracks from the inner detector [72]. Dynamic, variable-sized clusters called *superclusters* are used in order to recover energy lost by electrons through bremsstrahlung. In this Section, the reconstruction of electrons in the region $|\eta| < 2.47$ is described, which is the region covered by the ID and the high-granularity region of the ECal. Additional selections are made in order to distinguish *prompt* electrons, originating from the primary vertex, from *non-prompt* electrons, which may originate from decays of heavy-flavour hadrons or photons undergoing pair production. *Fake electrons* may also be reconstructed from similar signatures in the detector to real electrons, such as $\pi^0 \rightarrow \gamma\gamma$ decays.

Electron reconstruction starts with the selection of energy deposit clusters, measured in topologically connected ECal cells, called *topo-clusters*. The seed cells initiating the cluster must have cell energy-to-noise ratio above four, after which the clustering algorithm continues to add neighbouring cells around the seed based on successively smaller energy-to-noise ratio thresholds. Topo-clusters with energies greater than 400 MeV are then matched to electron tracks based on RoIs created in the calorimeter from topo-clusters. Track seeds which fail the standard pattern recognition, but are within an RoI, are re-fitted using the Gaussian-sum filter algorithm [73] which allows for 30% energy loss at each material intersection. These re-fitted tracks are then matched to topo-clusters in $(\eta - \phi)$, where the track momentum may be rescaled to improve matching for electron candidates with significant energy loss due to bremsstrahlung. If multiple tracks are matched, those with hits in the pixel detector are preferred.

Superclusters are formed by combining neighbouring topo-clusters, called *satellite clusters*, in order to recover energy lost due to bremsstrahlung radiation. The topo-cluster with the largest E_{T} is chosen as the seed cluster, if this satisfies $E_{\mathrm{T}} > 1$ GeV and is matched to a track with at least four silicon hits in the ID. Satellite clusters with smaller E_{T} than the seed, and which fall within a window of $\Delta\eta \times \Delta\phi = 0.075 \times 0.125$ around the seed cluster barycentre, are combined, as these are compatible with secondary EM showers originating from the same electron. Satellite clusters corresponding to distant bremsstrahlung radiation can be recovered if these fall within a looser window of $\Delta\eta \times \Delta\phi = 0.125 \times 0.3$, and share matched silicon tracks with the seed cluster.

Electron energies are then calibrated using a multivariate approach, where a boosted decision tree is trained on simulation. Other steps to the calibration procedure include corrections accounting for the discrepancy between data and simulation, calibration of the calorimeter layers and a final calibration of the global energy scale using $Z \rightarrow e^+e^-$ events [74].

Following the reconstruction and calibration steps, identification criteria are applied to select prompt electrons and reduce the background from non-prompt and fake electrons. A likelihood discriminant is built using a multivariate technique that evaluates several variables simultaneously. Variables with sufficient discriminating power between prompt and background electrons, such as shower shape variables, track conditions and track-cluster matching variables are chosen to build the discriminant. The advantage of using a likelihood-based discriminant over a cut-based approach is that a prompt electron may fail a cut-based identification if it is limited to a single quantity, whereas by combining information from more discriminating variables, higher prompt electron efficiency is achieved [75]. Three working points (WPs) are defined for this discriminant: *loose*, *medium* and *tight*, where electrons selected by each constitute a subset of the previous. Tighter WPs result in higher purities of prompt electrons over backgrounds, at the expense of loss of efficiency, as shown in Figure 2.10. In this thesis, electrons satisfying the medium WP are used.

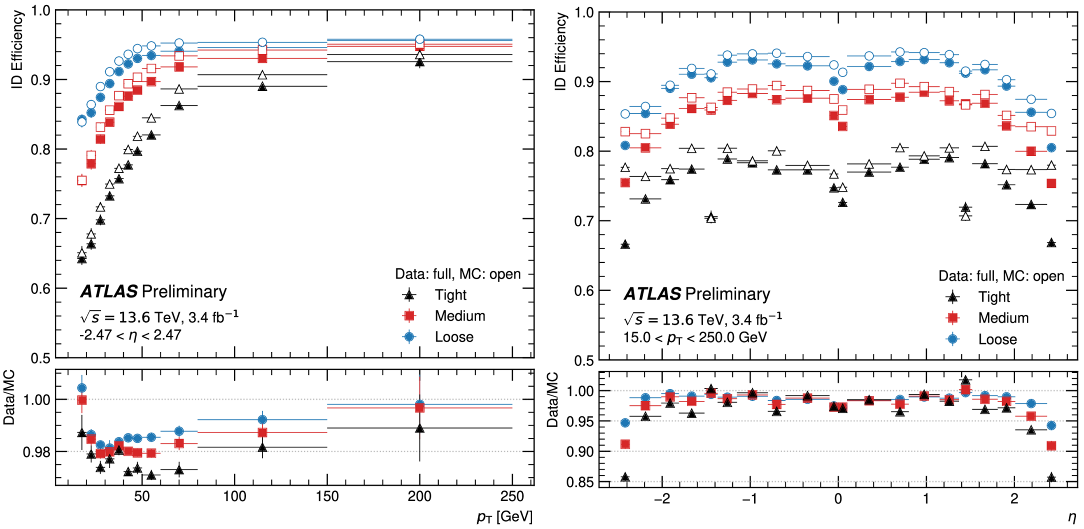

Figure 2.10.: Electron identification efficiencies as a function of (a) the electron p_T integrated over the full pseudo-rapidity range, and as a function of (b) the electron pseudo-rapidity, for electrons with 15 GeV $< p_\mathrm{T} <$ 250 GeV, measured using $Z \to e^+e^-$ events from data and MC. Figure taken from [76].

Further selection criteria are applied to separate prompt electrons from background in the form of *isolation*, which measures the amount of hadronic activity in their vicinity. This can be quantified from the nearby tracks of charged particles or from energy deposits in the calorimeter, and leads to two classes of isolation variables: track- and calorimeter-based [72]. The calorimeter isolation variable, $E_\mathrm{T}^\mathrm{cone20}/p_\mathrm{T}$, is defined as the sum of cluster E_T in a cone defined by $\Delta R < 0.2$ surrounding the electron, excluding the E_T associated with the electron itself, divided by the electron p_T. Similarly, the track isolation variable, $p_\mathrm{T}^\mathrm{varcone30}/p_\mathrm{T}$ is defined as the sum of track p_T surrounding the electron, excluding the p_T of the electron, in a cone defined by $\Delta R < 0.3$ surrounding the electron, divided by the electron p_T. Additional requirements are considered in the track isolation variable definition, including a variable cone size in order to account for electrons produced from in-flight decays of high momentum heavy particles, where the decay products can be very close to the electron direction, and additional track-to-vertex-association (TTVA) requirements to reduce contamination from tracks produced from pile-up. Different WPs are defined based on different prompt electron efficiencies and purities. In this thesis, the Tight_VarRad working point is used, which requires $p_{\mathrm{T}}^{\mathrm{varcone30}}/p_{\mathrm{T}} < 0.06$ and $E_{\mathrm{T}}^{\mathrm{cone20}}/p_{\mathrm{T}} < 0.06$.

2.3.3. Muons

Muons are reconstructed using information from the ID, calorimeters and MS, where fragments are reconstructed in each sub-detector first. Tracks in the ID are reconstructed as described in Section 2.3.1. In the MS, muon reconstruction starts with the formation of track segments using hit patterns in each of the muon chambers. Several different types of muons may be reconstructed, depending on the available sub-detector information [77]:

Combined (CB): tracks are resonstructed independently in the ID and MS, and then combined using a global re-fit, where MS hits can be added or removed to improve the fit quality. Most muons are reconstructed following the *outside-in* approach, where the fit begins in the MS and is then extrapolated inward to match an ID track. CB muons are the most commonly reconstructed muons and have the highest purity across the largest acceptance range.

Segment-tagged (ST): ID tracks associated with at least one track segment in the MS tracking chambers are classified as segment-tagged. Typically, these are low p_{T} muons which may not reach more than one layer in the MS chambers or fall in regions of reduced MS acceptance.

Calorimeter-tagged (CT): muons are minimum-ionising particles and deposit a small amount of energy in the calorimeter. CT muons are reconstructed using ID tracks that can be matched with such an energy deposit in the calorimeter in order to recover acceptance in the central region ($|\eta| < 0.1$) of the MS, where performance is reduced due to a large amount of material including support structure and cables.

Extrapolated (ME): these muons are reconstructed only using hits in the MS and loosely extrapolated to the beamline. This category is used to recover acceptance in the region $2.5 < |\eta| < 2.7$, which is not covered by the ID.

The muon momentum is then calibrated, where corrections are applied to both data and simulation [78]. A charge-dependent bias on the muon momentum scale is introduced by imperfect knowledge of the real detector geometry. A correction is applied to the data, derived from $Z \rightarrow \mu^+\mu^-$ events in data, where the di-muon invariant mass is sensitive to this bias. Another correction is applied to simulation to improve the agreement between data and simulation, derived using $Z \rightarrow \mu^+\mu^-$ and $J/\psi \rightarrow \mu^+\mu^-$ events in data. This correction accounts for mis-modelling effects, such as inaccuracies in the magnetic field description, energy loss in the calorimeter, and smearing effects as a result of multiple scattering and the intrinsic detector resolution.

Identification requirements for muons are defined in order to discriminate between prompt and background muons, such as those produced in decays of heavy-flavour hadrons, pions or kaons. Cut-based selections are made based on the number of hits in the different ID sub-detectors and MS stations, track fit properties and compatibility between the individual measurements in the ID and MS. Three nominal WPs are defined, in order of decreasing efficiency and increasing purity: *loose*, *medium* and *tight*. The medium WP, which is used for muons in this thesis, only accepts CB muons, among other requirements. This WP provides an efficiency and purity compatible with the requirements for most analyses, while keeping uncertainties small.

Isolation criteria are also used to discriminate against non-prompt muons surrounded by large amounts of hadronic activity, such as those produced from decays of heavy-flavour hadrons. Track and calorimeter isolation variables representing the level of activity close to the muon are defined, just as for electrons, which are used to define several working points. In this thesis, muons satisfying the Tight_VarRad working are used, which require $p_{\mathrm{T}}^{\mathrm{varcone30}}/p_{\mathrm{T}} < 0.04$ and $E_{\mathrm{T}}^{\mathrm{cone20}}/p_{\mathrm{T}} < 0.15$. The reconstruction and identification efficiency for muons satisfying the medium identification WP is shown in Figure 2.11 (left), and isolation efficiency for Tight_VarRad muons in Figure 2.11 (right), where both efficiencies have been evaluated using $Z \rightarrow \mu^+\mu^-$ events from data collected in 2022 at $\sqrt{s} = 13.6$ TeV. The differences between simulation and data in the identification efficiency are due to the fact that only a small fraction of the data collected in 2022 included NSW hits.

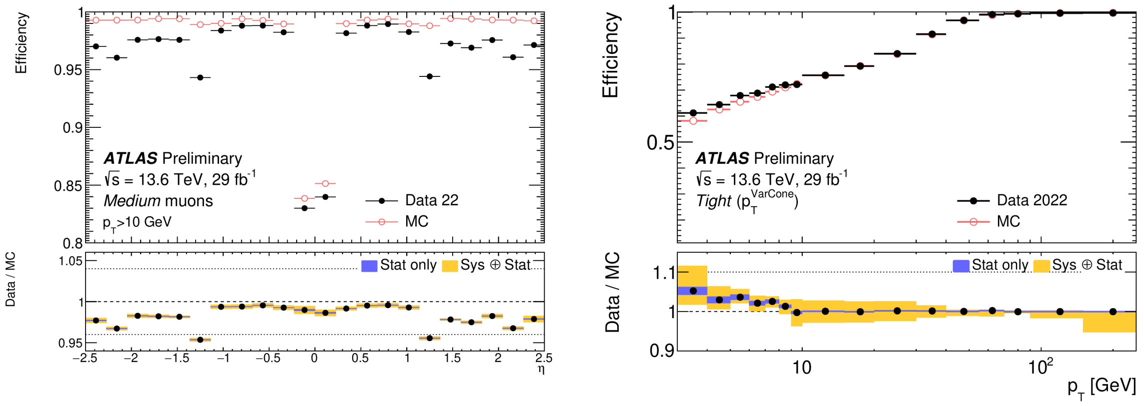

Figure 2.11.: Reconstruction and identification efficiency for muons with $p_{\mathrm{T}} > 10$ GeV passing the Medium identification working point as a function of muon η (left), taken from [79]. Isolation efficiency for muons passing the Tight_VarRad isolation working point as a function of the muon p_{T} (right), taken from [80]. Efficiencies are measured using $Z \to \mu^+\mu^-$ events in data and simulation.

2.3.4. Jets

Quarks and gluons undergoing hadronization and fragmentation, producing streams of hadrons in the detector, are reconstructed as *jets* through the use of a sequential clustering algorithm, called the anti-k_t jet clustering algorithm [81]. Topo-clusters, reconstructed from energy deposits in the calorimeter, can be combined based on a distance parameter d_{ij} between clusters i and j:

$$d_{ij} = \min\left(p_{\mathrm{T},i}^{2p}, p_{\mathrm{T},j}^{2p}\right) \frac{\Delta R_{ij}^2}{R^2}, \tag{2.8}$$

where $p_{\mathrm{T},i}$ and $p_{\mathrm{T},j}$ are the transverse momenta of the clusters i and j, ΔR_{ij} is the angular distance between them, R is a radius parameter and p is an exponential parameter which sets the relative power of the geometrical versus energy scales. For the anti-k_t algorithm, $p = -1$ [5]. Nominally, jets are reconstructed by ATLAS using a radius parameter $R = 0.4$. Clustering begins by finding objects with the smallest d_{ij}, and comparing it to the distance between object i and the beam axis, $d_{iB} = p_{\mathrm{T},i}^{2p}$. If d_{ij} is smaller, objects i and j are combined, and if d_{iB} is smaller, i is considered a jet and j is discarded. The algorithm proceeds iteratively, where the distances are re-calculated

---

[5] The case of $p = 0$ and $p = 1$ correspond to the Cambridge/Aachen [82] and k_t [83] algorithms, respectively.

following each combination of objects or removal until no objects are left. The result is typically a jet with a hard component, surrounded by softer components, as shown in Figure 2.12. As the distance parameter d_{ij} favours larger values of $p_{\mathrm{T},i}$, soft objects will tend to cluster to hard objects rather than amongst themselves. A result of this is that soft objects do not modify the shape of the jet in $\eta - \phi$ space, but hard objects do. Thus, the algorithm is *infrared and collinear safe*, where soft (infrared) radiation and collinear splitting does not modify the jet boundary [84].

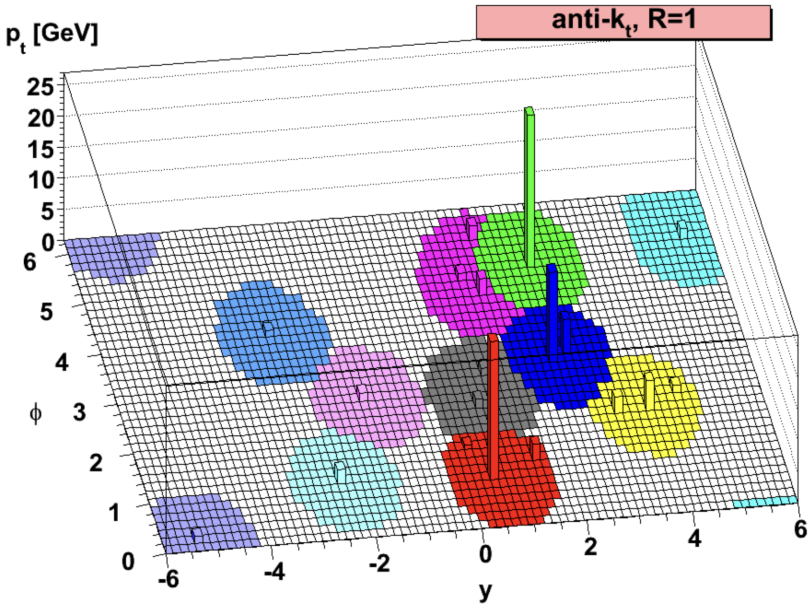

s

Figure 2.12.: Simulation of jet reconstruction performed with the anti-k_t jet clustering algorithm on an event simulated with HERWIG, taken from [81].

As mentioned previously, jets can be reconstructed from topo-clusters, thus only using the energy obtained from calorimeter information. These *topo-jets* may be susceptible to losses in resolution due to pile-up effects, which can be corrected using tracking information. In this thesis, *particle flow* (PFlow) jets are used, where both tracking and calorimeter information is combined to form single objects [85]. The energy deposited in the calorimeter by charged particles is removed and replaced with the momentum of the track matched to the calorimeter topo-clusters and to the primary vertex. The jet reconstruction is performed using PFlow objects, which constitute the remaining calorimeter energy and the momenta of these matched tracks. PFlow jets thus have better energy and angular resolutions due to the superior performance of the tracker at smaller momenta compared to the calorimeter energy resolution, and pile-up can be more easily rejected by additional vertex requirements using tracking information. Reconstruction efficiencies are also superior to topo-jets as charged particles with small p_{T} may be recovered from tracking information, which would otherwise not pass calorimeter noise thresholds in topo-cluster reconstruction.

Reconstructed jets are calibrated to restore the jet energy to that of jets at the generator level, using a sequence of simulation-based corrections and *in-situ* corrections called the jet energy scale (JES) calibration, where all stages aim to correct the jet energy, momentum and mass [62].

Pile-up corrections remove excess energy from multiple interactions in the bunch crossing, based on the average pile-up contribution and including a simulation-based correction, parametrised in terms of the mean number of interactions per bunch crossing $\langle \mu \rangle$, and number of reconstructed vertices per event.

The absolute JES calibration corrects the four-momentum of reconstructed jets to the energy scale from simulation at the truth level. This correction accounts for differences between the electromagnetic and hadronic calorimeters, energy losses in dead material, energy deposited outside the jet cone and biases in η reconstruction, which may be caused by regions over which calorimeter technology differs or calorimeter granularity changes. The correction is derived by comparing reconstructed jets in data to truth jets in simulation, and is applied as a function of the jet energy and η.

The global sequential calibration (GSC) reduces effects from fluctuations in the jet response in the calorimeter, designed to improve the jet resolution and associated uncertainties without altering the average jet energy response. This correction uses global observables based on information from the energy deposits in the calorimeter, tracking information and activity in the muon chambers behind jets.

In-situ jet calibrations are applied on data to correct for final discrepancies in the jet response between simulation and data.

After these calibrations are performed, related uncertainties are calculated as a function of the jet p_{T}. Additionally, the jet energy resolution (JER) is derived using di-jet events in data [62].

Despite applying pile-up corrections to the jet energy scale, pile-up jets may still affect overall jet performance, especially at low p_{T}. In order to remove these pile-up jets, which are mis-reconstructed as jets associated with the hard interaction, an artificial neural-network-based discriminant is constructed (NNJVT). This discriminant is the successor of the likelihood-based JVT discriminant used during Run 2 [86]. Different cuts can be applied to this discriminant, based on the required efficiency and pile-up fake rate.

Jets originating from the hadronisation of heavy-flavour quarks such as *b* quarks can be identified based on several distinguishing features of their decays, such as the long lifetimes of *b* hadrons, resulting in a distinct secondary vertex with a measurable displacement from the primary vertex, the high decay multiplicity of *b* hadrons and the large transverse momentum of *b*-hadron decay products [87]. These features are used to define several distinguishing variables, which are used as input variables in *b*-tagging algorithms such as the DL1d algorithm [88] used by ATLAS.

2.3.5. Missing transverse momentum

Particles which do not interact with the detector material, such as neutrinos from a W boson decay, can still be inferred from the missing transverse momentum in the event. Following the principle of momentum conservation, the transverse momentum of the pp collision must balance to zero. The missing transverse momentum $\boldsymbol{p}_{\mathrm{T}}^{\mathrm{miss}}$, with magnitude $E_{\mathrm{T}}^{\mathrm{miss}}$, is calculated using information from all sub-detectors by building a negative sum of the momenta of all calibrated physics objects in the event [89]:

$$\boldsymbol{p}_{\mathrm{T}}^{\mathrm{miss}} = -\left(\underbrace{\sum \boldsymbol{p}_{\mathrm{T}}^{e} + \sum \boldsymbol{p}_{\mathrm{T}}^{\gamma} + \sum \boldsymbol{p}_{\mathrm{T}}^{\tau} + \sum \boldsymbol{p}_{\mathrm{T}}^{\mu} + \sum \boldsymbol{p}_{\mathrm{T}}^{\mathrm{jet}}}_{\text{hard term}} + \underbrace{\sum \boldsymbol{p}_{\mathrm{T}}^{\mathrm{track}}}_{\text{soft term}} \right), \tag{2.9}$$

where e denotes electrons, γ denotes photons, τ denotes tau-leptons and μ denotes muons.

The $\boldsymbol{p}_{\mathrm{T}}^{\mathrm{miss}}$ sum is split into a *hard term*, accounting for calibrated physics objects which have originated from the hard-scatter interaction, and a *soft term*, which consists of reconstructed charged-particle tracks that are associated with the hard-scatter vertex but not with physics objects. Prior to the $\boldsymbol{p}_{\mathrm{T}}^{\mathrm{miss}}$ calculation, physics objects are reconstructed independently of each other, implying that the same tracks or calorimeter clusters may be used to reconstruct two different objects in the same event. Thus, a *signal ambiguity* step is applied after the summation in order to remove this double counting, and minimise the effect of fake $\boldsymbol{p}_{\mathrm{T}}^{\mathrm{miss}}$ in the event.

Additionally, the hard objects entering the summation are analysis-dependent, such that some types of objects may not enter the calculation if they are not present in the final state considered by the analysis selection criteria. This is done in order to exploit any improvements on the calibration of the hard objects performed specific to the analysis. In this thesis, only electrons, muons and jets are considered in the final state and enter the $\boldsymbol{p}_{\mathrm{T}}^{\mathrm{miss}}$ calculation. Several WPs are defined for the $\boldsymbol{p}_{\mathrm{T}}^{\mathrm{miss}}$ calculation, which only differ in the requirements on forward jets ($2.5 < |\eta| < 4.5$) in order to reduce pile-up contamination. Tighter WPs increase the $\boldsymbol{p}_{\mathrm{T}}^{\mathrm{miss}}$ resolution at the expense of a loss in efficiency as real jets may be categorised as pile-up. The Tight WP is used in this thesis, which requires forward jets to satisfy $p_{\mathrm{T}} > 30$ GeV.

The soft term is constructed from charged soft particles associated to the primary vertex, which were not used in the reconstruction of other hard objects in the event. Additional contributions include tracks associated with jets that did not pass the ambiguity step. The addition of the soft term to the $\boldsymbol{p}_{\mathrm{T}}^{\mathrm{miss}}$ calculation is important as it captures components of the event that are not included in the reconstruction and calibration of hard objects and would otherwise be discarded. Thus, it improves the $\boldsymbol{p}_{\mathrm{T}}^{\mathrm{miss}}$ resolution and the agreement between the reconstructed and true $\boldsymbol{p}_{\mathrm{T}}^{\mathrm{miss}}$, especially for events with a small number of hard objects.

The performance of the $\boldsymbol{p}_{\mathrm{T}}^{\mathrm{miss}}$ is susceptible to the performance of each hard object that enters the summation. Events with real $\boldsymbol{p}_{\mathrm{T}}^{\mathrm{miss}}$ contributions, for example W boson decays with neutrinos in the final state, are expected to have large $E_{\mathrm{T}}^{\mathrm{miss}}$ values. Non-zero $E_{\mathrm{T}}^{\mathrm{miss}}$ values can also arise due to miscalibrated objects, objects which are outside the detector acceptance or detector noise, all of which contribute to fake $\boldsymbol{p}_{\mathrm{T}}^{\mathrm{miss}}$ and to the degradation in resolution of real $\boldsymbol{p}_{\mathrm{T}}^{\mathrm{miss}}$. The performance of the $\boldsymbol{p}_{\mathrm{T}}^{\mathrm{miss}}$ reconstruction in terms of the resolution and scale is assessed in data and simulation, using events with no real sources of $\boldsymbol{p}_{\mathrm{T}}^{\mathrm{miss}}$ such as $Z \rightarrow e^{+}e^{-}$ and $Z \rightarrow \mu^{+}\mu^{-}$ events, as well as events with expected $\boldsymbol{p}_{\mathrm{T}}^{\mathrm{miss}}$ such as W boson and top quark decays, where neutrinos are present in the final state [89].

Chapter 3.

Energy corrections for the upgraded Level-1 Calorimeter Trigger

Selecting efficiently which events to record for permanent storage during data-taking is essential towards maximising the physics potential of the ATLAS experiment. This task is handled by the trigger system, described in Section 2.2.4, where the first selection of events is performed in real time by the Level-1 (L1) trigger, which uses reduced granularity information from the calorimeters and muon system, processed by the L1 Calorimeter (L1Calo) and Muon (L1Muon) triggers respectively. The L1 trigger reduces the rate of events from the 40 MHz bunch crossing rate to 100 kHz, after which the HLT trigger can use full detector granularity and higher complexity algorithms to further reduce the rate to about 3 kHz [67].

One of the most useful signatures to trigger events on are single isolated, high-p_{T} electrons, where the presence of such an electron can indicate the decay of particles such as the W, Z and Higgs bosons. Triggering on electrons also allows the possibility to search for physics Beyond the Standard Model, where electrons may be present in the final state of these processes. For this reason, L1 single EM object triggers, which are the first to identify electron candidates in the detector, are allocated approximately 25% of the 100 kHz L1 rate budget [90], equivalent to 25 kHz. In preparation for Run 3, where the LHC operates at twice the design instantaneous luminosity, the L1Calo trigger was upgraded to process higher-granularity information from the calorimeters, using more complex algorithms in order to mitigate any increase in the trigger rate. The increase in granularity also allowed the addition of new corrections to the electron identification algorithm, resulting in more efficient triggers with reduced rates [67].

In this Chapter, the *dead material corrections* are presented, which correct the transverse energy of electron candidates identified by the new L1Calo electron feature extractor (eFEX) [91]. Following an overview of the L1Calo system in Section 3.1 and of the eFEX electron identification algorithm in Section 3.1.1, the dead material corrections are presented in Section 3.2. Results for simulation-based corrections are presented in Section 3.2.1, which were used by the eFEX electron identification algorithm during data-taking in 2022 and early 2023, as part of the commissioning of the upgraded L1Calo system. The corrections were then tuned using pp collision data collected during early 2023 at $\sqrt{s} = 13.6$ TeV, and are presented in Section 3.2.2. As of July 2023, these data-driven corrections have replaced the simulation-based corrections previously used by the eFEX, and contribute to the increased efficiency of L1 single EM object triggers in Run 3.

3.1. Level-1 Calorimeter Trigger

The L1Calo trigger system processes reduced granularity information from the LAr and Tile calorimeters to identify signatures from high-E_{T} electrons, photons, jets, hadronically decaying tau leptons, and to identify events with large $E_{\mathrm{T}}^{\mathrm{miss}}$or transverse energy sum ΣE_{T}. Several algorithms run on custom hardware processors, based on field-programmable gate array (FPGA) technology, which calculate the energy and position of *trigger objects* (TOBs), as well as isolation variables [52].

During Run 3, peak instantaneous luminosity conditions ($\mathcal{L} = 2 \times 10^{34}\ \mathrm{cm}^{-2}\mathrm{s}^{-2}$) can be maintained for a larger fraction of the LHC fill, resulting in increased average pile-up of $\langle \mu \rangle \approx 50$ and beyond. At these pile-up levels, calorimeter resolution is degraded because of the higher denisity environments, which reduces trigger efficiencies and requires higher threshold triggers in order to prevent an increase in trigger rates. Thus, the primary purpose of the L1Calo Phase-1 upgrade, which took place prior to Run 3, was to reduce the impact of pile-up on trigger rates without the need to increase trigger thresholds, through the use of higher-granularity information from the EM calorimeter. Additionally, the calculation of isolation variables, and the optimisation of thresholds on these, provide identification of isolated electrons and photons and discrimination against jets from pile-up. The L1Calo system in Run 3 is shown in Figure 3.1, where the Phase-1 (Run 3) components were run in parallel with the legacy (Run 1 and 2) components during the commissioning of the Phase-1 system.

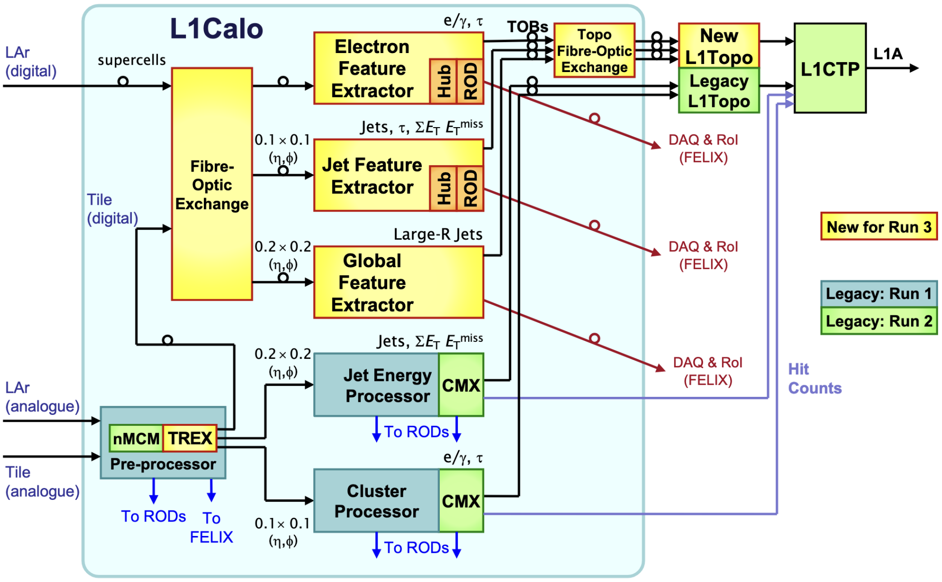

Figure 3.1.: Schematic diagram of the L1Calo trigger system during commissioning in Run 3, where the legacy (shown in green) and Phase-1 (shown in yellow) modules are run in parallel [92].

For the legacy system, analogue signals from the LAr and Tile calorimeters are digitised and calibrated in the pre-processor, and then sent to the jet energy processor (JEP) and the cluster processor (CP), where electron, photon, jet and tau candidates can be identified. The JEP also calculates $E_{\mathrm{T}}^{\mathrm{miss}}$ and ΣE_{T} based on the negative or scalar sum of the transverse energy in the event.

For the Phase-1 system, the LAr EM calorimeter signals are digitised by the new LAr Digital Processing System (LDPS), which provides the signals in the form of *supercells* containing sums of four or eight calorimeter cells. These supercells replace the legacy trigger towers supplied by the LAr in the new digital trigger path. In the region $|\eta| < 2.5$ supplied by the LAr calorimeter, trigger towers with granularities $\Delta\eta \times \Delta\phi = 0.1 \times 0.1$ are replaced by ten supercells [1], as shown in Figure 3.2. In the pre-sampler (Layer-0) and third layer, a region of $\Delta\eta \times \Delta\phi = 0.1 \times 0.1$ in the calorimeter is covered by one supercell for each, while in the first and second layers where most of the energy of the EM shower is deposited, a region of $\Delta\eta \times \Delta\phi = 0.1 \times 0.1$ in the calorimeter is covered by four supercells each, with granularities of $\Delta\eta \times \Delta\phi = 0.025 \times 0.1$.

Data from the Tile calorimeter is still received in analogue format and digitised by the pre-processor. The new Tile Rear Extension (TREX) module, which is installed as

---

[1] In the region $1.8 < |\eta| < 2.5$ not covered by the pre-sampler, only 9 supercells are present.

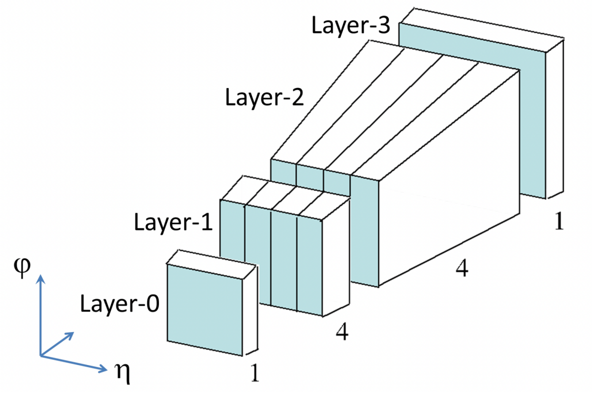

Figure 3.2.: Diagram showing trigger towers with granularity $\Delta\eta \times \Delta\phi = 0.1 \times 0.1$ after the upgrade to the LAr electronics. Ten supercells with position and E_T information, one from the pre-sampler, four from the first and second layers and one from the third layer, are provided per trigger tower as input to the L1Calo system [91].

an extension to the pre-processor module, sends the output signals to the new feature extractor (FEX) modules, and to the legacy system.

There are three different types of FEXs, each specialised in identifying different types of signatures in the L1Calo trigger. The electron feature extractor (eFEX), described further in Section 3.1.1, uses the full granularity supercell information from the LAr calorimeter to identify electron, photon and hadronically decaying tau candidates. The jet feature extractor (jFEX) identifies jets, hadronically decaying tau leptons, $E_\mathrm{T}^\mathrm{miss}$ and ΣE_T in the full range of the calorimeter system, $|\eta| < 4.9$. Compared to the legacy system, which uses $\Delta\eta \times \Delta\phi = 0.2 \times 0.2$ trigger towers from the LAr calorimeter in the region $|\eta| < 2.5$, the jFEX receives more granular $\Delta\eta \times \Delta\phi = 0.1 \times 0.1$ trigger towers, allowing the use of more complex jet and tau algorithms. The jFEX can also identify forward electrons in the region $2.3 < |\eta| < 4.9$ outside the acceptance of the eFEX. As opposed to the eFEX and jFEX systems, which are composed of several modules each, the global feature extractor (gFEX) is a single module. This design enables data from the entire calorimeter to be processed in the same module, allowing the use of full-scan algorithms. While the functions of the eFEX and jFEX can be considered analogous to the CP and JEP, the gFEX extends the acceptance of L1Calo to identify Lorentz boosted objects, such as the decay products of Higgs bosons produced with large p_T, and global event observables such as $E_\mathrm{T}^\mathrm{miss}$, with additional pile-up subtraction capabilities.

The output of L1Calo consists of TOBs, reconstructed by the legacy JEP and CP or the Phase-1 FEX modules, which encode information on the type of object, E_T, energy sum and position in $(\eta - \phi)$. These TOBs are sent to the topological trigger, L1Topo, which calculates how many objects pass pre-defined thresholds, and sends this information to the central trigger processor (CTP). The final L1 accept (L1A) decision is made by the CTP, which receives inputs from L1Calo, L1Muon and L1Topo. This can accept events based on the number of objects in the event, their type and whether they satisfy certain thresholds. These requirements constitute an L1 trigger item, where up to 512 distinct L1 items may be configured in the CTP [52].

3.1.1. Electron Feature Extractor (eFEX)

The eFEX system, covering the region $|\eta| < 2.5$, consists of 24 modules whose task is to identify electrons and photons (e/γ) [2], and hadronically decaying tau leptons (τ). Each module may send a maximum of six TOBs produced by the e/γ algorithm, and further six TOBs produced by the τ algorithm. The eFEX receives full supercell granularity information from the LAr calorimeter as described previously, and trigger towers with granularity $\Delta\eta \times \Delta\phi = 0.1 \times 0.1$ from the Tile calorimeter.

The e/γ algorithm begins with a seed-finding procedure, using $\Delta\eta \times \Delta\phi = 0.3 \times 0.3$ supercell grids from the second LAr calorimeter layer, as illustrated in Figure 3.3. A "core" region composed of four supercells is defined in the supercell grid, surrounded by the rest of the supercells, making up the "environment region". A sliding-window algorithm is used, where all supercells are considered as part of the core region in the seed-finding procedure. Seeds are determined by local maxima in the core region, where the E_{T} of each supercell in the core region is compared to the supercells surrounding it. A 3×2 supercell cluster area in $\eta - \phi$ is formed using the seed supercell and the highest E_{T} neighbours in $\eta - \phi$, where the upward (U) and downward (D) direction of the cluster must be defined for ambiguity resolution purposes in the case where supercells neighbouring the seed have the same E_{T} [52].

When the seed has been found, the transverse energy of the TOB $E_{\mathrm{T}}^{\mathrm{TOB}}$ is calculated by summing the cluster E_{T} in the second layer (L2) with the corresponding clusters in the rest of the trigger tower layers:

---

[2] At the L1 trigger level, electron and photons leave very similar signatures in the detector, and are not differentiated due to lack of tracking information available at this level.

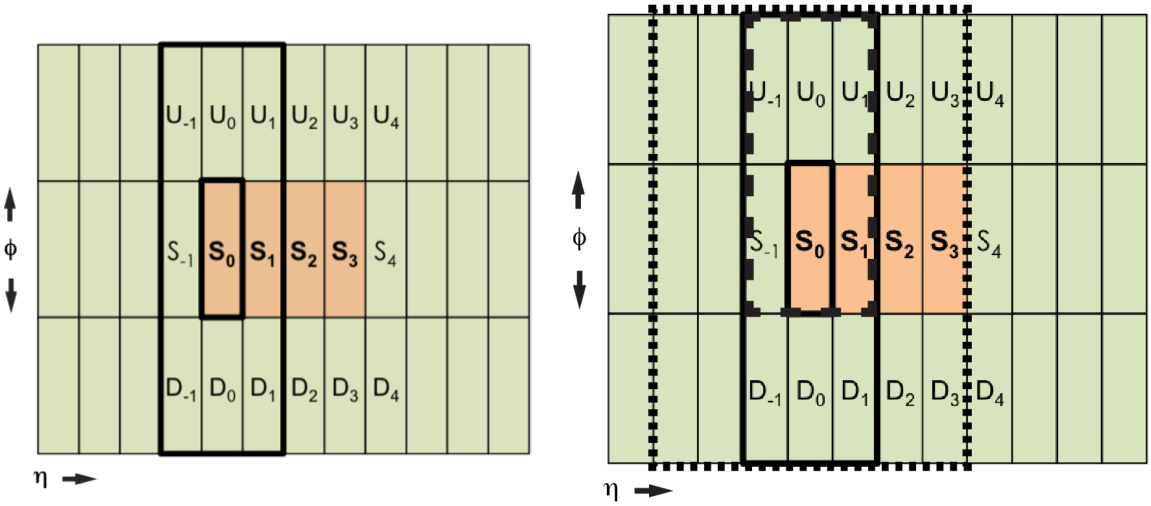

Figure 3.3.: Diagram illustrating the e/γ eFEX seed-finder algorithm (left) on a $\Delta\eta \times \Delta\phi = 0.3 \times 0.3$ supercell grid from the second calorimeter layer. The energy of four potential seeds (S) are compared in order to find the local maximum. A 3×2 supercell cluster in $\eta - \phi$ is formed (right), centered around the supercell seed, where the direction of the cluster, upward (U) or downward (D), is defined by finding the largest E_T neighbouring supercells surrounding the seed. The dotted rectangle shows the 7×3 supercell area used for the calculation of the R_η isolation variable [52].

$$E_\mathrm{T}^\mathrm{TOB} = E_\mathrm{T}^\mathrm{PS} + E_\mathrm{T}^\mathrm{L1} + E_\mathrm{T}^\mathrm{L2} + E_\mathrm{T}^\mathrm{L3}. \tag{3.1}$$

E_T^L1 represents the E_T sum in the cluster composed of 3×2 supercells in $\eta - \phi$ in the first layer (L1), while E_T^PS and E_T^L3 represent the E_T sum in the pre-sampler (PS) and third layer (L3) clusters respectively, where the corresponding clusters have areas of 1×2 supercells in $\eta - \phi$.

The eFEX also exploits the full supercell granularity information from the LAr calorimeter in calculating isolation variables based on the longitudinal and lateral EM shower shape, which allow discrimination between e/γ candidates and jets [52].

The R_η variable, representing the shower width in the second calorimeter layer, is defined as

$$R_\eta = 1 - \frac{E_{\mathrm{T}}^{3\times 2}}{E_{\mathrm{T}}^{7\times 3}}, \tag{3.2}$$

where $E_{\mathrm{T}}^{3\times 2}$ is the E_{T} sum in the 3×2 supercell cluster area in $\eta - \phi$, centered around the seed, and $E_{\mathrm{T}}^{7\times 3}$ is the E_{T} sum in the 7×3 supercell cluster area in $\eta - \phi$, also centered around the seed. The supercell cluster areas used in the R_η calculation are illustrated in Figure 3.3 (right). The R_η variable exploits the narrow shower shapes produced by e/γ candidates, where smaller R_η values indicate narrower showers.

The hadronic fraction R_{had} is defined as

$$R_{\mathrm{had}} = \frac{E_{\mathrm{T}}^{\mathrm{had}}}{E_{\mathrm{T}}^{\mathrm{EM}} + E_{\mathrm{T}}^{\mathrm{had}}}, \tag{3.3}$$

where $E_{\mathrm{T}}^{\mathrm{had}}$ is the E_{T} sum in a $\Delta\eta \times \Delta\phi = 0.3 \times 0.3$ window in the hadronic calorimeter, and $E_{\mathrm{T}}^{\mathrm{EM}}$ is $E_{\mathrm{T}}^{\mathrm{TOB}}$ for the TOB centered around the seed, as defined in Eq. 3.1. Thus, the R_{had} variable can be used to identify e/γ candidates which deposit almost all of their energy in the EM calorimeter, where smaller R_{had} values indicate less energy deposited in the hadronic layer, consistent with e/γ candidates.

The final isolation variable is the shower width in the first calorimeter layer, $w_{\mathrm{s,tot}}$, which also exploits the narrow shower shapes produced by e/γ candidates and is defined as

$$w_{\mathrm{s,tot}} = \sqrt{\frac{\Sigma E_{\mathrm{T}}^{i} \times (i - i_{\mathrm{max}})^2}{\Sigma E_{\mathrm{T}}^{i}}}, \tag{3.4}$$

where i spans over the $\Delta\eta = 0.1$ range of five supercells in the first layer, centered around the supercell (i_{max}) with the largest E_{T} in that layer ($E_{\mathrm{T}}^{i_{\mathrm{max}}}$). Smaller values of the $w_{\mathrm{s,tot}}$ isolation variable indicate narrower showers consistent with e/γ candidates.

3.2. Dead material corrections

As described in Section 3.1.1, after a seed has been found by the e/γ algorithm, the E_{T} of the e/γ trigger object (TOB) in the eFEX is calculated, using Eq. 3.1, by summing E_{T} of the 3×2 supercell clusters from the first and second calorimeter layers, and the 1×2 supercell clusters from the pre-sampler and the third calorimeter layer. A similar algorithm is used for e/γ identification in the legacy CP, where the algorithm uses coarser granularity $\Delta\eta \times \Delta\phi = 0.1 \times 0.1$ trigger towers instead of supercells, without E_{T} information from the individual layers of the LAr calorimeter and the pre-sampler [44]. Thus, the increased granularity of the LAr information available to the e/γ identification algorithm in the Phase-1 L1Calo trigger allows the introduction of additional correction to the TOB E_{T}, accounting for the energy response in the different layers of the LAr EM calorimeter.

The motivation behind this correction is to increase the efficiency of L1 EM object triggers by improving the agreement between the p_{T} of an electron reconstructed offline (described in Section 2.3.2) and the corresponding TOB E_{T} identified using the eFEX. Figure 3.4 shows the electron response, or the ratio between the TOB E_{T} and the offline reconstructed electron $p_{\mathrm{T}}^{\mathrm{off}}$ as a function of the TOB η, where the response is on average smaller than 1, and has a dependence on η. This was measured using simulated $Z \to e^+e^-$ events, where the offline electron and TOB are matched in $\eta - \phi$, and the angular distance defined in Eq. 2.6 is required to satisfy $\Delta R < 0.1$. Additionally, the offline electron p_{T} is required to be larger than 15 GeV and the TOB E_{T} is required to be larger than 20 GeV.

Some legacy L1 EM object trigger items account for this η dependence in the electron response to recover trigger efficiency by applying η-dependent E_{T} thresholds. The E_{T} threshold is shifted by a maximum of 3 GeV up or down from the nominal threshold, depending on the TOB η. For Phase-1 L1 EM object triggers, this η dependence in the electron response is reduced by applying η-dependent corrections directly to the TOB cluster E_{T} summation, so that Eq. 3.1 becomes

$$E_{\mathrm{T}}^{\mathrm{TOB}} = a \cdot E_{\mathrm{T}}^{\mathrm{PS}} + b \cdot E_{\mathrm{T}}^{\mathrm{L1}} + c \cdot E_{\mathrm{T}}^{\mathrm{L2}} + E_{\mathrm{T}}^{\mathrm{L3}}, \tag{3.5}$$

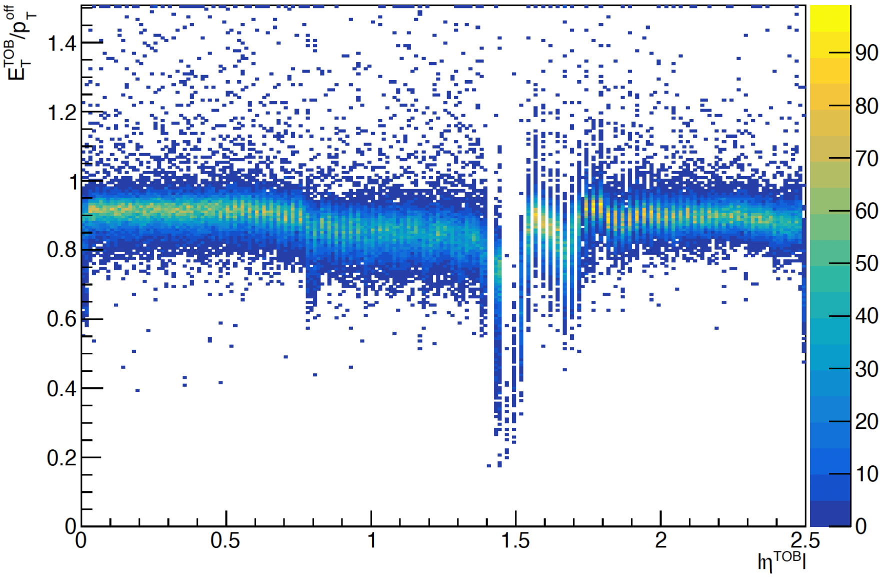

Figure 3.4.: Electron response, measured using simulated $Z \to e^+e^-$ events as the ratio between the TOB E_{T} and the offline reconstructed electron $p_{\mathrm{T}}^{\mathrm{off}}$, as a function of the TOB pseudo-rapidity η.

where the correction factors a, b and c are η-dependent and constitute the *dead material corrections* (DMCs).

As described in Section 2.2.2, the amount of upstream material before the LAr calorimeter, and before the pre-sampler, varies in thickness with η. The upstream material, including material from the ID and support structures, can also be referred to as *dead material* since the energy deposited in this material is not measured by the calorimeters. The amount of dead material in units of radiation length X_0 before the pre-sampler and the LAr detector ("accordion"), and the energy lost by simulated electrons with energies of 100 GeV, is illustrated in Figure 3.5 as a function of $|\eta|$. The largest amount of material, and consequently the largest energy loss, is in the transition region ($1.37 < |\eta| < 1.52$) where the detector geometry changes between the barrel and endcap EM calorimeters.

For electrons reconstructed offline, described in Section 2.3.2, a calibration is applied to data, accounting for different responses in the LAr calorimeter layers and pre-sampler [74]. This calibration, also called the *LAr layer calibration*, is derived as a function of η, in order to equalize the energy scales in the different layers and reduce discrepancies between data and simulation as a result of mismodelling of the dead material upstream of the calorimeter. Following the same logic, the DMCs applied

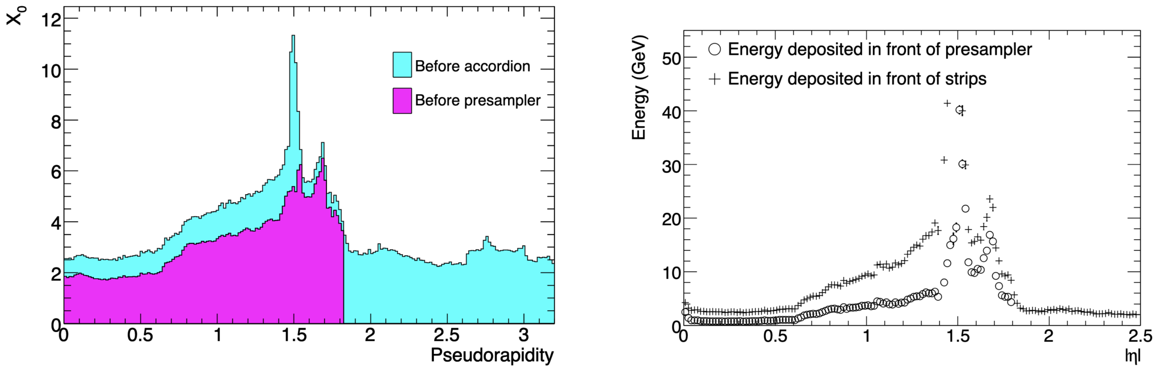

Figure 3.5.: Amount of dead material, in units of radiation length X_0, as a function of the pseudorapidity $|\eta|$, in front of the pre-sampler, and in front of the LAr calorimeter with accordion geometry (left). Energy loss for 100 GeV electrons before the pre-sampler and the first LAr calorimeter layer ("strips"), as a function of $|\eta|$ (right) [44].

in the E_T calculation of e/γ candidates identified by the eFEX also aim to equalise the response in each layer, as a function of η, although using coarser granularity calorimeter information than what is available in offline reconstruction, performing this correction to the online energy scale at the trigger level.

The DMCs presented in this Chapter are derived based on an earlier, less complex, version of the LAr layer calibration, which was used to calibrate electrons reconstructed offline during the commissioning period of the ATLAS detector [93]. The parameters a, b and c can be obtained through a least squares minimisation procedure by minimising the function

$$\frac{(E_\mathrm{T}^\mathrm{TOB} - p_\mathrm{T}^\mathrm{off})^2}{\sigma^2 \times p_\mathrm{T}^\mathrm{off}}, \tag{3.6}$$

where $E_\mathrm{T}^\mathrm{TOB}$ is defined in terms of the DMC parameters by Eq. 3.5, $p_\mathrm{T}^\mathrm{off}$ is the p_T of the offline electron matched to the TOB, and σ is a the stochastic term of $10\% \cdot \sqrt{\mathrm{GeV}}$ in the energy resolution of the EM calorimeter [44]. The minimisation is performed in bins of $|\Delta\eta| = 0.1$, using either simulation or data.

The simulation-based corrections, presented in Section 3.2.1, were obtained using $Z \to e^+e^-$ simulated events before the beginning of Run 3 when there were no eFEX data available. In order to further tune these corrections, pp collision data collected in early 2023 at $\sqrt{s}$ = 13.6 TeV were used to re-derive these, where results for the data-driven corrections are presented in Section 3.2.2. All minimisations for extracting the DMCs were performed using the Minuit algorithm [94].

3.2.1. Simulation-based corrections

The results presented in this Section use $Z \to e^+e^-$ events simulated at $\sqrt{s}$ = 13 TeV, as samples simulated at $\sqrt{s}$ = 13.6 TeV in the required data format for accessing cluster information in the eFEX were not available at the time of this measurement. The ATLAS detector response was simulated by the GEANT4 toolkit [95] with the full simulation of the ATLAS detector [96]. Events where at least one of the offline electrons satisfies $p_{\mathrm{T}}^{\mathrm{off}} > 15$ GeV and at least one of the TOBs satisfies $E_{\mathrm{T}} > 20$ GeV are selected. Offline electrons and TOBs are matched in $\eta - \phi$ by minimising the angular distance ΔR between the offline electrons from the Z boson decay and the TOBs present in the event, where the angular distance is also required to satisfy ΔR <0.1 to ensure a good match. Additionally, the TOB E_{T}^{TOB} and the electron $p_{\mathrm{T}}^{\mathrm{off}}$ are required to be compatible by applying a selection on the ratio between the two: $0.5 < E_{\mathrm{T}}/p_{\mathrm{T}}^{\mathrm{off}} < 1.5$.

The DMC parameters a, b and c are fit by minimising the function defined in Eq. 3.6 in each TOB bin of width $|\Delta\eta^{TOB}| = 0.1$ for the range $|\eta^{TOB}| < 2.5$, resulting in 25 bins in total. The results for the three DMC parameters are shown in Figure 3.6, where the values for a, b and c during the fit are limited between 1 and 2. The a parameter corrects the pre-sampler term in the E_{T}^{TOB} summation described by Eq. 3.5. As the pre-sampler only extends to the range $|\eta^{TOB}| < 1.8$, a is only included in the fit for this range. The b parameter corrects the first layer term in Eq. 3.5 and c corrects the second layer term. No parameter for the third layer term is considered as $E_{\mathrm{T}}^{\mathrm{L3}}$ is typically close to zero for EM showers. Overall, the DMC parameters appear to be proportional to the amount of dead material before the calorimeter as a function of η shown in Figure 3.5.

In order to assess whether the DMCs succeed in improving the energy scale in the TOB E_{T}, the mean response $E_{\mathrm{T}}^{TOB}/p_{\mathrm{T}}^{\mathrm{off}}$ in each 0.1 $|\Delta\eta^{TOB}|$ bin for matched offline electrons and TOBs is calculated before and after applying the DMCs. The mean response and its uncertainty in each 0.1 $|\Delta\eta^{TOB}|$ bin, shown in Figure 3.7 for TOBs with and without the corrections applied, are calculated by fitting a Gaussian function to the distribution of the response in that bin. Examples of these Gaussian fits can be found in Appendix A. The effect of applying the DMCs to the TOB E_{T} calculation

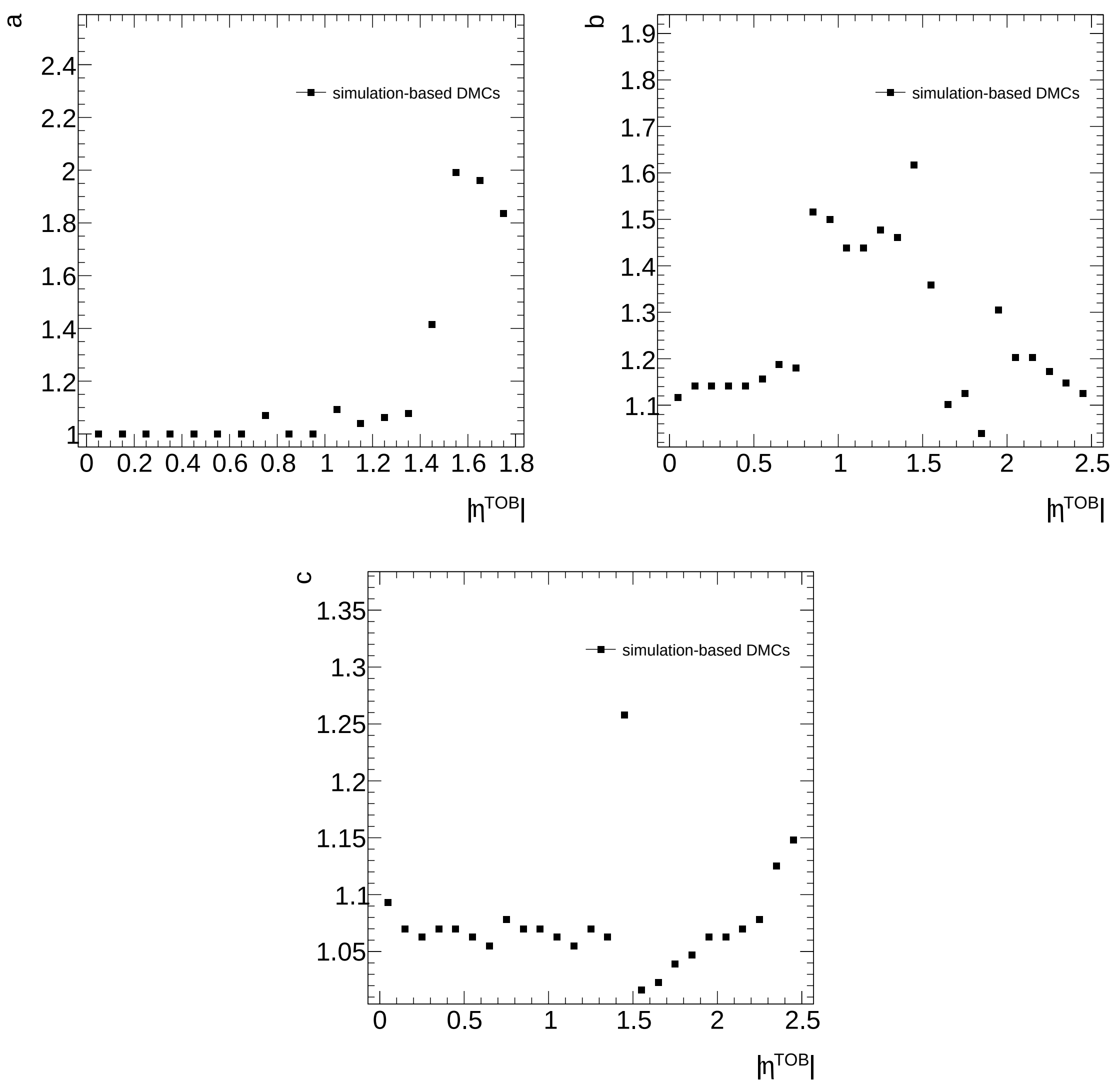

Figure 3.6.: Results for DMC parameters a (upper left), b (upper right) and c (bottom) as a function of the TOB $|\eta|$, derived using $Z \rightarrow e^{+}e^{-}$ simulated events.

in the eFEX is to bring the response closer to 1 in each bin. The mean response for corrected TOBs, shown in red in the plot, is closer to 1 in each 0.1 $|\Delta\eta^{TOB}|$ bin, and flatter as a function of η compared to the uncorrected response, shown in black. Thus, the DMCs reduce the discrepancy between the E_{T}^{TOB} calculated on the eFEX and the $p_{\mathrm{T}}^{\mathrm{off}}$ reconstructed offline by accounting for the varying response in the EM calorimeter layers as a function of η.

The effect of the DMCs on the trigger efficiency is also assessed, where this describes the performance of the online trigger selection with respect to the offline selection on reconstructed objects. This is calculated by dividing the number of events passing

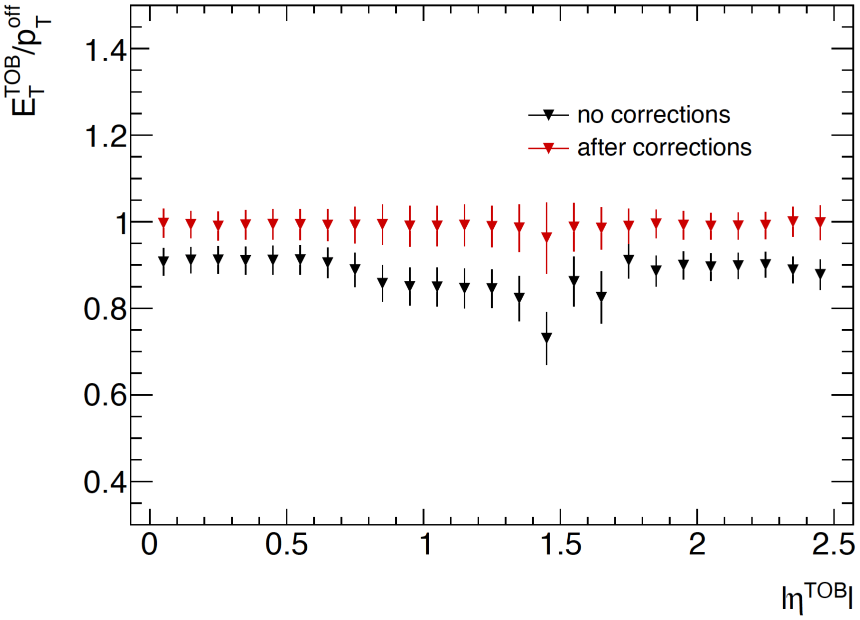

Figure 3.7.: Mean response $E_T^{TOB}/p_T^{\text{off}}$ per 0.1 $|\Delta\eta|$ bin, for TOBs with and without the dead material corrections to the E_T^{TOB}.

both the trigger and offline requirements, $E_T^{TOB} > 20$ GeV and $p_T^{\text{off}} >15$ GeV, to the number of events passing the offline requirement $p_T^{\text{off}} >15$ GeV, and is measured as a function of the offline electron p_T^{off}. The resulting trigger efficiency *turn-on curves* are shown in Figure 3.8, where a higher E_T^{TOB} threshold is used to calculate efficiencies for corrected TOBs ($E_T^{\text{corrected}}$). Since the DMCs increase the overall E_T^{TOB}, as seen in Figure 3.7, the threshold for the corrected E_T^{TOB} is chosen such that it produces the same rate as the uncorrected threshold, where the rates are calculated using multijet simulated samples. Although both curves appear to turn-on at the same p_T^{off} values, the DMC curve has higher efficiencies for p_T^{off} values beyond 25 GeV, demonstrating that the DMCs improve the trigger efficiency as well as the electron response.

3.2.2. Data-driven corrections

In this Section, data-driven DMC results are presented, where these are extracted using $\sqrt{s}$ = 13.6 TeVpp collision data from run 452843, recorded on 23 May 2023, and corresponding to an integrated luminosity of 857 pb^{-1}. An unbiased electron sample is selected from $Z \to e^+e^-$ events using the *tag-and-probe method* [97], which uses characteristic signatures of this known decay to select events, such as the presence of

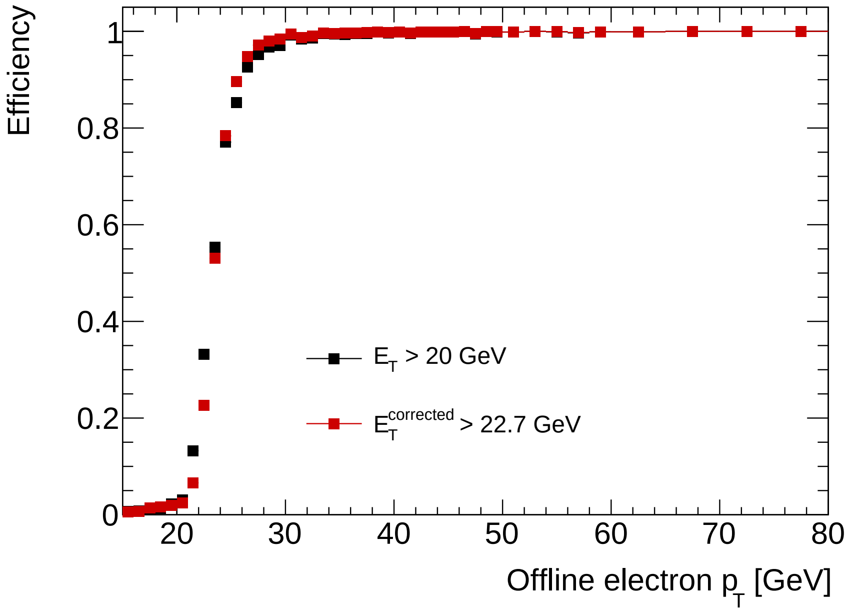

Figure 3.8.: Efficiency turn-on curves for TOBs with and without the DMCs, where the corrected E_{T}^{TOB} threshold is increased in order to match the rate for the uncorrected threshold.

two isolated electrons with invariant mass close to the Z boson mass. Strict selection criteria are applied to one of the electrons in the decay, called the *tag* electron, and the second *probe* electron is used for the measurement. Each valid combination of electron pairs in the event passing the tag and probe selection criteria are considered, in order not to bias the probe sample, such that an electron can be the tag in one pair and the probe in another pair.

Events are selected using the Phase-1 trigger item `L1_eEM26M`, which is the primary single electron trigger for the Phase-1 L1Calo trigger system. For this trigger item, e/γ candidates identified in the eFEX must satisfy $E_{\mathrm{T}}^{TOB} > 25$ GeV and must also pass a *medium* (M) working point for the isolation variables described in Section 3.1.1. Events are also required to have at least one primary vertex, defined as the vertex with the largest p_{T}^2 sum of tracks in the event [70].

At least two offline reconstructed electrons with $p_{\mathrm{T}} > 20$ GeV and $|\eta| < 2.47$ are required in each event, where both must satisfy the medium identification working point, as described in Section 2.3.2. The electrons must have opposite charge, and their invariant mass m_{ee} must be in the range 76.2 GeV $< m_{ee} <$ 106.2 GeV. Electrons must originate from the primary vertex by applying requirements on the longitudinal impact parameter z_0, and on the transverse impact parameter d_0, where these parameters are described in Section 2.3.1. Thus, electrons must satisfy $|z_0 \sin\theta| < 0.5$ mm, where θ is the polar angle, and $|d_0|/\sigma(d_0) < 5$, where $\sigma(d_0)$ is the estimated uncertainty on d_0.

Tag electrons are further required to satisfy tight identification criteria, and a loose isolation point, based on the calorimeter and track isolation variables described in Section 2.3.2. Both tag and probe electrons must be matched to a TOB in ΔR, satisfying $\Delta R < 0.15$. Additionally, the TOB matched to the tag electron must also satisfy the `L1_eEM26M` trigger criteria.

The sample of probe electrons are used to derive the DMC parameters a, b and c by minimising Eq. 3.6 in each 0.1 $|\Delta\eta^{TOB}|$ bin, following the same method described in Section 3.2.1. Figure 3.9 shows the DMC parameters extracted using data and the simulation-based parameters from Figure 3.6, where both sets of parameters have a similar η-dependence. The larger discrepancy between the simulation-based and data-driven a parameter values can be attributed to the smaller contribution of the pre-sampler E_{T} to the E_{T}^{TOB} calculation, compared to the first two layers.

The mean response as a function of $|\eta^{TOB}|$ is shown in Figure 3.10 for probe electrons from data with simulation-based, data-driven or no DMCs applied to the E_{T}^{TOB}. The data-driven corrections improve the response compared to the simulation-based corrections, where the response in each bin is closer to 1 and less dependent on the $|\eta^{TOB}|$. For the uncorrected TOBs, the same η-dependence as in the simulated electron sample (Figure 3.7) is observed.

Finally, the effect of both simulation-based and data-driven DMCs on the trigger efficiency is assessed using probe electrons from data, shown in Figure 3.11. The efficiency is calculated by dividing the number of probe electrons with TOBs satisfying a E_{T}^{TOB} threshold by the total number of probe electrons. For uncorrected TOBs, a 22 GeV E_{T}^{TOB} threshold is used, while for TOBs corrected by simulation-based and data-driven DMCs, the threshold is increased to 25 GeV to account for the effect of the DMCs on increasing the overall E_{T}^{TOB}. The turn-on curve for the data-driven DMCs shows the highest overall efficiency, followed by the simulation-based DMCs and the uncorrected TOB curves.

Following the improvement in trigger efficiency and response achieved by the data-driven DMCs over the simulation-based DMCs presented in this Section, the

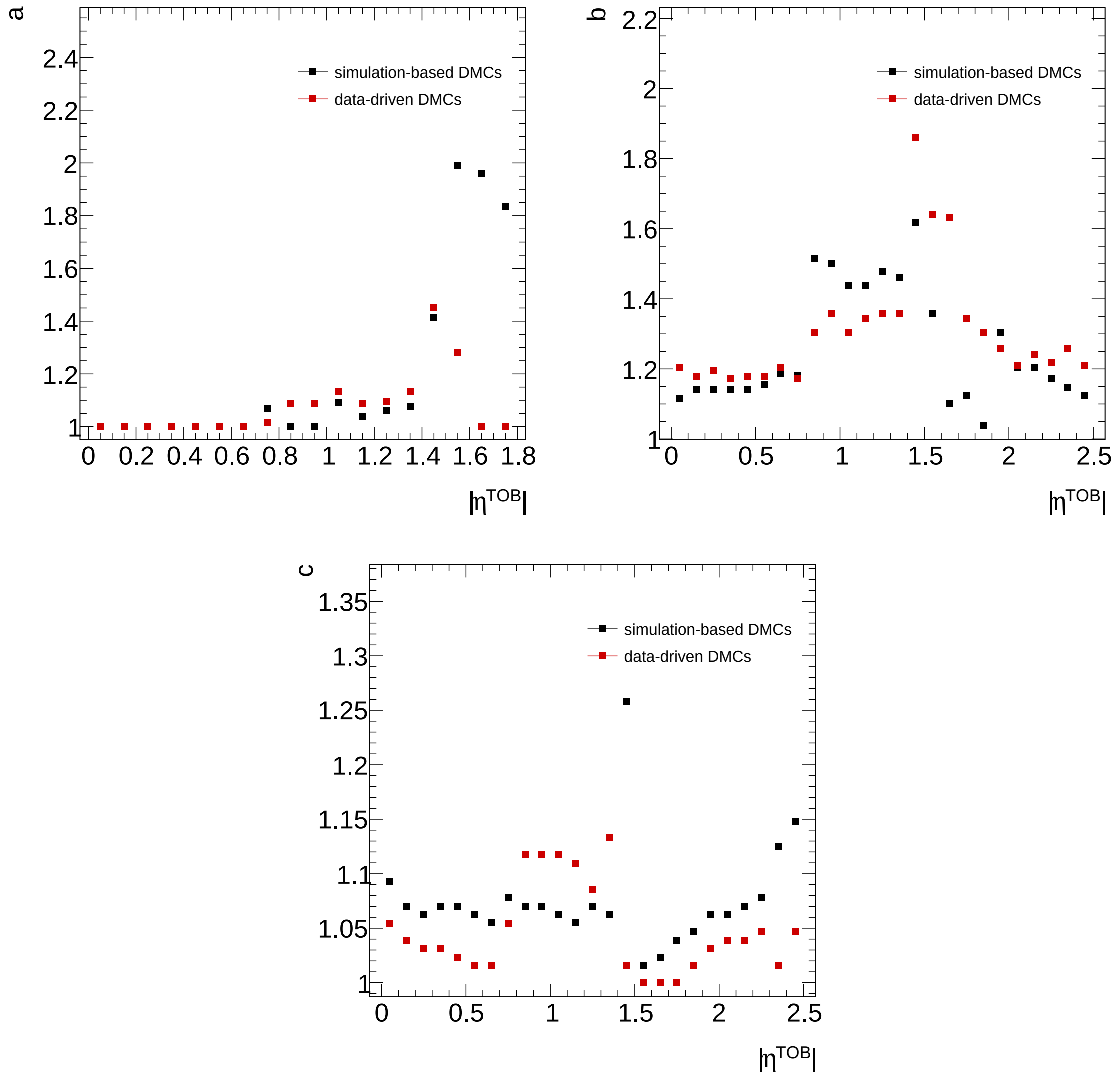

Figure 3.9.: Results for DMC parameters a (upper left), b (upper right) and c (bottom) as a function of the TOB $|\eta|$, derived using $Z \to e^+e^-$ events from data collected in early 2023 at $\sqrt{s} = 13.6$ TeV.

data-driven DMCs were added to the eFEX e/γ algorithm in July 2023 [3], replacing the simulation-based DMCs which were used during the commissioning of the eFEX in 2022 and early 2023.

---

[3] These corrections are subject to continuous tuning throughout the Run 3 data-taking period, so the actual values of the DMCs used in the eFEX at the time of writing may differ from those presented in this thesis.

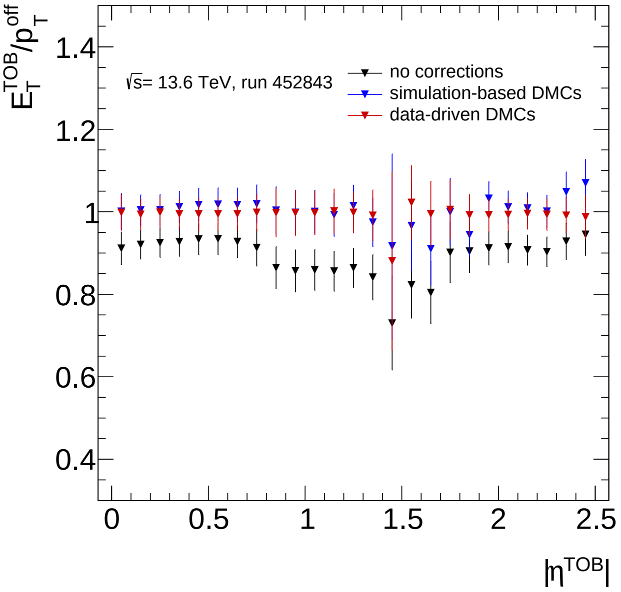

Figure 3.10.: Mean response E_T^{TOB}/p_T^{off} per 0.1 $|\Delta\eta|$ bin, before and after applying the simulation-based and data-driven DMCs shown in Figures 3.6 and 3.9, following the E_T^{TOB} calculation in Eq. 3.5.

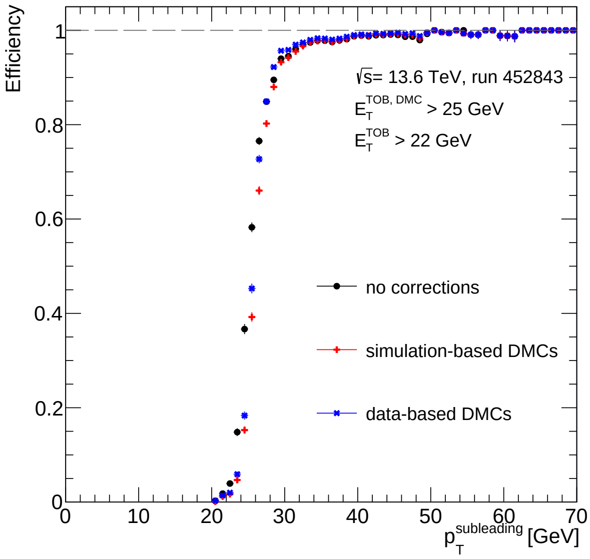

Figure 3.11.: Efficiency for simulation-based and data-driven DMCs compared to uncorrected TOBs as a function of the offline probe (or subleading) electron p_T. Different E_T^{TOB} thresholds are used in order to provide the same trigger rates for corrected and uncorrected TOBs.

3.3. L1 single EM object trigger performance

Figure 3.12 shows the efficiencies of L1 single EM object triggers for the Phase-1 system (`L1_eEM26M` and `L1_eEM26T`), compared to the corresponding legacy L1 single EM object trigger (`L1_EM22VHI`) efficiency as a function of the offline electron p_{T}. The trigger efficiencies are calculated using $Z \to e^{+}e^{-}$ events from pp collision data collected during 2023 at $\sqrt{s}$ = 13.6 TeV, selected using the tag-and-probe method described in Section 3.2.2. The Phase-1 and legacy triggers have equivalent E_{T} thresholds, which achieve 50% efficiency around 26 GeV [4]. For the Phase-1 triggers, a *medium* (M) and *tight* (T) working point is defined, representing different thresholds for the isolation variables R_{η}, R_{had} and $w_{\mathrm{s,tot}}$, which have been optimised using data during the commissioning period of the eFEX [98]. Additionally, the data-driven DMCs presented in Section 3.2.2 are used by the Phase-1 trigger items to compensate for the varying response in the different calorimeter layers. For the legacy trigger item, the suffix `V` represents that the p_{T} threshold varies with trigger object η to account for energy loss, and `HI` indicates that hadronic and electromagnetic isolation criteria are applied. Both Phase-1 trigger items have higher overall efficiencies than the legacy trigger item, reaching a plateau at lower p_{T} values. Additionally, the `L1_eEM26M` Phase-1 item has a trigger rate of 26.5 kHz, which is approximately 5 kHz smaller than the `L1_EM22VHI` legacy trigger item, which has a trigger rate of approximately 32.5 kHz. The `L1_eEM26T` Phase-1 item has a trigger rate of 23.5 kHz. As a result of this improved performance, the L1 EM trigger items provided by the legacy system were deactivated on 11 May 2023, and are now provided by the Phase-1 eFEX instead, thus completing its commissioning period [99].

---

[4] For legacy triggers, the number in the trigger name after "EM" represents the E_{T} threshold in GeV applied to the TOB, while for Phase-1 triggers, this represents the value in GeV at which 50% efficiency is achieved.

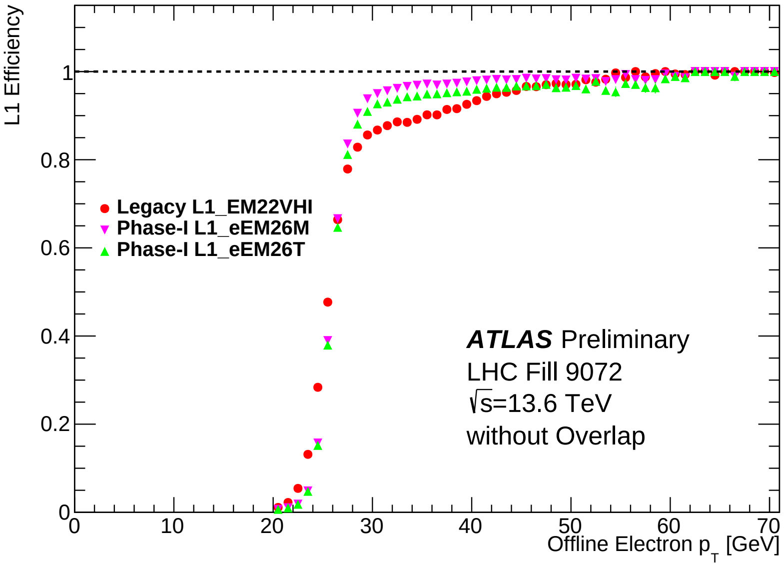

Figure 3.12.: Efficiencies of L1 single EM object triggers for the Phase-1 system (`L1_eEM26M` and `L1_eEM26T`), compared to the corresponding legacy L1 single EM object trigger (`L1_EM22VHI`) efficiency as a function of the offline electron p_T [99].

Chapter 4.

Measurement of the W and Z Boson Cross Sections

The inclusive production cross section measurement of W and Z bosons is one of the benchmark measurements performed at a new energy regime, in order to provide early validation for the detector performance and reconstruction techniques, and to validate theory predictions for the new centre-of-mass energy. The large production cross sections of these processes, together with the clean experimental signatures achieved through their leptonic decays, allow an excellent experimental precision reaching the percent level, and in the case of the cross-section ratios, the sub-percent level. Similar measurements have been previously performed by ATLAS at centre-of-mass energies of 2.76 TeV [100], 5 TeV [101], 7 TeV [102], 8 TeV [103, 104], and 13 TeV [105, 106].

In this chapter, an overview of the measurement of the inclusive fiducial and total cross sections of $W^+ \to \ell^+\nu$, $W^- \to \ell^-\bar{\nu}$, $Z \to \ell^+\ell^-$ and their ratios are presented [1], including the data and simulated samples used in the analysis, the event selection, theoretical predictions and the systematic uncertainties.

This analysis uses a data sample of proton-proton collisions corresponding to 29 fb^{-1}, recorded by the ATLAS detector at $\sqrt{s} = 13.6$ TeV, during the beginning of Run 3 in 2022. The results for the fiducial cross section for $Z \to \ell^+\ell^-$ production from this analysis have been published together with the top quark-antiquark pair $t\bar{t}$ production cross section and their ratio in Ref. [107]. The ratios between $t\bar{t}$ and $W^\pm$-boson fiducial cross sections are also measured, where the $t\bar{t}$ results used in this measurement are obtained from the result in Ref. [107].

The data-driven multijet background estimation for the W-boson channels is presented in Chapter 5, and the results for this analysis are presented in Chapter 6, where they are also compared to theoretical predictions at $\sqrt{s} = 13.6$ TeV.

4.1. Cross Section Measurement Methodology

Cross section measurements are most often restricted to a fiducial phase space to limit the influence of the geometric and kinematic acceptance of the detector, to enhance the signal contribution over that of background processes, and to reduce the respective systematic uncertainties. The cross section measurement for W and Z boson inclusive production is performed in a fiducial phase space defined by the selection summarised in Table 4.1, where the transverse momentum of the neutrino, p_{T}^{ν}, can be inferred from the missing transverse momentum in the event.

Table 4.1.: Fiducial selection requirements for the inclusive W and Z boson production measurement.

	$pp \to \ell^+\ell^-$	$pp \to \ell^-\bar{\nu}_\ell$ / $pp \to \ell^+\nu_\ell$
Lepton p_{T}	$p_{\mathrm{T}} > 27$ GeV	$p_{\mathrm{T}} > 27$ GeV
Lepton η	$\lvert\eta\rvert < 2.5$	$\lvert\eta\rvert < 2.5$
Mass	$66 < m_{\ell\ell} < 116$ GeV	$m_{\mathrm{T}}^{W} > 50$ GeV
Neutrino p_{T}	-	$p_{\mathrm{T}}^{\nu} > 25$ GeV

The transverse mass of the W boson, m_{T}^{W}, is defined as

$$m_{\mathrm{T}}^{W} = \sqrt{2 p_{\mathrm{T}}^{\nu} p_{\mathrm{T}}^{\ell} (1 - \cos \Delta\phi^{\ell\nu})}, \tag{4.1}$$

where p_{T}^{ν} and p_{T}^{ℓ} are the transverse momenta of the neutrino and lepton from the W-boson decay, and $\Delta\phi^{\ell\nu}$ is the opening angle between the neutrino and the lepton in the azimuthal plane.

The fiducial cross section is then calculated as

$$\sigma^{\text{fid}} = \frac{\mathrm{N}_{\text{data}} - \mathrm{N}_{\text{bkg}}}{\mathcal{L} \cdot \mathrm{C}}, \tag{4.2}$$

where N_{data} is the number of observed candidate events, N_{bkg} is the expected number of background events, $\mathcal{L}$ is the integrated luminosity of the dataset and C is the correction factor which accounts for the selection efficiency at the reconstruction level and detector resolution effects. C is defined as the number of events which pass the final analysis event selection to the number of events at generator level within the fiducial volume, and is calculated using simulations.

The total cross section, σ^{tot}, can then be calculated by dividing the fiducial cross section, σ^{fid}, by the acceptance A, which is defined as the number of generator level events that pass the fiducial selection to the total number of events generated in the entire phase space, and is also calculated using simulations:

$$\sigma^{\text{tot}} = \sigma^{\text{fid}} / A. \tag{4.3}$$

The correction and acceptance factors are defined at *Born level*, before leptons emit photons via QED final state radiation [108].

For this measurement, the W and Z fiducial cross sections are extracted using the profile likelihood method [109]. Using this technique, systematic uncertainties are included as part of the likelihood and *profiled* during the fit to the data, as described in Section 4.1.1.

4.1.1. Profile Likelihood Method

The *likelihood* is a quantity that can describe the probability of the data given a hypothesis [110]. For measurements at the LHC, the hypothesis is most often the Standard Model and the data are usually represented in the form of a binned histogram of an observable. The hypothesis is formulated as a probability model in terms of the observable, where in the case of a binned histogram each bin may be thought of as an independent counting experiment so that the probability model is described by a product of Poisson distributions. In each bin, the expected number of events is given by adding the expected number of signal and background events, estimated using simulation or a data-driven method. The likelihood is defined in terms of a parameter of interest (POI), which is the parameter to be inferred from the data. In this measurement, the POI is the signal strength, μ, defined as the ratio between the measured fiducial cross section and the cross section from the theoretical prediction, $\sigma^{\text{fid}}_{\text{meas}}/\sigma^{\text{fid}}_{\text{pred}}$, such that a value $\mu = 1$ implies that the measured result is in perfect agreement with the Standard Model prediction.

Systematic uncertainties that affect the modelling of the distribution of the observable are introduced in the likelihood as a set of nuisance parameters (NPs), $\vec{\theta}$, whose values are unknown and must be estimated during the fit to the data. Nuisance parameters are not of intrinsic interest but are included in the likelihood such that there is at least one point in the parameter space for which the likelihood describes the data with sufficient accuracy. These are parametrised such that each systematic uncertainty is associated with one or more NPs, and constrained by Gaussian terms, $G(\theta_i)$ [1], where the initial values of these terms are usually based on an auxiliary measurement.

Thus, the likelihood can be written as

$$L(\vec{n};\mu,\vec{\theta}) = \prod_{b\in\text{bins}} \text{Pois}(n_b|\mu S_b(\vec{\theta}) + B_b(\vec{\theta})) \prod_{i\in\text{NPs}} G(\theta_i)\,, \tag{4.4}$$

where $\vec{n}$ is the data vector, n_b is the number of data events observed in each bin, and S_b and B_b are the number of expected signal and background events in each bin, which depend on the nuisance parameters $\vec{\theta}$. Thus, the likelihood comprises two parts: the response model for the physics measurement, which describes the signal and background distributions for each value of μ and $\vec{\theta}$, and the component due to the subsidiary measurement of the nuisance parameters.

Then, according to the maximum likelihood method, the best estimate of μ is obtained by maximising the likelihood $L(\vec{n};\mu,\vec{\theta})$ from Eq. (4.4) with respect to the parameter of interest μ and the nuisance parameters $\vec{\theta}$ [110]. Depending on the sensitivity of the likelihood to the systematic uncertainties, and in turn to the NPs which parametrise these, the data may constrain these during the fit.

---

[1] Nuisance parameters which account for the statistical uncertainties of the binned histograms used to build the signal and background model can also be included as Poisson constraints on each bin.

For this analysis, all profile likelihood models are implemented using the `TREx` statistical analysis framework [111], which is based on the `HistFactory` framework [112].

4.2. Data and Simulation Samples

4.2.1. Data

Data used in these measurements correspond to a luminosity of 29.0 ± 0.6 fb^{-1} [113], and were recorded between the 6th of August and 27th of November in 2022. The luminosity measurement was performed using the LUCID-2 detector [114], based on the methodology detailed in Ref. [49]. Events must pass data-quality requirements by checking the corresponding luminosity blocks are on the “Good Run List", which keeps a record of the detector status during data-taking [115].

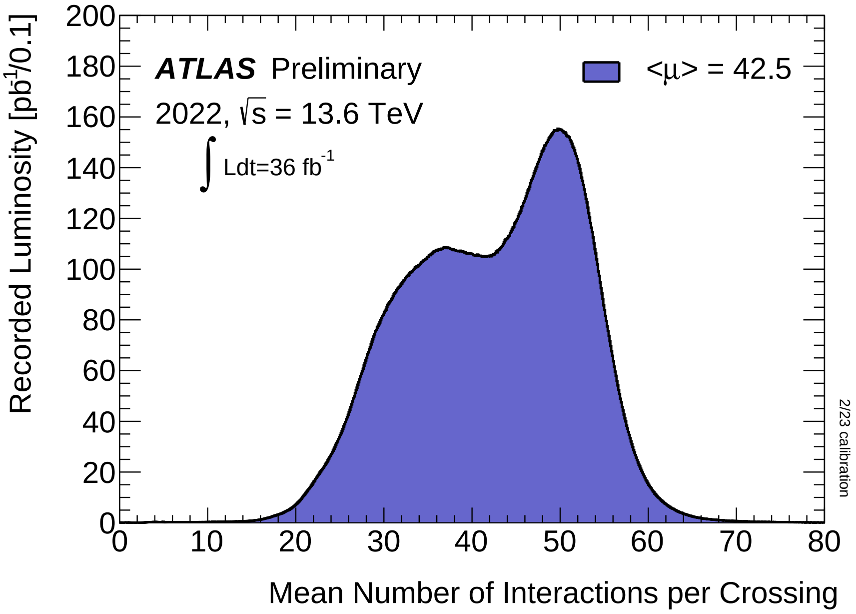

Figure 4.1.: Distribution of the mean number of interactions per bunch crossing, weighted to the luminosity, for pp collision data at $\sqrt{s} = 13.6$ TeV collected in 2022 [51].

The distribution of the mean number of interactions per bunch crossing $\langle\mu\rangle$ for the data recorded in 2022 is shown in Figure 4.1, where the average $\langle\mu\rangle = 42.5$.

As this is data recorded early during Run 3, it can be useful to assess the stability as a function of time, which can be measured using the event selection efficiency

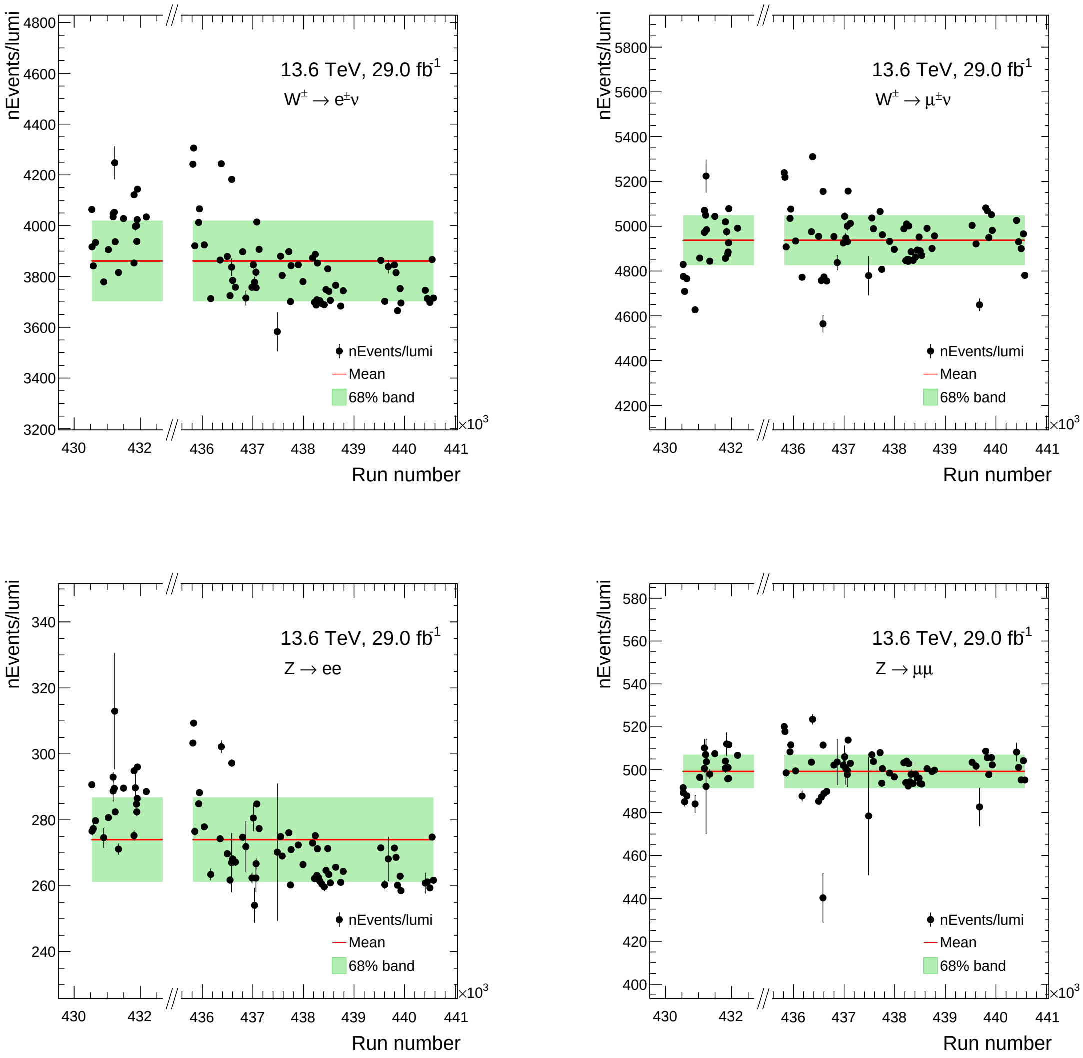

Figure 4.2.: Number of events in the (a) $W^\pm \to e^\pm\nu$, (b) $W^\pm \to \mu^\pm\nu$, (c) $Z \to ee$ and (d) $Z \to \mu\mu$ channels per run number, normalised to the luminosity of the corresponding run. The error bars show the statistical uncertainty and the green band contains 68% of all points centred around the mean. The break in the x-axis is introduced to remove the large gap due to run numbers which are not used for physics analysis.

as a function of time, and a flat distribution represents stability in the data-taking conditions. This is done by measuring the ratio between the number of events passing the event selection[2] for the $W^\pm \to e^\pm\nu$, $W^\pm \to \mu^\pm\nu$, $Z \to e^+e^-$ and $Z \to \mu^+\mu^-$ channels, and the ATLAS luminosity measurement. Figure 4.2 shows the data stability

---

[2] The full event selection is presented in Section 4.3.

as a function of the run number, where the spread of these values is estimated by the 68^{th} percentile of all points closest to the mean, shown as a green band.

Overall, the luminosity-normalised event yield appears to be stable as a function of the run number; however, there is some discrepancy observed between earlier and later runs in the electron channels $W^{\pm} \rightarrow e^{\pm}\nu$ and $Z \rightarrow e^{+}e^{-}$. The discrepancy may be explained by the difference in the running conditions, especially the pile-up, which was lower in earlier runs. A similar trend was observed in the data stability study done at the beginning of Run 2 [116], as the trigger and reconstruction efficiencies are more pile-up-dependent for electrons than for muons, and corrections for these efficiencies were calculated using data in units of luminosity blocks (LBs) [3] in order to reflect the time evolution of actual data-taking conditions. For this measurement done on the early Run 3 data, no such corrections were applied to the data as these recommendations were not yet available.

4.2.2. Signal and Background Modelling

Simulated Monte Carlo (MC) event samples are used in this analysis to optimise the event selection, estimate the backgrounds, and perform the signal-extraction fit.

W and Z boson samples were simulated using the SHERPA 2.2.12 [117] generator, using the next-to-leading order (NLO) matrix element (ME) for up to two partons, and leading order (LO) matrix element for up to five partons. These were calculated using the COMIX [117] and OPENLOOPS [118–120] libraries. The MEs were matched with the SHERPA parton shower [121] using the MEPS@NLO prescription [122] in order to avoid double-counting emissions, using the set of tuned parameters developed by the SHERPA authors. The NNPDF3.0NNLO PDF set [123] was used for these samples. Additionally, the samples were normalised to a NNLO prediction [124].

Diboson samples were simulated using the SHERPA 2.2.12 generator, including contributions from Higgs boson and off-shell effects added where appropriate. The MEs were generated at NLO accuracy in QCD for up to one additional parton emission, and at LO accuracy for up to three additional parton emissions, for semi-leptonic and fully leptonic final states. Semi-leptonic final states include one boson decaying hadronically and the other leptonically. Since no dedicated calculation for the cross

---

[3] A luminosity block is a period of time, usually 60 s, during which instantaneous luminosity, detector and trigger configuration and data quality conditions are considered constant [115].

section at 13.6 TeV is available at the time of writing, the same k-factors [4] as used in Run 2 analyses, evaluated to be 0.91, are used for the Run 3 analysis normalisation.

The production of a top-quark pair $t\bar{t}$ and the associated production of a single top-quark and a W boson, Wt, were modelled using the POWHEG BOX V2 generator interfaced to PYTHIA 8.307 with the parton shower tune A14 [125]. The MEs are calculated at NLO precision in QCD using the NNPDF3.0NLO PDF set. The $t\bar{t}$ sample was normalised to the cross-section prediction at NNLO in perturbative QCD, including the resummation of next-to-next-to-leading logarithmic (NNLL) soft-gluon terms calculated using TOP++[2.0] [126–132].

The simulated samples used in this analysis are summarized in Tables 4.2- 4.3, where three categories are defined for the simulated W and Z boson samples, which are filtered according to their b hadron and c hadron content at the particle level.

The effect of pile-up was modelled by overlaying [137] the simulated hard-scattered events with inelastic pp events, simulated using EPOS 2.0.1.4 [138, 139] and the EPOS LHC tune, and PYTHIA 8.307 using the NNPDF 2.3 LO PDF set [140] and the A3 tune [141]. The effect of the detector response was simulated by the GEANT4 toolkit [95], including the full simulation of the ATLAS detector [96]. Finally, all simulated samples were processed with the same software framework as the data [142].

The simulated samples are produced before data-taking with a best estimate of data pile-up conditions. Therefore, it is necessary to reweight the pile-up distribution of simulated samples to improve the agreement between data and MC on the actual pile-up distribution $\langle\mu\rangle$, as shown in Figure 4.1. The pile-up weight for a simulated event is calculated with the default pile-up profile used to generate the simulated samples, and the actual $\langle\mu\rangle$ in data runs included in the analysis.

4.3. Event Selection

The event selection is described in this Section, where events are categorised in two Z boson channels, $Z \rightarrow e^+e^-$ and $Z \rightarrow \mu^+\mu^-$, and four W boson channels, $W^+ \rightarrow e^+\nu$, $W^- \rightarrow e^-\bar{\nu}$, $W^+ \rightarrow \mu^+\nu$, and $W^- \rightarrow \mu^-\bar{\nu}$. The pre-selection is described

---

[4] k-factors are multiplicative correction factors applied to theoretical predictions to account for higher order effects beyond the order to which the calculation was performed.

Table 4.2.: Simulated W and Z samples used in this analysis. The `BFilter` category contains events with at least one b quark per event, `CFilterBVeto` contains events with at least one c quark while vetoing any b quarks, and `CVetoBVeto` contain neither b or c quarks in the event.

Channel	Filter	$\sigma \cdot$ BR [pb]	k-factor	Generator
$W^{\pm} \rightarrow e\nu$	`BFilter`	220.132	0.9059	SHERPA2.2.12 [117]
	`CFilterBVeto`	3402.25	0.9059	
	`CVetoBVeto`	19290.2	0.9059	
$W^{\pm} \rightarrow \mu\nu$	`BFilter`	218.007	0.9059	SHERPA2.2.12 [117]
	`CFilterBVeto`	3411.47	0.9059	
	`CVetoBVeto`	19326.7	0.9059	
$W^{\pm} \rightarrow \tau\nu$	`BFilter`	220.519	0.9059	SHERPA2.2.12 [117]
	`CFilterBVeto`	3411.31	0.9059	
	`CVetoBVeto`	19337.6	0.9059	
$Z \rightarrow ee$	`BFilter`	59.841	0.9340	SHERPA2.2.12 [117]
	`CFilterBVeto`	303.25	0.9340	
	`CVetoBVeto`	1974.0	0.9340	
$Z \rightarrow \mu\mu$	`BFilter`	58.688	0.9340	SHERPA2.2.12 [117]
	`CFilterBVeto`	304.48	0.9340	
	`CVetoBVeto`	1974.2	0.9340	
$Z \rightarrow \tau\tau$	`BFilter`	59.655	0.9340	SHERPA2.2.12 [117]
	`CFilterBVeto`	302.53	0.9340	
	`CVetoBVeto`	1971.0	0.9340	

Table 4.3.: Simulated electroweak and top background samples used in this analysis. For the Wt associated production samples, OS denotes "opposite sign" charged leptons in the final state, while SS denotes "same-sign" charged leptons.

Channel	$\sigma \cdot$ BR [pb]	k-factor	Generator
$t\bar{t}$ (1ℓ)	355.63972	1.1381	POWHEGBOX v2 [133–135] + PYTHIA 8.307 [136]
$t\bar{t}$ (2ℓ)	85.482	1.1381	
$\bar{t}$ (t-channel)	24.203	1.0858	POWHEGBOX v2 [133–135] + PYTHIA 8.307 [136]
t (t-channel)	39.936	1.1066	
$\bar{t}$ (s-channel)	1.3525	1.0872	
t (s-channel)	2.1455	1.0963	
$W\bar{t}$	39.839	1.10269	
Wt	39.876	1.10269	
$WW \to \ell\nu qq$	51.226	0.91	SHERPA2.2.12 [117]
$WZ \to \ell\nu bb$	2.5961	0.91	
$WZ \to \ell\nu qq$	9.2309	0.91	
$WZ \to qq\ell\ell$	3.5549	0.91	
$ZZ \to bb\ell\ell$	0.4986	0.91	
$ZZ \to qq\ell\ell$	1.7741	0.91	
$ZZ \to \ell\ell\ell\ell$	1.3351	0.91	
$WZ \to \ell\ell\ell\nu$	4.8181	0.91	
$\ell\ell\nu\nu$ OS	12.618	0.91	
$\ell\ell\nu\nu$ SS	0.0241	0.91	
$WZ \to \ell\nu\nu\nu$	3.289	0.91	

in Section 4.3.1, followed by the selection applied on the different physics objects relevant to this analysis, including electrons in Section 4.3.2, muons in Section 4.3.3, jets in Section 4.3.4 and missing transverse momentum in Section 4.3.5. The overlap removal procedure is described in Section 4.3.6, followed by the W boson selection in Section 4.3.7, and the Z boson selection in Section 4.3.8. Finally, the selection criteria for the two top-antitop quark pair channels relevant for the calculation of the $t\bar{t}$ and $W^{\pm}$-boson fiducial cross section ratios is described briefly in Section 4.3.9. The event selection is also summarised in Table 4.4.

Table 4.4.: Overview of the event selection for the W and Z bosons.

	Electron selection
p_{T}	$p_{\mathrm{T}} > 27\,\mathrm{GeV}$
η	$\lvert\eta\rvert < 2.47$ and veto $1.37 < \lvert\eta\rvert < 1.52$
ID	Tight
Isolation	Tight_VarRad
	Muon selection
p_{T}	$p_{\mathrm{T}} > 27\,\mathrm{GeV}$
η	$\lvert\eta\rvert < 2.5$
ID	Medium
Isolation	Tight_VarRad
	W boson selection
N leptons	exactly 1
$E_{\mathrm{T}}^{\mathrm{miss}}$	$E_{\mathrm{T}}^{\mathrm{miss}} > 25\,\mathrm{GeV}$
m_{T}^{W}	$m_{\mathrm{T}}^{W} > 50\,\mathrm{GeV}$
	Z boson selection
N leptons	exactly 2 same flavour opposite charged leptons
$m_{\ell\ell}$	$66 < m_{\ell\ell} < 116\,\mathrm{GeV}$

4.3.1. Pre-selection

Events are selected using single-lepton (electron or muon) triggers, as shown in Table 4.5. As described in Section 2.2.4, a trigger chain is composed of a set of algorithms

Table 4.5.: A list of single electron and muon triggers used in the analysis. A logical OR is applied between the triggers.

Electron triggers	Muon triggers
HLT_e26_lhtight_ivarloose_L1EM22VHI	HLT_mu24_ivarmedium_L1MU14FCH
HLT_e60_lhmedium_L1EM22VHI	HLT_mu50_L1MU14FCH
HLT_e140_lhloose_L1EM22VHI	

performed in several steps, where selection criteria are applied on the output of these algorithms.

Trigger chain names begin with the algorithms and selection performed by the HLT system, starting with the p_{T} threshold applied on the physics object, and followed by the identification and isolation criteria. This is followed by the *L1 item*, which similarly describes the same set of selection criteria. For the lowest threshold electron trigger, `HLT_e26_lhtight_ivarloose_L1EM22VHI`, the `e26` denotes a $p_{\mathrm{T}} > 26$ GeV threshold on the electron object reconstructed at the HLT level. The electron must pass the `lhtight` identification, reconstructed using a similar algorithm to that described in Section 2.3.2, and the `ivarloose` isolation working point requires a variable cone size loose isolation $p_{\mathrm{T}}^{\mathrm{varcone20}}/E_{\mathrm{T}} < 0.1$. The lowest threshold muon trigger, `HLT_mu24_ivarmedium_L1MU14FCH`, has a $p_{\mathrm{T}} > 24$ GeV threshold on the muon reconstructed at HLT level. The `ivarmedium` isolation working point requires $p_{\mathrm{T}}^{\mathrm{varcone30}}/p_{\mathrm{T}} < 0.07$. All electron triggers contain the `L1EM22VHI` L1 items, which have a p_{T} threshold of 22 GeV applied to the trigger object reconstructed at the L1Calo level, as described in Section 3.1. The `V` suffix represents that the p_{T} threshold varies with trigger object η to account for energy loss, and `HI` indicates that hadronic and electromagnetic isolation criteria are applied. The muon trigger L1 items, `L1MU14FCH`, indicate a p_{T} threshold of 14 GeV on the trigger object, and require a coincidence between all three wheels in the end-cap of the MS trigger chambers (“**F**ull-station”), additional coincidence between outer TGC and one of inner muon detectors if available (“inner-**C**oincidence”), and only consider events which have a good magnetic field flag (“**H**ot-RoI mask”).

The single-lepton triggers differ in their requirements on the object identification, isolation and p_{T}. Triggers with lower p_{T} requirements impose tighter identification and isolation criteria, since these are responsible for most of the trigger rate, while the triggers with higher p_{T} threshold require looser (or no) identification and isolation criteria, and are added in order to recover efficiency losses at higher momenta [67]. A logical OR is applied between the triggers, such that events can be selected either via electron or muon triggers.

Events are also required to have at least one primary vertex, defined as the vertex with the largest p_{T}^2 sum of tracks in the event [70].

4.3.2. Electron selection

To operate in the efficiency plateau regime of the triggers, events are required to have electrons with transverse momenta $p_{\mathrm{T}} > 27$ GeV. Additionally, the electrons that "fired" the trigger are required to have the object reconstructed offline and object reconstructed online at the trigger level matched in $(\eta - \phi)$ space. Following this, electrons are required to pass the tight identification criteria [72], in order to match the identification requirement applied at the trigger level, and fall within the geometrical acceptance of the electromagnetic calorimeter for which electrons can be reconstructed accurately, $|\eta| < 2.47$, excluding the transition region $1.37 < |\eta| < 1.52$.

Electrons must originate from the primary vertex by applying requirements on the longitudinal impact parameter z_0, and on the transverse impact parameter d_0, where these parameters are described in Section 2.3.1. Thus, electrons must satisfy $|z_0 \sin\theta| < 0.5$ mm, where θ is the polar angle, and $|d_0|/\sigma(d_0) < 5$, where $\sigma(d_0)$ is the estimated uncertainty on d_0.

In order to select electrons from the prompt decays of W and Z bosons, isolation criteria are applied on calorimeter and track isolation variables, as defined in Section 2.3.2. The Tight_VarRad working point is used, which requires $p_{\mathrm{T}}^{\mathrm{varcone30}}/p_{\mathrm{T}} < 0.06$ and $E_{\mathrm{T}}^{\mathrm{cone20}}/p_{\mathrm{T}} < 0.06$.

Scale factors (SFs) accounting for discrepancies between data and simulation in the efficiencies for the trigger, reconstruction, identification and isolation of electrons are derived and applied to the simulated events. These are expressed as efficiency ratios between the data and simulation, and are parametrised in terms of the electron η and E_{T}.

4.3.3. Muon selection

Following similar arguments, muons are required to have transverse momenta $p_{\mathrm{T}} > 27$ GeV, where the offline muon must be matched in $(\eta - \phi)$ space with the muon trigger object. Muons must then pass the medium identification criteria [143], matching the selection applied at the trigger level, and fall within the geometrical acceptance of the muon spectrometer trigger chambers, $|\eta| < 2.4$.

Muons must originate from the primary vertex by applying similar requirements as for electrons, where they must satisfy $|z_0 \sin\theta| < 0.5$ mm and $|d_0|/\sigma(d_0) < 3$.

Isolation criteria are also applied to select prompt muons, where the Tight_VarRad working point is used, requiring $p_{\mathrm{T}}^{\mathrm{varcone30}}/p_{\mathrm{T}} < 0.04$ and $E_{\mathrm{T}}^{\mathrm{cone20}}/p_{\mathrm{T}} < 0.15$.

Similarly to electrons, SFs accounting for the discrepancy between data and simulation in muon trigger, identification, isolation and track-to-vertex-association (TTVA) efficiencies are applied to the simulation. These are derived using derived using $Z \to \mu^+\mu^-$ events in data and simulation.

4.3.4. Jet selection

Jets are reconstructed by means of a particle flow algorithm [85], using both calorimeter and ID information and calibrated as described in Section 2.3.4. Selected jets are required to have $p_{\mathrm{T}} > 20$ GeV for $|\eta| < 2.5$ and $p_{\mathrm{T}} > 30$ GeV for $2.5 < |\eta| < 4.5$. Furthermore, jets with $p_{\mathrm{T}} < 60$ GeV are required to satisfy a neural-network-based jet vertex tagger (NNJVT) discriminant in order to reduce contamination from pile-up jets. Jets passing these criteria are then used in the reconstruction of the missing transverse momentum, described in Section 4.3.5.

4.3.5. Missing transverse momentum

The missing transverse momentum $\boldsymbol{p}_{\mathrm{T}}^{\mathrm{miss}}$, with magnitude E_{T}^{miss}, is calculated as the negative sum of the transverse momenta of all hard objects considered in the final states (electrons, muons and jets), and an additional term including soft contributions from tracks and calorimeter clusters not included in the hard object calculation [89]. A detailed description of the missing transverse momentum reconstruction is provided in Section 2.3.5.

In the definition of the jet term in the $\boldsymbol{p}_{\mathrm{T}}^{\mathrm{miss}}$ summation, several working points are defined with different p_{T} requirements on jets in the forward ($2.5 < |\eta| < 4.5$) region of the detector where pile-up jets are more common. Thus, tighter working points reduce the contamination from pile-up jets and the dependency of the E_{T}^{miss} on pile-up. For this analysis, the default tight working point has been selected, which was found to improve the E_{T}^{miss} resolution in the W boson channels with respect to the loose working point [89].

4.3.6. Overlap removal

An overlap removal procedure is applied to remove either duplicates, in the case where a physics object is reconstructed as two different objects, or deal with two separate but close-by objects, which would affect the reconstruction performance if both are kept in the event [144].

The procedure only involves objects considered in this analysis, ie. electrons, muons and jets. A separate overlap removal procedure is applied internally in the missing transverse momentum reconstruction, which takes into account the overlap between leptons and jets. Considering electrons, muons and jets which pass the selection criteria described in the previous sections, including isolation, the following steps are applied for overlap removal:

1. Any jet found within $\Delta R < 0.2$ of an electron is removed;
2. Any electron subsequently found within $\Delta R < 0.4$ of a jet is removed;
3. Any jet with less than three tracks associated to it found within $\Delta R < 0.2$ of a muon is removed;
4. Any muon subsequently found within $\Delta R < 0.4$ of a jet is removed.

The first step removes jets which are also reconstructed as electrons, since the electron clusters and bremsstrahlung radiation should be contained within a cone $\Delta R < 0.2$, while the second step removes electrons which would reduce the reconstruction efficiency for both the jet and electron if both are kept. The last two steps deal with muon-jet overlap removal, where the aim is to separate prompt muons from muons originating from the decay of hadrons within a jet and to remove jets produced by final state radiation or bremsstrahlung photons being emitted from a high-energy muon. The third step in the overlap procedure removes the latter type of jet, that can be characterised by a very small number of ID tracks. The final step then removes muons from decays within heavy flavour jets.

No overlap removal is applied to the Z boson selection, as jets are not used in the final state.

4.3.7. W boson selection

For the W boson selection, events are required to have exactly one identified and isolated lepton, with missing transverse momentum magnitude $E_{\mathrm{T}}^{miss} > 25$ GeV and a transverse mass $m_{\mathrm{T}}^{W} > 50$ GeV.

4.3.8. Z boson selection

For the Z boson selection, events with two leptons of opposite sign and same flavour are selected, where the leptons must pass the identification and isolation criteria. Furthermore, the di-lepton invariant mass must be in the range $66 < m_{\ell\ell} < 116\,\mathrm{GeV}$.

4.3.9. Top-antitop quark pair selection

The $t\bar{t}$ event selection, described in further detail in Ref. [107], includes the presence of exactly one electron and muon of opposite charge, and one or two b-tagged jets. The DL1d algorithm [88] is used for b-tagging, which operates at the 77% efficiency working point. The electron and muon selection applied for $t\bar{t}$ events in Ref. [107] is identical to that described for this analysis, in order to facilitate calculating the ratios betwen the $t\bar{t}$ and $W^{\pm}$-boson fiducial cross sections, discussed in Chapter 6.

4.4. Background estimation

Background contributions to the W and Z final states correspond to two main categories: electroweak (EW) and top processes, estimated using simulations, and the multijet (MJ) background, which is derived using data-driven techniques. The expected background event yields together with signals are shown in Tables 4.9 and 4.10 in Section 4.7.

4.4.1. Electroweak and top backgrounds

The EW backgrounds include single boson productions, $W^{\pm} \rightarrow \tau^{\pm}\nu$ and $Z \rightarrow \tau\tau$ for both channels, $Z \rightarrow ee$ and $Z \rightarrow \mu\mu$ for the W channels and $W^{\pm} \rightarrow e^{\pm}\nu$ and $W^{\pm} \rightarrow \mu^{\pm}\nu$ for the Z channels. In particular for W processes, the Z boson background is expected from events where one lepton is selected and one lepton fails the selection requirements. Events from diboson production, WW, WZ and ZZ can have similar signatures to W or Z events if one of the bosons decays hadronically or invisibly or if leptonic decay products fail the object selection. Likewise, $t\bar{t}$ and associated Wt production can result in similar signatures to W or Z events if one or two of the W bosons decay leptonically. Due to the lower production cross-section of these processes compared to the single W or Z boson production, their contribution is expected to be small.

4.4.2. Multijet background

One of the dominant sources of background in the W boson channels is the QCD multijet background, contributing around 6% - 8% of the event yield in the electron channels, and 2% - 3% in the muon channels. This has contributions from a large number of sources, including semileptonic decays of heavy quarks, pion and kaon decays and photon conversions, which give rise to both *non-prompt* and *fake* leptons in the final state. Additionally, fake $E_{\mathrm{T}}^{\mathrm{miss}}$ can arise from effects such as dead material, jet punch-through and pile-up, which can be difficult to model accurately in simulation. Due to the diverse set of processes contributing to this background, it is difficult to accurately estimate it using simulation, since doing so would require significant computing resources, and data-driven methods are used instead [145].

The data-driven multijet background estimation for the W boson channels methodology is based on defining different event regions besides the signal region, where control regions based on looser selection requirements are used to generate distributions (or *templates*) for this background, and extrapolation factors based on the ratio of multijet events in the control regions is used to obtain the expected multijet yield in the signal region. A complete description of this method and the results for the multijet background in the W boson channels are presented in Section 5.2.

The multijet contribution in the Z boson channels is expected to be very small due to the Z boson selection which requires two opposite-sign, isolated and well identified leptons. To estimate this, the number of charge mis-identified leptons is calculated using a same-sign lepton selection, where all the other selection requirements as described in Section 4.3.8 remain the same. Using the sidebands of the di-lepton invariant mass, $66 < m_{ee} < 76\,\text{GeV}$ and $106 < m_{ee} < 116\,\text{GeV}$, a conservative upper limit is placed on the multijet contribution in the Z channels by assuming all these events are multijet production. As the contribution for the electron channel is found to be at the sub-percent level, and the muon channel contribution even smaller, the multijet background in the Z boson channels is not considered in the analysis.

4.5. Theoretical Predictions

The $W^{\pm}$ and Z boson cross sections at $\sqrt{s} = 13.6$ TeV were computed for comparison to the measured results. These were calculated at NNLO+NNLL QCD and NLO EW accuracy using `DYTurbo-1.3.1` [33, 146–148] and `ReneSANCe-1.3.3` [149, 150], and combined by means of an additive prescription, as used in the W/Z boson cross-section measurement in 7 TeV ATLAS data [102].

Uncertainties on the cross sections arising from missing higher orders, the variation of the strong coupling constant α_s, and variations of the input PDFs were also assessed and provided. The G_μ scheme was employed [148], where the input EW parameters specified by this scheme are the Fermi constant G_μ and the masses of the Z and W boson.

Total and fiducial cross sections were calculated, where the fiducial selection requirements, reported in Table 4.1, mimic the event selection detailed in Section 4.3. Total cross sections were computed with no selections applied to the W boson channels, while the only requirement for the Z boson channels is an invariant mass window of 66 GeV $< m_{\ell\ell} <$ 116 GeV, the same window as in the fiducial selection.

Cross sections were calculated for a series of state-of-the-art PDF sets: PDF4LHC21 [151], CT18, CT18A [152], MSHT20 [21, 153, 154], NNPDF4.0 [30], ABMP16 [155], and ATLASpdf21 [156].

QCD scale uncertainties were evaluated using the standard 7-points variation for the renormalisation scale μ_R and factorisation scale μ_F, which corresponds to varying μ_R and μ_F independently by factors of 1/2 and 2. The envelope of the varied predictions was taken as the corresponding uncertainty estimate. An estimate for the α_s uncertainty was calculated based on the PDF4LHC21 set [151] as $\delta\alpha_s = 0.0010$ at the 68% CL.

For the Drell-Yan (DY) production mechanism, the QED radiation from the final-state leptons constitutes the dominant part of the higher-order electroweak corrections. This contribution was included in the fully-simulated SHERPA DY MC samples, which were used to extract the cross section via the fit to the data. Therefore, this component was already taken into account and no corrections were applied here. The remaining NLO EW corrections include NLO contributions from initial-state photon radiation, EW loop corrections, and initial-state–final-state photon interference. The NLO EW corrections applied to the NNLO+NNLL QCD fiducial cross sections were about −0.4% for the W^+ and W^- boson channels and −0.3% for the Z boson channels, respectively. Additional two-loop EW corrections for the leading contributions were calculated, and found to be $< 0.1\%$. The $t\bar{t}$-over-W boson cross-section ratios were derived using the predictions for W bosons described above and $t\bar{t}$ predictions calculated in Ref. [107] at NNLO in QCD including the resummation of NNLL soft-gluon terms calculated using TOP++[2.0] [126–132].

The uncertainties include also variations in the renormalisation and factorisation scales, α_s and PDFs. For the nominal prediction, the renormalisation and factorisation scales were set equal to the top-quark mass, and the strong coupling constant was set to $\alpha_s(m_Z) = 0.118$. Predictions were calculated for all PDF sets described above with the top mass parameter set to $m_t = 172.5\,\text{GeV}$. For the PDF4LHC21 set, $t\bar{t}$ predictions were calculated with three input masses: $m_t = 171.5\,\text{GeV}$, $m_t = 172.5\,\text{GeV}$ and $m_t = 173.5\,\text{GeV}$. The theory predictions based on the PDF4LHC21 set are detailed in Table 4.6. Additional theory predictions based on the remaining PDF sets presented in this section can be found in Appendix D.

Table 4.6.: Predicted cross sections based on the PDF4LHC21 set. Predictions for the W-boson over $t\bar{t}$ cross-section ratios are presented for three different top mass configurations.

	Channels		
	$W^- \to \ell^- \bar{\nu}$	$W^+ \to \ell^+ \nu$	$Z \to \ell^+ \ell^-$
$\sigma^{\text{fid}} \pm \delta\sigma_{\text{stat}} \pm \delta\sigma_{\text{scale}} \pm \delta\sigma_{\text{PDF}}$ [pb]	$3387.0^{+0.1\%\,+1.0\%\,+1.5\%}_{-0.1\%\,-1.1\%\,-1.5\%}$	$4345.9^{+0.1\%\,+0.9\%\,+1.5\%}_{-0.1\%\,-1.0\%\,-1.5\%}$	$746.1^{+0.1\%\,+0.4\%\,+2.8\%}_{-0.1\%\,-0.6\%\,-2.8\%}$
$\sigma^{\text{tot}} \pm \delta\sigma_{\text{stat}} \pm \delta\sigma_{\text{scale}} \pm \delta\sigma_{\text{PDF}}$ [nb]	$8.9^{+0.05\%\,+1.0\%\,+1.5\%}_{-0.05\%\,-1.1\%\,-1.5\%}$	$12.0^{+0.05\%\,+0.9\%\,+1.5\%}_{-0.05\%\,-1.0\%\,-1.5\%}$	$2.0^{+0.04\%\,+0.4\%\,+4.6\%}_{-0.04\%\,-0.6\%\,-4.6\%}$
	W^+/W^-		$W^\pm/Z$
$\text{R} \pm \delta\text{R}$	$1.283^{+0.5\%}_{-0.5\%}$		$10.36^{+2.4\%}_{-2.4\%}$
	$t\bar{t}/W^-$	$t\bar{t}/W^+$	$t\bar{t}/W^\pm$
$\text{R}(m_t = 171.5\text{ GeV}) \pm \delta\text{R}_{\text{stat}} \pm \delta\text{R}_{\text{scale}} \pm \delta\text{R}_{\text{PDF},\alpha_s}$	$0.28^{+0.03\%\,+0.75\%\,+0.81\%}_{-0.03\%\,-1.05\%\,-0.81\%}$	$0.22^{+0.02\%\,+0.58\%\,+0.61\%}_{-0.02\%\,-0.81\%\,-0.61\%}$	$0.12^{+0.01\%\,+0.35\%\,+0.35\%}_{-0.01\%\,-0.46\%\,-0.35\%}$
$\text{R}(m_t = 172.5\text{ GeV}) \pm \delta\text{R}_{\text{stat}} \pm \delta\text{R}_{\text{scale}} \pm \delta\text{R}_{\text{PDF},\alpha_s}$	$0.27^{+0.03\%\,+0.73\%\,+0.79\%}_{-0.03\%\,-1.02\%\,-0.79\%}$	$0.21^{+0.02\%\,+0.56\%\,+0.60\%}_{-0.02\%\,-0.79\%\,-0.60\%}$	$0.12^{+0.01\%\,+0.34\%\,+0.34\%}_{-0.01\%\,-0.45\%\,-0.34\%}$
$\text{R}(m_t = 173.5\text{ GeV}) \pm \delta\text{R}_{\text{stat}} \pm \delta\text{R}_{\text{scale}} \pm \delta\text{R}_{\text{PDF},\alpha_s}$	$0.27^{+0.03\%\,+0.71\%\,+0.77\%}_{-0.03\%\,-1.00\%\,-0.77\%}$	$0.21^{+0.02\%\,+0.55\%\,+0.58\%}_{-0.02\%\,-0.77\%\,-0.58\%}$	$0.12^{+0.01\%\,+0.33\%\,+0.33\%}_{-0.01\%\,-0.43\%\,-0.33\%}$

4.6. Systematic uncertainties

Systematic uncertainties are categorised into two groups: experimental uncertainties, which arise from detector-related issues including the calibration procedure and the intrinsic resolution of the detector, and modelling uncertainties on the signal and background simulated samples, which arise from assumptions in the simulation chain such as the parton shower and hadronisation.

4.6.1. Experimental uncertainties

The experimental systematic uncertainties considered in the cross section measurement are shown in Table 4.7, where the relative uncertainty from each source, estimated before performing the final cross-section extraction fit, is shown separately for each of the six channels considered in this analysis.

Electrons: Uncertainties on electrons constitute two categories. The first category encompasses uncertainties associated to the energy calibration, which are calculated

Table 4.7.: Summary of the relative experimental systematic uncertainties, estimated before performing the fit to the data.

$\delta\sigma/\sigma[\%]$	$W^- \to e^-\bar{\nu}$	$W^+ \to e^+\nu$	$Z \to e^+e^-$	$W^- \to \mu^-\bar{\nu}$	$W^+ \to \mu^+\nu$	$Z \to \mu^+\mu^-$
Pile-up modelling	1.1	1.2	1.2	0.4	0.4	0.3
Electron trigger efficiency	1.2	1.2	0.2	-	-	-
Electron reconstruction efficiency	0.3	0.3	0.6	-	-	-
Electron identification efficiency	0.2	0.2	0.5	-	-	-
Electron isolation efficiency	0.6	0.6	1.2	-	-	-
Electron calibration	0.1	0.1	0.1	-	-	-
Muon trigger efficiency	-	-	-	1.1	1.1	0.4
Muon identification efficiency	-	-	-	0.2	0.2	0.4
Muon isolation efficiency	-	-	-	1.0	1.0	2.0
Muon TTVA efficiency	-	-	-	<0.1	<0.1	0.1
Muon calibration	-	-	-	0.2	0.2	0.1
Jet energy scale	1.7	1.6	-	1.6	1.6	-
Jet energy resolution	0.4	0.4	-	0.4	0.5	-
$E_{\mathrm{T}}^{\mathrm{miss}}$ soft term scale	<0.1	<0.1	-	<0.1	<0.1	-
$E_{\mathrm{T}}^{\mathrm{miss}}$ soft term resolution	0.2	0.2	-	0.2	0.3	-
Electroweak+top background	0.2	0.2	0.2	0.2	0.1	0.2
Multijet background	2.9	2.4	-	1.3	1.1	-
NNJVT	1.6	1.5	-	1.4	1.3	-
Luminosity	2.2	2.2	2.2	2.2	2.2	2.2

based on the Run 2 calibrations using $Z \to e^+e^-$ events, as described in Section 2.3.2. To account for differences between the Run 2 and Run 3 reconstruction, these uncertainties are increased, based on differences between simulated Run 2 and Run 3 $Z \to e^+e^-$ events using the methods presented in Ref. [74]. The second category includes uncertainties on the trigger, reconstruction, identification and isolation efficiencies, which are parametrised as uncertainties on the scale factors associated to each of these efficiencies, and provided as a function of electron η and E_{T}. The trigger efficiency uncertainties are obtained using Run 3 data, and cover differences between data and simulation. Reconstruction, identification and isolation efficiency uncertainties are based on the Run 2 results [97]. As this is an early measurement, some uncertainties were not derived yet using the Run 3 data and Run 2 results are used instead, with increased uncertainties from differences between Run 2 and Run 3 simulations.

Muons: Muon uncertainties are categorised similarly to electron uncertainties. The uncertainty on the muon momentum correction, described in Section 2.3.3, is derived using $Z \to \mu^+\mu^-$ events from Run 3 data and simulation, based on the methods described in Ref. [77]. The uncertainties on the trigger, identification, isolation and TTVA are also derived using $Z \to \mu^+\mu^-$ events from Run 3 data and simulation, using the same techniques as in Ref. [157].

Jets: Uncertainties related to the JES calibration and JER, described in Section 2.3.4, are derived from comparisons between data and simulation, where different processes such as dijet and vector boson with additional jets are used to cover different jet p_{T} and η ranges. Additional uncertainties accounting for differences between Run 2 and Run 3 simulations are included. As there is no calibration available at the time of writing for the NNJVT SFs, these are assigned values of 1 with conservative uncertainties of 10% per bin [5]. The jet uncertainties are only considered for the W boson channels.

Missing transverse momentum: Uncertainties related to the track soft term of the $E_{\mathrm{T}}^{\mathrm{miss}}$ calculation, described in Section 2.3.5, are calculated based on events without true E_{T}^{miss} by comparing data to predictions from different MC generators [89]. Uncertainties corresponding to scaling the soft term magnitude up or down in the direction of the hard component, and resolution uncertainties corresponding to smearing the soft term magnitude in the direction parallel or perpendicular to the direction of the hard component are considered. The $E_{\mathrm{T}}^{\mathrm{miss}}$ uncertainties are only considered for the W boson channels.

Multijet: Uncertainties due to the data-driven estimate of the multijet background normalisation in the W boson channels are calculated as described in Section 5.2, where several sources of uncertainties are considered for the method.

Luminosity & pile-up reweighting: The uncertainty on the integrated luminosity for the data collected in 2022 is 2.2% [113], based on the luminosity measurement performed with the LUCID-2 detector [114] and the methodology detailed in Ref. [49]. The uncertainty due to pile-up reweighting is determined by varying the average number of interactions per bunch crossing in the simulation by 3%, which reflects the uncertainty on the measurement of the pileup conditions in the detector.

---

[5] These uncertainties are considered conservative as they cover all differences between data and simulation in the preliminary measurements of NNJVT efficiencies.

4.6.2. Modelling uncertainties

W and Z signal processes

Theoretical predictions for the W and Z signal processes are presented in Section 4.5. In this section, the prescription for including the uncertainties due to these theoretical predictions into the cross section measurement is presented. The theoretical uncertainties on the W and Z signal processes are categorised into two distinct components: the uncertainty δA related to the *acceptance* A, which is the ratio between the number of events in the fiducial volume and the total phase space at the particle level, and the uncertainty δC on the *correction factor* C, which is the ratio between the expected signal events at the detector level and particle level in the fiducial volume. The definition of the fiducial volume is described in Table 4.1 and the relation between the cross section and the correction and acceptance factors C and A is described by Eq. (4.2) and Eq. (4.3). For the total phase space, no selections are applied for the W-channels, while for the Z-channels, an invariant mass window of $66 < m_{\ell\ell} < 116\,\text{GeV}$ is applied.

Various sources of the theoretical uncertainty are evaluated using the W and Z signal samples:

QCD scale (Matrix element and parton showers): The QCD scale uncertainty is estimated by a 7-point variation of the renormalisation and factorisation scales. The variations on the matrix element only and the simultaneous variations of the matrix element and the parton shower scale are both considered, and the maximum variation of these 2×7 sets is taken as the final uncertainty.

PDF set: The PDF uncertainty is estimated by considering the internal variations of the PDF4LHC21 PDF set [151]. The 40 Hessian sets are considered as independent eigenvectors, and included into the fit as independent nuisance parameters.

Strong coupling constant: The α_s uncertainty is estimated by considering two different α_s values in PDF4LHC21: $\alpha_s = 0.117$ and $\alpha_s = 0.119$.

PDF choice: The PDF choice uncertainty is estimated by comparing cross section predictions calculated with two different PDF sets: NNPDF3.0NNLO [123] and PDF4LHC21.

The theoretical uncertainties δC are added in the cross-section fit as several independent nuisance parameters, and then propagated to the measured fiducial cross sections. The theoretical uncertainties δA are only propagated to the final measured total cross sections. These two components are combined as independent uncertainty sources in the total cross section calculation.

The uncertainty arising from QCD scale and parton shower variations are summarised in Table 4.8 while the contribution of the other theoretical uncertainties (PDF set, α_s and PDF choice) is $\sim 0.2\%$ in the correction factor for the Z-boson fiducial cross section, C_Z, and $\sim 0.4\%$ in the correction factor for the W-boson fiducial cross section, C_W. For the acceptance, the theoretical uncertainty is $\sim 2.9\%$ for A_Z and $\sim 2.4\%$ for A_W.

Table 4.8.: The impact of QCD scale uncertainty on the correction factor C.

$\delta C/C[\%]$	$W^- \rightarrow e^- \bar{\nu}$	$W^+ \rightarrow e^+ \nu$	$Z \rightarrow e^+ e^-$	$W^- \rightarrow \mu^- \bar{\nu}$	$W^+ \rightarrow \mu^+ \nu$	$Z \rightarrow \mu^+ \mu^-$
QCD scale	1.36	1.05	0.59	0.59	0.53	0.13

Background processes

As the contribution of the background processes based on simulated samples, described in Section 4.4.1, is at the percent level or smaller, conservative modelling uncertainties accounting for the PDF input, α_s and QCD scale variations are assigned to each type of background. A 5% modelling uncertainty is considered for the W and Z background processes, and a 10% modelling uncertainty is assigned for the diboson $VV, V = W, Z$ processes. The modelling uncertainties for the $t\bar{t}$ and single-top processes are 5.1% and 3.5%, as evaluated in Ref. [107]. These uncertainties are included in the cross section fit as constraints to the normalisation for these backgrounds.

4.7. Kinematic distributions and event yields in the signal region

In this section, kinematic distributions for the Z boson invariant mass and the W boson transverse mass, m_T^W, are presented in Figure 4.3, for each of the two Z boson channels and four W boson channels. Contributions from all backgrounds, including the multijet in the W boson channels, are displayed as stacked histograms, and the contributions from the systematic uncertainties described in Section 4.6 are displayed as a blue hashed band. The shapes of the multijet templates are estimated as described in Section 5.2.3. Additional distributions for the missing transverse momentum magnitude $E_{\mathrm{T}}^{\mathrm{miss}}$, and the lepton p_{T}, η and ϕ in the four W channels can be found in Appendix B.

The number of observed candidate events for the W and Z boson channels are displayed in Tables 4.9 and 4.10 respectively. The expected numbers of signal and background events are also displayed, estimated using simulations with the exception of the multijet background in the W boson channels, which is estimated using a data-driven method. Statistical uncertainties on the expected signal and background are included, except for the multijet where the normalisation uncertainty is displayed instead. The data agrees with the predictions, within the uncertainties.

Table 4.9.: Data event yields and predictions for the W-channels after the selections. Statistical uncertainties are shown for the electroweak and top processes. For the multijet process, the normalisation uncertainty is displayed instead [1].

	$W^- \rightarrow e^-\bar{\nu}$	$W^+ \rightarrow e^+\nu$	$W^- \rightarrow \mu^-\bar{\nu}$	$W^+ \rightarrow \mu^+\nu$
$W \rightarrow e\nu$	$43,650,000 \pm 70,000$	$55,370,000 \pm 80,000$	–	–
$W \rightarrow \mu\nu$	–	–	$57,760,000 \pm 80,000$	$74,900,000 \pm 90,000$
$W \rightarrow \tau\nu$	$684,000 \pm 8,000$	$819,000 \pm 9,000$	$906,000 \pm 10,000$	$1,120,000 \pm 10,000$
$Z \rightarrow ee/\mu\mu$	$1,416,000 \pm 4,000$	$1,459,000 \pm 4,000$	$4,638,000 \pm 8,000$	$4,903,000 \pm 8,000$
$Z \rightarrow \tau\tau$	$88,000 \pm 1,000$	$91,000 \pm 1,000$	$107,000 \pm 1,000$	$111,000 \pm 1,000$
$t\bar{t}$+single-top	$863,800 \pm 400$	$905,400 \pm 500$	$802,200 \pm 400$	$843,400 \pm 400$
VV	$93,500 \pm 300$	$97,600 \pm 300$	$98,500 \pm 300$	$102,800 \pm 300$
Multi-jet	$4,000,000 \pm 1,000,000$	$4,000,000 \pm 1,000,000$	$2,100,000 \pm 700,000$	$2,200,000 \pm 800,000$
Total predicted	$51,000,000 \pm 1,000,000$	$63,000,000 \pm 1,000,000$	$66,400,000 \pm 700,000$	$84,200,000 \pm 800,000$
Data	$50,748,537$	$62,610,338$	$65,053,470$	$82,360,980$

Table 4.10.: Event yields of data and predictions for the Z channels after the selections. Statistical uncertainties are shown for the electroweak and top processes [1].

	$Z \rightarrow e^+e^-$	$Z \rightarrow \mu^+\mu^-$
$Z \rightarrow ee$	$7,710,000 \pm 10,000$	–
$Z \rightarrow \mu\mu$	–	$13,961,000 \pm 10,000$
$Z \rightarrow \tau\tau$	$2,500 \pm 200$	$3,900 \pm 200$
$W \rightarrow \ell\nu$	139 ± 57	40 ± 27
$t\bar{t}$+single-top	$24,950 \pm 50$	$37,000 \pm 50$
VV	$14,960 \pm 80$	$23,800 \pm 100$
Total predicted	$7,750,000 \pm 10,000$	$14,030,000 \pm 10,000$
Data	$7,812,978$	$14,242,875$

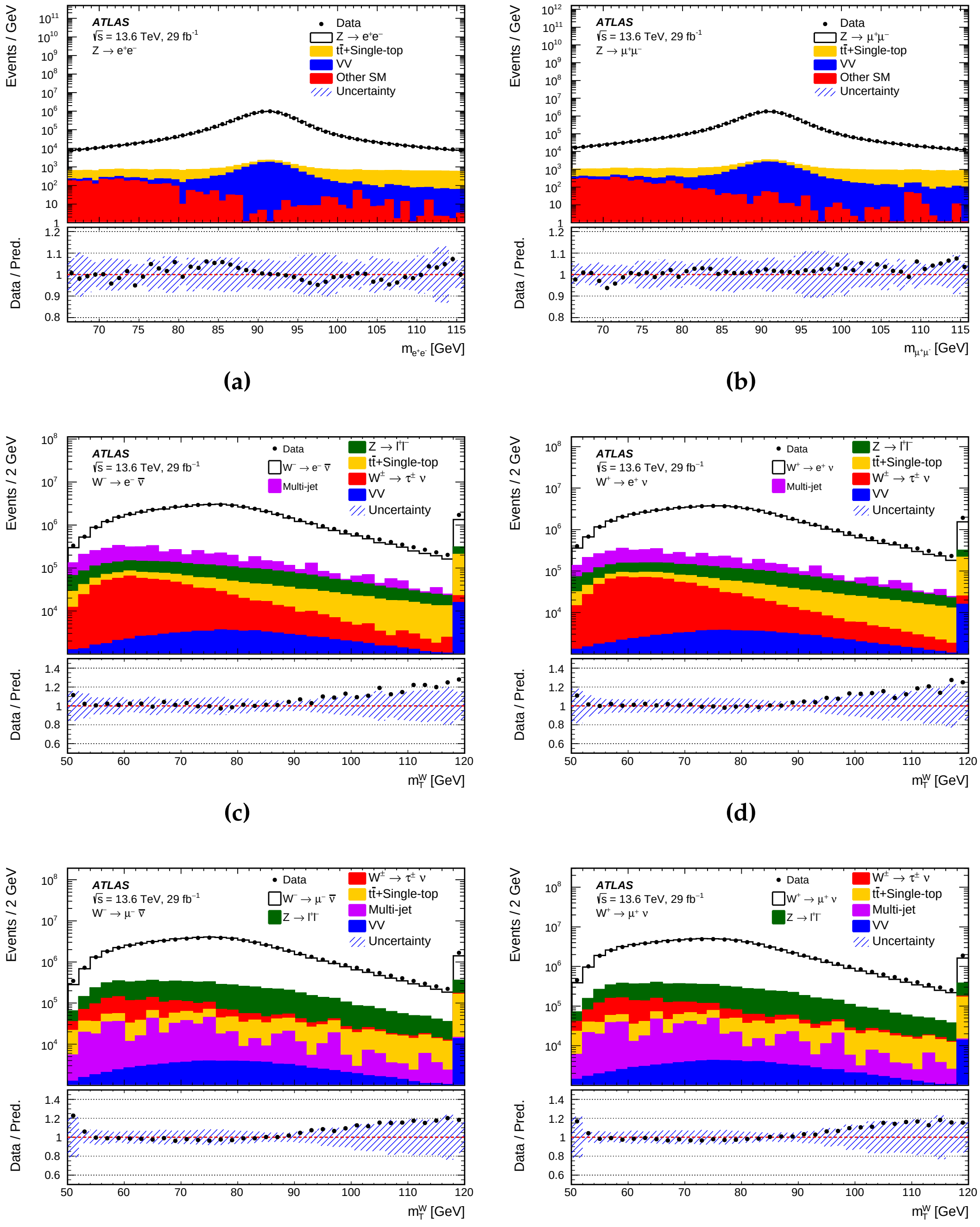

(a) **(b)**

(c) **(d)**

(e) **(f)**

Figure 4.3.: Comparison of data (black markers) and predictions (stacked histograms) for (a, b) $m_{\ell\ell}$ for the Z boson selections and (c-f) m_T^W for the W boson selections. The blue hashed band in the ratio plot denotes the total systematic uncertainty on the prediction [1].

Chapter 5.

Data-driven estimation of the multijet background

In this Chapter, the data-driven estimation of the multijet background in the W boson channels for the W boson cross section measurement is presented [1]. Several methods for measuring this challenging background were assessed, based on other W boson cross section measurements performed by ATLAS [32, 105], and on original ideas suggested by the author of this thesis or other members of the collaboration. An introduction to the multijet background is presented in Section 5.1. Section 5.2 presents the nominal method that was used for the published result, while the additional methods that were studied throughout the analysis are shown in Section 5.3.

5.1. Multijet background

The QCD-induced multijet background has a diverse composition including real leptons from semi-leptonic decays of heavy quarks, and fake leptons as a result of jets being misidentified as leptons. It is most often produced at low values of lepton p_{T}, $E_{\mathrm{T}}^{\mathrm{miss}}$ and m_{T}^{W} compared to electroweak-induced W production, and as a result most of this background can be suppressed by selecting events with large $E_{\mathrm{T}}^{\mathrm{miss}}$ and m_{T}^{W}. Additionally, QCD-induced events are characterised by significant hadronic activity, such that this background can be further reduced by requiring leptons in the final state to be isolated. Despite these selection criteria, multijet processes still contribute to the background in $W^{\pm} \rightarrow \ell^{\pm}\nu$ events due to the very high production cross-section and non-negligible probability of jets mimicking isolated leptons and $E_{\mathrm{T}}^{\mathrm{miss}}$ generated through energy mis-measurement in the event. As it is difficult to precisely simulate all these effects, data-driven techniques are used to estimate this background.

A generic prescription for deriving the multijet background is the ABCD method, which involves defining four event regions A, B, C and D, based on selection criteria made on two orthogonal variables. The variables are chosen such that region A is enriched in signal events, while the other three regions B, C and D are enriched in background events, with minimal contamination from signal and vice-versa. Figure 5.1 shows an illustration of the generic ABCD method, where a two-dimensional phase space is defined in terms of two orthogonal variables x and y, where the different event regions are separated by selection criteria on these variables.

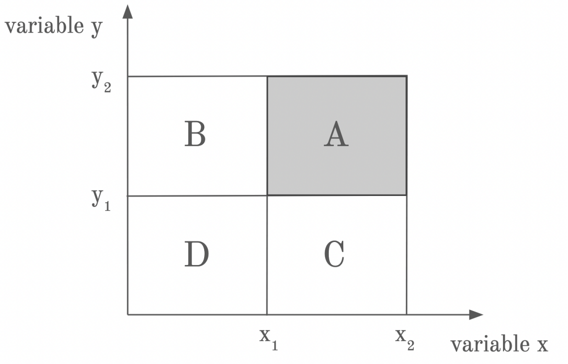

Figure 5.1.: Representation of the ABCD method, where four regions are defined by selections made on two generic orthogonal variables x and y.

The background estimate in the signal-enriched region A can then be calculated by extrapolating the number of background events from the background-enriched regions B, C and D:

$$N_A = N_B \times \frac{N_C}{N_D} \,, \tag{5.1}$$

where N denotes the number of background events in each region. Some key assumptions need to be fulfilled for an accurate estimation of the background using the ABCD method. Firstly, the event regions should be defined such that there is minimal background in the signal-enriched region A, and minimal signal contamination in the background regions B, C and D. Secondly, the discriminating variables should be chosen such that they are mostly uncorrelated.

For this analysis, the lepton isolation and a combination of the event kinematic requirements are chosen as the discriminating variables, motivated by the performance observed in previous W boson cross section measurements [32, 105]. Figure 5.2 shows an illustration of the ABCD event regions used for this analysis.

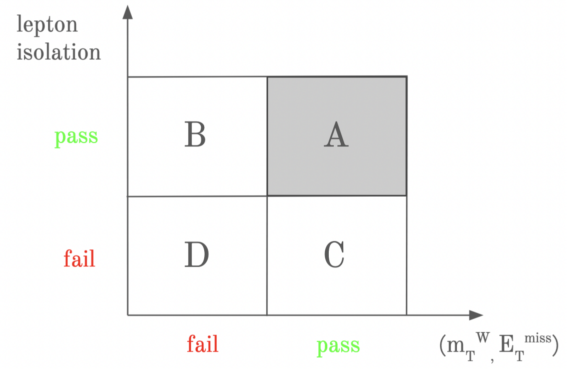

Figure 5.2.: Representation of the ABCD method, where the four regions used in this analysis are defined by selections made on the lepton isolation and event kinematics, including the $E_{\mathrm{T}}^{\mathrm{miss}}$ and m_{T}^{W} variables.

Since the lepton isolation requirement for the signal region, described for electrons in Section 4.3.2 and for muons in Section 4.3.3, is defined in terms of a working point described by two isolation variables, leptons can either "pass" or "fail" this working point, as shown in Figure 5.2. Similarly, the signal region definition in Section 4.3 includes requirements on both the W transverse mass and missing transverse momentum magnitude, $m_{\mathrm{T}}^{W} > 50$ GeV and $E_{\mathrm{T}}^{\mathrm{miss}} > 25$ GeV. Thus, the event regions are divided by requiring events to either "pass" or "fail" both of these two kinematic requirements.

The method begins with deriving multijet distributions (or *templates*) from the data selected in regions containing leptons failing the isolation working point, C and D, also called *control regions*. These templates are produced for kinematic variables that have discriminating power between the signal and background. The use of support triggers with looser requirements than the nominal triggers used in the signal region selection may also be required in order not to limit the phase space for events selected in the control region. Contamination from signal and other backgrounds is then subtracted using simulation. The resulting template in control region D is then used to estimate the multijet normalisation in region B, also called the *fitting region* (FR), through a fit to the data. This multijet normalisation can be then extrapolated to the signal region (SR) using Eq. 5.1, where an appropriate extrapolation factor is obtained from the ratio of multijet events in the two control regions. As the W boson cross sections are extracted from fits using only one bin per channel [1], the aim of this method is to extract the multijet normalisation, and its associated uncertainty, for each of the four W boson channels.

One of the limitations of this method is the possible bias introduced due to different production processes contributing to this background at different regions of phase space. To correct for this bias, an isolation-based correction is applied to the multijet estimate for the signal region, as will be described in the following Section.

Several similar methods for estimating the multijet background have been used for the W boson cross-section measurements at different centre-of-mass energies performed by the ATLAS experiment [102, 104, 105], gradually becoming more complex with each analysis as the multijet contribution in the signal region increases with increasing pile-up in the data. Thus, several methods for estimating the multijet background have been studied for this analysis, using either the nominal triggers to select events in the control regions, or support triggers with no isolation requirements before selecting a final method.

5.2. Nominal method for estimating multijet

5.2.1. Event regions

The multijet background is obtained by performing profile likelihood fits to the data in the FR that is enriched with multijet contribution, where the signal [2] and background kinematic distributions have sufficient discriminating power. Thus, the distributions in the $E_{\mathrm{T}}^{\mathrm{miss}}$ and m_{T}^{W} kinematic variables are used for these fits as multijet production is more prominent at low $E_{\mathrm{T}}^{\mathrm{miss}}$ and m_{T}^{W} than the signal. The fitting region (FR) is defined similarly to the signal region (SR), but where the $E_{\mathrm{T}}^{\mathrm{miss}}$ and m_{T}^{W} kinematic selections are inverted, so that $E_{\mathrm{T}}^{\mathrm{miss}} < 25\,\mathrm{GeV}$ and $m_{\mathrm{T}}^{W} < 50\,\mathrm{GeV}$.

The signal, electroweak (EW) production of single boson and diboson, and top contributions in this region are estimated using simulation, as shown in Figure 5.3. This illustrates the comparison between data and predictions in $E_{\mathrm{T}}^{\mathrm{miss}}$ and m_{T}^{W} distri-

---

[1] The cross section fits are described further in Section 6.1.

[2] Here the signal refers to the $W^{\pm} \to \ell^{\pm}\nu$ processes.

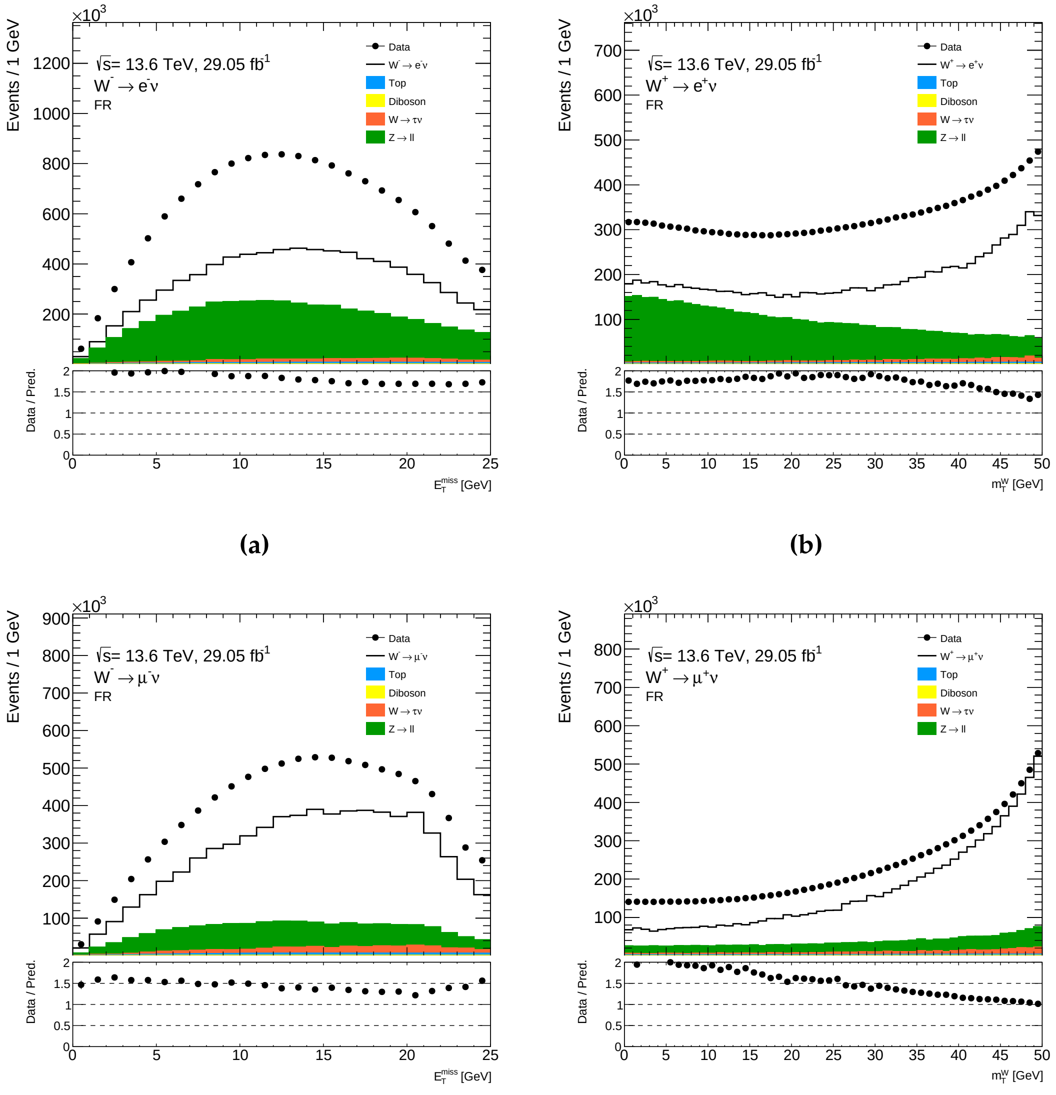

(a) (b)

(c) (d)

Figure 5.3.: Comparison between data and predictions for the top, diboson, W and Z processes in the FR for (a) $E_{\mathrm{T}}^{\mathrm{miss}}$ distribution in the $W^- \to e^- \bar{\nu}$ channel, (b) m_{T}^{W} distribution in the $W^+ \to e^+ \nu$ channel, (c) $E_{\mathrm{T}}^{\mathrm{miss}}$ distribution in the $W^- \to \mu^- \bar{\nu}$ channel and (d) m_{T}^{W} distribution in the $W^+ \to \mu^+ \nu$ channel. The discrepancy between data and predictions observed in the ratio in the bottom panels is due to the missing multijet contribution.

butions in the FR, where the missing multijet contribution can be observed from the discrepancy between the data and predictions in the ratios.

The multijet distributions are derived instead from a control region (CR1) with similar kinematic selection as the FR, but where the lepton is required to fail the isolation requirement, denoted as anti-isolated. A second control region (CR2) is similarly defined using anti-isolated leptons, but the same kinematic selection as the SR is used. The contamination from signal and other backgrounds in these control regions is also estimated using simulation and subtracted from the data in order to build the multijet templates. The four event regions defined so far are summarised in Table 5.1.

Table 5.1.: The four regions used to extract the MJ background.

Fit region (FR)	Signal region (SR)
$E_{\mathrm{T}}^{\mathrm{miss}} < 25\,\mathrm{GeV}$ $m_{\mathrm{T}}^{W} < 50\,\mathrm{GeV}$ Pass isolation	$E_{\mathrm{T}}^{\mathrm{miss}} > 25\,\mathrm{GeV}$ $m_{\mathrm{T}}^{W} > 50\,\mathrm{GeV}$ Pass isolation
Control regon 1 (CR1)	Control region 2 (CR2)
$E_{\mathrm{T}}^{\mathrm{miss}} < 25\,\mathrm{GeV}$ $m_{\mathrm{T}}^{W} < 50\,\mathrm{GeV}$ Fail isolation	$E_{\mathrm{T}}^{\mathrm{miss}} > 25\,\mathrm{GeV}$ $m_{\mathrm{T}}^{W} > 50\,\mathrm{GeV}$ Fail isolation

Since the triggers used in the nominal selection have isolation requirements, described in Section 4.3.1, support triggers with no isolation requirements have been used to select events in the control regions, shown in Table 5.2. The trigger chain names follow the same logic as described in Section 4.3.1. The `idperf_tight_nogsf` HLT algorithms in the second electron trigger chain denote there is no track selection applied, a cut-based tight identification working point is used instead of a likelihood-based one, and no Gaussian-sum filter (GSF) track re-fitting to account for energy loss is performed. Due to the looser requirements on these triggers compared to the nominal triggers, large pre-scales are applied, only allowing 1 in approximately 2000 events that pass the trigger requirements to be recorded.

The templates for the signal, EW and top contributions in the control regions, estimated using simulation, are scaled to the luminosity of the events selected using

Table 5.2.: A list of single electron or muon support triggers used to select events for the multijet background templates. A logical OR is applied between the triggers.

Electron triggers	Muon triggers
HLT_e20_lhvloose_L1EM15VH	HLT_mu22_L1MU14FCH
HLT_e26_idperf_tight_nogsf_L1EM22VHI	

the support triggers, which is measured using the alternative method presented in Section 5.2.2.

5.2.2. Luminosity measurement for support triggers

The multijet templates are sensitive to contamination from signal, EW and top background, which is subtracted from the data in the control regions using simulation. Thus, an accurate luminosity measurement for the support triggers is needed. Since estimating the luminosity of a combination of pre-scaled triggers is challenging [67], as is the case for the electron channel, a method exploiting Z boson event counting used. To do this, the Z boson selection, as detailed in Section 4.3.8, is applied using both the nominal triggers and support triggers for the electron and muon channel separately. The nominal luminosity of 29.05 fb^{-1} is scaled by the ratio of events selected by the two sets of triggers. The efficiency and acceptance is accounted for using the sum of weights obtained from simulation. Figures 5.4 and 5.5 show the events passing the Z boson selection using the nominal and support triggers, for the electron and muon channel respectively, and Table 5.3 shows the luminosity obtained for events collected using support triggers, as calculated using the Z boson counting method. The results are compared to the integrated luminosity obtained using the individual prescale factors of the support triggers. The uncertainties on the luminosity results obtained using the Z boson event counting method are statistical, based on the number of events passing the support triggers in each channel. The luminosity results obtained from the standard calculation, where the nominal luminosity is scaled by the pre-scale factor, and from the Z boson event counting obtained using a single support trigger, are compatible within the statistical uncertainty from the Z boson event counting method. Thus, the integrated luminosity results calculated using the Z boson event counting method are used in the control regions.

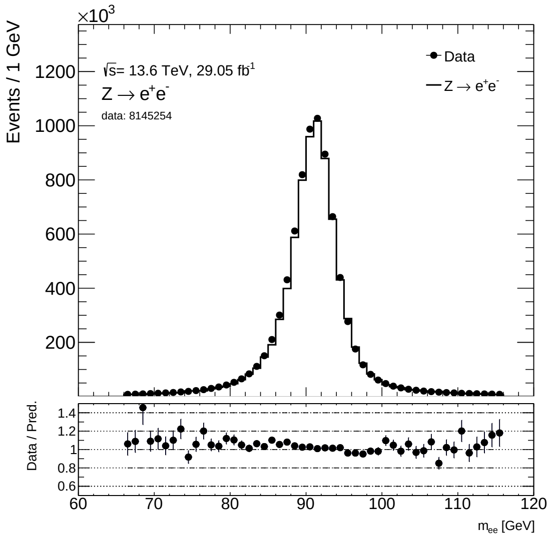

(a) **(b)**

Figure 5.4.: Events passing the Z-boson selection, selected using (a) nominal triggers and (b) support triggers for the $Z \to e^+e^-$ channel.

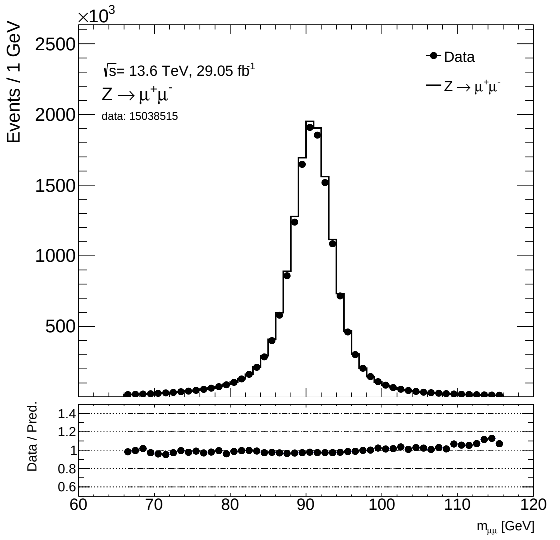

(a) **(b)**

Figure 5.5.: Events passing the Z boson selection, selected using (a) nominal triggers and (b) support triggers for the $Z \to \mu^+\mu^-$ channel.

Table 5.3.: Results for luminosity calculation using the Z boson event counting method. Results using the integrated luminosity, scaled by the prescale factor for individual support triggers for the electron and muon channels are also shown.

	Trigger chain	Lumi scaled [pb^{-1}]	Lumi from Z events counting [pb^{-1}]
Electron triggers	HLT_e20_lhvloose_L1EM15VH	5.77	5.61 ± 0.14
	HLT_e26_idperf_tight _nogsf_L1EM22VHI	13.59	14.10 ± 0.22
	both	-	19.65 ± 0.26
Muon trigger	HLT_mu22_L1MU14FCH	19.92	19.69 ± 0.19

5.2.3. Isolation slices and multijet templates

The control regions shown in Table 5.1, CR1 and CR2, are further divided into four mutually exclusive isolation slices, iso1-4, by varying the track isolation variable, $p_{\mathrm{T}}^{\mathrm{varcone30}}/p_{\mathrm{T}}$, progressively further from the signal region, while the calorimeter isolation, $E_{\mathrm{T}}^{\mathrm{cone20}}/p_{\mathrm{T}}$, is kept at the nominal value. Table 5.4 details the complete selection of the track isolation slices used in these scans while Figure 5.6 shows the isolation slices on the track/calorimeter isolation map.

Table 5.4.: Boundaries of isolation slices used to divide the control regions for the $W \to e\nu$ and $W \to \mu\nu$ channels.

	$W \to e\nu$	$W \to \mu\nu$
Fixed cut	$E_{\mathrm{T}}^{\mathrm{cone20}}/p_{\mathrm{T}} < 0.06$	$E_{\mathrm{T}}^{\mathrm{cone20}}/p_{\mathrm{T}} < 0.15$
iso1	$0.06 < p_{\mathrm{T}}^{\mathrm{varcone30}}/p_{\mathrm{T}} < 0.12$	$0.04 < p_{\mathrm{T}}^{\mathrm{varcone30}}/p_{\mathrm{T}} < 0.08$
iso2	$0.12 < p_{\mathrm{T}}^{\mathrm{varcone30}}/p_{\mathrm{T}} < 0.18$	$0.08 < p_{\mathrm{T}}^{\mathrm{varcone30}}/p_{\mathrm{T}} < 0.12$
iso4	$0.18 < p_{\mathrm{T}}^{\mathrm{varcone30}}/p_{\mathrm{T}} < 0.24$	$0.12 < p_{\mathrm{T}}^{\mathrm{varcone30}}/p_{\mathrm{T}} < 0.16$
iso3	$0.24 < p_{\mathrm{T}}^{\mathrm{varcone30}}/p_{\mathrm{T}} < 0.3$	$0.16 < p_{\mathrm{T}}^{\mathrm{varcone30}}/p_{\mathrm{T}} < 0.2$

The $E_{\mathrm{T}}^{\mathrm{miss}}$ distribution for the four isolation slices defined in CR1 is displayed in Figure 5.7, which shows the data and contributions from the signal, EW and top backgrounds in the $W^{\pm} \to e^{\pm}\nu$ channel, estimated using simulations. Thus, the resulting discrepancy between the data and simulations is the multijet contribution, which is then obtained by subtracting the simulation from the data. Due to limited statistics in the control regions as a result of using pre-scaled triggers to select data, positively and negatively charged channels of the same lepton flavour are combined

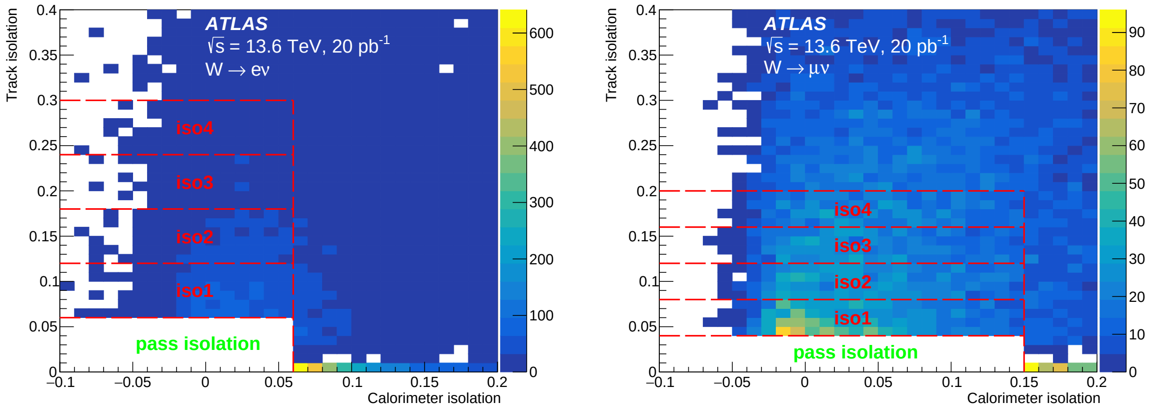

(a) **(b)**

Figure 5.6.: Track isolation slices used to extract the multijet templates (a) in the electron channel and (b) in the muon channel [1].

when constructing the multijet templates [3]. Figures 5.8 and 5.9 show the $E_{\mathrm{T}}^{\mathrm{miss}}$ and m_{T}^{W} CR1 MJ templates obtained for each of the four isolation slices iso1-4. Further plots similar to Figure 5.7 for the electron and muon channel $E_{\mathrm{T}}^{\mathrm{miss}}$ and m_{T}^{W} distributions in CR1 and CR2 can be found in Appendix C.

A similar procedure is applied in the CR2 event region to derive the MJ template shapes. These templates, together with the multijet normalisations presented in Section 5.2.5, are then used to obtain the MJ template shape used in the signal region, shown in Figure 4.3, and in the additional Figures provided in Appendix B. The MJ shapes are not used in the final cross section measurement, since the W boson cross sections are extracted from fits using only one bin per channel.

As the track isolation range used to select the isolation slice is progressively increased, differences appear in the MJ template shape. Thus, to first order approximation, it follows that the shape of the MJ template in the signal region will also change as a function of the track isolation variable, so that a shape correction must be applied to obtain the template shape in the signal region. The MJ shape in the signal region, $H_{\mathrm{MJ}}^{\mathrm{SR}}[X]$, where X is one of the m_{T}^{W} and $E_{\mathrm{T}}^{\mathrm{miss}}$ kinematic variables used to build the template, is obtained by adjusting the shape of the template in the isolation slice from CR2 closest to the signal region, $H_{\mathrm{MJ}}^{\mathrm{CR2,\ iso1}}[X]$, using a shape correction factor, $\Delta^{\mathrm{CR2}}[X]$:

---

[3] No discrepancies are observed between the shapes of these templates in the positively and negatively charged channels, within the statistical uncertainties on the templates.

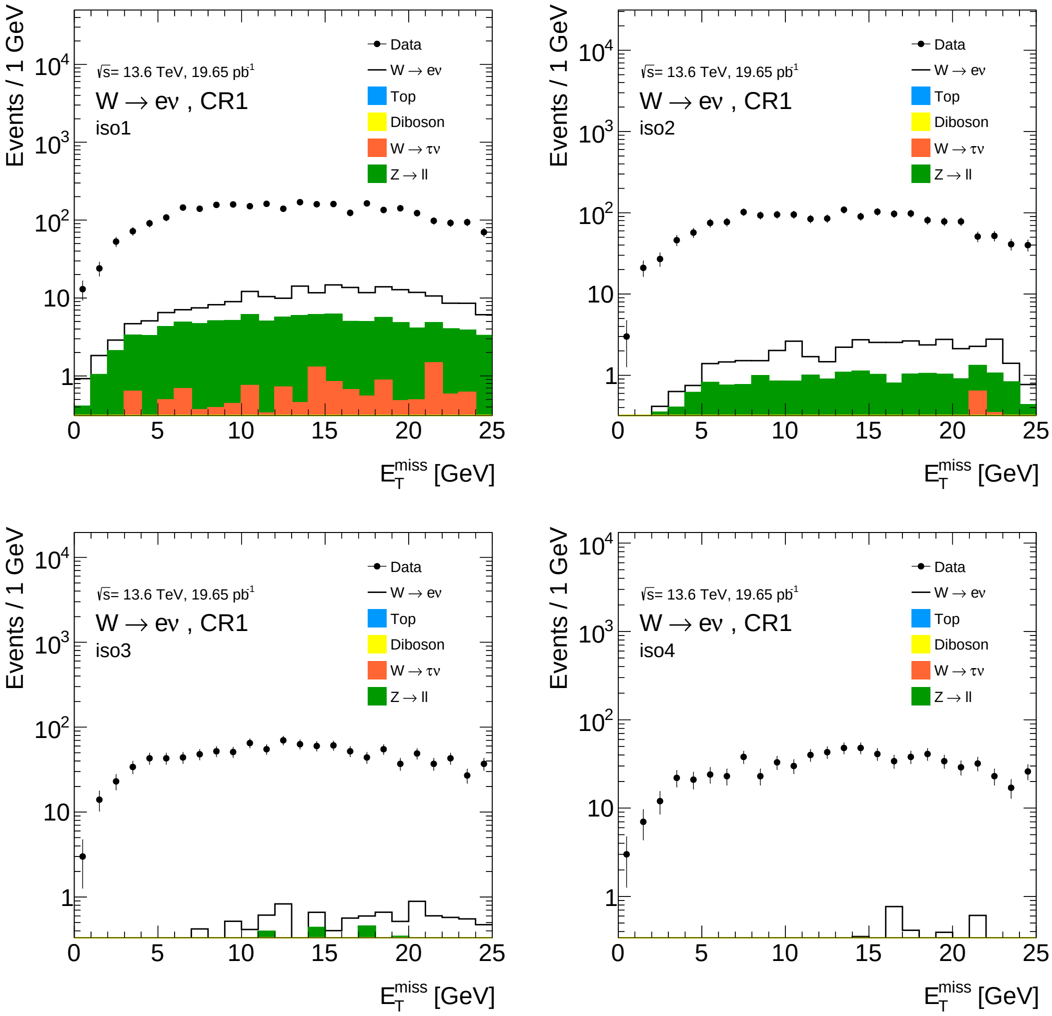

Figure 5.7.: Comparison between data and predictions for the signal, EW and top processes in electron channel $E_{\mathrm{T}}^{\mathrm{miss}}$ distributions for the four isolation slices in CR1.

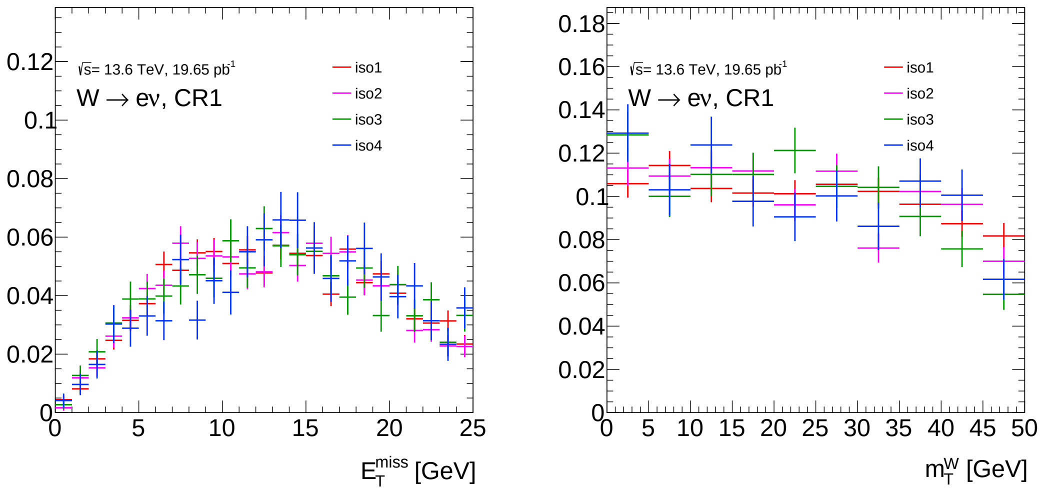

(a) **(b)**

Figure 5.8.: CR1 multijet templates for the electron channel for (a) $E_\mathrm{T}^\mathrm{miss}$ and (b) m_T^W, normalised to unity.

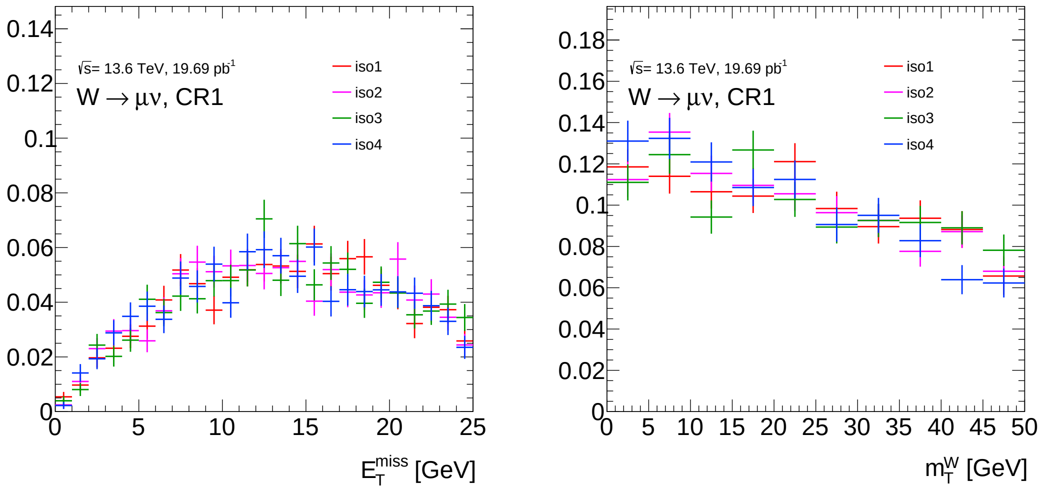

(a) **(b)**

Figure 5.9.: CR1 multijet templates for the muon channel for (a) $E_\mathrm{T}^\mathrm{miss}$ and (b) m_T^W, normalised to unity.

$$H_{\mathrm{MJ}}^{\mathrm{SR}}[X] = H_{\mathrm{MJ}}^{\mathrm{CR2,\,iso1}}[X] + \Delta^{\mathrm{CR2}}[X]. \tag{5.2}$$

The shape correction factor is built using the MJ shapes in the 4 isolation slices from CR2, $H_{\mathrm{MJ}}^{\mathrm{CR2,\,iso1\text{-}4}}[X]$ as

$$\Delta^{\mathrm{CR2}}[X] = \frac{1}{2}\frac{H_{\mathrm{MJ}}^{\mathrm{CR2,\,iso1}}[X] - H_{\mathrm{MJ}}^{\mathrm{CR2,\,iso3}}[X]}{2} + \frac{H_{\mathrm{MJ}}^{\mathrm{CR2,\,iso2}}[X] - H_{\mathrm{MJ}}^{\mathrm{CR2,\,iso4}}[X]}{2}, \tag{5.3}$$

where a linear change in the shape of the MJ templates is assumed, motivated by a linear change in the range of the track isolation variable used to build these templates. This shape correction is done separately for the $E_{\mathrm{T}}^{\mathrm{miss}}$ and m_{T}^{W} templates, and for the electron and muon channel, as shown in Figures 5.10 and 5.11, where the template denoted "isoSR" is the multijet template in the signal region.

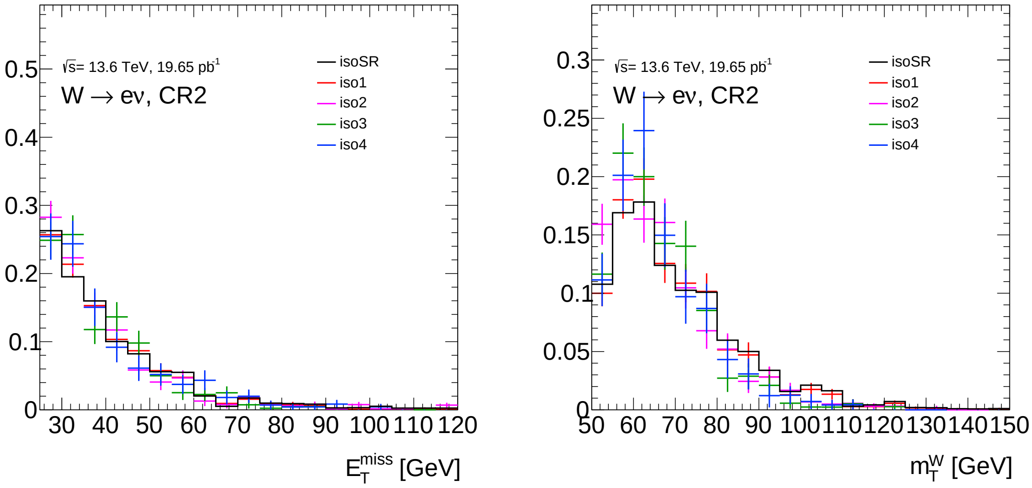

(a) **(b)**

Figure 5.10.: CR2 multijet templates for the electron channel for (a) $E_{\mathrm{T}}^{\mathrm{miss}}$ and (b) m_{T}^{W}, normalised to unity. The template denoted "isoSR" is obtained by applying a correction factor defined in Eq. (5.3) to the template "iso1".

Table 5.5 summarises the number of multijet events in each isolation slice, iso1-4, for the $W^{\pm} \to e^{\pm}\nu$ and $W^{\pm} \to \mu^{\pm}\nu$ channels, where the quoted uncertainties are statistical.

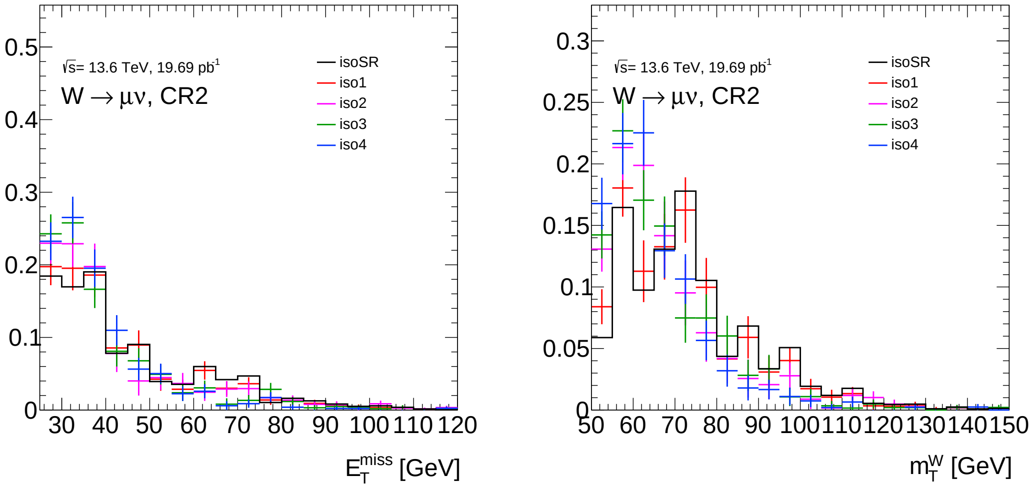

(a) **(b)**

Figure 5.11.: CR2 multijet templates for the muon channel for (a) $E_{\mathrm{T}}^{\mathrm{miss}}$ and (b) m_{T}^{W}, normalised to unity. The template denoted "isoSR" is obtained by applying a correction factor defined in Eq. (5.3) to the template "iso1".

Table 5.5.: Number of multijet events in each isolation slice, iso1-4, for the $W^{\pm} \to e^{\pm}\nu$ and $W^{\pm} \to \mu^{\pm}\nu$ channels. Statistical uncertainties due to the number of events used to build these templates are shown.

	$W^{\pm} \to e^{\pm}\nu$		$W^{\pm} \to \mu^{\pm}\nu$	
	CR1	CR2	CR1	CR2
iso1	2723 ± 54	1161 ± 51	1765 ± 47	1161 ± 51
iso2	1734 ± 42	574 ± 29	1596 ± 41	574 ± 29
iso3	1098 ± 33	370 ± 21	1467 ± 38	370 ± 21
iso4	724 ± 27	226 ± 15	1340 ± 36	226 ± 15

5.2.4. Template fitting and extrapolation factors

Using the CR1 multijet templates shown in Figures 5.8 and 5.9, the normalisation of the corresponding multijet template in the FR is then extracted using profile likelihood fits to the data, as described in Section 4.1.1, using distributions in the $E_{\mathrm{T}}^{\mathrm{miss}}$ and m_{T}^{W} kinematic variables. The full set of systematic uncertainties, as described in Section 4.6, are included as nuisance parameters. Additional nuisance parameters which account for the statistical uncertainty in the multijet templates (gamma parameters) are included in these fits as well. Normalisation factors for the W and Z samples with respect to the SM expectations, μ_{W} and μ_{Z}, are included, both constrained by Gaussian terms. For the W term, a large width of $\pm 20\%$ is used with the nominal value set at 1. For the Z term, the width is set at $\pm 5\%$ and the nominal value set at 1.01. As the Z cross-section is measured independently from the multijet estimation, the nominal value for μ_Z is based on the measured Z cross-section result which was published prior to the W cross-section measurement [107]. The parameter of interest, which is a free parameter in the fit, is defined as the ratio between the post-fit and pre-fit multijet normalisation μ_{MJ}, where the pre-fit normalisation value is chosen as the difference between the data and the predictions in each fit.

Figure 5.12 shows the pre-fit and post-fit distributions of the multijet and the EW processes obtained from isolation slice 1 (iso1) for the $W^- \rightarrow e^- \bar{\nu}$ channel, based on the $E_{\mathrm{T}}^{\mathrm{miss}}$ variable in the FR, as well as the post-fit multijet signal strength, nuisance parameters and gamma parameters. The post-fit nuisance parameter (NP) pulls for the systematic uncertainties, which quantify how the fit to the data influences the central values and uncertainties on the NPs, are shown in Figure C.8 in Appendix C. No significant pulls are observed for this fit, or any of the other fits perfomed for this measurement.

The multijet normalisation in the signal region for isolation slice i ($\mathrm{N}_{\mathrm{MJ}}^{\mathrm{SR,i}}$) is then obtained by scaling the normalisation from the fitting region for the corresponding isolation slice i ($\mathrm{N}_{\mathrm{MJ}}^{\mathrm{FR,i}}$) using an extrapolation factor:

$$\mathrm{N}_{\mathrm{MJ}}^{\mathrm{SR,i}} = \epsilon_i \mathrm{N}_{\mathrm{MJ}}^{\mathrm{FR,i}}. \tag{5.4}$$

The extrapolation factor ϵ_i is also calculated separately for each isolation slice, using the ratio of multijet events in the corresponding slices in CR2 ($N_{MJ}^{CR2,i}$) and CR1 ($N_{MJ}^{CR1,i}$):

$$\epsilon_i = \frac{\mathrm{N}_{\mathrm{MJ}}^{\mathrm{CR2,i}}}{\mathrm{N}_{\mathrm{MJ}}^{\mathrm{CR1,i}}}\,. \tag{5.5}$$

The ϵ_i values are calculated by combining the positively and negatively charged channels, separately for each isolation slice, such that for a given isolation slice, ϵ_i takes the same value in both channels of the same lepton flavour.

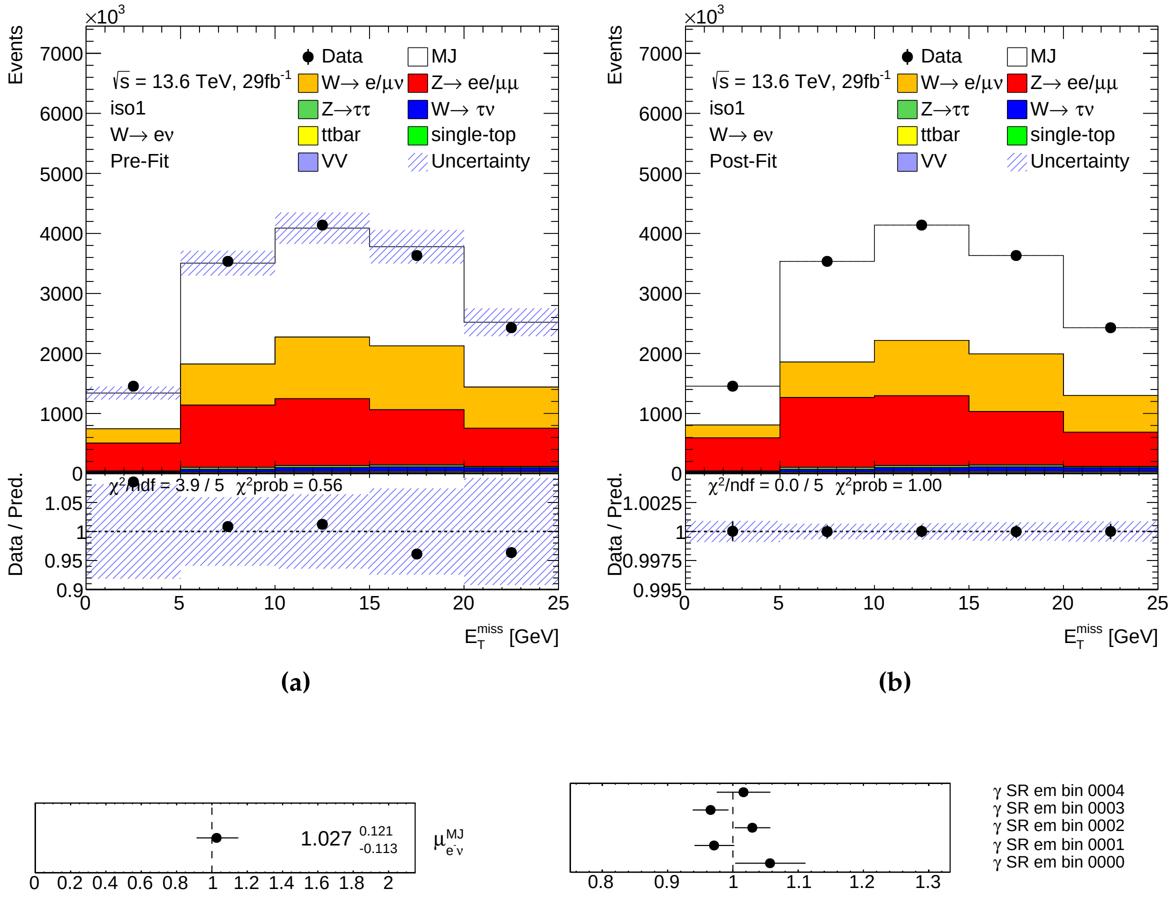

(a)

(b)

(c)

(d)

Figure 5.12.: The (a) pre-fit and (b) post-fit distribution for the $W^- \to e^-\bar{\nu}$ channel on the $E_{\mathrm{T}}^{\mathrm{miss}}$ distribution using the multijet template obtained from isolation slice 1 (iso1). The dashed error band in the pre-fit figure (a) gives the total systematic uncertainty before the fit, while in the post-fit figure (b), it represents the statistical uncertainty derived from the fit. Post-fit results including (c) the multijet signal strength and (d) gamma parameters are also illustrated. NP pulls for this fit are shown in Figure C.8 in Appendix C

Figure 5.13 shows the results of the profile likelihood fits performed in the FR in terms of the absolute multijet yield in each isolation slice, $\mathrm{N}_{\mathrm{MJ}}^{\mathrm{FR}}$, for all four W boson channels. The uncertainties on $\mathrm{N}_{\mathrm{MJ}}^{\mathrm{FR}}$ are the post-fit uncertainties on the μ_{MJ} parameter, scaled by the pre-fit multijet normalisation. The results for ϵ are also displayed for each isolation slice separately, where the uncertainties are due to the statistical uncertainties on the number of multijet events in CR1 and CR2.

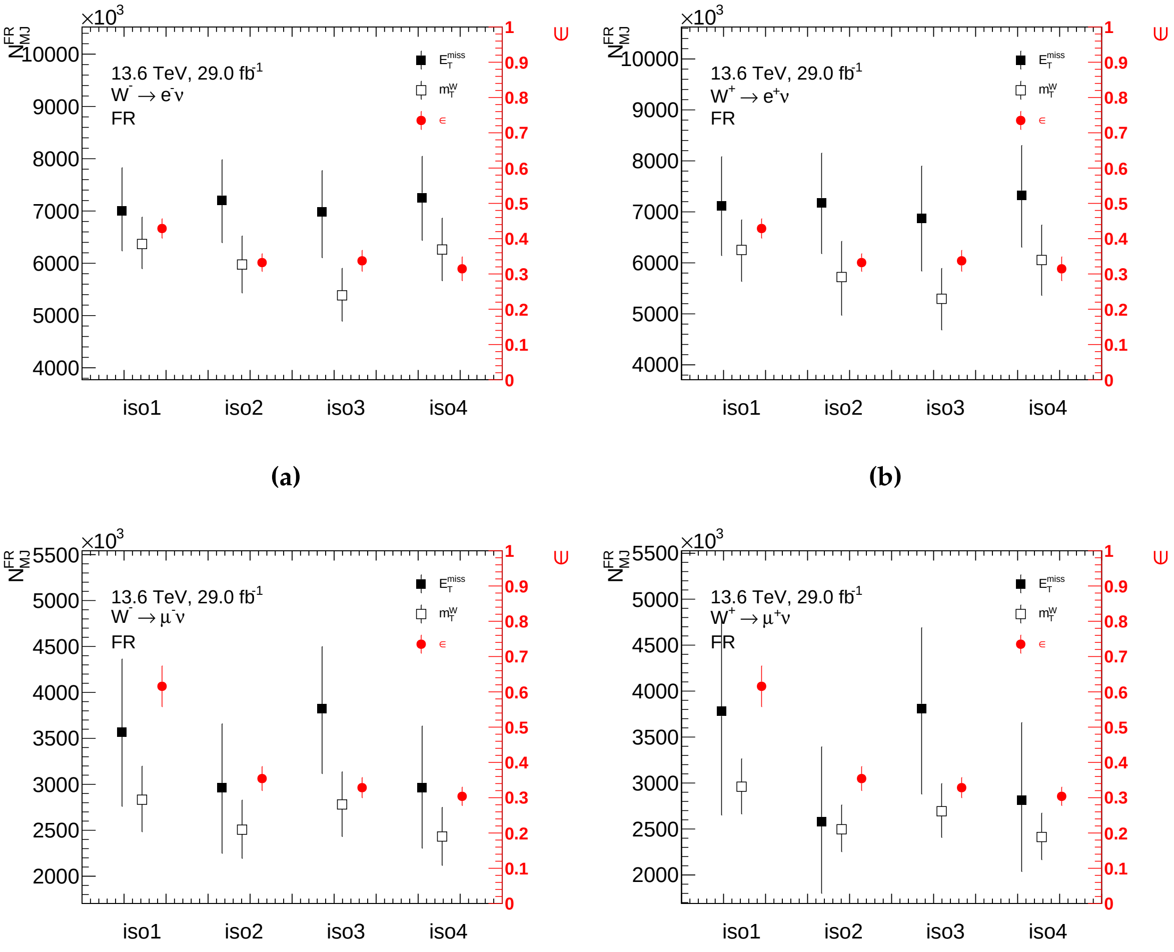

(a) **(b)**

(c) **(d)**

Figure 5.13.: Multijet normalisation results in FR, $\mathrm{N}_{\mathrm{MJ}}^{\mathrm{FR}}$, and extrapolation factors ϵ in each of the four isolation slices, iso1-4, for (a) the $W^- \to e^-\bar{\nu}$ channel, (b) the $W^+ \to e^+\nu$ channel, (c) the $W^- \to \mu^-\bar{\nu}$ channel and (d) the $W^+ \to \mu^+\nu$ channel. The uncertainties on the $\mathrm{N}_{\mathrm{MJ}}^{\mathrm{FR}}$ values are the post-fit uncertainties on the μ_{MJ} parameter, scaled to the pre-fit multijet normalisation, and the uncertainties on ϵ are due to the statistical uncertainties on the number of multijet events in CR1 and CR2 used to calculate ϵ. The ϵ factors are calculated by combining the positively and negatively charged channels.

5.2.5. Results

Following Eq. (5.4) and the results displayed in Figure 5.13, the multijet normalisation in the SR is obtained. Thus, this procedure leads to two sets of four SR multijet yields (two fit variables and four isolation slices) for each of the four W boson channels. The multijet estimates obtained in each isolation slice are then used to build an extrapolation to the track isolation selection used in the signal region, in order to reduce the effects of the track isolation slices on the multijet yield in the SR.

Figure 5.14 shows the relative multijet yield in the SR obtained using the $E_{\mathrm{T}}^{\mathrm{miss}}$ and m_{T}^{W} templates for each of the four isolation slices, in each of the four W boson channels. For each point, the average value of the track isolation of the events in the respective isolation slice is used as the central value on the x-axis, and the uncertainty of the multijet fit in the FR is propagated into the multijet yield and enters the uncertainty of the final extrapolation. A linear (dashed line) and quadratic (solid line) function has been fitted in order to obtain an estimate for the multijet yield corresponding to the track isolation in the SR for the $E_{\mathrm{T}}^{\mathrm{miss}}$ and m_{T}^{W} multijet yields separately. The linear behaviour in the multijet yields as a function of the track isolation is motivated by the linear increase in the range of the track isolation variable used to define each isolation slice. However, this does not necessarily mean that a linear fit is the most appropriate choice for the extrapolation, and thus quadratic fits have also been performed over the same inputs.

The quadratic fits are observed to better model the dependence of the multijet normalisation as a function of the track isolation than the linear fits in each channel, verified with a χ^2 criterion, and are used to define the central value for the final multijet yield. The difference between the linear and quadratic fit results are used as an additional source of uncertainty, described below. Additional plots illustrating the linear and quadratic fits separately, together with the χ^2 values adjusted for the number of degrees of freedom for each, can be found in Figures C.9 and C.10 in Appendix C.

As the extrapolations using the $E_{\mathrm{T}}^{\mathrm{miss}}$ and m_{T}^{W} distributions are found to be compatible, the central value for the final multijet yield in each channel corresponds to the the weighted average of these results of the two quadratic extrapolations, denoted $f_{\mathrm{MJ}}^{\mathrm{SR}}$ in the plots. The uncertainty on $f_{\mathrm{MJ}}^{\mathrm{SR}}$ has two contributions. The first is calculated using the combined uncertainties from the m_{T}^{W} and $E_{\mathrm{T}}^{\mathrm{miss}}$ fits, and the difference between these fit results. The second is due to the difference between linear and quadratic fit results, which constitutes the dominant contribution to the systematic uncertainty on the multijet estimate.

The relative MJ background yields are shown in Table 5.6, where the first two columns show the yields extracted from the quadratic fits to the $m_{\mathrm{T}}^{\mathrm{W}}$ and $E_{\mathrm{T}}^{\mathrm{miss}}$, including the uncertainties associated with these fits. The last column shows the weighted average obtained from the $m_{\mathrm{T}}^{\mathrm{W}}$ and $E_{\mathrm{T}}^{\mathrm{miss}}$ results, including the two contributions to the systematic uncertianty described above.

Table 5.6.: Relative multi-jet yield in the SR, derived with quadratic fits, shown as a fraction [%] of the total data yield in the SR. The third column represents the weighted average from the quadratic fit, where the first contribution to the uncertainty corresponds to the weighted average between the fit uncertainty and the difference between the m_{T}^{W} and $E_{\mathrm{T}}^{\mathrm{miss}}$ quadratic fits, while the second is due to the difference between linear and quadratic fit results on the track isolation scan [1].

Channel	% of data		
	$m_{\mathrm{T}}^{\mathrm{W}}$	$E_{\mathrm{T}}^{\mathrm{miss}}$	Combined MJ yield
$W^- \to e^-\bar{\nu}$	8.0 ± 1.2	7.7 ± 2.0	7.9 ± 1.1 ± 2.3
$W^+ \to e^+\nu$	6.2 ± 1.2	6.4 ± 1.9	6.3 ± 1.0 ± 1.9
$W^- \to \mu^-\bar{\nu}$	3.3 ± 0.6	3.7 ± 1.3	3.3 ± 0.5 ± 0.8
$W^+ \to \mu^+\nu$	2.7 ± 0.4	2.9 ± 1.4	2.7 ± 0.4 ± 0.9

5.3. Additional methods for estimating multijet backgrounds

In this section, alternative methods for estimating the multijet background in the $W^{\pm} \to \ell^{\pm}\nu$ channels are presented. These were either studied before the nominal method (denoted method 3 in this Section) was chosen for the published result, or throughout the internal ATLAS approval process, based on ideas from the author of this thesis or other members of the collaboration.

A method very similar to the nominal, denoted method 2, includes similar event regions as those described in Section 5.2.1, but where the kinematic selections on the $E_{\mathrm{T}}^{\mathrm{miss}}$ and m_{T}^{W} in FR and CR1 are relaxed instead of inverted, so that $E_{\mathrm{T}}^{\mathrm{miss}} > 0\,\mathrm{GeV}$ and $m_{\mathrm{T}}^{W} > 0\,\mathrm{GeV}$. The event regions used in this method are summarised in Table 5.7.

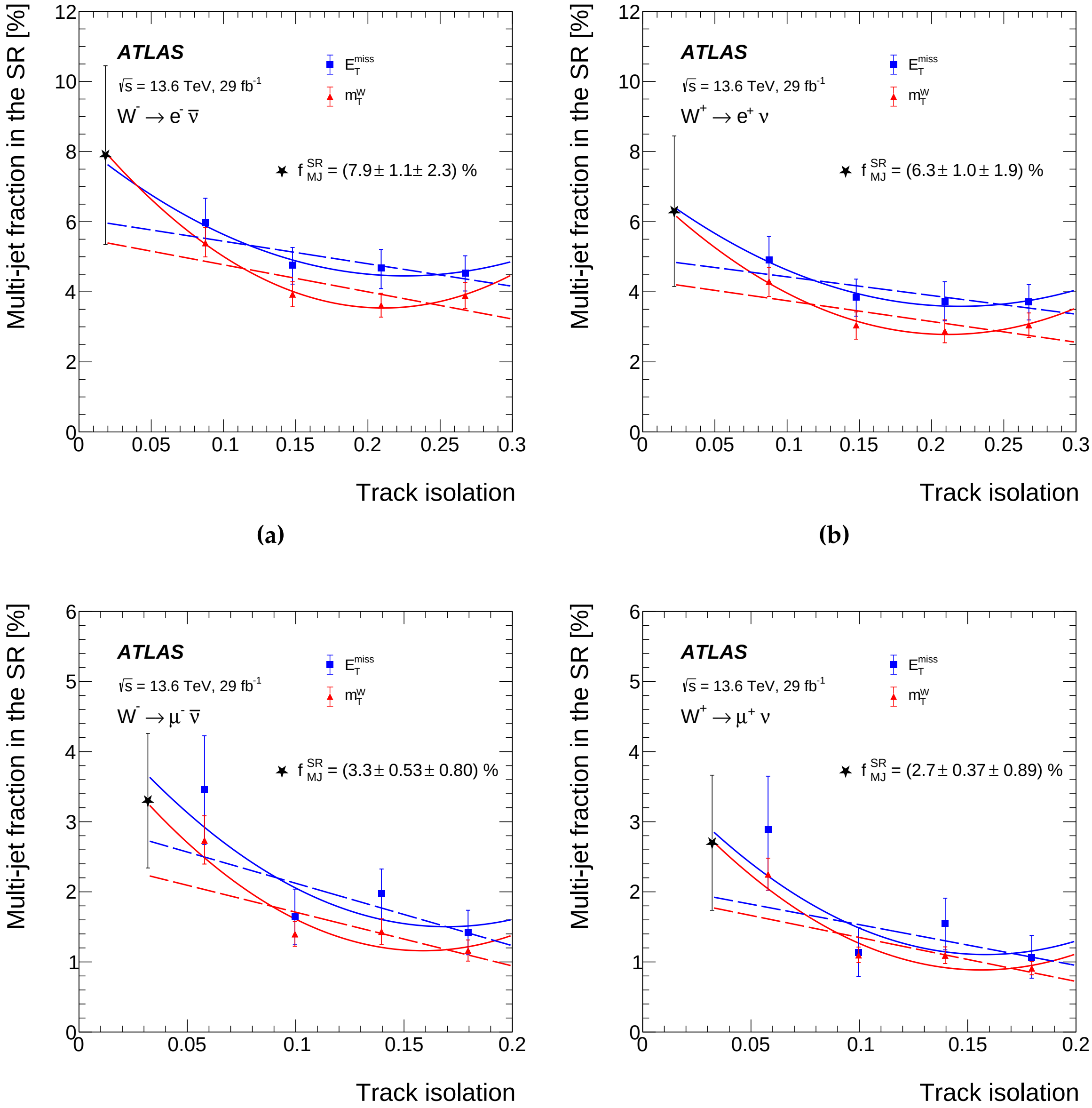

(a) (b)

(c) (d)

Figure 5.14.: Relative multijet yield in the SR as a function of the track isolation variable for (a) the $W^- \rightarrow e^-\bar{\nu}$ channel, (b) the $W^+ \rightarrow e^+\nu$ channel, (c) the $W^- \rightarrow \mu^-\bar{\nu}$ channel and (d) the $W^+ \rightarrow \mu^+\nu$ channel. Results obtained using the $E_{\mathrm{T}}^{\mathrm{miss}}$ and the m_{T}^{W} distributions are shown in blue and in red respectively, with the markers indicating the input measurements. The lines represent the extrapolation of the points to the signal region using a quadratic function (solid lines) and linear function (dashed lines). The x-axis corresponds to the position of the average of a track-isolation slice in the track isolation. $N_{\mathrm{MJ}}^{\mathrm{SR}}$, represented as a starred marker, denotes the final MJ fraction and is calculated using the weighted average of the quadratic fits in each channel. The first uncertainty on $N_{\mathrm{MJ}}^{\mathrm{SR}}$ corresponds to the weighted average between the fit uncertainty and the difference between the m_{T}^{W} and $E_{\mathrm{T}}^{\mathrm{miss}}$ quadratic fits, while the second is due to the difference between linear and quadratic fit results [1].

.

Table 5.7.: The four regions used to extract the MJ background using an alternative method.

Fit region (FR)	Signal region (SR)
$E_{\mathrm{T}}^{\mathrm{miss}} > 0\,\mathrm{GeV}$ $m_{\mathrm{T}}^{W} > 0\,\mathrm{GeV}$ Pass isolation	$E_{\mathrm{T}}^{\mathrm{miss}} > 25\,\mathrm{GeV}$ $m_{\mathrm{T}}^{W} > 50\,\mathrm{GeV}$ Pass isolation
Control region 1 (CR1)	**Control region 2 (CR2)**
$E_{\mathrm{T}}^{\mathrm{miss}} > 0\,\mathrm{GeV}$ $m_{\mathrm{T}}^{W} > 0\,\mathrm{GeV}$ Fail isolation	$E_{\mathrm{T}}^{\mathrm{miss}} > 25\,\mathrm{GeV}$ $m_{\mathrm{T}}^{W} > 50\,\mathrm{GeV}$ Fail isolation

Multijet templates are produced using the same approach, where data is collected using the support triggers from Table 5.2, and the contamination from the signal and other backgrounds is subtracted using MC. The multijet normalisation is then extracted from profile likelihood fits in the FR using a simpler approach for handling systematic uncertainties. These are included only as normalisation contraints for the luminosity (2.2%), signal experimental uncertainty (5%) and single boson modelling (5%), modelled using Gaussian terms for each. Similarly to method 3 presented in Section 5.2, Poisson terms are included for each bin as nuisance parameters to account for the multijet template statistical uncertainty.

Figure 5.15 shows the pre-fit and post-fit distributions of the multijet and the EW processes obtained from isolation slice 1 (iso1) for the $W^{-} \rightarrow e^{-}\bar{\nu}$ channel based on the $E_{\mathrm{T}}^{\mathrm{miss}}$ distribution, as well as the post-fit multijet signal strength, nuisance parameters and gamma parameters. The fitting region for the fit is reduced to [0, 30] GeV in order to avoid the peak and the tail of these distributions, where the multijet contribution is very small and the signal contamination dominates.

The multijet yields obtained from $E_{\mathrm{T}}^{\mathrm{miss}}$ and m_{T}^{W} profile likelihood template fits in the FR are then extrapolated to the SR and a track isolation scan over these results is performed, in the same approach as for method 3. Figures C.11 and C.12 in Appendix C show the results for the linear and quadratic track isolation scans for method 2.

Another simpler method for estimating the multijet background, denoted method 1, involves the same event regions as method 2, but where the data in the control regions is selected using the nominal triggers from Table 4.5. As the lowest threshold triggers, `HLT_e26_lhtight_ivarloose_L1EM22VHI` and `HLT_mu24_ivarmedium_L1MU14FCH` have tight track isolation cuts at $p_{\mathrm{T}}^{\mathrm{varcone20}}/p_{\mathrm{T}} < 0.1$ and $p_{\mathrm{T}}^{\mathrm{varcone30}}/p_{\mathrm{T}} < 0.07$ respectively,

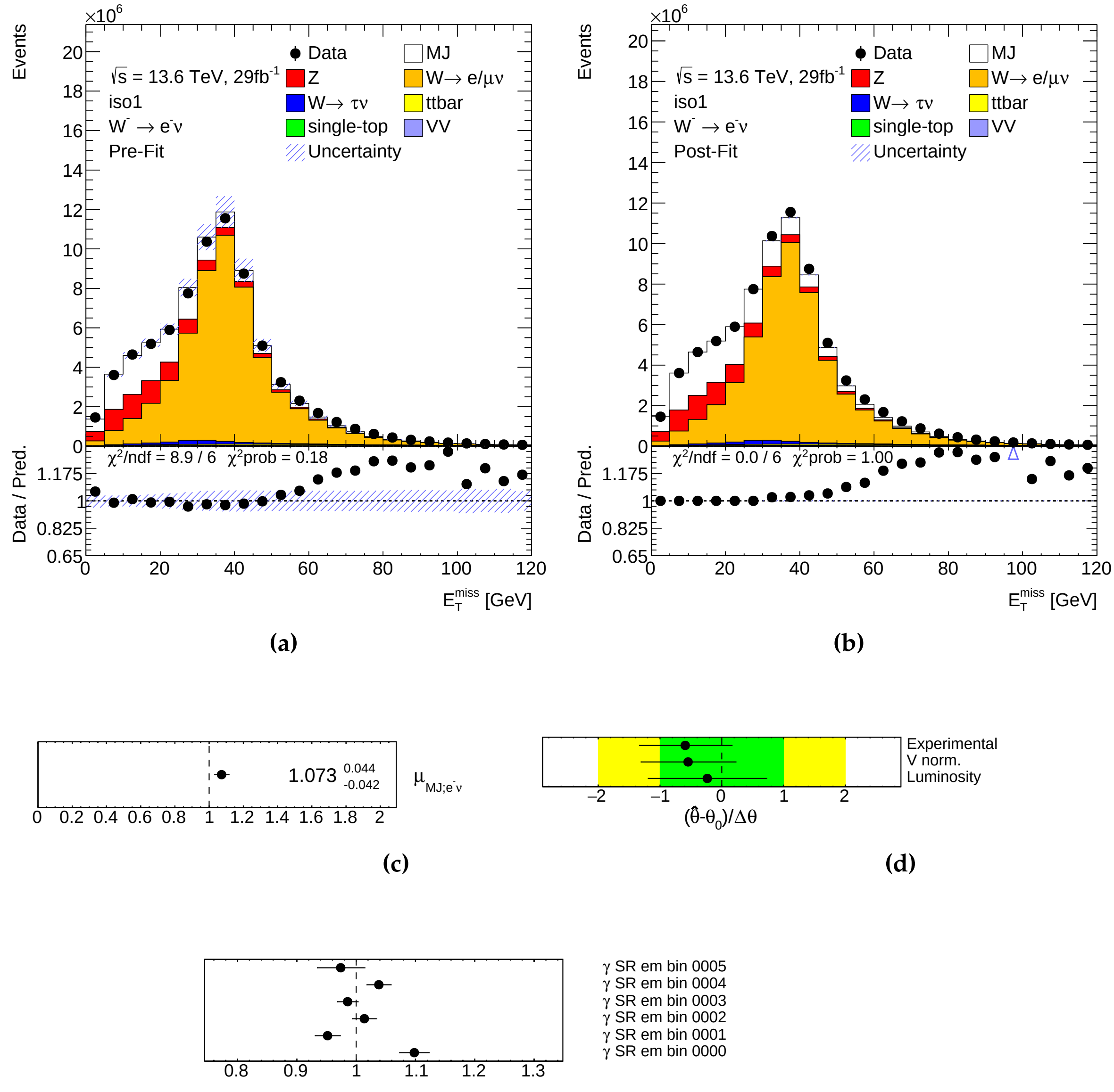

(a)

(b)

(c)

(d)

(e)

Figure 5.15.: The (a) pre-fit and (b) post-fit distribution for the $W^- \to e^-\bar{\nu}$ channel on the $E_{\mathrm{T}}^{\mathrm{miss}}$ distribution using the multijet template obtained from isolation slice 1 (iso1). In the post-fit plots, scale factors on the MJ template and on the EW processes resulting from the fit are also applied outside the fit region. The dashed error band in the pre-fit figure (a) gives the total systematic uncertainty before the fit, while in the post-fit figure (b), it represents the statistical uncertainty derived from the fit. Post-fit results including (c) the multijet signal strength, (d) nuisance parameters pulls and (e) gamma parameters are also illustrated.

no isolation slices are defined. Instead, only two multijet templates are defined for each channel, using the $E_{\mathrm{T}}^{\mathrm{miss}}$ and m_{T}^{W} distributions obtained from CR1. A similar template fit to that from method 2 is performed in the FR, and the final MJ yield in each channel is given by the average between the $E_{\mathrm{T}}^{\mathrm{miss}}$ and m_{T}^{W} fit results, extrapolated to SR using a similar extrapolation factor based on the MJ ratio between CR2 and CR1.

An advantage of method 1 is that by using unprescaled triggers, the multijet templates are sufficiently populated and do not suffer from large statistical fluctuations as for those in method 2 and the nominal method. The largest disadvantage, however, is that the lowest threshold nominal triggers have track isolation requirements, so it is not possible to perform a track isolation scan on the multijet yields. Thus this method does not take into account the bias due to the isolation on the lepton.

The results from each of the three methods are presented in Figure 5.16, which shows the multijet yields in the SR and uncertainties from the $E_{\mathrm{T}}^{\mathrm{miss}}$ and m_{T}^{W} fits, and the weighted average for each of the four W-boson channels. The nominal multijet yield presented in Section 5.2.5 is displayed as a red line, and the uncertainty associated with this as a yellow band. The results from all three methods agree, within uncertainties.

In addition to methods 1 and 2, the potential to use the calorimeter isolation variable as the scanning variable was also studied, using either the nominal or the support triggers. Using a method similar to method 3, multijet templates were produced in four calorimeter isolation slices. When using the nominal triggers to select data in the control regions, the contamination from signal and other backgrounds was found to be too large to sufficiently populate the multijet templates after subtracting these contributions from the data. On the other hand, when the using support triggers to select data in the control regions, the statistical precision was too limited to extract a meaningful multijet estimate. Several definitions for calorimeter slices were tested in an attempt to sufficiently populate the multijet templates, though none yielded satisfactory results.

Several methods for estimating the multijet background in the W boson channels have been presented in this Chapter, where method 3, described in Section 5.2, is chosen as the nominal method. The multijet yields obtained using this method, displayed in Table 5.6, are used to calculate the W boson cross sections, which are presented in Chapter 6.

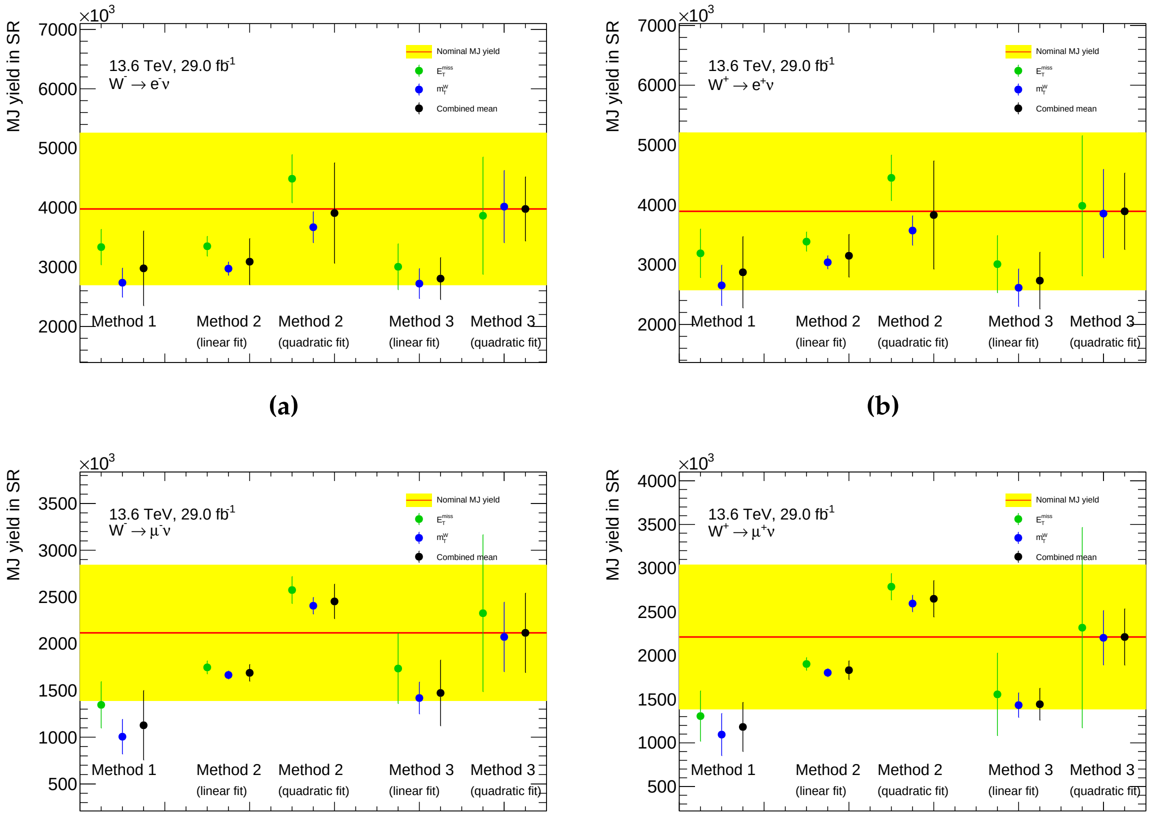

(a) (b)

(c) (d)

Figure 5.16.: Multijet yields in the SR calculated using the three methods presented so far for (a) the $W^- \rightarrow e^-\bar{\nu}$ channel, (b) the $W^+ \rightarrow e^+\nu$ channel, (c) the $W^- \rightarrow \mu^-\bar{\nu}$ channel and (d) the $W^+ \rightarrow \mu^+\nu$ channel. Results are presented from fits using the $E_{\mathrm{T}}^{\mathrm{miss}}$ and m_{T}^{W} distributions, and linear and quadratic extrapolations in the case of methods 2 and 3. The nominal multijet yield is given by the weighted average between the $E_{\mathrm{T}}^{\mathrm{miss}}$ and m_{T}^{W} method 3 quadratic fits, with contributions to the uncertainty from the weighted average, difference between the $E_{\mathrm{T}}^{\mathrm{miss}}$ and m_{T}^{W} quadratic fits, and difference between the linear and quadratic fits, as detailed in Section 5.2.

.

Chapter 6.

Results

In this Chapter, measured results for the W and Z inclusive production cross sections, their ratios, and the $t\bar{t}$ and $W^{\pm}$ fiducial cross-section ratios are presented, and compared to the theory predictions presented in Section 4.5.

The fiducial cross sections and their ratios are extracted using a profile likelihood fit (detailed in Section 6.1), using two Z boson channels, $Z \to e^{+}e^{-}$ and $Z \to \mu^{+}\mu^{-}$, and four W boson channels, $W^{+} \to e^{+}\nu$, $W^{-} \to e^{-}\bar{\nu}$, $W^{+} \to \mu^{+}\nu$, and $W^{-} \to \mu^{-}\bar{\nu}$. The $t\bar{t}$ and $W^{\pm}$ fiducial cross-section ratios are extracted from the same channels and additionally the two $t\bar{t}$ channels from Ref. [107], with one or two b-tagged jets. The fiducial cross sections are presented in Section 6.2. Fiducial cross-section ratios are presented in Section 6.3 and the energy dependence of the total cross sections of the W^{+}, W^{-} and Z bosons is presented in Section 6.4.

All results presented in this Chapter are published in Ref. [1].

6.1. Statistical Analysis

Fiducial cross sections and their ratios are extracted using the profile likelihood fit method, as described in Section 4.1.1. The W and Z boson fiducial cross sections, $\sigma_{W^{-}\to\ell^{-}\bar{\nu}}$ $\sigma_{W^{+}\to\ell^{+}\nu}$ and $\sigma_{Z\to\ell^{+}\ell^{-}}$ are extracted from simultaneous fits using the two Z boson channels, $Z \to e^{+}e^{-}$ and $Z \to \mu^{+}\mu^{-}$, and the four W boson channels, $W^{+} \to e^{+}\nu$, $W^{-} \to e^{-}\bar{\nu}$, $W^{+} \to \mu^{+}\nu$, and $W^{-} \to \mu^{-}\bar{\nu}$. A single bin per channel is used in all cross-section fits. Thus the likelihood function from Eq. (4.4) becomes

$$L(\vec{n};\mu_s,\vec{\theta}) = \prod_{c\in\text{channels}} \text{Pois}(n_{\text{data}}|\mu_{s,c}S_c(\vec{\theta}) + B_c(\vec{\theta})) \prod_{i\in\text{NPs}} G(\theta_i)\,, \tag{6.1}$$

where the product of Poissonian probabilities is over channels. Systematic uncertainties, described in Section 4.6, are included as nuisance parameters, $\vec{\theta}$, in the fit.

The fiducial cross-section ratios are extracted using simultaneous fits as well. As the signal strength for the W^+ boson, μ_{W^+} can be expressed as the product between the W^+ to W^- ratio, R_{W^+/W^-}, and the W^- signal strength, μ_{W^-}, the likelihood from Eq. (6.1) can be re-written as

$$\begin{aligned} L(\vec{n};\mu_s,\vec{\theta}) = & \prod_{c\in W^+\ \text{channels}} \text{Pois}(n_{\text{data}}|R_{W^+/W^-}\ \mu_{W^-}S_c(\vec{\theta}) + B_c(\vec{\theta})) \times \\ & \prod_{c\in W^-\ \text{channels}} \text{Pois}(n_{\text{data}}|\mu_{W^-}S_c(\vec{\theta}) + B_c(\vec{\theta})) \times \\ & \prod_{c\in Z\ \text{channels}} \text{Pois}(n_{\text{data}}|\mu_Z S_c(\vec{\theta}) + B_c(\vec{\theta})) \prod_{i\in\text{NPs}} G(\theta_i)\,. \end{aligned}$$

The ratio $R_{W^\pm/Z}$ is extracted in the same manner by rearranging the likelihood in terms of this ratio. Several fits are performed using the same channels and changing the parameter of interest for each fit. For the ratios $R_{t\bar{t}/W^\pm}$, $R_{t\bar{t}/W^+}$, and $R_{t\bar{t}/W^-}$, two additional $t\bar{t}$ channels are included in the fit, using the results published in [107].

The fiducial cross sections, σ^{fid}, are then calculated by multiplying the signal strength parameter, μ, obtained from the fits with the predicted cross sections used for the simulated signal samples, presented in Table 4.2 in Section 4.2.2. Uncertainties on μ obtained from the fits are propagated to uncertainties on σ^{fid}. Total cross sections, σ^{tot}, are calculated by extrapolating the fiducial cross section σ^{fid} to the full phase-space, using the acceptance A, as described in Section 4.1.

The impact of the fits on the systematic uncertainties is shown in Table 6.1, where nuisance parameters associated to uncertainties arising from similar sources are grouped into the same category. The impact is assessed for each category by fixing the nuisance parameters from that category to their best-fit values as constants, and

Table 6.1.: Observed impact (in %) of the different sources of uncertainty on the measured fiducial cross sections [1].

Category	$\sigma(Z \to ee)$	$\sigma(Z \to \mu\mu)$	$\sigma(Z \to \ell\ell)$	$\sigma(W^- \to e^-\bar{\nu})$	$\sigma(W^+ \to e^+\nu)$	$\sigma(W^- \to \mu^-\bar{\nu})$	$\sigma(W^+ \to \mu^+\nu)$
Luminosity	2.2	2.2	2.2	2.5	2.5	2.5	2.4
Pile-up	1.2	0.3	0.8	1.1	1.1	0.3	0.4
MC statistics	< 0.2	< 0.2	< 0.2	< 0.2	0.4	< 0.2	0.4
Lepton trigger	0.2	0.4	0.2	1.2	1.3	1.0	1.0
Electron reconstruction	1.4	–	0.9	0.7	0.8	–	–
Muon reconstruction	–	2.1	1.4	–	–	1.0	1.0
Multi-jet	–	–	–	2.9	2.4	1.3	1.1
Other background modelling	< 0.2	< 0.2	< 0.2	< 0.2	< 0.2	0.5	0.4
Jet energy scale	–	–	–	1.4	1.4	1.3	1.4
Jet energy resolution	–	–	–	< 0.2	0.3	0.2	0.2
NNJVT	–	–	–	1.6	1.5	1.3	1.3
$E_{\mathrm{T}}^{\mathrm{miss}}$ track soft term	–	–	–	< 0.2	0.4	< 0.2	< 0.2
PDF	0.2	0.2	< 0.2	0.8	0.8	0.6	0.5
QCD scale (ME and PS)	0.6	< 0.2	0.3	1.3	1.2	0.6	0.6
Flavour tagging	–	–	–	–	–	–	–
$t\bar{t}$ modelling	–	–	–	–	–	–	–
Total systematic impact [%]	3.0	3.1	2.7	5.0	4.5	3.8	3.6
Statistical impact [%]	0.04	0.03	0.02	0.02	0.01	0.01	0.01

Category	$\sigma(W^- \to \ell^-\bar{\nu})$	$\sigma(W^+ \to \ell^+\nu)$	$\sigma(W^\pm \to \ell\nu)$	R_{W^+/W^-}	$R_{W^\pm/Z}$	$R_{t\bar{t}/W^\pm}$
Luminosity	2.5	2.4	2.4	< 0.2	0.3	< 0.2
Pile-up	0.5	0.7	0.6	< 0.2	< 0.2	< 0.2
MC statistics	< 0.2	0.2	< 0.2	< 0.2	< 0.2	< 0.2
Lepton trigger	1.0	0.9	0.9	< 0.2	0.7	0.8
Electron reconstruction	0.4	0.5	0.4	< 0.2	0.5	0.4
Muon reconstruction	0.6	0.6	0.6	0.2	0.8	0.6
Multi-jet	1.2	1.2	1.2	1.6	1.1	1.0
Other background modelling	0.4	0.4	0.4	< 0.2	0.3	0.9
Jet energy scale	1.3	1.3	1.3	< 0.2	1.3	1.3
Jet energy resolution	< 0.2	0.2	< 0.2	< 0.2	< 0.2	< 0.2
NNJVT	1.4	1.3	1.3	< 0.2	1.3	< 0.2
$E_{\mathrm{T}}^{\mathrm{miss}}$ track soft term	< 0.2	0.3	0.3	< 0.2	0.3	0.3
PDF	0.5	0.5	0.3	0.5	0.2	0.4
QCD scale (ME and PS)	0.8	0.7	0.6	< 0.2	0.7	0.7
Flavour tagging	–	–	–	–	–	< 0.2
$t\bar{t}$ modelling	–	–	–	–	–	1.1
Total systematic impact [%]	3.7	3.5	3.5	1.7	2.4	2.5
Statistical impact [%]	0.01	0.01	0.01	0.01	0.02	0.32

performing the fit again. The result is a reduced uncertainty on the signal strength μ, compared to the nominal uncertainty. Thus, the impact is the difference (in quadrature) between these two uncertainties, assessed separately for results in each channel.

The comparison between data and predictions before and after the fits in all regions is shown in Figure 6.1. For the single lepton W and same flavour di-lepton Z boson channels, good agreement is observed between the predictions and data after the fit. In the $e\mu$ regions from the $t\bar{t}$ selection, however, the data event yields are slightly lower than the predictions in the pre-fit.

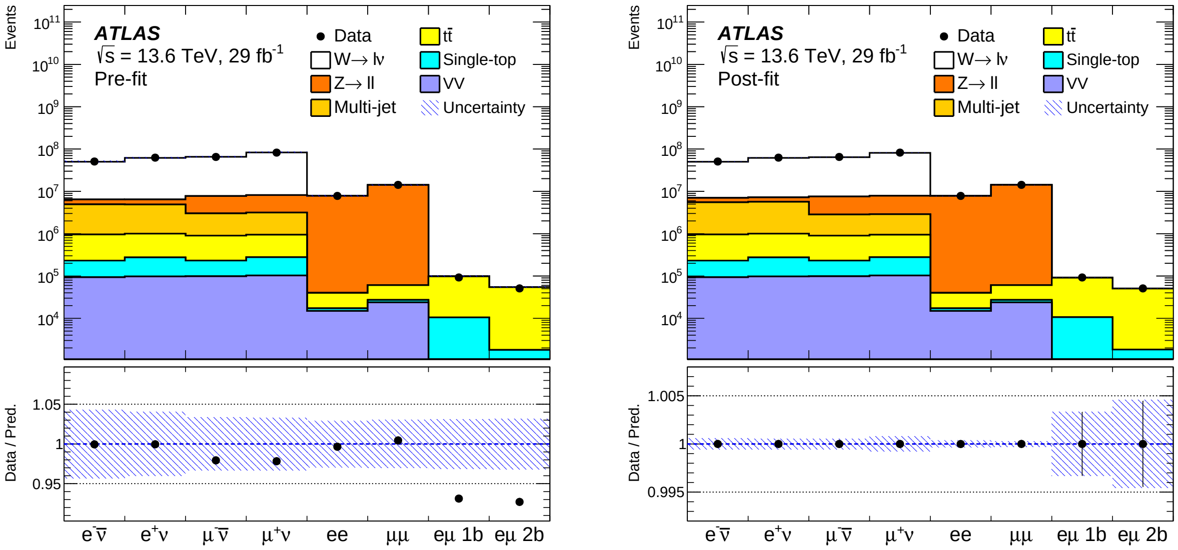

(a) **(b)**

Figure 6.1.: Comparison of the number of data events in each channel with the predictions shown (a) before and (b) after the fits. The dashed error band in the pre-fit figure gives the total systematic uncertainty before the fit, while in the post-fit figure, it represents the statistical uncertainty derived from the fit [1].

Results for the measured fiducial cross sections, their ratios, the total cross sections and the corresponding acceptance factors used to calculate these are summarised in Table 6.2.

6.2. Fiducial cross sections

Figure 6.2 compares the measured results for the W^-, W^+ and Z fiducial cross sections to the theoretical predictions calculated using different PDF sets, as described in Section 4.5. The results are presented as ratios to the measured fiducial cross sections, such that the measured results are equal to 1, and the different theoretical predictions can be easily compared. The largest source of theoretical uncertainties is the PDF uncertainties, represented by the inner error bars. Systematic uncertainties are represented by shaded bands, where the impact of the luminosity uncertainty is highlighted separately as this represents the largest source of uncertainty for all three fiducial cross sections. For the W^+ and W^- fiducial cross sections, the other largest contributions

Table 6.2.: Summary of the measured cross sections for the W and Z bosons and their ratios, as well as the $t\bar{t}$ to W boson ratios. Total uncertainties are quoted, where the uncertainties uncertainty are negligibly small compared to the systematic uncertainties. Rounding has been applied to all quoted numbers [1].

Channel	$\sigma^{\text{fid}} \pm \delta\sigma_{\text{stat}\oplus\text{syst}}$ [pb]	Acceptance A	$\sigma^{\text{tot}} \pm \delta\sigma_{\text{stat}\oplus\text{syst}}$ [pb]
$Z \to e^+e^-$	740 ± 22	0.374 ± 0.011	1981 ± 82
$Z \to \mu^+\mu^-$	747 ± 23	0.374 ± 0.011	1997 ± 82
$Z \to \ell^+\ell^-$	744 ± 20	0.374 ± 0.011	1989 ± 77
$W^- \to e^-\bar{\nu}$	3380 ± 170	0.381 ± 0.009	8880 ± 490
$W^- \to \mu^-\bar{\nu}$	3310 ± 130	0.381 ± 0.009	8680 ± 390
$W^- \to \ell^-\bar{\nu}$	3310 ± 120	0.381 ± 0.009	8690 ± 390
$W^+ \to e^+\nu$	4350 ± 200	0.366 ± 0.009	11880 ± 620
$W^+ \to \mu^+\nu$	4240 ± 160	0.365 ± 0.010	11620 ± 530
$W^+ \to \ell^+\nu$	4250 ± 150	0.366 ± 0.009	11620 ± 520
$W^\pm \to \ell^\pm\nu$	7560 ± 270	0.372 ± 0.009	20310 ± 890

Ratio	$R \pm \delta R_{\text{stat}\oplus\text{syst}}$
W^+/W^-	1.286 ± 0.022
$W^\pm/Z$	10.17 ± 0.25
$t\bar{t}/W^-$	0.256 ± 0.008
$t\bar{t}/W^+$	0.199 ± 0.006
$t\bar{t}/W^\pm$	0.112 ± 0.003

to the total uncertainty are the multijet and jet-related (NNJVT and jet energy scale) uncertainties, as shown in Table 6.1. For the Z fiducial cross section, the electron and muon reconstruction uncertainties also dominate. An overall good agreement is observed between all measured fiducial cross sections and predictions, where the largest difference from the measured result is observed for the prediction calculated using the ATLASpdf21 PDF set.

6.3. Fiducial cross-section ratios

Fiducial cross-section ratios benefit from cancellations of systematic uncertainties, and thus have smaller overall uncertainties. Additionally, due to the different production dynamics for W^+, W^- and Z bosons at the LHC, as described in Section 1.2.2, ratios of their fiducial cross sections are sensitive to different PDFs [17]. The ratio of W^+ to W^-

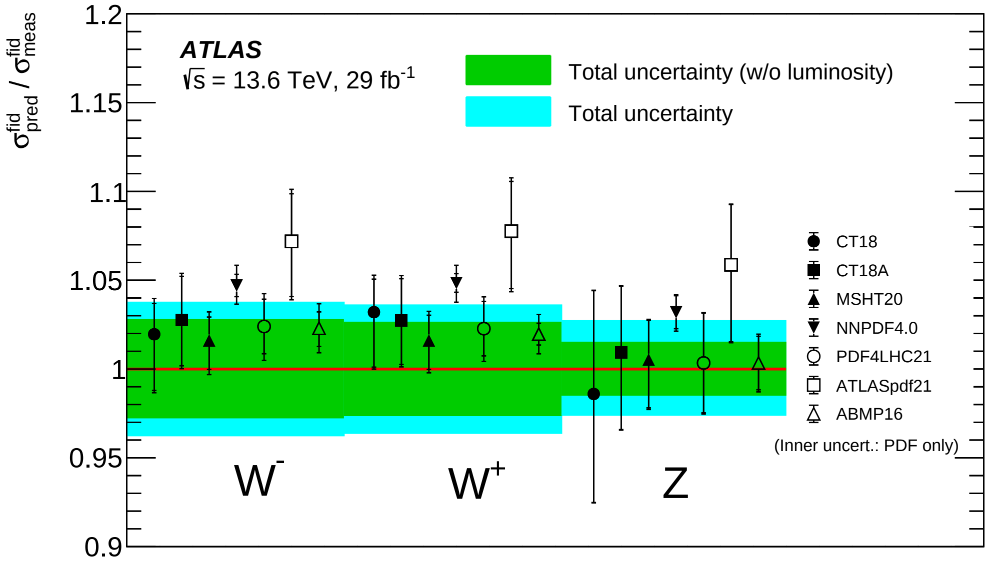

Figure 6.2.: Ratios between the theoretical predictions obtained with different PDF sets and unfolded fiducial cross sections for: W^-, W^+ and Z bosons. The error bars on the predictions correspond to the theory uncertainties discussed in Section 4.5, where the inner error bars represent the contributions from PDF uncertainty. The inner (outer) band corresponds to the experimental uncertainty without (with) the luminosity uncertainty [1].

production, R_{W^+/W^-}, is sensitive to the $u_V - d_V$ valence quark distribution function at low Bjorken-x while the ratio of $W^\pm$ to Z production, $R_{W^\pm/Z}$, is sensitive to the $s - \bar{s}$ strange quark distribution function. Additionally, as $t\bar{t}$ production is mostly driven by the gluon PDF at high Bjorken-x values, the $t\bar{t}$ and $W^\pm$ ratios are sensitive to the gluon-to-quark PDF ratio [156]. Thus, measured cross-section ratios may have constraining power to PDFs.

Figure 6.3 shows the fiducial cross-section ratios $R_{W^\pm/Z}$ and R_{W^+/W^-}, where these are compared with theory predictions calculated using different PDF sets. An overall good agreement is again observed between the measured results and predictions using all PDF sets. Systematic uncertainties are represented by a shaded band, showing no contribution from luminosity uncertainties as these are fully correlated between the different measured fiducial cross sections and are cancelled in the ratios. Thus, the dominant sources of uncertainty for the R_{W^+/W^-} ratio comes from the multijet uncertainties, which are treated as uncorrelated between the four W boson channels and do not cancel in the ratio. For the $R_{W^\pm/Z}$ ratio result, the jet-related uncertainties, NNJVT and the jet energy scale, and the multijet uncertainties dominate, as these are not considered for the Z boson cross section and thus do not cancel out in the ratio.

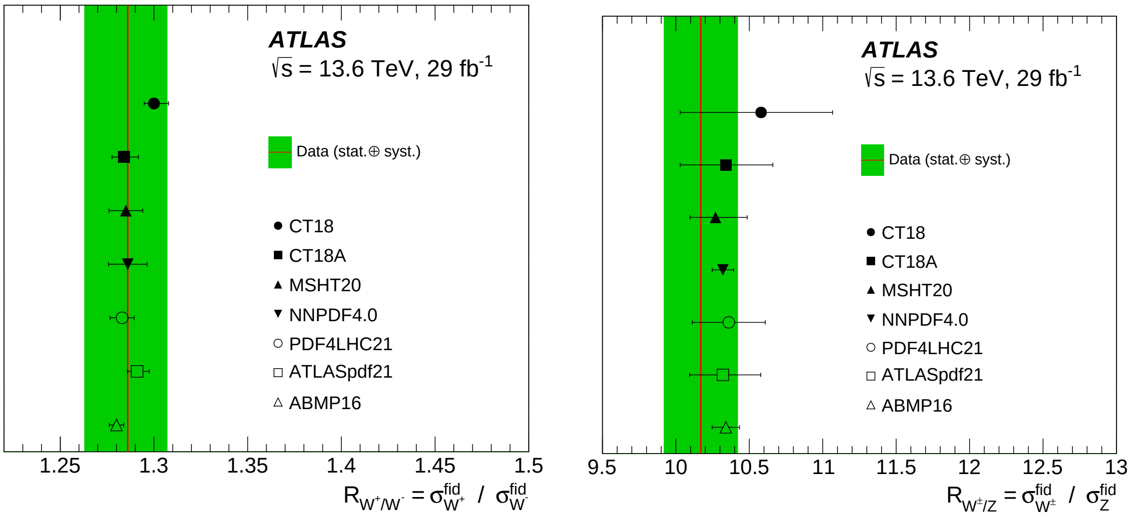

(a) **(b)**

Figure 6.3.: Comparison between theoretical predictions obtained with different PDF sets and fiducial cross-section ratios for: (a) $R_{W^\pm/Z}$ and (b) R_{W^+/W^-}. The error bars on the predictions correspond to the theory uncertainties discussed in Section 4.5. The green band shows statistical and systematic uncertainties on the data added in quadrature [1].

The fiducial cross section ratios between $t\bar{t}$ and W production, $R_{t\bar{t}/W^\pm}$, $R_{t\bar{t}/W^+}$, and $R_{t\bar{t}/W^-}$, are shown in Figure 6.4, where these are also compared to theoretical predictions calculated with different PDF sets, including predictions based on the PDF4LHC21 set calculated for alternative top-quark masses, $m_t = 171.5\,\text{GeV}$ and $m_t = 173.5\,\text{GeV}$, as well as the nominal mass, $m_t = 172.5\,\text{GeV}$. The measured results for these cross-section ratios are slightly lower than the predictions for most PDFs. Uncertainties for these ratios are dominated by the multijet, jet energy scale and $t\bar{t}$ modelling uncertainties, as these do not cancel out in the ratio.

6.4. Total cross sections

The total cross sections for the $W^\pm$ and Z bosons as a function of $\sqrt{s}$ are shown in Figure 6.5, and for the W^+ and W^- bosons in Figure 6.6. Results from this measurement are shown, as well as previous measurements performed by ATLAS at different centre-of-mass energies, referenced in the plots. The measured results are compared

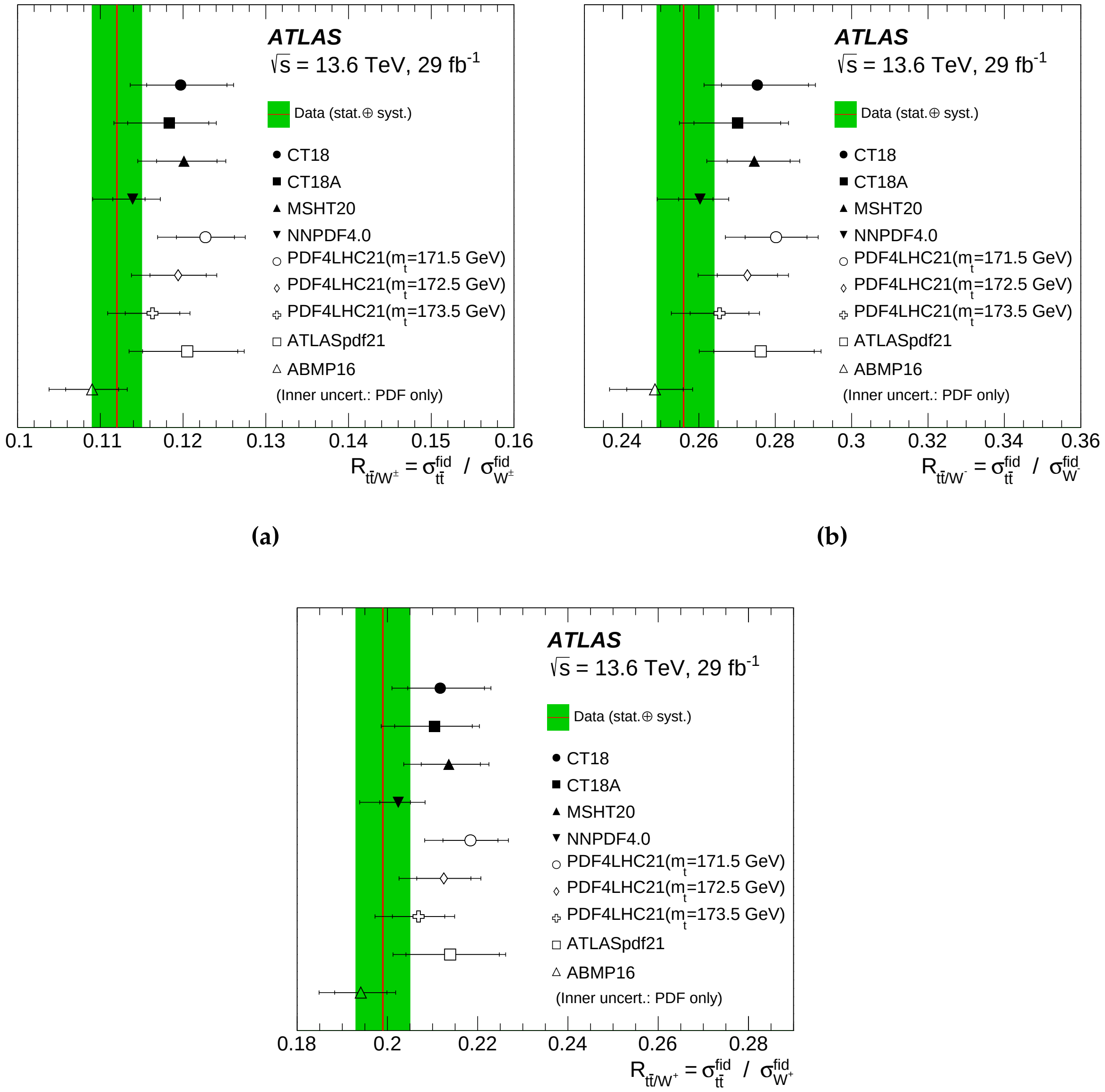

(a) **(b)**

(c)

Figure 6.4.: Comparison between theoretical predictions obtained with different PDF sets and fiducial cross-section ratios for: (a) $R_{t\bar{t}/W^{\pm}}$, (b) $R_{t\bar{t}/W^{+}}$ and (c) $R_{t\bar{t}/W^{-}}$. The error bars on the predictions correspond to the theory uncertainties discussed in Section 4.5 and, for $t\bar{t}$, in Ref. [107], with the inner error bars representing the contributions from the PDF uncertainty. The green band shows statistical and systematic uncertainties on the data added in quadrature [1].

to theoretical predictions based on the CT14NNLO PDF set [158], where the energy dependence of the total cross sections appear to be well described.

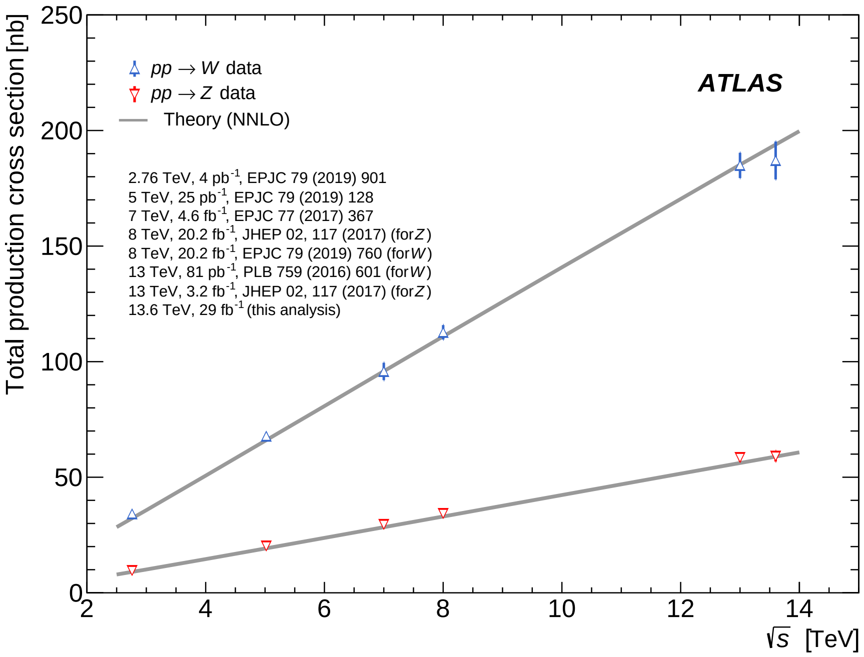

Figure 6.5.: Comparison between the central values of the NNLO predictions calculated with the CT14NNLO PDF set and ATLAS measured $W^{\pm} \to \ell^{\pm}\nu$ and $Z \to \ell^{+}\ell^{-}$ cross sections as a function of $\sqrt{s}$ [1].

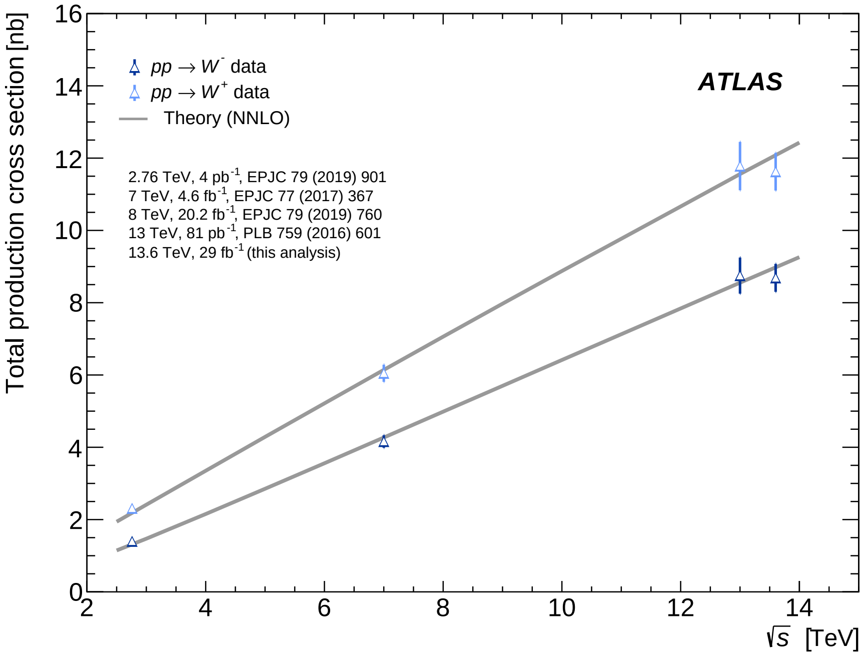

Figure 6.6.: Comparison between the central values of the NNLO predictions calculated with the CT14NNLO PDF set and ATLAS measured $W^{+} \to \ell^{+}\nu$ and $W^{-} \to \ell^{-}\bar{\nu}$ cross sections as a function of $\sqrt{s}$ [1].

Chapter 7.

Conclusion

One of the principal aims of modern high-energy physics is to continue to test predictions of the Standard Model with increasing experimental precision, a task which is achieved using the extensive amounts of proton-proton collision data generated by the LHC and recorded by detectors such as ATLAS. To extend the available dataset for such measurements, Run 3 at the LHC is currently underway, where protons are collided at twice the design instantaneous luminosity of the LHC, and at a new centre-of-mass energy of 13.6 TeV.

In order to maintain and extend its operational performance for this new regime, several sub-components of the ATLAS detector have been upgraded, including the L1Calo trigger system. New feature extractors have been added to L1Calo to replace the legacy processor modules, including the electron feature extractor (eFEX), which is capable of processing higher-granularity information from the EM calorimeter, using more complex algorithms resulting in more efficient triggers with reduced rates. The increase in the granularity of the EM calorimeter information available to the eFEX allows a new energy correction to be applied to the online energy calculation for e/γ objects identified on the eFEX. This energy correction was presented in this thesis, which was shown to correct the energy response in the different EM calorimeter layers as a function of the pseudo-rapidity, and to contribute to the increase in the efficiency of L1 single EM object triggers in Run 3.

One of the early measurements most often done at the beginning of a new energy regime at hadron colliders are the W and Z boson production cross section measurements. The very large cross sections of these processes, together with their clean experimental signatures through their leptonic decay modes allow excellent experimental precision to be reached even with smaller datasets, providing the ideal testing ground for early validation of the detector and for testing Standard Model predictions at the new centre-of-mass energy.

The measurement of the inclusive $W^{\pm}$ and Z boson production cross sections using 29 fb^{-1} of pp collision data collected by the ATLAS detector at $\sqrt{s}$ = 13.6 TeV was presented in this thesis. The data-driven measurement of the QCD multijet background for the W boson cross-section measurements was also presented, where the multijet contribution in the signal region used for the cross-section fit was estimated using several control regions, obtained by inverting the lepton isolation and kinematic selection requirements in the event selection. A correction for the choice of lepton isolation in the definition of the multijet normalisation was also performed.

The fiducial cross sections for the production of $W^{+} \rightarrow \ell^{+}\nu$, $W^{-} \rightarrow \ell^{-}\bar{\nu}$ and $Z \rightarrow \ell^{+}\ell^{-}$ bosons were measured to be 4250 ± 150 pb, 3310 ± 120 pb, and 744 ± 20 pb, respectively, where the uncertainties correspond to the total uncertainties. The fiducial cross-section ratios $R_{W^{+}/W^{-}}$ and $R_{W^{\pm}/Z}$ were also presented, where cancellations of systematic uncertainties, including the 2.2% luminosity uncertainty, resulted in reduced uncertainties in the ratios. These measurements were compared to Standard Model predictions calculated using different PDF sets, where good agreement was found for all results. The $R_{t\bar{t}/W^{\pm}}$, $R_{t\bar{t}/W^{+}}$, and $R_{t\bar{t}/W^{-}}$ fiducial cross-section ratios were also presented, where these measurements were also found to be in agreement with Standard Model predictions, although slightly lower than the predictions for most PDF sets. Finally, the energy dependence on the total cross sections for W^{+}, W^{-} and Z boson production was assessed, and found to be in good agreement with Standard Model predictions.

This measurement, performed during the early period of Run 3 data taking, is essential for evaluating the performance of the detector and reconstruction software. As the W and Z boson production cross sections are very large, this measurement is limited by systematic uncertainties rather than statistical, despite only using a partial Run 3 dataset. Some uncertainties, such as those related to lepton reconstruction and calibration, are expected to be reduced as more data is collected during Run 3, such that future measurements of the W and Z boson cross sections are expected to have improved precision.

Appendix A.

Additional plots for dead material corrections

The plots provided in this appendix illustrate Gaussian fit performed to calculate the mean response and its uncertainty in $\Delta\eta^{TOB} = 0.1$ bins, as shown in Figure 3.7. The fits performed for the $0.0 < |\eta^{TOB}| < 0.1$ and $1.3 < |\eta^{TOB}| < 1.4$ bins are shown in Figure A.1 before the simulation-based corrections are applied, and for the same bins in Figure A.2 after these corrections are applied. Similar fits are performed for the mean response for data-driven corrections shown in Figure 3.10.

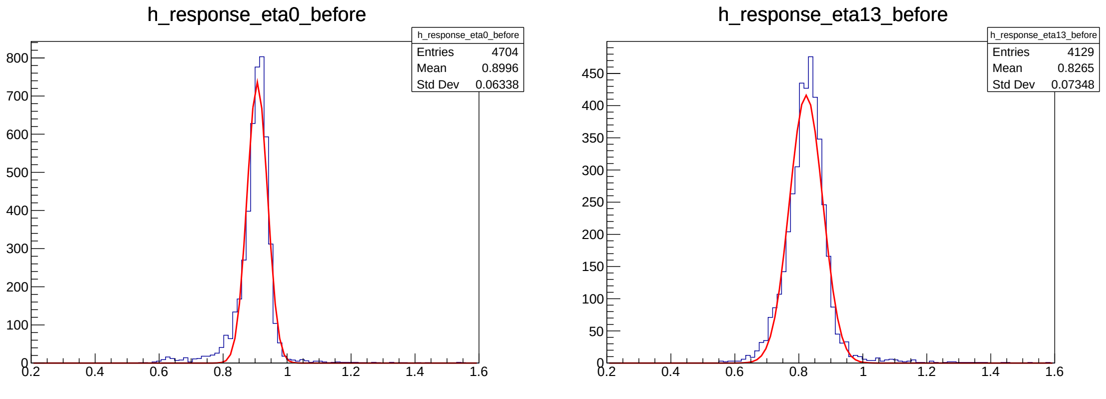

(a) **(b)**

Figure A.1.: Gaussian fits performed for the calculation of the mean response and its uncertainty before simulation-based corrections are applied, in the $0.0 < |\eta^{TOB}| < 0.1$ (left) and $1.3 < |\eta^{TOB}| < 1.4$ (right) bins, as shown in Figure 3.7.

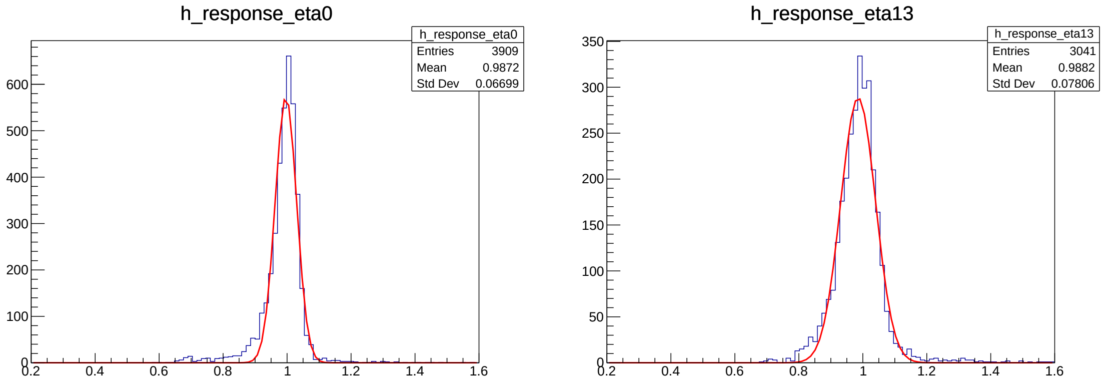

(a) **(b)**

Figure A.2.: Gaussian fits performed for the calculation of the mean response and its uncertainty after simulation-based corrections are applied, in the $0.0 < |\eta^{TOB}| < 0.1$ (left) and $1.3 < |\eta^{TOB}| < 1.4$ (right) bins, as shown in Figure 3.7.

Appendix B.

Additional validation plots for *W* channels

In this appendix, additional kinematic distribution for the missing transverse energy magnitude $E_{\mathrm{T}}^{\mathrm{miss}}$, and the lepton p_{T}, η and ϕ in the four W boson channels are provided. The corresponding distributions for the W boson transverse mass are found in Figure 4.3 in Section 4.7

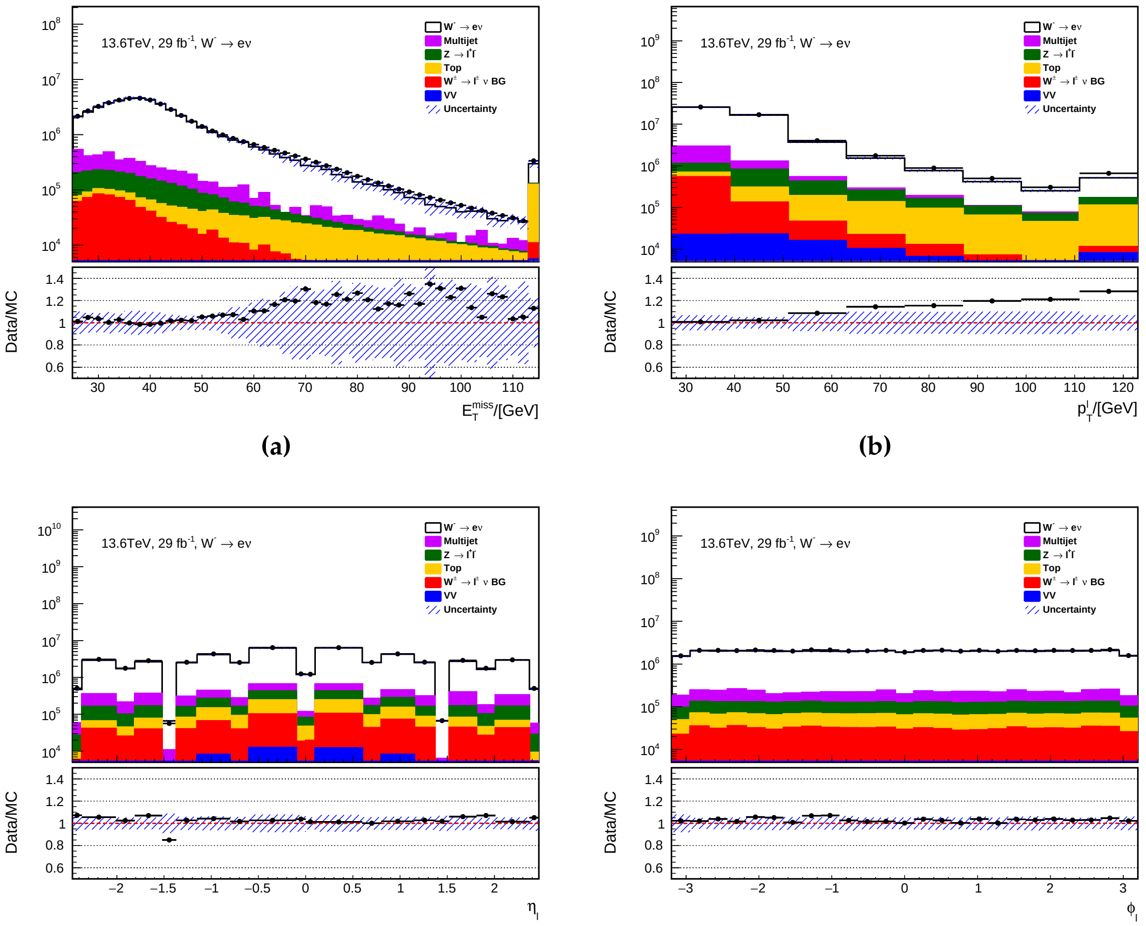

(a) **(b)**

(c) **(d)**

Figure B.1.: Comparison of data (black markers) and predictions (stacked histograms) for $E_{\mathrm{T}}^{\mathrm{miss}}$, lepton p_{T}, η and ϕ for the $W^{-} \to e^{-}\bar{\nu}$ channel. The blue hashed band in the ratio plot denotes the total systematic uncertainty on the prediction.

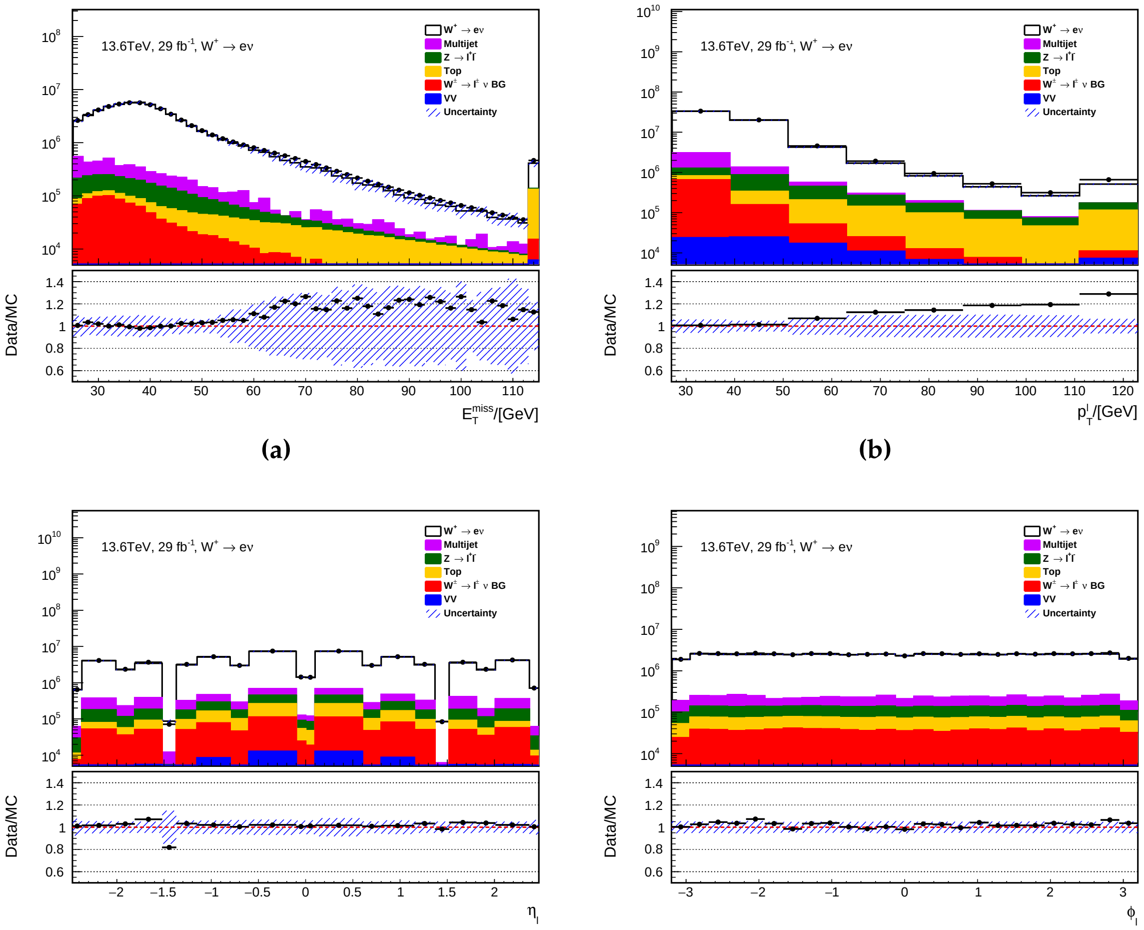

(a) **(b)** **(c)** **(d)**

Figure B.2.: Comparison of data (black markers) and predictions (stacked histograms) for $E_{\mathrm{T}}^{\mathrm{miss}}$, lepton p_{T}, η and ϕ for the $W^{+} \rightarrow e^{+}\nu$ channel. The blue hashed band in the ratio plot denotes the total systematic uncertainty on the prediction.

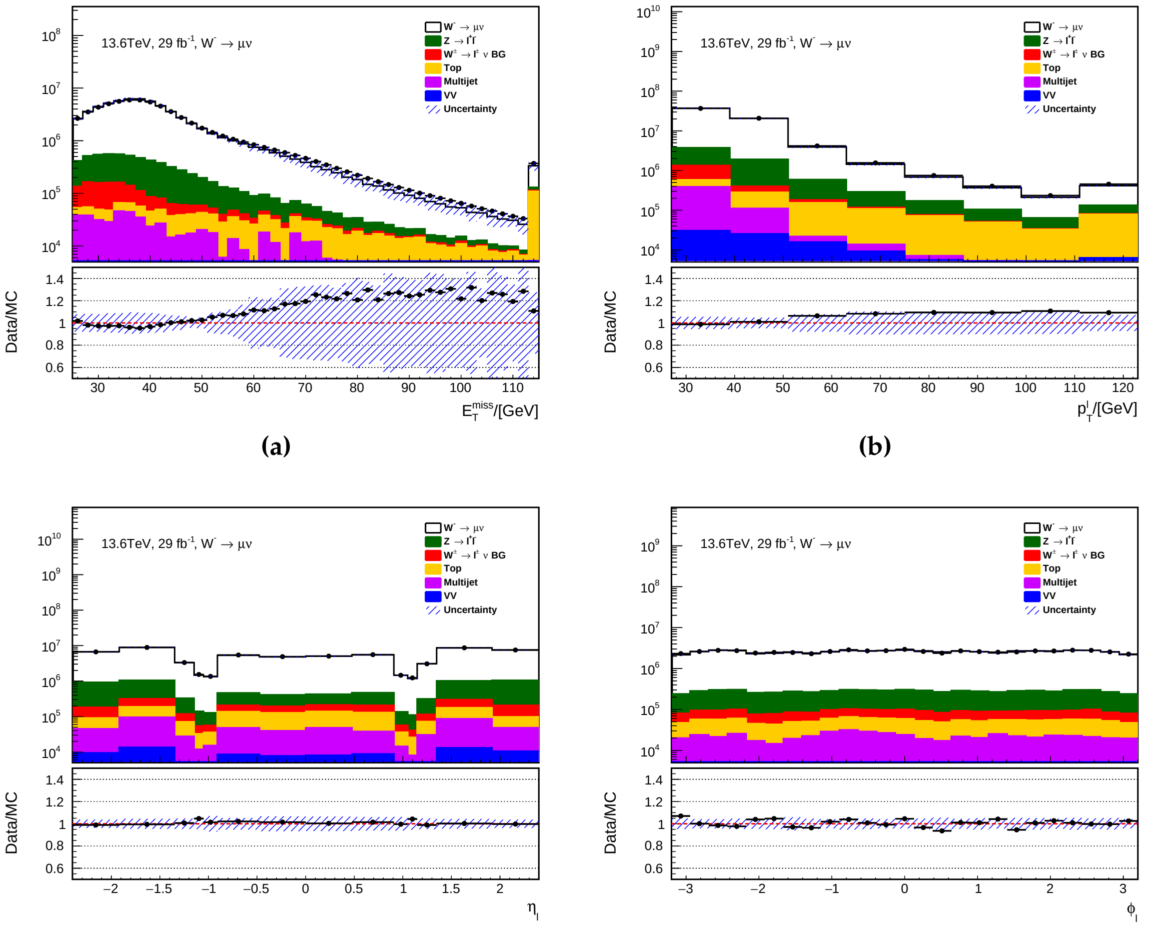

(a) (b)

(c) (d)

Figure B.3.: Comparison of data (black markers) and predictions (stacked histograms) for $E_{\mathrm{T}}^{\mathrm{miss}}$, lepton p_{T}, η and ϕ for the $W^{-} \to \mu^{-}\bar{\nu}$ channel. The blue hashed band in the ratio plot denotes the total systematic uncertainty on the prediction.

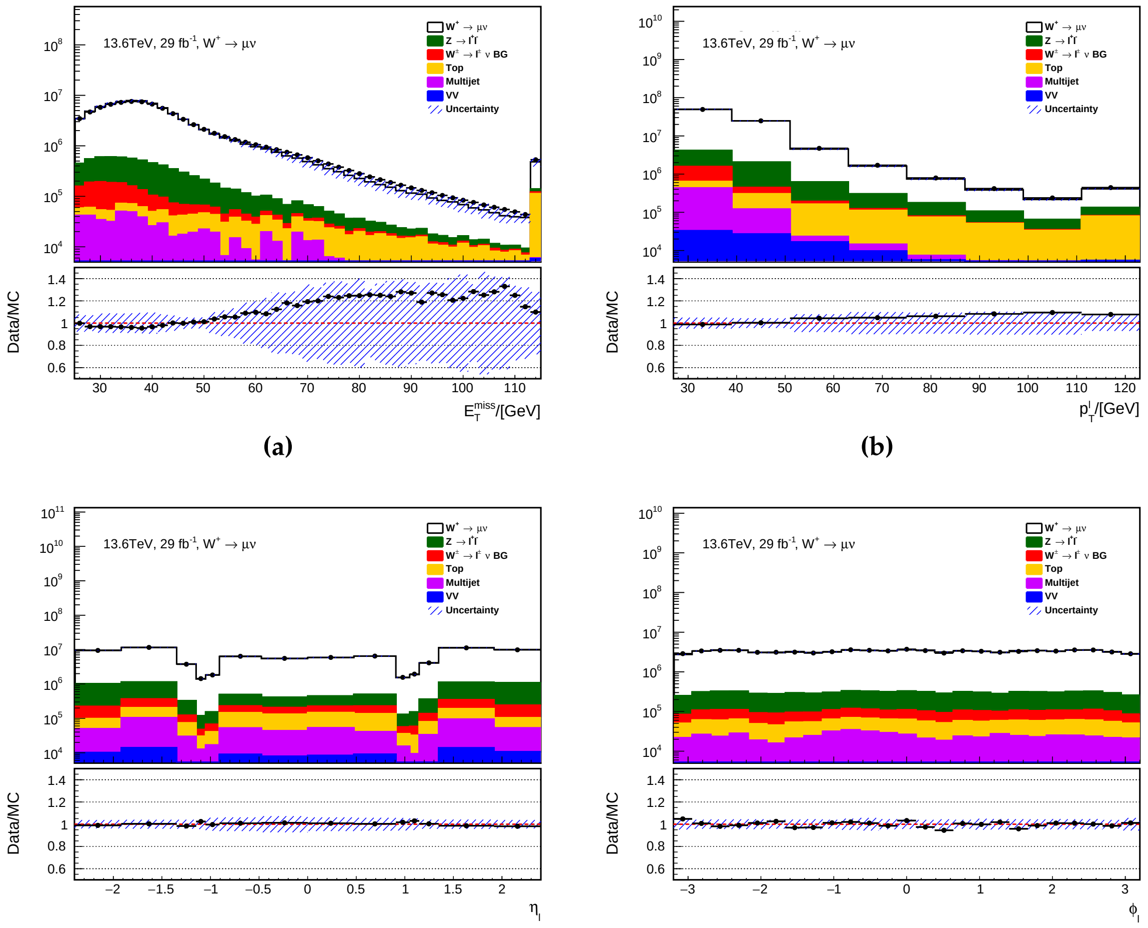

(a) (b)

(c) (d)

Figure B.4.: Comparison of data (black markers) and predictions (stacked histograms) for $E_{\mathrm{T}}^{\mathrm{miss}}$, lepton p_{T}, η and ϕ for the $W^+ \rightarrow \mu^+\nu$ channel. The blue hashed band in the ratio plot denotes the total systematic uncertainty on the prediction.

Appendix C.

Additional plots for multijet background

In this appendix, additional plots are provided for the data-driven multijet background estimation in Chapter 5. Figures C.1- C.7 show the comparison between data and MC predictions in the four isolation slices defined for control regions 1 and 2 presented in Section 5.2.3. Figure C.8 shows the nuisance parameter pulls for a profile likelihood fit performed in the FR in the $W^- \rightarrow e^-\bar{\nu}$ channel on the $E_{\mathrm{T}}^{\mathrm{miss}}$ distribution, using the multijet template obtained from isolation slice 1, as described in Section 5.2.4. Figures C.9 and C.10 show the linear and quadratic track isolation extrapolations to the multijet yields in the SR for the nominal multijet method, as described in Section 5.2.5. Finally, Figures C.11 and C.12 show similar track isolation extrapolations to the multijet yields in the SR for the additional multijet estimation method 2, presented in Section 5.3.

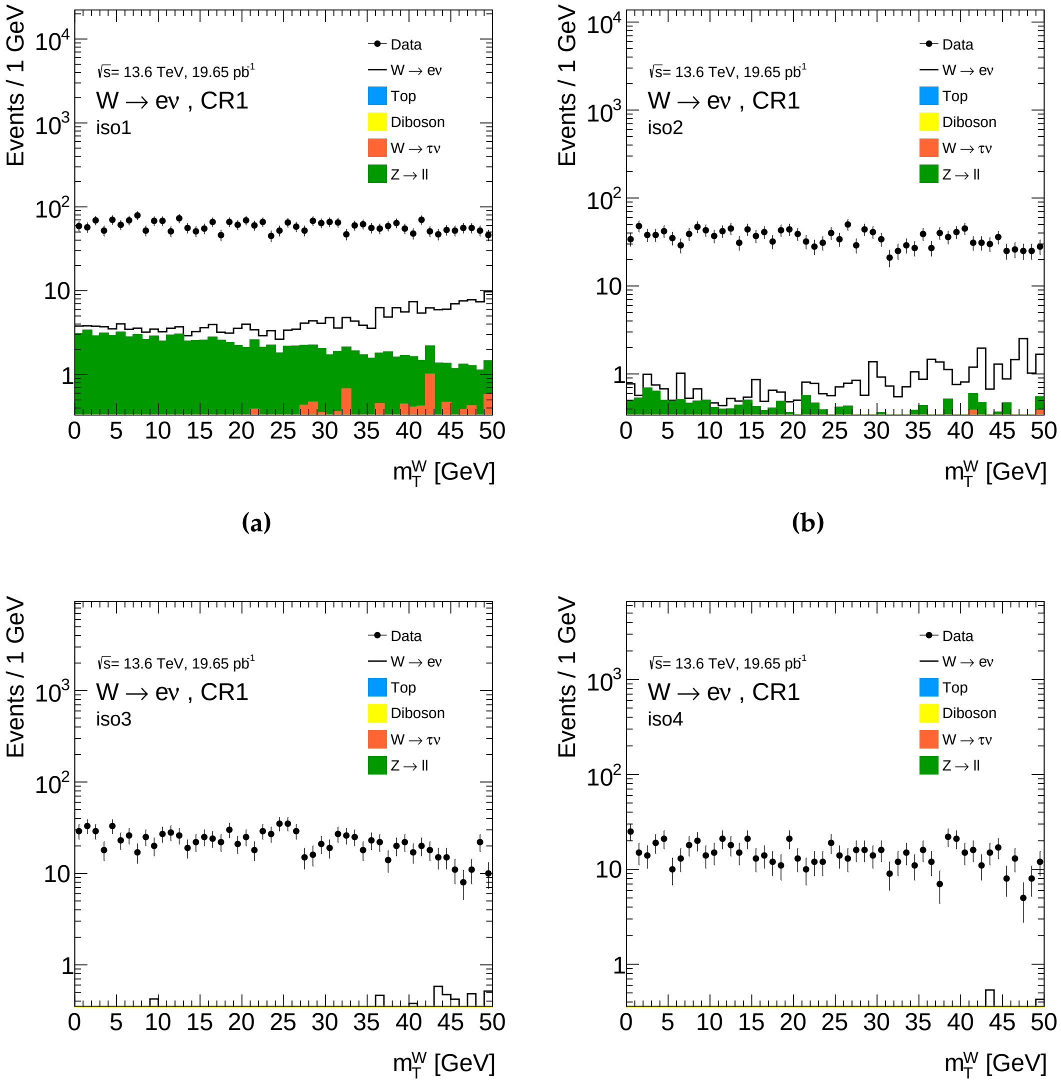

(a)

(b)

(c)

(d)

Figure C.1.: Comparison between data and predictions in the electron channel m_T^W distributions for the four isolation slices in CR1.

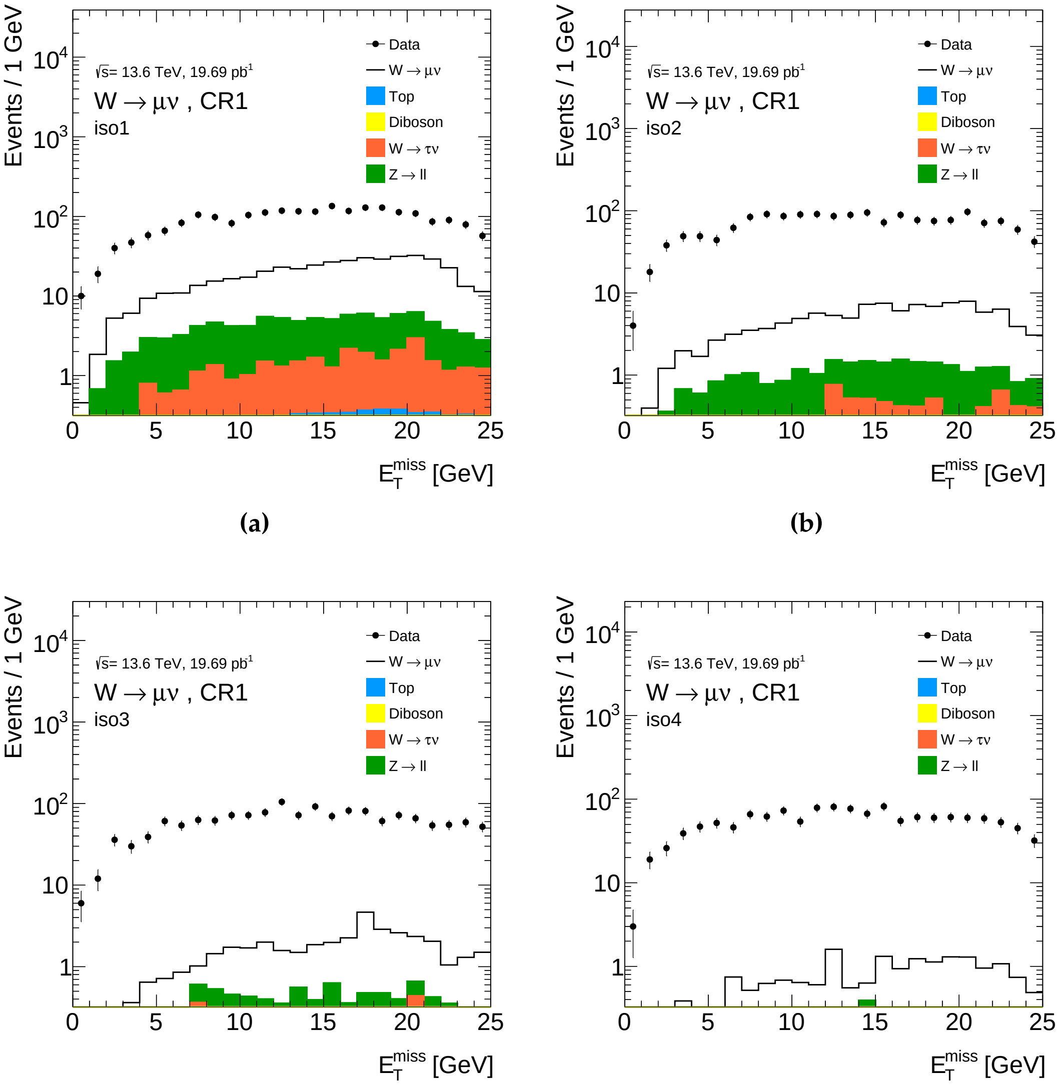

(a)

(b)

(c)

(d)

Figure C.2.: Comparison between data and predictions in the muon channel $E_{\mathrm{T}}^{\mathrm{miss}}$ distributions for the four isolation slices in CR1.

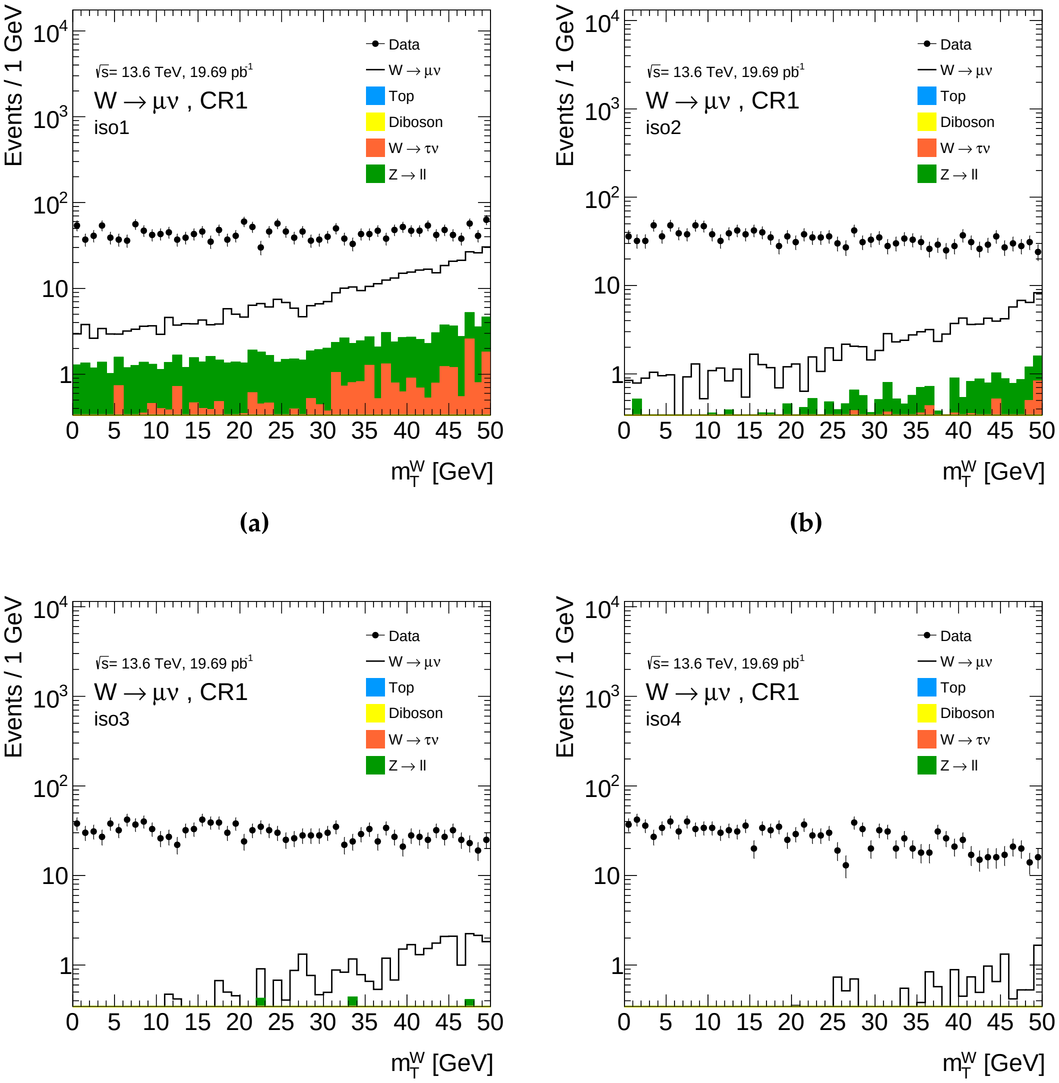

(a) (b)

(c) (d)

Figure C.3.: Comparison between data and predictions in the muon channel m_{T}^{W} distributions for the four isolation slices in CR1.

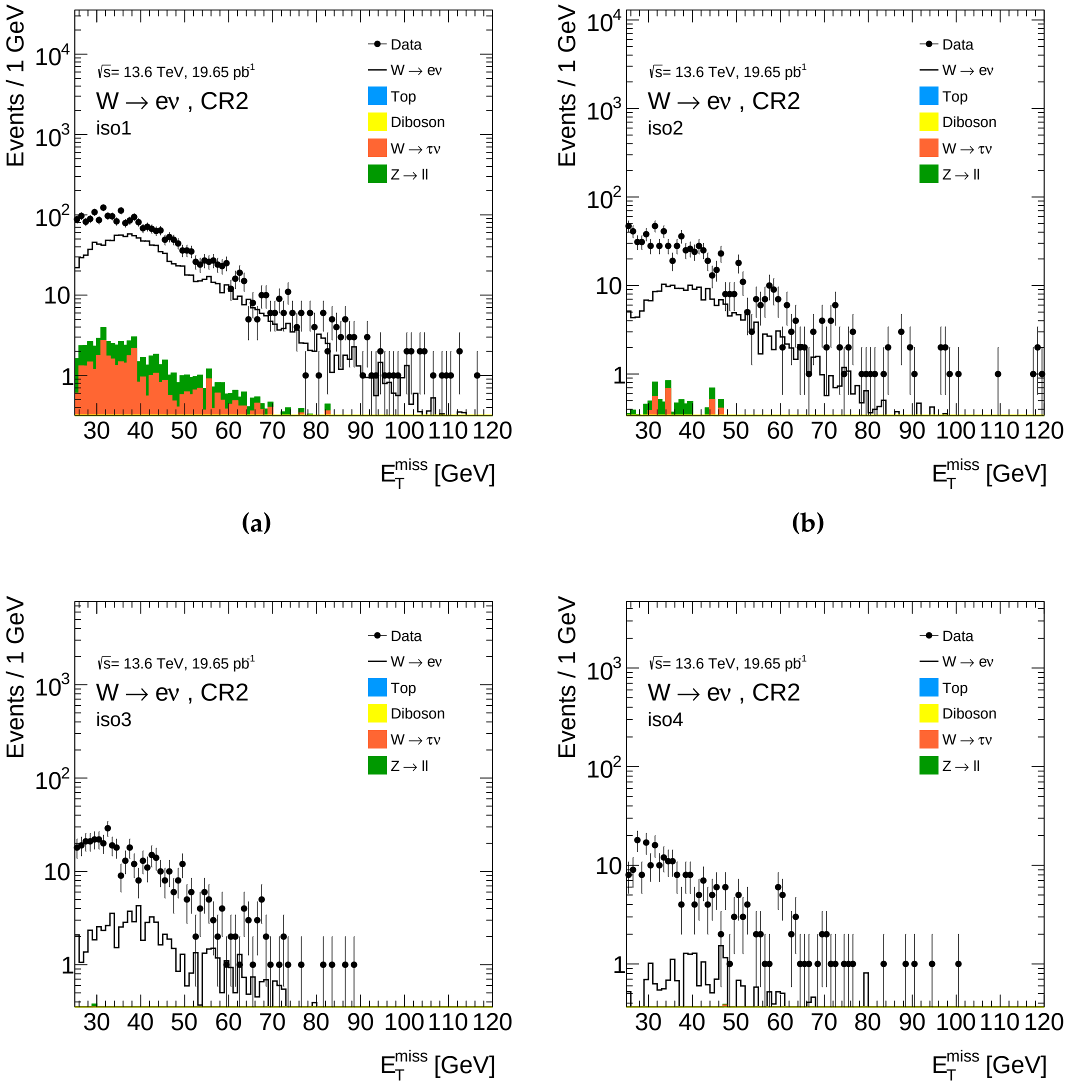

(a)

(b)

(c)

(d)

Figure C.4.: Comparison between data and predictions in the electron channel $E_{\mathrm{T}}^{\mathrm{miss}}$ distributions for the four isolation slices in CR1.

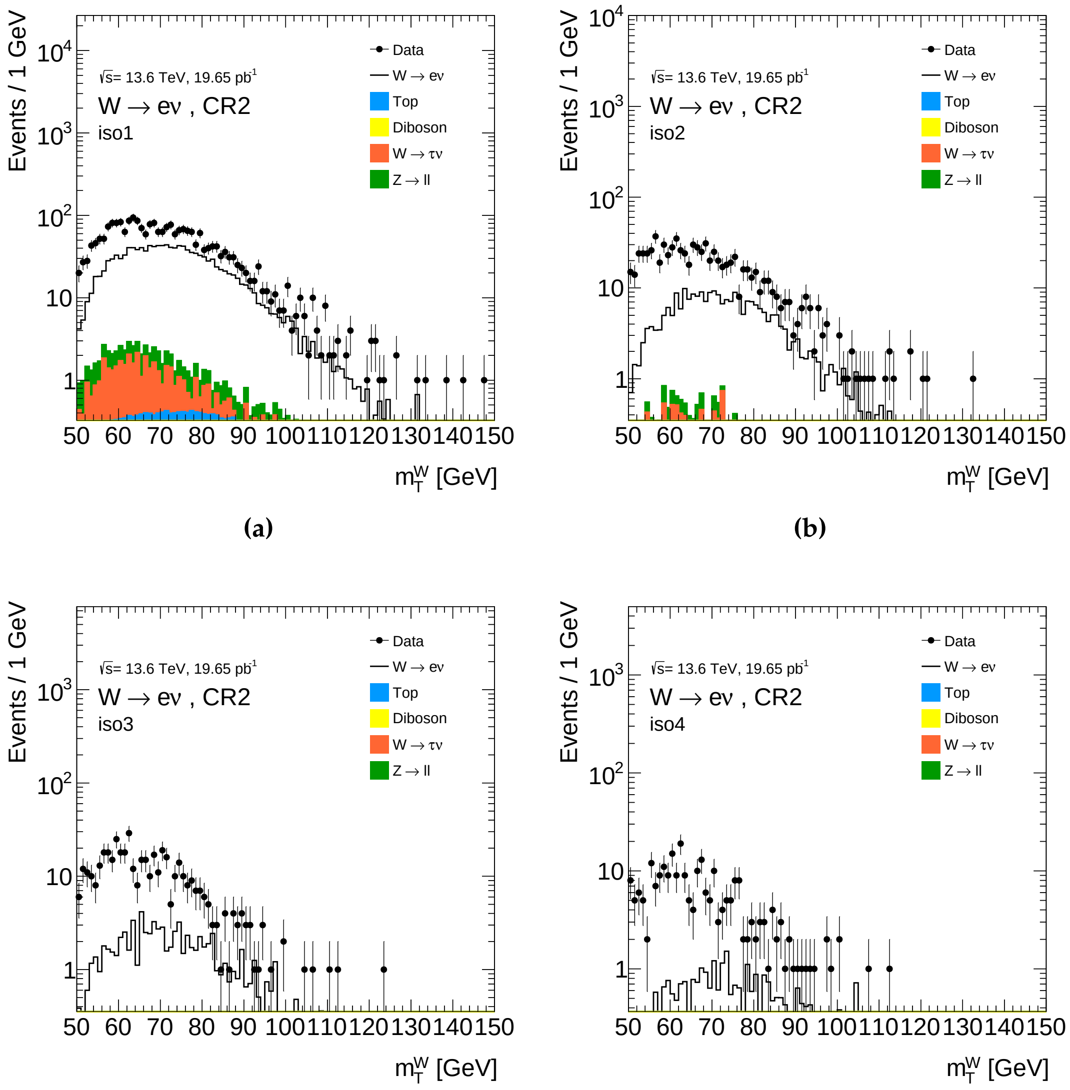

(a) **(b)**

(c) **(d)**

Figure C.5.: Comparison between data and predictions in the electron channel m_T^W distributions for the four isolation slices in CR2.

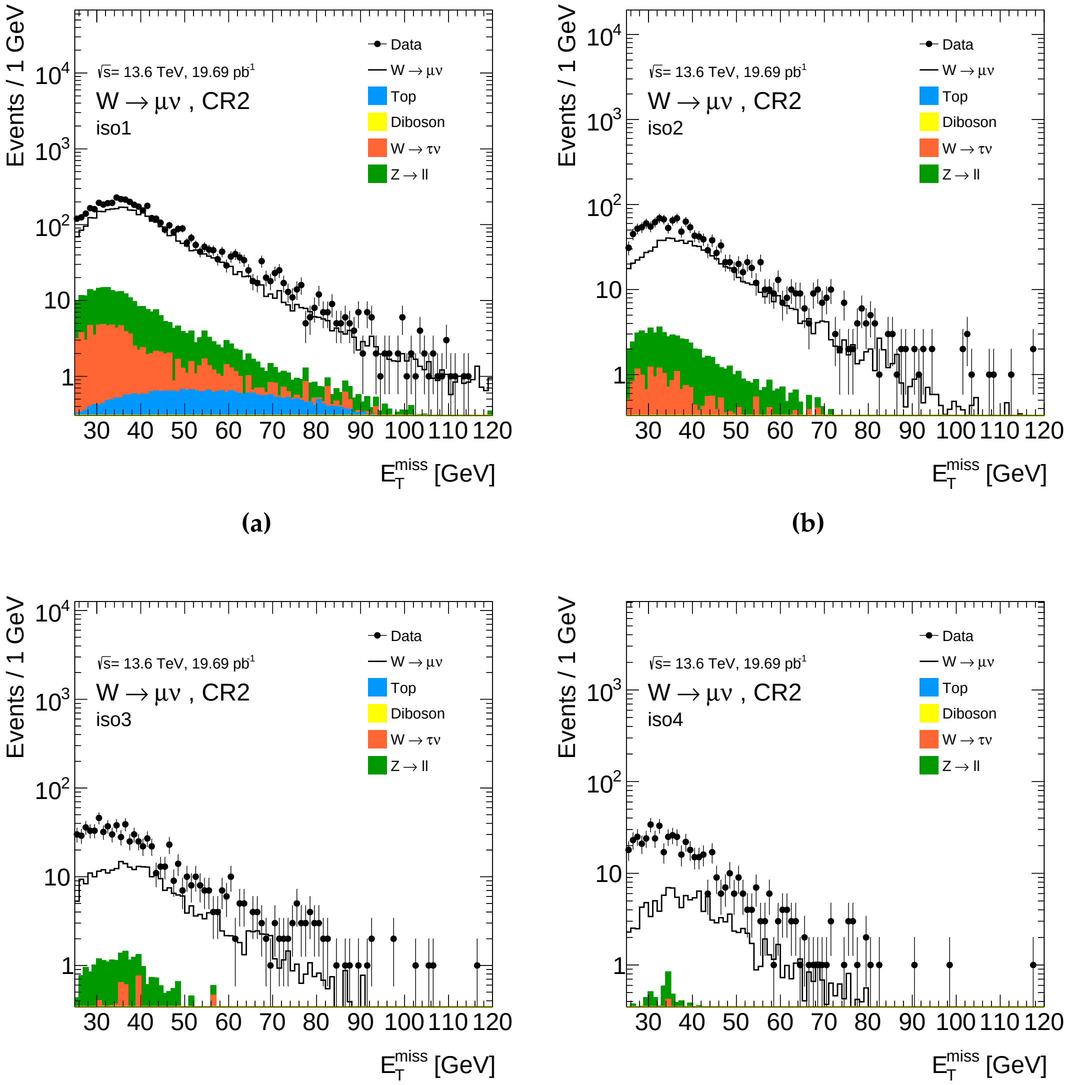

(a)

(b)

(c)

(d)

Figure C.6.: Comparison between data and predictions in the muon channel $E_{\mathrm{T}}^{\mathrm{miss}}$ distributions for the four isolation slices in CR2.

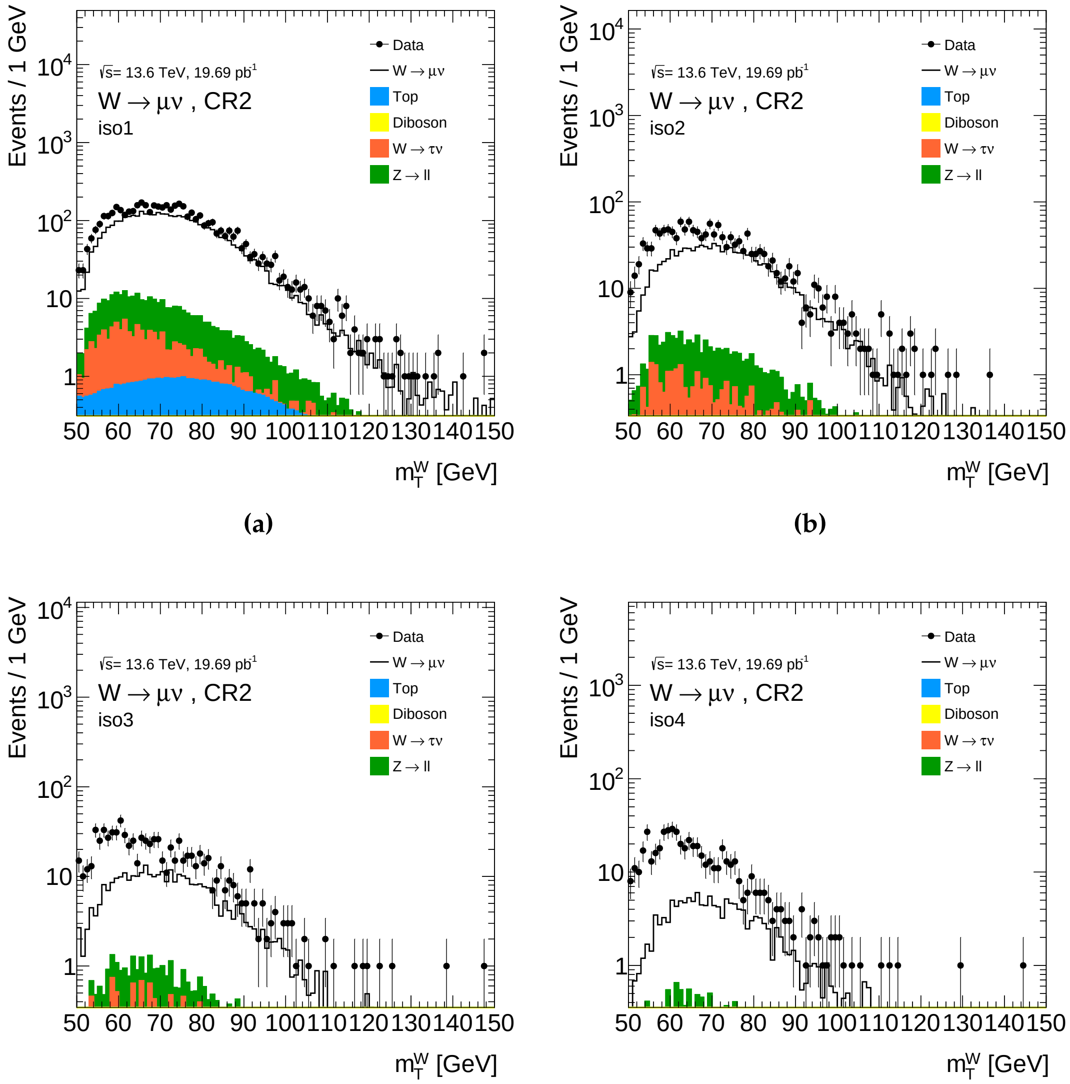

(a) (b)

(c) (d)

Figure C.7.: Comparison between data and predictions in the muon channel m_{T}^{W} distributions for the four isolation slices in CR2.

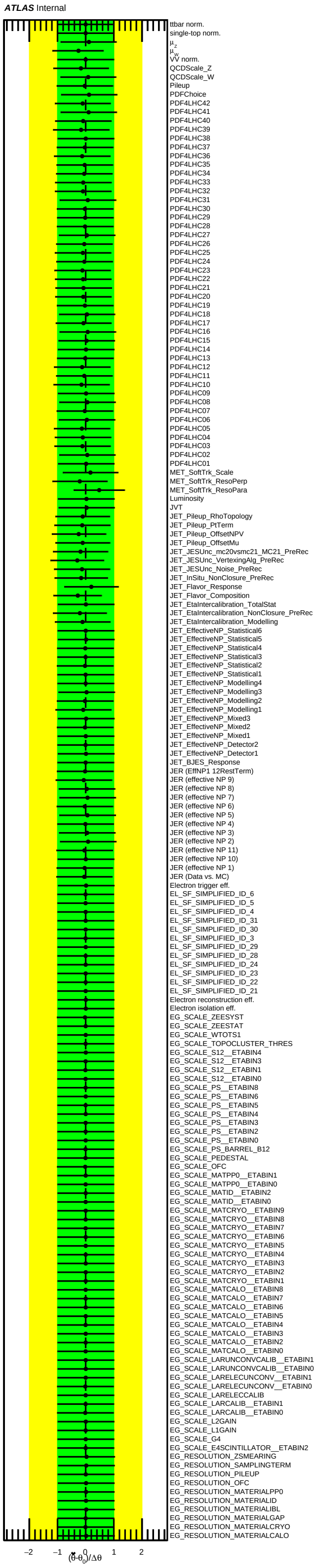

Figure C.8.: Nuisance parameters for the fit in the $W^- \to e^- \bar{\nu}$ channel on the $E_{\mathrm{T}}^{\mathrm{miss}}$ distribution using the multijet template obtained from isolation slice 1 (iso1).

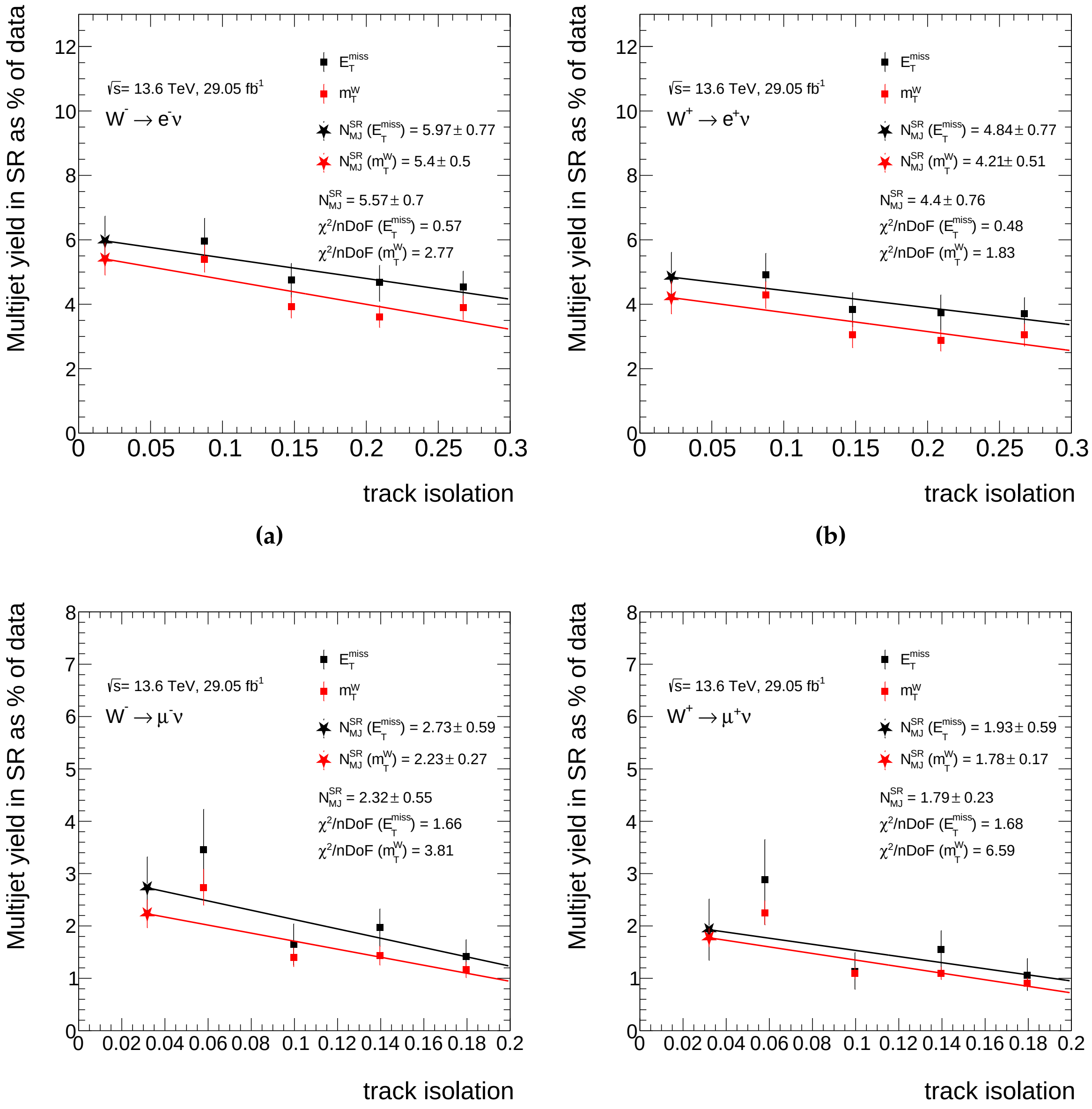

(a) **(b)**

(c) **(d)**

Figure C.9.: Linear fit for extracting the multijet yields in the SR, based on method 3, using scans in the track isolation variable for (a) the $W^- \to e^-\bar{\nu}$ channel, (b) the $W^+ \to e^+\nu$ channel, (c) the $W^- \to \mu^-\bar{\nu}$ channel and (d) the $W^+ \to \mu^+\nu$ channel. Results using the $E_{\mathrm{T}}^{\mathrm{miss}}$ distribution are shown in black and $m_{\mathrm{T}}^{\mathrm{W}}$ in red. The MJ fractions extrapolated from the fits are included in a different marker style.

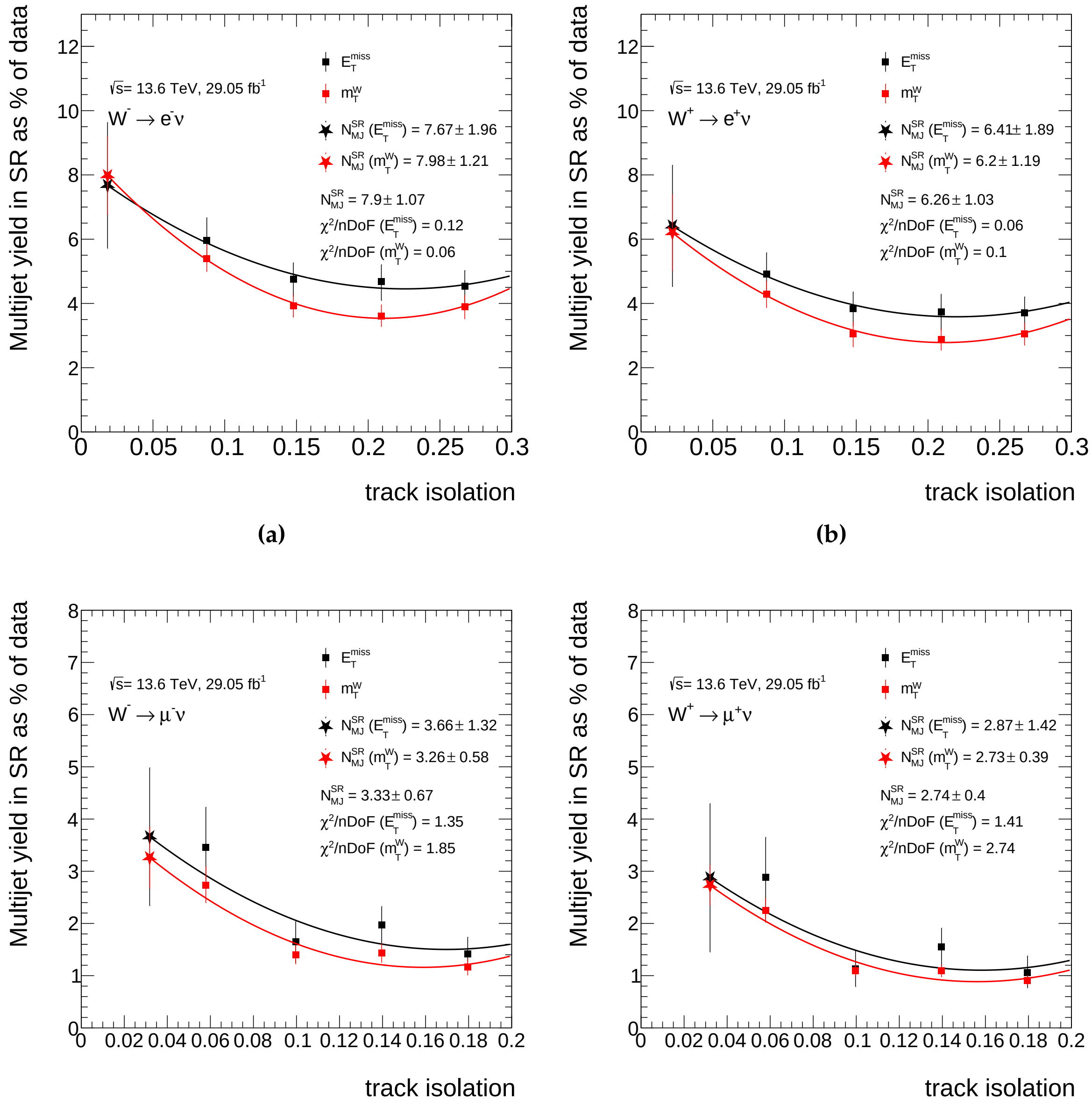

(a) (b)

(c) (d)

Figure C.10.: Quadratic fit for extracting the multijet yields in the SR, based on method 3, using scans in the track isolation variable for (a) the $W^- \to e^-\bar{\nu}$ channel, (b) the $W^+ \to e^+\nu$ channel, (c) the $W^- \to \mu^-\bar{\nu}$ channel and (d) the $W^+ \to \mu^+\nu$ channel. Results using the E_T^{miss} distribution are shown in black and m_T^W in red. The MJ fractions extrapolated from the fits are included in a different marker style.

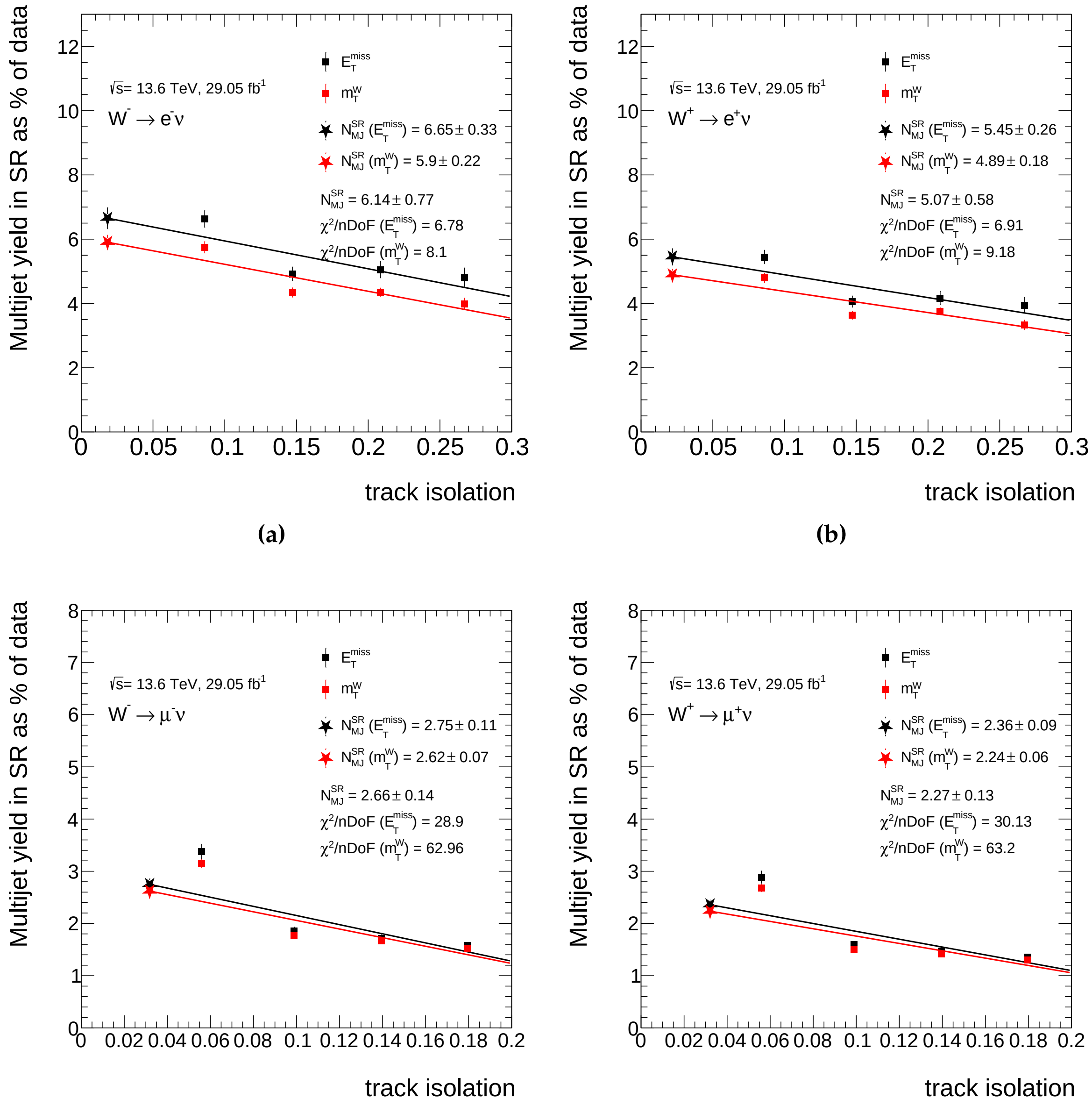

(a) (b)

(c) (d)

Figure C.11.: Linear fit for extracting the multijet yields in the SR, based on method 2, using scans in the track isolation variable for (a) the $W^- \to e^-\bar{\nu}$ channel, (b) the $W^+ \to e^+\nu$ channel, (c) the $W^- \to \mu^-\bar{\nu}$ channel and (d) the $W^+ \to \mu^+\nu$ channel. Results using the E_T^{miss} distribution are shown in black and m_T^W in red. The MJ fractions extrapolated from the fits are included in a different marker style.

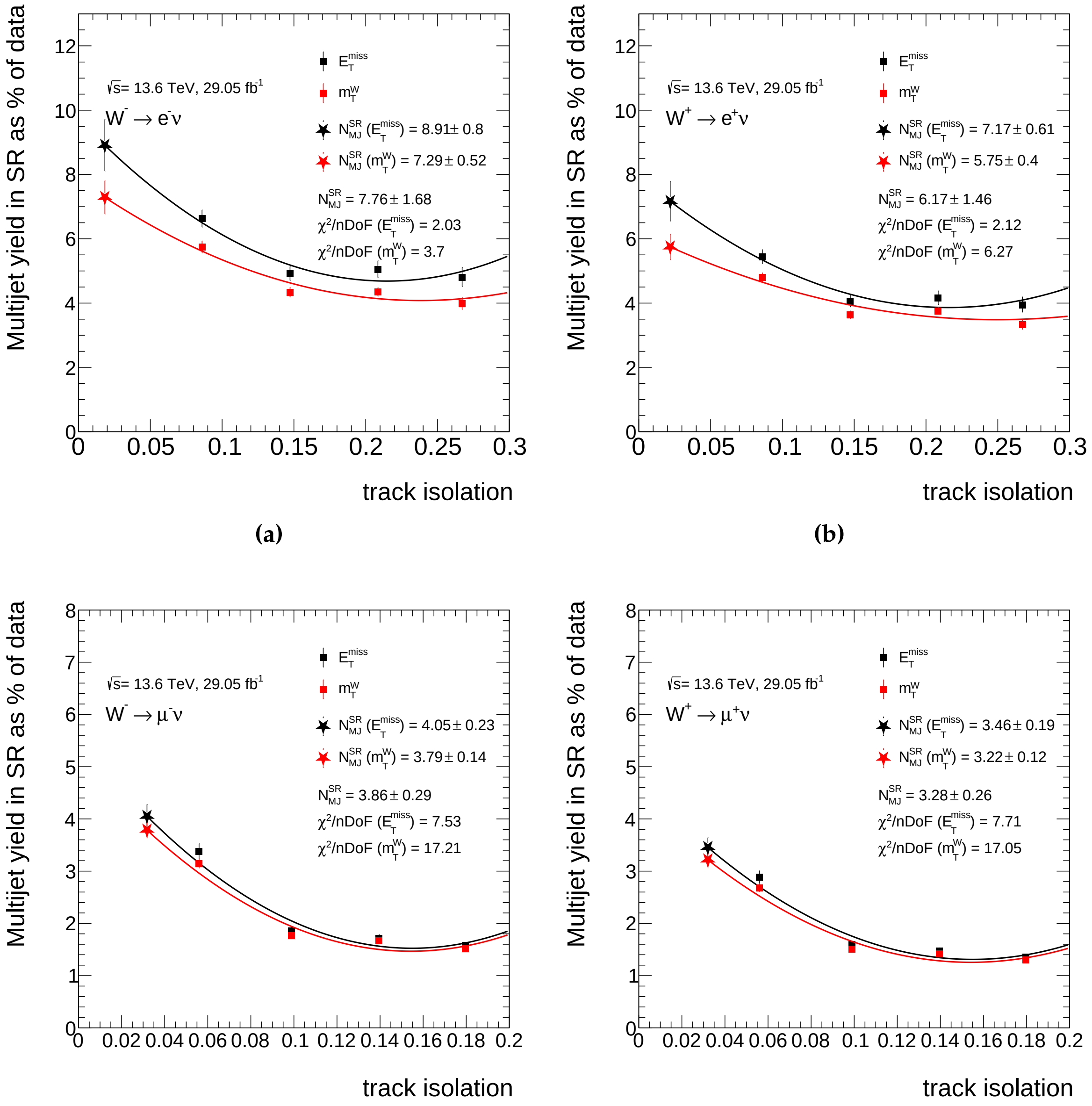

(a) **(b)**

(c) **(d)**

Figure C.12.: Quadratic fit for extracting the multijet yields in the SR, based on method 2, using scans in the track isolation variable for (a) the $W^- \to e^- \bar{\nu}$ channel, (b) the $W^+ \to e^+ \nu$ channel, (c) the $W^- \to \mu^- \bar{\nu}$ channel and (d) the $W^+ \to \mu^+ \nu$ channel. Results using the E_T^{miss} distribution are shown in black and m_T^W in red. The MJ fractions extrapolated from the fits are included in a different marker style.

Appendix D.

Theoretical predictions for the W and Z boson cross sections and their ratios at $\sqrt{s} = 13.6$TeV

In this appendix, additional theoretical predictions for the W and Z boson cross sections are shown, calculated with the different PDF sets presented in Section 4.5. Table D.1 shows the fiducial W and Z boson cross sections, while Table D.2 shows the total W and Z boson cross sections. Finally, the fiducial cross-section ratios $R_{W^{\pm}/Z}$ and $R_{W^{+}/W^{-}}$ are presented in Table D.3, and the fiducial cross-section ratios between $t\bar{t}$ and $W^{\pm}$ are shown in Table D.4.

The predictions for ratios of W^{+}, W^{-} and $W^{\pm}$ boson to $t\bar{t}$ production are reported in Table D.4. The quoted $t\bar{t}$ cross sections are taken from Ref. [107].

Table D.1.: Single boson production fiducial cross-section results for a series of different PDF sets. The first error which is quoted corresponds to statistical uncertainty, the second to scale error, while the third to PDF error.

PDF set	$pp \to \ell^+\ell^-$ [pb]	$pp \to \ell^-\bar{\nu}_\ell$ [pb]	$pp \to \ell^+\nu_\ell$ [pb]
CT18	$733.16^{+0.1\%,+0.5\%,+5.9\%}_{-0.1\%,-0.5\%,-6.2\%}$	$3372.54^{+0.1\%,+1.0\%,+1.7\%}_{-0.1\%,-0.9\%,-3.1\%}$	$4385.38^{+0.1\%,+0.9\%,+1.8\%}_{-0.1\%,-0.8\%,-3.0\%}$
CT18A	$750.52^{+0.1\%,+0.5\%,+3.7\%}_{-0.1\%,-0.5\%,-4.3\%}$	$3398.85^{+0.1\%,+0.9\%,+2.4\%}_{-0.1\%,-0.9\%,-2.5\%}$	$4364.99^{+0.1\%,+0.9\%,+2.3\%}_{-0.1\%,-0.8\%,-2.4\%}$
MSHT20	$747.52^{+0.1\%,+0.5\%,+2.2\%}_{-0.1\%,-0.7\%,-2.7\%}$	$3360.94^{+0.1\%,+0.9\%,+1.3\%}_{-0.1\%,-1.0\%,-1.6\%}$	$4317.57^{+0.1\%,+0.8\%,+1.4\%}_{-0.1\%,-0.8\%,-1.6\%}$
NNPDF4.0	$767.39^{+0.1\%,+0.3\%,+0.9\%}_{-0.1\%,-0.5\%,-0.9\%}$	$3463.40^{+0.1\%,+0.9\%,+0.6\%}_{-0.1\%,-0.8\%,-0.6\%}$	$4455.24^{+0.1\%,+0.8\%,+0.5\%}_{-0.1\%,-0.9\%,-0.5\%}$
PDF4LHC21	$746.14^{+0.1\%,+0.4\%,+2.8\%}_{-0.1\%,-0.6\%,-2.8\%}$	$3387.04^{+0.1\%,+1.0\%,+1.5\%}_{-0.1\%,-1.1\%,-1.5\%}$	$4345.91^{+0.1\%,+0.9\%,+1.5\%}_{-0.1\%,-1.0\%,-1.5\%}$
ATLASpdf21	$787.24^{+0.1\%,+0.4\%,+3.2\%}_{-0.1\%,-0.6\%,-4.1\%}$	$3545.58^{+0.1\%,+1.1\%,+2.5\%}_{-0.1\%,-1.0\%,-2.9\%}$	$4579.11^{+0.1\%,+1.0\%,+2.6\%}_{-0.1\%,-1.0\%,-3.0\%}$
ABMP16	$746.11^{+0.1\%,+0.6\%,+1.5\%}_{-0.1\%,-0.6\%,-1.5\%}$	$3383.72^{+0.1\%,+1.0\%,+0.9\%}_{-0.1\%,-0.9\%,-1.0\%}$	$4332.77^{+0.1\%,+0.9\%,+0.6\%}_{-0.1\%,-0.9\%,-0.6\%}$

Table D.2.: Single boson production total cross-section results for a series of different PDF sets. The first error which is quoted corresponds to statistical uncertainty, the second to scale error, and the third to PDF error.

PDF set	$pp \to \ell^+\ell^-$ [nb]	$pp \to \ell^-\bar{\nu}_\ell$ [nb]	$pp \to \ell^+\nu_\ell$ [nb]
CT18	$1.984^{+0.04\%,+0.5\%,+5.9\%}_{-0.04\%,-0.5\%,-6.2\%}$	$8.922^{+0.05\%,+1.0\%,+1.7\%}_{-0.05\%,-0.9\%,-3.1\%}$	$12.055^{+0.05\%,+0.9\%,+1.8\%}_{-0.05\%,-0.8\%,-3.0\%}$
CT18A	$2.010^{+0.04\%,+0.5\%,+3.7\%}_{-0.04\%,-0.5\%,-4.3\%}$	$8.962^{+0.05\%,+0.9\%,+2.4\%}_{-0.05\%,-0.9\%,-2.5\%}$	$12.087^{+0.05\%,+0.9\%,+2.3\%}_{-0.05\%,-0.8\%,-2.4\%}$
MSHT20	$1.999^{+0.04\%,+0.5\%,+2.2\%}_{-0.04\%,-0.7\%,-2.7\%}$	$8.866^{+0.05\%,+0.9\%,+1.3\%}_{-0.05\%,-1.0\%,-1.6\%}$	$11.948^{+0.05\%,+0.8\%,+1.4\%}_{-0.05\%,-0.8\%,-1.6\%}$
NNPDF4.0	$2.034^{+0.04\%,+0.3\%,+0.9\%}_{-0.04\%,-0.5\%,+0.9\%}$	$9.069^{+0.05\%,+0.9\%,+0.6\%}_{-0.05\%,-0.8\%,-0.6\%}$	$12.194^{+0.05\%,+0.8\%,+0.5\%}_{-0.05\%,-0.9\%,-0.5\%}$
PDF4LHC21	$2.000^{+0.04\%,+0.4\%,+4.6\%}_{-0.04\%,-0.6\%,-4.6\%}$	$8.911^{+0.05\%,+1.0\%,+1.5\%}_{-0.05\%,-1.1\%,-1.5\%}$	$12.012^{+0.05\%,+0.9\%,+1.5\%}_{-0.05\%,-1.0\%,-1.5\%}$
ATLASpdf21	$2.098^{+0.04\%,+0.4\%,+3.2\%}_{-0.04\%,-0.6\%,-4.1\%}$	$9.334^{+0.05\%,+1.1\%,+2.5\%}_{-0.05\%,-1.0\%,-2.9\%}$	$12.465^{+0.05\%,+1.0\%,+2.6\%}_{-0.05\%,-1.0\%,-3.0\%}$
ABMP16	$1.998^{+0.04\%,+0.6\%,+1.5\%}_{-0.04\%,-0.6\%,-1.5\%}$	$8.847^{+0.05\%,+1.0\%,+0.9\%}_{-0.05\%,-0.9\%,-1.0\%}$	$11.974^{+0.05\%,+0.9\%,+0.6\%}_{-0.05\%,-0.9\%,-0.6\%}$

Table D.3.: Predictions of the ratios of W^+ to W^- boson and $W^\pm$ to Z boson combined production cross sections in the fiducial region based on different PDF sets. The quoted error is due to PDF uncertainties.

PDF set	W^+/W^-	$W^\pm/Z$
CT18	$1.300^{+0.6\%}_{-0.4\%}$	$10.58^{+4.6\%}_{-5.2\%}$
CT18A	$1.284^{+0.6\%}_{-0.5\%}$	$10.34^{+3.1\%}_{-3.0\%}$
MSHT20	$1.285^{+0.7\%}_{-0.7\%}$	$10.27^{+2.1\%}_{-1.7\%}$
NNPDF4.0	$1.286^{+0.8\%}_{-0.8\%}$	$10.32^{+0.7\%}_{-0.7\%}$
PDF4LHC21	$1.283^{+0.5\%}_{-0.5\%}$	$10.36^{+2.4\%}_{-2.4\%}$
ATLASpdf21	$1.291^{+0.5\%}_{-0.4\%}$	$10.32^{+2.5\%}_{-2.2\%}$
ABMP16	$1.280^{+0.3\%}_{-0.3\%}$	$10.34^{+0.9\%}_{-0.9\%}$

Table D.4.: Predictions of the ratios of W^+, W^- and $W^\pm$ boson to $t\bar{t}$ production cross sections in the fiducial region based on different PDF sets. The quoted errors are due to statistical, scales and PDF+α_s uncertainties respectively.

PDF set	$t\bar{t}/W+$	$t\bar{t}/W-$	$t\bar{t}/W\pm$
CT18	$0.2117^{+0.09\%,2.6\%,4.6\%}_{-0.09\%,3.7\%,3.4\%}$	$0.2753^{+0.11\%,2.6\%,4.9\%}_{-0.11\%,3.7\%,3.4\%}$	$0.1197^{+0.08\%,2.6\%,4.7\%}_{-0.08\%,3.8\%,3.4\%}$
CT18A	$0.2104^{+0.1\%,2.6\%,4.0\%}_{-0.1\%,3.7\%,4.2\%}$	$0.2702^{+0.11\%,2.6\%,4.1\%}_{-0.11\%,3.7\%,4.3\%}$	$0.1183^{+0.08\%,2.6\%,4.1\%}_{-0.08\%,3.7\%,4.2\%}$
MSHT20	$0.2136^{+0.09\%,2.6\%,3.3\%}_{-0.09\%,3.7\%,2.9\%}$	$0.2745^{+0.11\%,2.7\%,3.4\%}_{-0.11\%,3.7\%,2.6\%}$	$0.1201^{+0.08\%,2.6\%,3.3\%}_{-0.08\%,3.7\%,2.7\%}$
NNPDF4.0	$0.2024^{+0.1\%,2.6\%,1.3\%}_{-0.1\%,3.7\%,2.0\%}$	$0.2603^{+0.12\%,2.6\%,1.3\%}_{-0.12\%,3.7\%,2.2\%}$	$0.1139^{+0.09\%,2.6\%,1.3\%}_{-0.09\%,3.7\%,2.1\%}$
PDF4LHC21 ($m_t = 171.5$ GeV)	$0.2184^{+0.09\%,2.7\%,2.8\%}_{-0.09\%,3.7\%,2.8\%}$	$0.2802^{+0.11\%,2.7\%,2.9\%}_{-0.11\%,3.7\%,2.9\%}$	$0.1227^{+0.08\%,2.7\%,2.9\%}_{-0.08\%,3.7\%,2.9\%}$
PDF4LHC21 ($m_t = 172.5$ GeV)	$0.2125^{+0.09\%,2.6\%,2.8\%}_{-0.09\%,3.7\%,2.8\%}$	$0.2727^{+0.11\%,2.7\%,2.9\%}_{-0.11\%,3.7\%,2.9\%}$	$0.1194^{+0.08\%,2.7\%,2.8\%}_{-0.08\%,3.8\%,2.8\%}$
PDF4LHC21 ($m_t = 173.5$ GeV)	$0.2069^{+0.1\%,2.7\%,2.8\%}_{-0.1\%,3.7\%,2.8\%}$	$0.2654^{+0.11\%,2.7\%,2.9\%}_{-0.11\%,3.8\%,2.9\%}$	$0.1163^{+0.09\%,2.7\%,2.8\%}_{-0.09\%,3.7\%,2.8\%}$
ATLASpdf21	$0.2139^{+0.09\%,2.7\%,5.1\%}_{-0.09\%,3.7\%,4.6\%}$	$0.2762^{+0.11\%,2.6\%,5.1\%}_{-0.11\%,3.8\%,4.5\%}$	$0.1205^{+0.08\%,2.7\%,5.1\%}_{-0.08\%,3.7\%,4.5\%}$
ABMP16	$0.1941^{+0.1\%,2.6\%,3.0\%}_{-0.1\%,3.7\%,3.0\%}$	$0.2485^{+0.12\%,2.6\%,3.0\%}_{-0.12\%,3.7\%,3.0\%}$	$0.109^{+0.09\%,2.6\%,2.9\%}_{-0.09\%,3.8\%,2.9\%}$

Bibliography

[1] ATLAS Collaboration, *Measurement of vector boson production cross sections and their ratios using pp collisions at $\sqrt{s} = 13.6$ TeV with the ATLAS detector*, Phys. Lett. B **854** (2024) 138725, arXiv: `2403.12902 [hep-ex]` (cit. on pp. v, 1, 75, 99–101, 110, 119, 120, 125, 127–133).

[2] *Standard Model of Elementary Particles*, visited on 26/08/2024, URL: `https://commons.wikimedia.org/wiki/File:Standard_Model_of_Elementary_Particles.svg` (cit. on p. 2).

[3] M. Thomson, *Modern particle physics*, Cambridge University Press, 2013, ISBN: 978-1-107-03426-6 (cit. on pp. 3, 6, 9).

[4] F. Englert and R. Brout, *Broken symmetry and the masses of gauge vector mesons*, Phys. Rev. Lett. **13** (1964) 321, URL: `https://cds.cern.ch/record/641592` (cit. on pp. 3, 5).

[5] P. W. Higgs, *Broken Symmetries and the Masses of Gauge Bosons*, Phys. Rev. Lett. **13** (1964) 508 (cit. on pp. 3, 5).

[6] ATLAS Collaboration, *Observation of a new particle in the search for the Standard Model Higgs boson with the ATLAS detector at the LHC*, Phys. Lett. B **716** (2012) 1, arXiv: `1207.7214 [hep-ex]` (cit. on p. 3).

[7] CMS Collaboration, *Observation of a New Boson at a Mass of 125 GeV with the CMS Experiment at the LHC*, Phys. Lett. B **716** (2012) 30, arXiv: `1207.7235 [hep-ex]` (cit. on p. 3).

[8] S. L. Glashow, *Partial Symmetries of Weak Interactions*, Nucl. Phys. **22** (1961) 579 (cit. on p. 4).

[9] S. Weinberg, *A Model of Leptons*, Phys. Rev. Lett. **19** (1967) 1264 (cit. on p. 4).

[10] A. Salam, *Weak and Electromagnetic Interactions*, Conf. Proc. C **680519** (1968) 367 (cit. on p. 4).

[11] N. Cabibbo, *Unitary Symmetry and Leptonic Decays*, Phys. Rev. Lett. **10** (1963) 531 (cit. on p. 4).

[12] M. Kobayashi and T. Maskawa, *CP Violation in the Renormalizable Theory of Weak Interaction*, Prog. Theor. Phys. **49** (1973) 652 (cit. on p. 4).

[13] J. Goldstone, A. Salam, and S. Weinberg, *Broken Symmetries*, Phys. Rev. **127** (1962) 965 (cit. on p. 6).

[14] G. S. Guralnik, C. R. Hagen, and T. W. B. Kibble, *Global Conservation Laws and Massless Particles*, Phys. Rev. Lett. **13** (20 1964) 585, URL: `https://link.aps.org/doi/10.1103/PhysRevLett.13.585` (cit. on p. 6).

[15] J. Campbell, J. Huston, and F. Krauss, *The Black Book of Quantum Chromodynamics: A Primer for the LHC Era*, Oxford University Press, 2017, ISBN: 9780199652747, URL: `https://doi.org/10.1093/oso/9780199652747.001.0001` (cit. on pp. 8, 9, 11, 15, 16).

[16] *Standard Model Summary Plots June 2024*, visited on 27/08/2024, URL: `https://atlas.web.cern.ch/Atlas/GROUPS/PHYSICS/PUBNOTES/ATL-PHYS-PUB-2024-011/` (cit. on p. 10).

[17] J. Gao, L. Harland-Lang, and J. Rojo, *The Structure of the Proton in the LHC Precision Era*, Phys. Rept. **742** (2018) 1, arXiv: `1709.04922 [hep-ph]` (cit. on pp. 11, 129).

[18] V. N. Gribov and L. N. Lipatov, *Deep inelastic e p scattering in perturbation theory*, Sov. J. Nucl. Phys. **15** (1972) 438 (cit. on p. 11).

[19] Y. L. Dokshitzer, *Calculation of the Structure Functions for Deep Inelastic Scattering and e+ e- Annihilation by Perturbation Theory in Quantum Chromodynamics.*, Sov. Phys. JETP **46** (1977) 641 (cit. on p. 11).

[20] G. Altarelli and G. Parisi, *Asymptotic Freedom in Parton Language*, Nucl. Phys. B **126** (1977) 298 (cit. on p. 11).

[21] S. Bailey, T. Cridge, L. A. Harland-Lang, A. D. Martin, and R. S. Thorne, *Parton distributions from LHC, HERA, Tevatron and fixed target data: MSHT20 PDFs*, Eur. Phys. J. C **81** (2021) 341, arXiv: `2012.04684 [hep-ph]` (cit. on pp. 12, 93).

[22] A. Buckley et al., *General-purpose event generators for LHC physics*, Phys. Rept. **504** (2011) 145, arXiv: `1101.2599 [hep-ph]` (cit. on p. 12).

[23] S. D. Drell and T.-M. Yan, *Massive Lepton Pair Production in Hadron-Hadron Collisions at High-Energies*, Phys. Rev. Lett. **25** (1970) 316, [Erratum: Phys.Rev.Lett. 25, 902 (1970)] (cit. on p. 14).

[24] A. V. Lipatov, M. A. Malyshev, and N. P. Zotov, *Drell-Yan lepton pair production at high energies in the k_t-factorization approach*, JHEP **12** (2011) 117, arXiv: `1110.6582 [hep-ph]` (cit. on pp. 15, 16).

[25] A. D. Martin, R. G. Roberts, W. J. Stirling, and R. S. Thorne, *Parton Distributions and the LHC: W and Z Production; rev. version*, Eur. Phys. J. C **14** (2000) 133, URL: `https://cds.cern.ch/record/392675` (cit. on p. 17).

[26] C. Albajar et al., *Intermediate Vector Boson Cross-Sections at the CERN Super Proton Synchrotron Collider and the Number of Neutrino Types*, Phys. Lett. B **198** (1987) 271 (cit. on p. 18).

[27] J. Alitti et al., *Measurement of W and Z Production Cross-sections at the CERN $\bar{p}p$ Collider*, Z. Phys. C **47** (1990) 11 (cit. on p. 18).

[28] B. Abbott et al., *Extraction of the width of the W boson from measurements of $\sigma(p\bar{p} \to W + X) \times B(W \to e\nu)$ and $\sigma(p\bar{p} \to Z + X) \times B(Z \to ee)$ and their ratio*, Phys. Rev. D **61** (2000) 072001, arXiv: `hep-ex/9906025` (cit. on p. 18).

[29] D. Acosta et al., *First measurements of inclusive W and Z cross sections from Run II of the Tevatron collider*, Phys. Rev. Lett. **94** (2005) 091803, arXiv: `hep-ex/0406078` (cit. on p. 18).

[30] NNPDF Collaboration, R. D. Ball, et al., *The path to proton structure at 1% accuracy: NNPDF Collaboration*, Eur. Phys. J. C **82** (2022) 428, arXiv: `2109.02653 [hep-ph]` (cit. on pp. 18, 93).

[31] CMS Collaboration, *Measurement of the inclusive cross sections for W and Z boson production in proton-proton collisions at $\sqrt{s} = 5.02$ and 13 TeV*, (2024), arXiv: `2408.03744 [hep-ex]` (cit. on pp. 18, 20, 21).

[32] ATLAS Collaboration, *Precise measurements of W- and Z-boson transverse momentum spectra with the ATLAS detector using pp collisions at $\sqrt{s} = 5.02$ TeV and 13 TeV*, (2024), arXiv: `2404.06204 [hep-ex]` (cit. on pp. 20, 23, 24, 101, 103).

[33] S. Camarda, L. Cieri, and G. Ferrera, *Drell–Yan lepton-pair production: q_T resummation at N^{3}LL accuracy and fiducial cross sections at N3LO*, Phys. Rev. D **104** (2021) L111503, arXiv: `2103.04974 [hep-ph]` (cit. on pp. 22, 92).

[34] ATLAS Collaboration, *Measurement of the W-boson mass and width with the ATLAS detector using proton-proton collisions at $\sqrt{s}$ = 7 TeV*, (2024), arXiv: `2403.15085 [hep-ex]` (cit. on p. 22).

[35] R. S. Thorne, A. D. Martin, W. J. Stirling, and G. Watt, "Parton Distributions and QCD at LHCb", *16th International Workshop on Deep Inelastic Scattering and Related Subjects*, 2008 30, arXiv: `0808.1847 [hep-ph]` (cit. on p. 22).

[36] R. Aaij et al., *Measurement of forward W and Z boson production in pp collisions at $\sqrt{s} = 8$ TeV*, JHEP **01** (2016) 155, arXiv: `1511.08039 [hep-ex]` (cit. on pp. 22, 25).

[37] R. Aaij et al., *Precision measurement of forward Z boson production in proton-proton collisions at $\sqrt{s} = 13$ TeV*, JHEP **07** (2022) 026, arXiv: `2112.07458 [hep-ex]` (cit. on p. 25).

[38] *LHC Machine*, JINST **3** (2008) S08001, ed. by L. Evans and P. Bryant (cit. on p. 27).

[39] G. Arduini et al., *LHC Upgrades in preparation of Run 3*, JINST **19** (2024) P05061, URL: `https://cds.cern.ch/record/2900025` (cit. on p. 27).

[40] *LEP design report*, Report, CERN, 1984, URL: `https://cds.cern.ch/record/102083` (cit. on p. 27).

[41] "LHC Guide", 2017, URL: `https://cds.cern.ch/record/2255762` (cit. on p. 27).

[42] X. C. Vidal and R. Cid, *Linac4*, visited on 27/05/2024, URL: `https://lhc-closer.es/taking_a_closer_look_at_lhc/0.linac4` (cit. on p. 27).

[43] E. Lopienska, *The CERN accelerator complex, layout in 2022*, (2022), URL: `https://cds.cern.ch/record/2800984` (cit. on p. 28).

[44] A. Collaboration, *The ATLAS Experiment at the CERN Large Hadron Collider*, JINST **3** (2008) S08003, URL: `https://dx.doi.org/10.1088/1748-0221/3/08/S08003` (cit. on pp. 29, 31, 40, 62, 64).

[45] CMS Collaboration, *The CMS experiment at the CERN LHC*, Journal of Instrumentation **3** (2008) S08004, URL: `https://dx.doi.org/10.1088/1748-0221/3/08/S08004` (cit. on p. 29).

[46] ALICE Collaboration, *The ALICE experiment at the CERN LHC*, JINST **3** (2008) S08002 (cit. on p. 29).

[47] LHCb Collaboration, *The LHCb Detector at the LHC*, JINST **3** (2008) S08005, Also published by CERN Geneva in 2010, URL: `https://cds.cern.ch/record/1129809` (cit. on p. 29).

[48] W. Herr and B. Muratori, *Concept of luminosity*, (2006), URL: `https://cds.cern.ch/record/941318` (cit. on p. 29).

[49] ATLAS Collaboration, *Luminosity determination in pp collisions at $\sqrt{s} = 13$ TeV using the ATLAS detector at the LHC*, Eur. Phys. J. C **83** (2023) 982, arXiv: `2212.09379 [hep-ex]` (cit. on pp. 29, 79, 96).

[50] O. Aberle et al., *High-Luminosity Large Hadron Collider (HL-LHC): Technical design report*, CERN Yellow Reports: Monographs, CERN, 2020, URL: `https://cds.cern.ch/record/2749422` (cit. on p. 30).

[51] *Public ATLAS Luminosity Results for Run-3 of the LHC*, visited on 21/07/2024, URL: `https://twiki.cern.ch/twiki/bin/view/AtlasPublic/LuminosityPublicResultsRun` (cit. on pp. 31, 42, 79).

[52] ATLAS Collaboration, *The ATLAS Experiment at the CERN Large Hadron Collider: A Description of the Detector Configuration for Run 3*, tech. rep., CERN, 2023, arXiv: `2305.16623`, URL: `https://cds.cern.ch/record/2859916` (cit. on pp. 31, 32, 34, 41, 42, 56, 59, 60).

[53] I. Neutelings, *ATLAS coordinate system*, visited on 07/08/2024, URL: `https://tikz.net/axis3d_cms/` (cit. on p. 33).

[54] C. Grupen, *Particle detectors / Claus Grupen, Boris Shwartz ; with contributions from Helmuth Spieler, Simon Eidelman, Tilo Stroh.*, eng, 2008 (cit. on pp. 34, 36, 37, 39).

[55] ATLAS Collaboration, *ATLAS Pixel Detector: Technical Design Report*, ATLAS-TDR-11; CERN-LHCC-98-013, 1998, URL: `https://cds.cern.ch/record/381263` (cit. on p. 34).

[56] ATLAS Collaboration, *ATLAS Insertable B-Layer Technical Design Report*, ATLAS-TDR-19; CERN-LHCC-2010-013, 2010, URL: `https://cds.cern.ch/record/1291633` (cit. on p. 35).

[57] ATLAS Collaboration, *Alignment of the ATLAS Inner Detector in Run-2*, Eur. Phys. J. C **80** (2020) 1194, arXiv: `2007.07624 [hep-ex]` (cit. on p. 35).

[58] ATLAS Collaboration, *Operation and performance of the ATLAS semiconductor tracker in LHC Run 2*, JINST **17** (2021) P01013, arXiv: `2109.02591 [physics.ins-det]` (cit. on p. 35).

[59] ATLAS Collaboration, *Performance of the ATLAS Transition Radiation Tracker in Run 1 of the LHC: tracker properties*, JINST **12** (2017) P05002, arXiv: `1702.06473 [hep-ex]` (cit. on p. 35).

[60] ATLAS Collaboration, *ATLAS liquid-argon calorimeter: Technical Design Report*, Technical design report. ATLAS, CERN, 1996, URL: `https://cds.cern.ch/record/331061` (cit. on p. 36).

[61] ATLAS Collaboration, *ATLAS tile calorimeter: Technical Design Report*, Technical design report. ATLAS, CERN, 1996, URL: `https://cds.cern.ch/record/331062` (cit. on p. 36).

[62] ATLAS Collaboration, *Jet energy scale and resolution measured in proton–proton collisions at* $\sqrt{s} = 13$ *TeV with the ATLAS detector*, Eur. Phys. J. C **81** (2021) 689, arXiv: `2007.02645 [hep-ex]` (cit. on pp. 37, 51).

[63] C. W. Fabjan and F. Gianotti, *Calorimetry for Particle Physics*, Rev. Mod. Phys. **75** (2003) 1243, URL: `https://cds.cern.ch/record/692252` (cit. on pp. 37, 39).

[64] ATLAS Collaboration, *Measurement of the photon identification efficiencies with the ATLAS detector using LHC Run 2 data collected in 2015 and 2016*, Eur. Phys. J. C **79** (2019) 205, arXiv: `1810.05087 [hep-ex]` (cit. on p. 38).

[65] ATLAS Collaboration, *ATLAS Muon Spectrometer: Technical Design Report*, ATLAS-TDR-10; CERN-LHCC-97-022, CERN, 1997, URL: `https://cds.cern.ch/record/331068` (cit. on p. 40).

[66] ATLAS Collaboration, *New Small Wheel Technical Design Report*, tech. rep., ATLAS New Small Wheel Technical Design Report, 2013, URL: `https://cds.cern.ch/record/1552862` (cit. on p. 40).

[67] ATLAS Collaboration, *The ATLAS trigger system for LHC Run 3 and trigger performance in 2022*, JINST **19** (2024) P06029, arXiv: `2401.06630 [hep-ex]` (cit. on pp. 42, 55, 87, 107).

[68] ATLAS Collaboration, *Performance of the ATLAS track reconstruction algorithms in dense environments in LHC Run 2*, Eur. Phys. J. C **77** (2017) 673, arXiv: `1704.07983 [hep-ex]` (cit. on p. 43).

[69] R. Fruhwirth, *Application of Kalman filtering to track and vertex fitting*, Nucl. Instrum. Meth. A **262** (1987) 444 (cit. on p. 43).

[70] ATLAS Collaboration, *Reconstruction of primary vertices at the ATLAS experiment in Run 1 proton–proton collisions at the LHC*, Eur. Phys. J. C **77** (2017) 332, arXiv: `1611.10235 [physics.ins-det]` (cit. on pp. 43, 68, 87).

[71] T. G. Cornelissen et al., *Updates of the ATLAS Tracking Event Data Model (Release 13)*, tech. rep., CERN, 2007, URL: `https://cds.cern.ch/record/1038095` (cit. on p. 44).

[72] ATLAS Collaboration, *Electron and photon performance measurements with the ATLAS detector using the 2015–2017 LHC proton–proton collision data*, JINST **14** (2019) P12006, arXiv: `1908.00005 [hep-ex]` (cit. on pp. 44, 46, 87).

[73] ATLAS Collaboration, *Improved electron reconstruction in ATLAS using the Gaussian Sum Filter-based model for bremsstrahlung*, tech. rep., CERN, 2012, URL: `https://cds.cern.ch/record/1449796` (cit. on p. 45).

[74] ATLAS Collaboration, *Electron and photon energy calibration with the ATLAS detector using LHC Run 2 data*, JINST **19** (2024) P02009, arXiv: `2309.05471`, URL: `https://cds.cern.ch/record/2870086` (cit. on pp. 45, 63, 95).

[75] ATLAS Collaboration, *Electron reconstruction and identification in the ATLAS experiment using the 2015 and 2016 LHC proton-proton collision data at $\sqrt{s} = 13$ TeV*, Eur. Phys. J. C **79** (2019) 639, arXiv: `1902.04655 [physics.ins-det]` (cit. on p. 46).

[76] *ATLAS public plots: Electron identification efficiency with Run3 early data*, visited on 15/08/2024, URL: `https://atlas.web.cern.ch/Atlas/GROUPS/PHYSICS/PLOTS/EGAM-2022-04/index.php` (cit. on p. 46).

[77] ATLAS Collaboration, *Muon reconstruction performance of the ATLAS detector in proton–proton collision data at $\sqrt{s} = 13\,TeV$*, Eur. Phys. J. C **76** (2016) 292, arXiv: `1603.05598 [hep-ex]` (cit. on pp. 47, 95).

[78] ATLAS Collaboration, *Studies of the muon momentum calibration and performance of the ATLAS detector with pp collisions at $\sqrt{s}$=13 TeV*, Eur. Phys. J. C **83** (2023) 686, arXiv: `2212.07338`, URL: `https://cds.cern.ch/record/2844624` (cit. on p. 48).

[79] *ATLAS public plots: Muon reconstruction and identification performance of the ATLAS detector using 2022 and 2023 LHC pp collision data at $\sqrt{s} = 13.6\,TeV$*, visited on 15/08/2024, URL: `https://atlas.web.cern.ch/Atlas/GROUPS/PHYSICS/PLOTS/MUON-2023-02/index.php` (cit. on p. 49).

[80] *ATLAS public plots: Muon reconstruction performance of the ATLAS detector in 2022*, visited on 15/08/2024, URL: `https://atlas.web.cern.ch/Atlas/GROUPS/PHYSICS/PLOTS/MUON-2023-01/index.php` (cit. on p. 49).

[81] M. Cacciari, G. P. Salam, and G. Soyez, *The anti-k_t jet clustering algorithm*, JHEP **04** (2008) 063, arXiv: `0802.1189 [hep-ph]` (cit. on pp. 49, 50).

[82] Y. L. Dokshitzer, G. D. Leder, S. Moretti, and B. R. Webber, *Better jet clustering algorithms*, JHEP **08** (1997) 001, arXiv: `hep-ph/9707323` (cit. on p. 49).

[83] S. D. Ellis and D. E. Soper, *Successive combination jet algorithm for hadron collisions*, Phys. Rev. D **48** (1993) 3160, arXiv: `hep-ph/9305266` (cit. on p. 49).

[84] G. P. Salam, *Towards Jetography*, Eur. Phys. J. C **67** (2010) 637, arXiv: `0906.1833 [hep-ph]` (cit. on p. 50).

[85] ATLAS Collaboration, *Jet reconstruction and performance using particle flow with the ATLAS Detector*, Eur. Phys. J. C **77** (2017) 466, arXiv: `1703.10485 [hep-ex]` (cit. on pp. 50, 88).

[86] ATLAS Collaboration, *Performance of pile-up mitigation techniques for jets in pp collisions at* $\sqrt{s} = 8$ *TeV using the ATLAS detector*, Eur. Phys. J. C **76** (2016) 581, arXiv: `1510.03823 [hep-ex]` (cit. on p. 51).

[87] ATLAS Collaboration, *ATLAS flavour-tagging algorithms for the LHC Run 2 pp collision dataset*, Eur. Phys. J. C **83** (2023) 681, arXiv: `2211.16345 [physics.data-an]` (cit. on p. 52).

[88] ATLAS Collaboration, *ATLAS b-jet identification performance and efficiency measurement with* $t\bar{t}$ *events in pp collisions at* $\sqrt{s} = 13$ *TeV*, Eur. Phys. J. C **79** (2019) 970, arXiv: `1907.05120 [hep-ex]` (cit. on pp. 52, 90).

[89] ATLAS Collaboration, *The performance of missing transverse momentum reconstruction and its significance with the ATLAS detector using 140* fb^{-1} *of* $\sqrt{s} = 13$ *TeV pp collisions*, (2024), arXiv: `2402.05858 [hep-ex]` (cit. on pp. 52, 53, 88, 89, 96).

[90] ATLAS Collaboration, *Performance of electron and photon triggers in ATLAS during LHC Run 2*, Eur. Phys. J. C **80** (2020) 47, arXiv: `1909.00761 [hep-ex]` (cit. on p. 55).

[91] ATLAS Collaboration, *Technical Design Report for the Phase-I Upgrade of the ATLAS TDAQ System*, tech. rep., 2013, URL: `https://cds.cern.ch/record/1602235` (cit. on pp. 56, 58).

[92] T. Mkrtchyan, *The Phase-I Upgrade of the ATLAS Level-1 Calorimeter Trigger*, tech. rep., CERN, 2022, URL: `https://cds.cern.ch/record/2843493` (cit. on p. 57).

[93] S. Paganis, K. Loureiro, T. Carli, and G. Unal, *Combined Intercalibration and Longitudinal Weight Extraction for the ATLAS Liquid-Argon EM Calorimeter*, tech. rep., CERN, 2004, URL: `https://cds.cern.ch/record/806940` (cit. on p. 64).

[94] F. James and M. Roos, *Minuit: A System for Function Minimization and Analysis of the Parameter Errors and Correlations*, Comput. Phys. Commun. **10** (1975) 343 (cit. on p. 65).

[95] GEANT4 Collaboration, S. Agostinelli, et al., GEANT4 – *a simulation toolkit*, Nucl. Instrum. Meth. A **506** (2003) 250 (cit. on pp. 65, 82).

[96] ATLAS Collaboration, *The ATLAS Simulation Infrastructure*, Eur. Phys. J. C **70** (2010) 823, arXiv: `1005.4568 [physics.ins-det]` (cit. on pp. 65, 82).

[97] ATLAS Collaboration, *Electron and photon efficiencies in LHC Run 2 with the ATLAS experiment*, JHEP **05** (2024) 162, arXiv: `2308.13362 [hep-ex]` (cit. on pp. 67, 95).

[98] D. F. Raßloff, "Installation, Commissioning and Calibration of the ATLAS Level-1 Calorimeter Trigger in Run 3", PhD thesis: U. Heidelberg (main), 2023, URL: `https://archiv.ub.uni-heidelberg.de/volltextserver/34198/1/Thesis_DamirRa%C3%9Floff.pdf` (cit. on p. 72).

[99] *ATLAS public plots: Level-1 Calorimeter Trigger Public Results*, visited on 20/08/2024, URL: `https://twiki.cern.ch/twiki/bin/view/AtlasPublic/L1CaloTriggerPublicResults` (cit. on pp. 72, 73).

[100] ATLAS Collaboration, *Measurement of $W^{\pm}$-boson and Z-boson production cross-sections in pp collisions at $\sqrt{s} = 2.76$ TeV with the ATLAS detector*, Eur. Phys. J. C **79** (2019) 901, arXiv: `1907.03567 [hep-ex]` (cit. on p. 75).

[101] ATLAS Collaboration, *Measurements of W and Z boson production in pp collisions at $\sqrt{s} = 5.02$ TeV with the ATLAS detector*, Eur. Phys. J. C **79** (2019) 128, arXiv: `1810.08424 [hep-ex]` (cit. on p. 75).

[102] ATLAS Collaboration, *Precision measurement and interpretation of inclusive W^+, W^- and Z/γ^* production cross sections with the ATLAS detector*, Eur. Phys. J. C **77** (2017) 367, arXiv: `1612.03016 [hep-ex]` (cit. on pp. 75, 92, 104).

[103] ATLAS Collaboration, *Measurement of the Drell–Yan triple-differential cross section in pp collisions at $\sqrt{s} = 8$ TeV*, JHEP **12** (2017) 059, arXiv: `1710.05167 [hep-ex]` (cit. on p. 75).

[104] ATLAS Collaboration, *Measurement of the cross-section and charge asymmetry of W bosons produced in proton–proton collisions at $\sqrt{s} = 8$ TeV with the ATLAS detector*, Eur. Phys. J. C **79** (2019) 760, arXiv: `1904.05631 [hep-ex]` (cit. on pp. 75, 104).

[105] ATLAS Collaboration, *Measurement of $W^{\pm}$ and Z-boson production cross sections in pp collisions at $\sqrt{s} = 13$ TeV with the ATLAS detector*, Phys. Lett. B **759** (2016) 601, arXiv: `1603.09222 [hep-ex]` (cit. on pp. 75, 101, 103, 104).

[106] ATLAS Collaboration, *Measurement of the transverse momentum distribution of Drell–Yan lepton pairs in proton–proton collisions at $\sqrt{s} = 13$ TeV with the ATLAS detector*, Eur. Phys. J. C **80** (2020) 616, arXiv: `1912.02844 [hep-ex]` (cit. on p. 75).

[107] ATLAS Collaboration, *Measurement of the $t\bar{t}$ cross section and its ratio to the Z production cross section using pp collisions at $\sqrt{s} = 13.6$ TeV with the ATLAS detector*, Phys. Lett. B **848** (2024) 138376, arXiv: `2308.09529 [hep-ex]` (cit. on pp. 75, 90, 93, 98, 115, 125, 126, 132, 159).

[108] ATLAS Collaboration, *Proposal for particle-level object and observable definitions for use in physics measurements at the LHC*, tech. rep., CERN, 2015, URL: `https://cds.cern.ch/record/2022743` (cit. on p. 77).

[109] W. A. Rolke, A. M. Lopez, and J. Conrad, *Limits and confidence intervals in the presence of nuisance parameters*, Nucl. Instrum. Meth. A **551** (2005) 493, ed. by L. Lyons and M. Karagoz, arXiv: `physics/0403059` (cit. on p. 77).

[110] S. Navas et al., *Review of particle physics*, Phys. Rev. D **110** (2024) 030001 (cit. on pp. 77, 78).

[111] Tomas Dado, Alexander Held, and Michele Pinamonti, *Top-related experiment (`TREx`) fitter*, `https://trexfitter-docs.web.cern.ch/trexfitter-docs/`, 2023 (cit. on p. 79).

[112] K. Cranmer, G. Lewis, L. Moneta, A. Shibata, and W. Verkerke, *HistFactory: A tool for creating statistical models for use with RooFit and RooStats*, (2012) (cit. on p. 79).

[113] ATLAS Collaboration, *Preliminary analysis of the luminosity calibration of the ATLAS 13.6 TeV data recorded in 2022*, tech. rep., CERN, 2023, URL: `https://cds.cern.ch/record/2853525` (cit. on pp. 79, 96).

[114] G. Avoni et al., *The new LUCID-2 detector for luminosity measurement and monitoring in ATLAS*, JINST **13** (2018) P07017, URL: `https://cds.cern.ch/record/2633501` (cit. on pp. 79, 96).

[115] ATLAS Collaboration, *ATLAS data quality operations and performance for 2015–2018 data-taking*, JINST **15** (2020) P04003, arXiv: `1911.04632 [physics.ins-det]` (cit. on pp. 79, 81).

[116] *Luminosity Determination using $Z \to \ell\ell$ events at $\sqrt{s} = 13$ TeV with the ATLAS detector*, tech. rep., CERN, 2021, URL: `https://cds.cern.ch/record/2752951` (cit. on p. 81).

[117] E. Bothmann et al., *Event generation with Sherpa 2.2*, SciPost Phys. **7** (2019) 034, arXiv: `1905.09127 [hep-ph]` (cit. on pp. 81, 83, 84).

[118] F. Buccioni et al., *OpenLoops 2*, Eur. Phys. J. C **79** (2019) 866, arXiv: `1907.13071 [hep-ph]` (cit. on p. 81).

[119] F. Cascioli, P. Maierhöfer, and S. Pozzorini, *Scattering Amplitudes with Open Loops*, Phys. Rev. Lett. **108** (2012) 111601, arXiv: `1111.5206 [hep-ph]` (cit. on p. 81).

[120] A. Denner, S. Dittmaier, and L. Hofer, COLLIER*: A fortran-based complex one-loop library in extended regularizations*, Comput. Phys. Commun. **212** (2017) 220, arXiv: `1604.06792 [hep-ph]` (cit. on p. 81).

[121] S. Schumann and F. Krauss, *A parton shower algorithm based on Catani–Seymour dipole factorisation*, JHEP **03** (2008) 038, arXiv: `0709.1027 [hep-ph]` (cit. on p. 81).

[122] S. Höche, F. Krauss, M. Schönherr, and F. Siegert, *QCD matrix elements + parton showers. The NLO case*, JHEP **04** (2013) 027, arXiv: `1207.5030 [hep-ph]` (cit. on p. 81).

[123] R. D. Ball et al., *Parton distributions for the LHC run II*, JHEP **04** (2015) 040, arXiv: `1410.8849 [hep-ph]` (cit. on pp. 81, 97).

[124] C. Anastasiou, L. Dixon, K. Melnikov, and F. Petriello, *High-precision QCD at hadron colliders: Electroweak gauge boson rapidity distributions at next-to-next-to leading order*, Phys. Rev. D **69** (2004) 094008, arXiv: `hep-ph/0312266` (cit. on p. 81).

[125] ATLAS Collaboration, *ATLAS Pythia 8 tunes to 7 TeV data*, ATL-PHYS-PUB-2014-021, 2014, URL: `https://cds.cern.ch/record/1966419` (cit. on p. 82).

[126] M. Beneke, P. Falgari, S. Klein, and C. Schwinn, *Hadronic top-quark pair production with NNLL threshold resummation*, Nucl. Phys. B **855** (2012) 695, arXiv: `1109.1536 [hep-ph]` (cit. on pp. 82, 93).

[127] M. Cacciari, M. Czakon, M. Mangano, A. Mitov, and P. Nason, *Top-pair production at hadron colliders with next-to-next-to-leading logarithmic soft-gluon resummation*, Phys. Lett. B **710** (2012) 612, arXiv: `1111.5869 [hep-ph]` (cit. on pp. 82, 93).

[128] P. Bärnreuther, M. Czakon, and A. Mitov, *Percent-Level-Precision Physics at the Tevatron: Next-to-Next-to-Leading Order QCD Corrections to* $q\bar{q} \to t\bar{t} + X$, Phys. Rev. Lett. **109** (2012) 132001, arXiv: `1204.5201 [hep-ph]` (cit. on pp. 82, 93).

[129] M. Czakon and A. Mitov, *NNLO corrections to top-pair production at hadron colliders: the all-fermionic scattering channels*, JHEP **12** (2012) 054, arXiv: `1207.0236 [hep-ph]` (cit. on pp. 82, 93).

[130] M. Czakon and A. Mitov, *NNLO corrections to top pair production at hadron colliders: the quark-gluon reaction*, JHEP **01** (2013) 080, arXiv: `1210.6832 [hep-ph]` (cit. on pp. 82, 93).

[131] M. Czakon, P. Fiedler, and A. Mitov, *Total Top-Quark Pair-Production Cross Section at Hadron Colliders Through* $O(\alpha_S^4)$, Phys. Rev. Lett. **110** (2013) 252004, arXiv: `1303.6254 [hep-ph]` (cit. on pp. 82, 93).

[132] M. Czakon and A. Mitov, *Top++: A program for the calculation of the top-pair cross-section at hadron colliders*, Comput. Phys. Commun. **185** (2014) 2930, arXiv: `1112.5675 [hep-ph]` (cit. on pp. 82, 93).

[133] P. Nason, *A new method for combining NLO QCD with shower Monte Carlo algorithms*, JHEP **11** (2004) 040, arXiv: `hep-ph/0409146` (cit. on p. 84).

[134] S. Frixione, P. Nason, and C. Oleari, *Matching NLO QCD computations with parton shower simulations: the POWHEG method*, JHEP **11** (2007) 070, arXiv: `0709.2092 [hep-ph]` (cit. on p. 84).

[135] S. Alioli, P. Nason, C. Oleari, and E. Re, *A general framework for implementing NLO calculations in shower Monte Carlo programs: the POWHEG BOX*, JHEP **06** (2010) 043, arXiv: `1002.2581 [hep-ph]` (cit. on p. 84).

[136] T. Sjöstrand et al., *An introduction to PYTHIA 8.2*, Comput. Phys. Commun. **191** (2015) 159, arXiv: `1410.3012 [hep-ph]` (cit. on p. 84).

[137] ATLAS Collaboration, *Emulating the impact of additional proton–proton interactions in the ATLAS simulation by presampling sets of inelastic Monte Carlo events*, Comput. Softw. Big Sci. **6** (2022) 3, arXiv: `2102.09495 [hep-ex]` (cit. on p. 82).

[138] S. Porteboeuf, T. Pierog, and K. Werner, *Producing Hard Processes Regarding the Complete Event: The EPOS Event Generator*, 2010, arXiv: `1006.2967 [hep-ph]` (cit. on p. 82).

[139] T. Pierog, I. Karpenko, J. M. Katzy, E. Yatsenko, and K. Werner, *EPOS LHC: Test of collective hadronization with data measured at the CERN Large Hadron Collider*, Phys. Rev. C **92** (2015) 034906, arXiv: `1306.0121 [hep-ph]` (cit. on p. 82).

[140] NNPDF Collaboration, R. D. Ball, et al., *Parton distributions with LHC data*, Nucl. Phys. B **867** (2013) 244, arXiv: `1207.1303 [hep-ph]` (cit. on p. 82).

[141] ATLAS Collaboration, *The Pythia 8 A3 tune description of ATLAS minimum bias and inelastic measurements incorporating the Donnachie–Landshoff diffractive model*, ATL-PHYS-PUB-2016-017, 2016, URL: `https://cds.cern.ch/record/2206965` (cit. on p. 82).

[142] ATLAS Collaboration, *The ATLAS Simulation Infrastructure*, Eur. Phys. J. C **70** (2010) 823, arXiv: `1005.4568 [physics.ins-det]` (cit. on p. 82).

[143] ATLAS Collaboration, *Muon reconstruction and identification efficiency in ATLAS using the full Run 2 pp collision data set at $\sqrt{s} = 13$ TeV*, Eur. Phys. J. C **81** (2021) 578, arXiv: `2012.00578 [hep-ex]` (cit. on p. 88).

[144] D. Adams et al., *Recommendations of the Physics Objects and Analysis Harmonisation Study Groups 2014*, tech. rep., CERN, 2014, URL: `https://cds.cern.ch/record/1743654` (cit. on p. 89).

[145] ATLAS Collaboration, *Expected Performance of the ATLAS Experiment - Detector, Trigger and Physics*, (2009), arXiv: `0901.0512 [hep-ex]` (cit. on p. 91).

[146] S. Camarda et al., *DYTurbo: fast predictions for Drell-Yan processes*, Eur. Phys. J. C **80** (2020) 251, arXiv: `1910.07049 [hep-ph]` (cit. on p. 92).

[147] S. Camarda, L. Cieri, and G. Ferrera, *Fiducial perturbative power corrections within the $\mathbf{q}_T$ subtraction formalism*, Eur. Phys. J. C **82** (2022) 575, arXiv: `2111.14509 [hep-ph]` (cit. on p. 92).

[148] S. Camarda, L. Cieri, and G. Ferrera, *Drell–Yan lepton-pair production: q_T resummation at N^4LL accuracy*, Phys. Lett. B **845** (2023) 138125, arXiv: `2303.12781 [hep-ph]` (cit. on p. 92).

[149] R. Sadykov and V. Yermolchyk, *Polarized NLO EW e^+e^- cross section calculations with ReneSANCe-v1.0.0*, Comput. Phys. Commun. **256** (2020) 107445, arXiv: `2001.10755 [hep-ph]` (cit. on p. 92).

[150] S. Bondarenko, Y. Dydyshka, L. Kalinovskaya, R. Sadykov, and V. Yermolchyk, *Hadron-hadron collision mode in ReneSANCe-v1.3.0*, Comput. Phys. Commun. **285** (2023) 108646, arXiv: `2207.04332 [hep-ph]` (cit. on p. 92).

[151] R. D. Ball et al., *The PDF4LHC21 combination of global PDF fits for the LHC Run III*, J. Phys. G **49** (2022) 080501, arXiv: `2203.05506 [hep-ph]` (cit. on pp. 93, 97).

[152] T.-J. Hou et al., *New CTEQ global analysis of quantum chromodynamics with high-precision data from the LHC*, Phys. Rev. D **103** (2021) 014013, arXiv: `1912.10053 [hep-ph]` (cit. on p. 93).

[153] T. Cridge, L. A. Harland-Lang, A. D. Martin, and R. S. Thorne, *An investigation of the α_S and heavy quark mass dependence in the MSHT20 global PDF analysis*, Eur. Phys. J. C **81** (2021) 744, arXiv: `2106.10289 [hep-ph]` (cit. on p. 93).

[154] T. Cridge, L. A. Harland-Lang, A. D. Martin, and R. S. Thorne, *QED parton distribution functions in the MSHT20 fit*, Eur. Phys. J. C **82** (2022) 90, arXiv: `2111.05357 [hep-ph]` (cit. on p. 93).

[155] S. Alekhin, J. Blümlein, S. Moch, and R. Plačakytė, *Parton distribution functions, α_s, and heavy-quark masses for LHC Run II*, Phys. Rev. D **96** (2017) 014011, arXiv: `1701.05838 [hep-ph]` (cit. on p. 93).

[156] ATLAS Collaboration, *Determination of the parton distribution functions of the proton using diverse ATLAS data from pp collisions at $\sqrt{s} = 7, 8$ and 13 TeV*, Eur. Phys. J. C **82** (2022) 438, arXiv: `2112.11266 [hep-ex]` (cit. on pp. 93, 130).

[157] ATLAS Collaboration, *Muon reconstruction and identification efficiency in ATLAS using the full Run 2 pp collision data set at $\sqrt{s} = 13$ TeV*, Eur. Phys. J. C **81** (2021) 578, arXiv: `2012.00578 [hep-ex]` (cit. on p. 96).

[158] S. Dulat et al., *New parton distribution functions from a global analysis of quantum chromodynamics*, Phys. Rev. D **93** (2016) 033006, arXiv: `1506.07443 [hep-ph]` (cit. on p. 132).

List of figures

List of tables